Design and Synthesis of Nanocrystal Heterostructures for Optoelectronic Applications

by

Jonathan E. Halpert

B.S. ACS Chemistry
Tufts University, Medford, MA.

Submitted to the Department of Chemistry in Partial Fulfillment of the Requirements for the Degree of

DOCTOR OF PHILOSOPHY

at the

MASSACHUSETTS INSTITUTE OF TECHNOLOGY

April 2008
[June 2008]

Signature of Author _____
Department of Chemistry
May 16, 2007

Certified by _____
Moungi G. Bawendi
Professor of Chemistry
Thesis Supervisor

Accepted by _____
Robert W. Field
Chairman, Department Committee of Graduate Students

This doctoral thesis has been examined by a committee of the Department of Chemistry as follows:

Professor Andrei Tokmakoff
Thesis Committee Chairman

Professor Moungi G. Bawendi
Thesis Supervisor

Professor Troy Van Voorhis
Thesis Committee Member

Design and Synthesis of Nanocrystal Heterostructures for Optoelectronic Applications

by

Jonathan E. Halpert

Submitted to the Department of Chemistry on April 30, 2008 in Partial Fulfillment of the Requirements for the Degree of Doctor of Philosophy in Chemistry

ABSTRACT

Colloidal semiconductor nanocrystals can be used for a variety of optoelectronic applications including light emitting devices (LEDs) and photovoltaics. Their narrow emission spectra make them excellent fluorophors for use in red, green and blue emitting organic LEDs and have been shown to achieve external quantum efficiencies as high as 2.7%, 1.8% and 0.4% respectively. Better synthetic methods have produced nanocrystal emitters with higher quantum yield, boosting efficiency, while a better understanding of QD-OLED function has led to improved organic transport materials. These QD-OLED devices can also be redesigned using inorganic hole and electron transport materials to produce inorganic QD-LEDs (QD-ILEDs) with EQE as high as 0.1%. Inorganic transport layers are more robust to solvents and oxygen, and are expected to greatly increase the device lifetime of QD-LEDs over devices employing organic materials. New QD deposition techniques using an inorganic hole transport layer include inkjet printing and Langmuir-Shaeffer dip-coating. Greater synthetic control of the II-VI nanocrystals has also yielded type-II CdSe/CdTe nanobarbells capable of internal exciton separation for photovoltaic applications. Although efficient solar cells using this material could not be produced, the material has given us several insights into the physics and future designs of bulk heterojunction photovoltaic devices. Finally, nanocrystal heterostructures formed using J-aggregate dyes electrostatically bound to QDs, have shown potential for use in LCD or lasing device applications.

Thesis Supervisor: Moungi G. Bawendi, Ph.D.
Title: Professor of Chemistry

For Kira and my family

Table of Contents

List of Figures

Chapter 1

Introduction

This thesis presents work done using semiconductor nanocrystals to produce functional optoelectronic devices. Nanocrystals were designed and synthesized in order to optimize certain device applications based on our understanding of device physics.

The introduction will begin with an extensive description of the properties and means of producing these nanocrystals. The second half of the introduction will focus on the history and functioning principles of the various devices in which nanocrystals are deployed, as well as provide motivation for their use over existing materials. Each section in the second half of the introduction provides an overview and history of a device structure and is intended to give the reader a better understanding of the context in which each device was researched and produced. This will allow the reader a greater understanding of why certain choices were made to include certain materials, or employ certain device structures, and ultimately to decide whether these devices were successful in achieving their goals.

Following the introduction, each chapter will describe the synthesis and characterization of different materials and their performance in optoelectronic devices. Each chapter will conclude with an evaluation of the current stage of the technology and some prediction of the future of each project.

1.1 Semiconductor Nanocrystals

The research pioneered in the Bawendi research group over the last 15 years has primarily focused on understanding the physical, optical and chemical properties of colloidal semiconductor quantum dots (QD's). Quantum dots are a class of nanocrystals with spherical dimensions on the order of 1-10 nm in diameter, which exhibit unique optical properties corresponding to the quantum confinement effect [1]. Colloidal QD's can be produced chemically in a flask at atmospheric pressures, using inexpensive equipment and precursors, and can be produced at nearly molar quantities of material at one time. In addition, they exhibit high quantum yields [2] and widely variable, tunable emission [1], as well as high absorption cross-sections [3] and chemical stability typical of II-VI semiconductor nanocrystals [[1,4-8]. This work will outline many of the applications to which the properties of nanocrystals confer a unique advantage and will demonstrate several methods by which to create nanocrystals more perfectly suited to functioning in specific types of devices. For example, high quantum yield materials are required for creating efficient LED's (Chapter 2 and 3), while materials capable of separating excitons into charge pairs are needed for creating suitable solar cells (Chapter 4). The purpose of this research has been to first synthesize materials particularly suited for such applications and then to implement them in devices designed to accommodate their unique physics and chemistry.

1.1.1 Optical Properties of Semiconductor Nanocrystals

As atoms come together to form crystalline solids, the available electronic states in the structure change from discrete molecular bonding states, for a small number of atoms in a molecule, to energetically distributed semi-continuous bands, for a large repeating pattern of atoms as is found in crystalline solids [9] (See Figure 1.1).

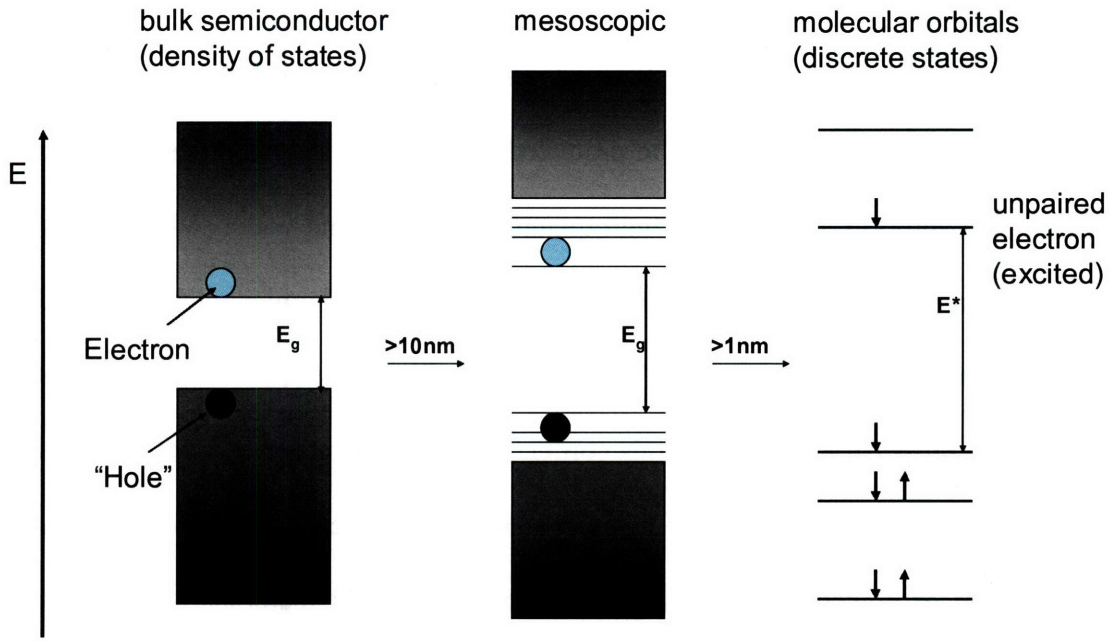

Figure 1.1: A diagram of the change in density of states with decreasing size of the material.

These bands of states are usually denoted by the mobility of an electron (or hole). Bands above the Fermi energy, where an electron can move freely through the crystal structure, are called the electron conduction bands. Bands below the Fermi energy, where the electrons are bound locally to a single atom in the crystal, are called the electron valence (or hole conduction) bands. In a metal, the bands are filled with electrons in states above the Fermi energy, such that electrons can move freely with the material. This is evidenced by the very high conductivity of most metals. In a semiconductor or an

insulator, these bands are distributed in such a way that there is a complete lack of electrons in states above the Fermi energy, and in fact there is an energy gap between the valence and conduction bands. Whether a material is considered semiconductor or insulator is determined only by the size of the gap, and hence the amount of energy required to promote an electron above the gap. Thus when a photon provides energy above the energy of the band gap to an electron in the valence band of a semiconductor, that electron becomes mobile in the conduction band and leaves behind a positively charged "hole". However, the mobility of the electron, in the absence of a field, is limited. The electron is electrostatically bound to the hole, forming an electron hole pair, or exciton (See Figure 1.2).

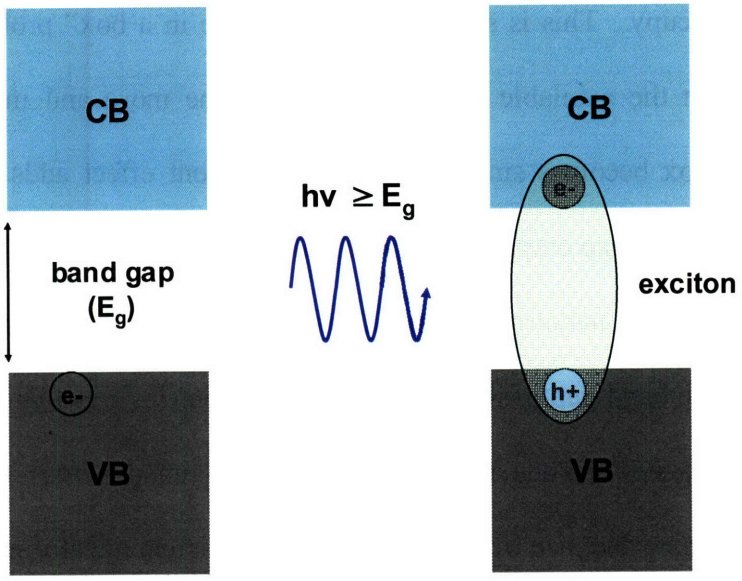

Figure 1.2: A diagram of the band gap in a bulk semiconductor. A photon with energy greater than the band gap will excite an electron into the conduction band (CB) where it becomes mobile in the solid, and leaves a positively charged hole behind in the valence band. The electron hole pair are linked electrostatically to form an exciton.

The exciton can be modeled much like a hydrogen atom, except with a significantly faster rate of decay [10]. Thus one can describe a Bohr radius for the probability distribution of the positions of the electron and hole in the exciton, and a band gap energy, which is emitted when the hole and electron recombine [10]. In direct gap solid state semiconductors, the energy of the photons emitted matches the band gap of the material, which is dictated by the bonding properties, states and electrons available in the atoms making up the crystal.

In nanocrystalline materials, which are between 10 and 10,000 atoms across, the radius of the nanocrystals is below that of the Bohr radius of the exciton. Thus the wavefunctions of the electron and hole are "squeezed" into a spherical (in the case of a quantum dot) boundary, increasing the energetic distance between the available states that charge can occupy. This is similar to the "particle in a box" problem of quantum mechanics wherein the available wavefunctions become more and more energetically separated as the box becomes smaller. This confinement effect adds a further energy term to that of the band gap energy upon recombination of the exciton. The energy of the photon emitted from a nanocrystals sized within the confinement regime is then a function of both the band gap of the material (which is intrinsic to that material) and the size of the nanocrystal. Thus the emission can be tuned across a wide range of wavelengths by tuning the size of the nanocrystal as it is chemically grown (see Figure 1.3).

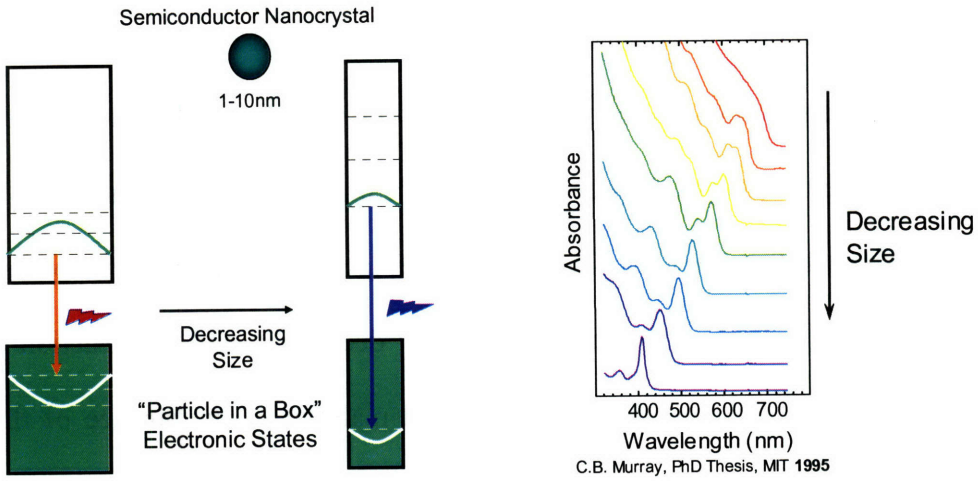

Figure 1.3: Two diagrams of the confinement effect. The first (left) shows the increase in spacing between the energy levels as the energy well becomes thinner. In the second (right), the decreasing size of the CdSe nanocrystals gives rise to bluer first absorption peaks, indicating a wider band gap. [11]

The result of this effect is that instead of being confined to materials that emit at few wavelengths for a few emissive semiconductors, we are now able to produce a literal rainbow of colors from the UV to the IR with just a few materials, by adjusting the size of the nanocrystal. The absorbing states of the material similarly change with size, being ~60 eV larger than that of the emission. This "Stokes" shift is due to small differences in the contributions of the fine structure states to absorption versus emission [12].

1.1.2 Synthesis of Monodisperse II-VI Quantum Dots

Monodisperse quantum dots are one set of materials that have been synthesized to take advantage of the properties described above. Monodisperse quantum dots are generally synthesized by the rapid addition of precursors into high boiling solvents at

high temperature [1,2,4-8,11,13-17] (see Figure 1.4). Trioctylphosphine oxide (TOPO), trioctylphosphine (TOP), octadecene (ODE), squalane and oleylamine are examples of commonly used solvents. Rapid introduction of the precursor at high temperature causes pyrolysis of the metal organic precursors to form small "nuclei" of material of just a few lattice cells (10-100 atoms). Nucleation becomes less prevalent once the concentration of precursors dips and the temperature is rapidly decreased, and the reaction enters the growth phase. In this regime, precursors add material to the surface of the existing nuclei, effectively growing the quantum dot in size and no longer forming new nuclei. This preserves the size distribution of the quantum dots in that by selecting the correct precursor materials, all the quantum dots grow at nearly the same rate in solution, and no new nuclei are formed. The resulting sample will thus contain a majority of quantum dots with radii distributed within a range of about 5-10% of the mean. Eventually the reaction will reach a steady state of material in quantum dot versus precursor form, and the size distribution will increase as larger QD's will slowly begin to retain the material lost from slightly smaller QD's in a process known as Ostwald ripening [18].

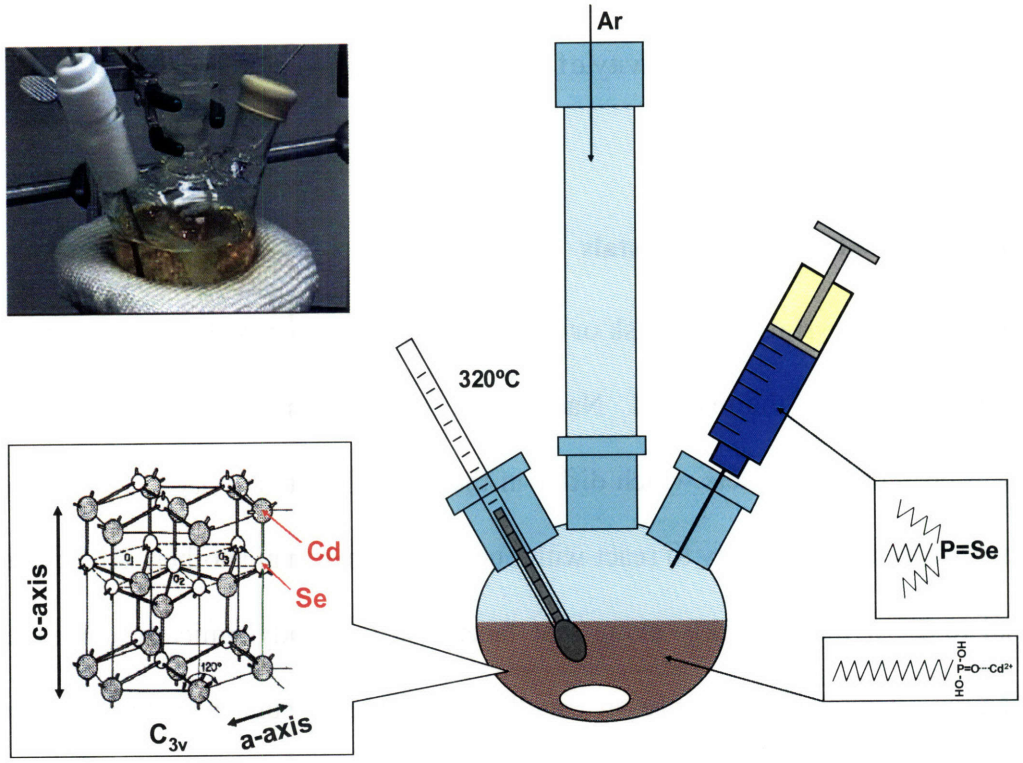

Figure 1.4: A diagram of the experimental setup for producing colloidal nanocrystals. (Inset) A crystalline structure of CdSe (Wurtzite) nuclei of a few unit cells. (Top Left) A photo of the reaction right after injection. (Photo courtesy of Wenhao Liu)

The desired optical properties of the sample are chosen by cooling the reaction once the desired radii of the QD's has been achieved. By selecting ligands and precursors with the correct reactivity, the size distribution can be minimized right at the point when the reaction is stopped, yielding an optimal sample with the desired peak emission wavelength and a small full width at half maximum (FWHM). For common materials emitting in the red part of the visible spectrum, a FWHM of 25-30 nm can generally be achieved for good samples. II-VI materials which are commonly synthesized in this manner are ME binary metal chalcogenides, where M = Zn, Cd, Pb and E = S, Se, Te. Oxides can also be formed but are generally not optically useful. It is also possible to

make terniary materials of the forms M_1M_2E or ME_1E_2 using the above approach by adjusting the concentrations and reactivity of the chosen precursors [7,15].

1.1.3 Growing Anisotropic Nanocrystals

Growing nanocrystals with a disk or rod-like shape is also possible, depending on the crystalline structure of the material. Nanocrystals that have a hexagonal or Wurtzite structure will present three facets which differ in their chemical reactivity. This causes some precursors to be more likely to react with one facet rather than another. This causes the material to grow more quickly along that facet in a thermodynamically controlled reaction regime. CdSe nanorods are an excellent example of such a material, where material is added along the c-axis (to the 0001) face of the nanocrystals [19]. It is also possible to kinetically control the reactivity of certain facets by using bulky ligand groups that react more strongly with one facet rather than another[4,14,19,20]. In the case of CdSe, maintaining high precursor concentrations throughout the reaction (by addition of excess material) and using long chain phosphonic acid ligands to cap the dangling bonds on the edge of the nanocrystals generally produces anistropic shapes. Other materials have been shown to grow rods[4,19], disks [21], and cubes [20]. In all these cases the defining feature is that the nanocrystals are more likely to grow along certain facets than others, thus contributing to the final shape of the nanocrystals [22]. In fact, most quantum dots are not spherical but rather form as faceted crystals. For example, CdSe quantum dots are Wurtzite in structure and thus form small hexagonally faceted crystals.

1.1.4 Overcoating and Formation of Heterostructures

Overcoated, or core-shell, nanocrystals [2,5,6,8,23,24] represent the simplest form of a heterostructure; a mixture of two materials with distinguishable domains within the nanocrystals. Core-shell nanocrystals are created by placing the core nanocrystals in a pot of high-boiling solvent with precursors for the second material. As an example, CdSe is overcoated by dispersing the cores in a mixture of TOPO and hexylphosphonic acid (HPA) at moderate temperatures (130 to 190 °C), and slowly adding reactive zinc and sulfur precursors [2,23,24]. Using reactive precursors, such as organometallics like diethyl zinc, ensures that material will react immediately and isotropically with the surface of the nanocrystals, forming an even shell. Slow addition of the precursors avoids building up a high concentration of precursor that could allow for nucleation of the precursor and formation of cores made from the overcoating material. Similarly, the low temperature of growth, compared to the growth temperature of the cores, is meant to avoid the formation of nuclei from the second material and also to prevent ligands in solution from removing any of the core material and thus allowing core material to be added to the shell, or even forming new cores. The amount of precursor to add for the second material is dependant on the intended thickness of the shell and is calculated using the number and size of the cores present, along with basic geometric assumptions about the bond lengths of the second material.

The choice of materials used to overcoat depends on the intended purpose of the nanocrystal sample. There are two types of core-shell heteostructures- type-I and type-II. The types vary on the location within the core-shell energy bands where the exciton is favored to reside (see Figure 1.5). In a type-I core-shell heterostructure [2,5,8] the exciton is

energetically favored to reside solely in the core due to the relative band edges of the two materials. A good example is the CdSe/ZnS nanocrystal, which is commonly used as a high quantum yield emitter [2,23-25]. Because of the difference in the valence bands and conduction bands of CdSe and ZnS, both the electron and the hole are likely to be trapped in the core material[2]. Furthermore, nanocrystals generally have a number of defect sites or unpassivated bonds on their surface, especially after purification. These sites represent interband states that can trap one of the charges of the exciton, generally promoting non-radiative decay. The ZnS layer represents an energy barrier, separating the charges from the surface of the nanocrystal and preventing non-radiative decay. This generally greatly enhances the quantum yield (QY) of the material and is considered a requirement for most emission applications. Quantum yield is the number of photons emitted for every photon absorbed. Generally a shell of about 5 monolayers is needed to thoroughly coat the nanocrystals and permanently improves the quantum yield from ~10% for purified cores to up to 90% for some CdSe/ZnS samples [23,24]. After overcoating, the nanocrystals are coated with the ligands present during the overcoating reaction and can be purified by precipitation in polar solvents. Although this process removes some ligands from the surface, generally the quantum yield suffers much less than for core materials. Quantum yields as high as 70% have been reported for materials after two purification steps [26,27].

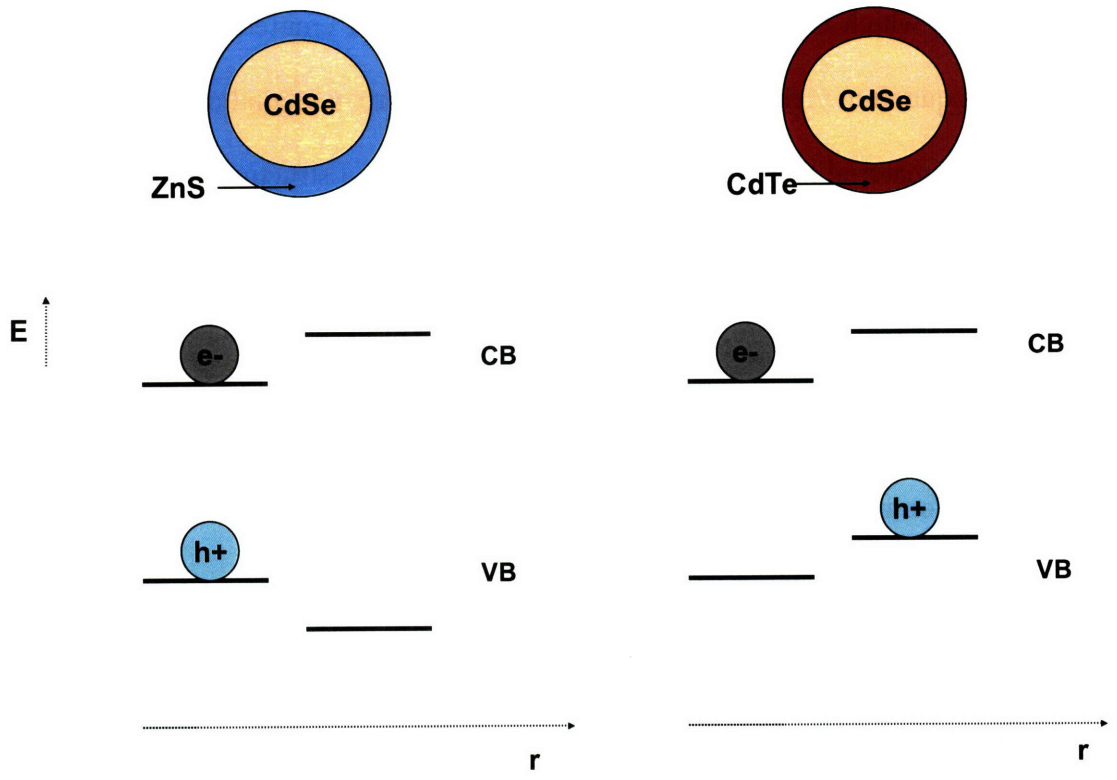

Figure 1.5: Energy level diagrams of a Type-I (left) and Type-II (right) structure. In the Type-I structure the hole and electron are confined in the core, in the Type-II structure they are separated between the core and shell materials.

In a type-II material [6,28] the second material is chosen so one charge will reside in the core material while the other exists in the shell material. An example of this is the material CdSe/CdTe in which the electron resides in the CdSe core, while the hole moves into the band structure of the CdTe. This creates a long lived (>100 ns) electron hole pair which can recombine to emit a photon with the energy of the difference between the valence band of CdTe and the conduction band of CdSe. This material is able to emit photons with wavelengths in the near infrared (IR), even though neither CdTe or CdSe alone could access this spectral range. Other useful examples of this phenomenon are

ZnSe/CdSe, which is an excellent material for creating emitters between 510-560 nm [16], and ZnSe/ZnTe, which is also useful for creating green light emitters. For applications requiring high quantum yield, it is often necessary to perform a second overcoating using a high band gap material like ZnS to create an effective Type-I structure around a Type-II core-shell. Materials made from ZnSe/CdSe/ZnS can be made with quantum yields as high as 70% [16,26,29].

1.1.6 Purification and Surface Treatments of Nanocrystals

Nanocrystals can be purified by precipitation using polar solvents, usually methanol/butanol or acetone [24]. The resulting precipitants are centrifuged at 3900 RPM and the supernatant, containing excess precursors, ligands and solvent from the reaction, are discarded. The precipitated nanocrystals are then redispersed in a (relatively) non-polar solvent such as hexane or chloroform by addition of the neat solvent, sometimes followed by vortexing and/or sonication. The process is generally repeated at least two or three times to ensure that all the precursor materials and excess ligands are removed from the sample prior to either a second reaction (like overcoating), or use in a device. Most devices are extremely sensitive to impurities. Impurities can affect the efficiency of the device by encouraging shorting through the nanocrystals film, degradation of the nanocrystals or oxidation of the surrounding organic films [30].

Nanocrystals can also be chemically altered to allow them to disperse in different solvents. This can be accomplished by several methods [31-33]. One of the most common, is to exchange the native capping ligands left on the nanocrystals after synthesis, with a new ligands with different end group functionalities. For example, TOPO capped

CdSe/ZnS nanocrystals can be easily cap-exchanged with aminopentanol (50% in ethanol) [33]. The amine functionality will bind preferentially with the nanocrystal surface to present a polar end group, making the nanocrystals soluble in polar alcohols like ethanol. Cap-exchanging can be performed in neat ligands, or in ligands mixed with the target solvent [32]. It can be done at room temperature if the new ligand binds preferentially, or by gently heating (40 °C-80 °C) the nanocrystals to release the native capping ligands and allow the new ligands to approach the surface. Purification of the nanocrystals after cap-exchange can be accomplished by either selective precipitation of the nanocrystals or purification through a size-exclusion column.

Another means of changing the end group functionality of the nanocrystals involves polymer encapsulation of the entire nanocrystal, including the native capping groups within an amphiphilic polymer [31,34]. Generally the polymer consists of long hydrophobic alkane groups, the polymer backbone and polar hydrophilic headgroups. The procedure for encapsulation is described in detail in Chapter 5, including synthesis of the polymer group. Essentially the two are mixed in a common solvent (generally chloroform) which is then gradually removed. As the solvent evaporates, the non-polar alkyl chains interdigitate with the non-polar end groups on the capping ligands, while the polar head groups are repelled. After removal of the solvent, a polar solvent (generally deionized water, or acid or base buffered water solution) is added in which the head groups, but not the alkyl chains, are soluble. Thus the polymer remains fixed to the nanocrystals but presents polar head groups to the aqueous solvent, providing a new solubility and also chemical functionality to the nanocrystals. These polar head groups

are often functional groups like hydroxyl, carboxylic acid or amino functional groups which can be used as attachment points for proteins, dyes, or other useful molecules.

1.1.7 Deposition of Nanocrystals into Thin Films

Semiconductor nanocrystals are generally deposited onto surfaces in order to create devices using the nanocrystals as a functional material. The method of deposition selected generally depends on the necessary properties of the film, including thickness, uniformity, patterning, and orientation of the nanocrystals themselves. Secondary considerations include the sensitivity of the nanocrystals to the heat or solvents required for a given deposition technique, as well as the chemical or physical sensitivity of the substrate. For example, inkjet printing works very well for depositing QD's onto silica, but the solvent, hexane, would damage organic substrates such as TPD.

1.1.7.1 Spin-casting

The easiest means of creating a monolayer of quantum dots is by spin-casting a solution of QD's in low boiling solvent onto a substrate [26,30,35,36]. Spin-casting is commonly used in optoelectronics applications to form films of organic materials or to form sol-gel inorganic films. Spin-casting is performed by depositing enough QD solution onto the surface of the substrate to cover it completely, then immediately rotating the substrate at high speed (>1000RPM), generally with a fast ramp (>1000 RPM/s) for about a minute. Immediately the centrifugal force acting on the solvent causes most of the solution to shear away, leaving behind an even film of QD solution

just a few hundred nanometers thick. The solvent then dries quickly, aided by the spinning action, leaving behind a uniform distribution of QD's on the substrate surface [26].

The film may then be annealed further, if necessary, by placing the substrate onto a heating plate for a given period of time [37]. The thickness of the film formed is related directly to the root of the concentration; hence increasing the concentration in the solution forms a thicker film. The film thickness can be verified through atomic force microscopy imaging of the surface (AFM). Generally, solutions must be prepared at a given concentration (A ~ 0.1 at the first absorption peak for a single monolayer film) and then calibrated using AFM [35,36]. Although this technique is very easy and reliable, it also requires large volumes of high concentration solutions to calibrate the solution concentration and create a monolayer film. Most of the QD solution prepared is sheared off and wasted during the spinning step.

1.1.7.2 Micro-contact printing QD's

A related means of deposition is through micro-contact printing [26,27,30,35,36,38] of an even film of QDs onto the substrate. This is accomplished by spin coating quantum dots onto a flexible polydimethylsiloxane (PDMS) polymer stamp, then stamping the resulting film onto the substrate [30] (see Figure 1.6).

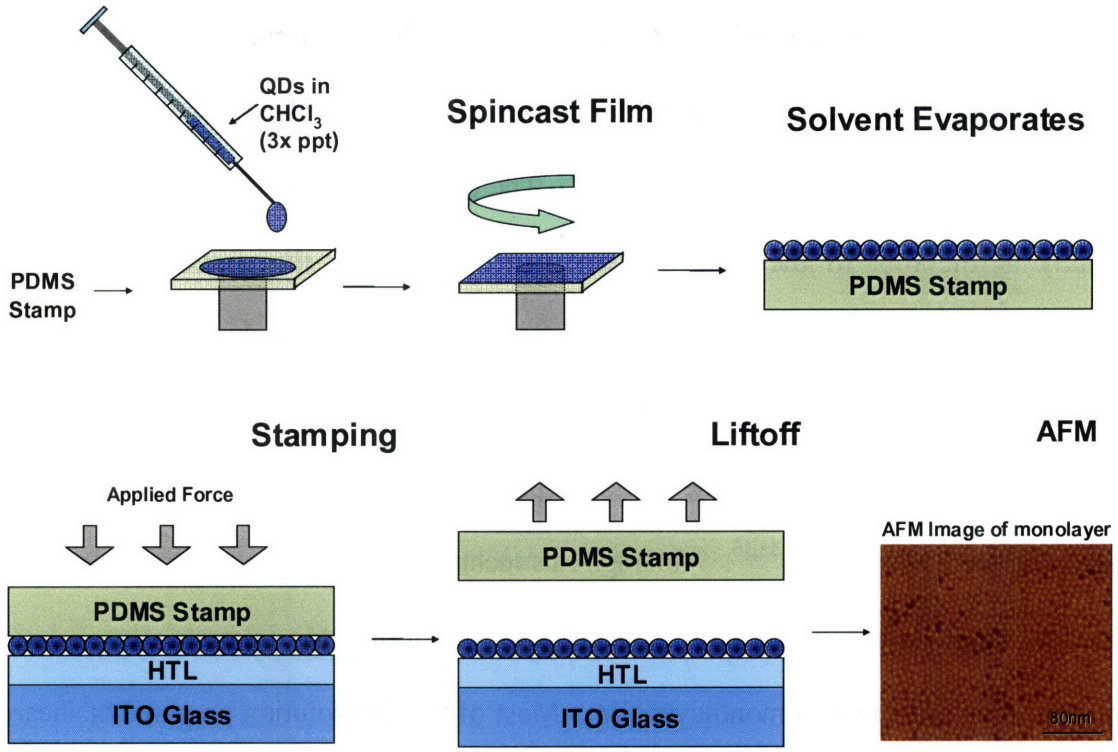

Figure 1.6: A diagram of the micro-contact printing process. [30]

This method works best when the affinity of the QD's for the substrate is greater than the affinity of the QD's for the stamp and thus the superior Van der Waal's attraction between the substrate and QD's causes them to physically transfer. The stamp can be patterned so that although the entire stamp is inked during the spin-coat step, only those QD's that come into contact with the substrate will be retained in the final pattern. The main reason for stamping, as opposed to spin coating, is to avoid letting the solvent from the QD solution come into contact with the substrate. This is particularly important when the substrate is formed from organic hole or electron transporting materials which are both chemically or physically sensitive to the solvent, either by reaction or solvation,

respectively. Such films also tend to function very differently in the device when impurities are present [30].

1.1.7.3 Drop-casting Techniques

Another means of depositing material is by drop-casting QD solution from a syringe needle onto a substrate [37,39]. This is the simplest means of deposition and can be used to form multilayers of close-packed (hexagonally packed) QD's in and around a small region, generally in the gap between electrodes in a planar device. Forming a close-packed film is mainly done by choosing solvents which evaporate and the correct rate so that material is deposited evenly in the center of the drop, not pushed toward the edges and left as the solvent edge retreats (thus forming "coffee stain" patterns) [40].

The key tends to be finding solvents with the proper affinity for the QD's and which evaporate at a slower, but steady rate. Fast drying solvents tend to leave coffee stain patterns. Generally the solvent system is discovered by trial and error; for CdSe, for example, it was found that 9:1 hexane:octane worked particularly well to form these close-packed, hexagonal superlattice structures [39]. Close packed films are useful mainly for conductivity and PV devices, as well as for lasing experiments [41].

1.1.7.4 Inkjet Printing Deposition

Another form of drop casting can be performed using an inkjet printer instead of a syringe as the means of deposition [42,43]. While suffering from many of the disadvantages of drop casting, including thick films and some irregularity of the surface, it enjoys the

particular advantage of enabling complex patterns to be formed without lithography. In fact the printer head can be programmed to deposit material in any arbitrary pattern with a minimal amount of preparation. To do so, QD's must be suspended in a solvent which does not degrade the printer head (hexane works for CdSe) and is expelled in micron sized drops at an arbitrarily chosen location. As the drops dry, the QD's and any accompanying materials, such as a polymer matrix, are left behind on the substrate surface (see Figure 1.7).

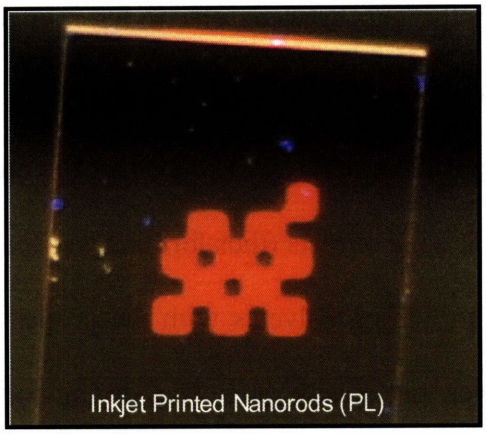

Figure 1.7: CdSe nanorods inkjet printed onto a glass substrate. (Photo courtesy of Gerry Chen)

Thus the only requirement to use this technique is that the substrate must be chemically and physically robust enough to withstand the presence of the solvent. The intended application also cannot rely on smooth, even monolayers of QD's since these are generally not generated using drop casting.

1.1.7.5 Langmuir-Blodgett Techniques

The final method of QD deposition presented in this work is Schaeffer dip-coating of QDs from a Langmuir trough [44,45]. A Langmuir trough consists of water in a well covered by a non-aqueous solution of QDs. As the QD's are slowly deposited out of the low boiling solvent (i.e. hexane, chloroform, toluene, etc) onto the aqueous phase, they spread out onto the surface but do not dissolve, as they are not soluble in water. The solvent then evaporates, leaving the QD's behind on the surface. The QDs can then be squeezed into the center of the aqueous phase by moving the walls of the trough closer together (Figure 1.8).

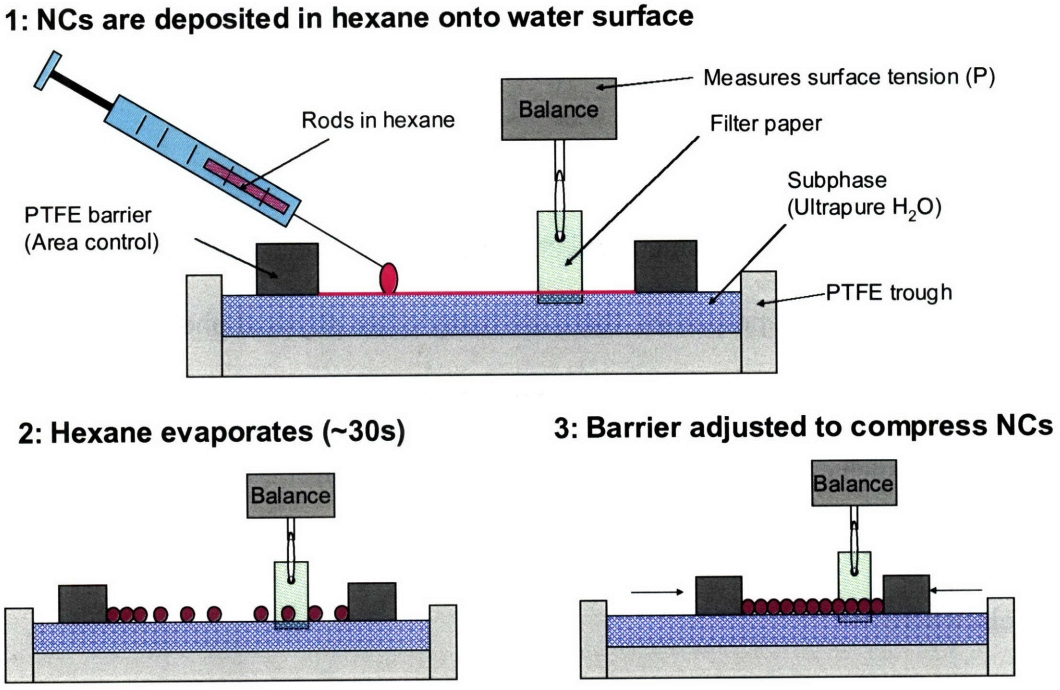

Figure 1.8: A cartoon diagram of the Langmuir Trough, which can be used to pack nanocrystals into a monolayer film by following the steps above.

The surface tension, which relates to the film tension, is measured by a force meter connected to a piece of filter paper dipped into the film. Although low-tech by design, this instrument is able to compress the nanosized QDs into a stable film with regular packing. The substrate may then be dipped into the trough, and as constant pressure is maintained on the QD film, the substrate is raised. If the QD's affinity for the substrate is greater than for the aqueous phase, for which they should have no affinity, then the QDs will stick to the substrate and maintain their pattern. Although this deposition technique has little application for QDs devices, it can be useful for depositing heterostructures such as nanorods, whereby the nanorods should align themselves parallel to the barriers of the trough prior to being deposited [44]. In theory this should allow the production of LED's using nanopatterned heterostructures.

1.1.8 Physics of Nanocrystals

Aside from the confinement effect, which gives nanocrystals their characteristic emission and absorption properties, there are many other physical phenomena of interest which occur in NCs. A few are presented here in detail as they pertain specifically to this work. Others, such as blinking [46,47], multiexciton generation [48,49], fine structure studies [50-52], and Stark effect [53], are not entirely pertinent to this work, and are discussed in greater detail elsewhere.

1.1.8.1 Forster Resonance Energy Transfer (FRET)

Forster Resonance Energy Transfer (FRET) is a form of energy transfer by which an exciton is non-radiatively transferred between two resonantly coupled oscillators. It

was first reported by T. Forster in 1946 [54,55], and is generally used to explain the interactions between closely associated dye molecules. As a dipole-dipole interaction FRET tends to occur on length scales of 1 - 10 nm. The rate of transfer between the two oscillators depends on a number of factors including: the overlap between the emission of the donor, on which the exciton initially resides, and the absorption of the acceptor; the distance between the two objects, the oscillator strength (of the acceptor), and the rate of other decay mechanisms in the donor. These factors are evident in several derived [56] expressions:

$$\langle \Gamma_{trans} \rangle = \frac{9}{8\pi} \frac{c^4}{n^4} \frac{\kappa^2}{R^6} \frac{1}{\tau} \int \frac{S_D(\omega)\sigma_A(\omega)}{\omega^4} d\omega \qquad (1.1.8.1a)$$

$$\langle \Gamma_{ET} \rangle = \frac{1}{\tau_D} \left(\frac{R_F}{R} \right)^6 \qquad (1.1.8.1b)$$

where Γ is the transfer rate, c is the speed of light, n is the index of refraction of the surrounding medium, K is a factor taking into account the orientation of the dipoles, R is the distance between the dipoles, τ is the lifetime of the exciton in the donor, S_D is the emission intensity of the donor, σ_A is the absorption cross-section of the acceptor and ω is the frequency. The overlap integral defines the degree to which the oscillators are in fact in resonance. As a dipole-dipole interaction, the distance between the two oscillators contributes an R^{-6} dependence. The oscillator strength of the acceptor determines the intensity of the absorption; stronger absorption leads to a greater likelihood of transfer. Other decay mechanisms in the donor can lead to decay of the exciton competing with the FRET rate, hence the longer the lifetime, the slower the transfer rate.

Understanding the mechanism of energy transfer from NCs to dye molecules provides a ready means of characterization of the synthesis of QD/J-aggregate constructs

in Chapter 5. The FRET equations can be used to define a probability and therefore a rate of transfer, as well as a characteristic distance within which the probability of transfer is >½. This distance is known as the Forster radius, R_F and is a useful means of determining the distance between two oscillators.

1.1.8.2 QD Lifetime Measurements

Finding the decay rate of excitons in nanocrystals is important for characterizing their composition and understanding their optical properties, as well as calculating FRET rates. Typical lifetimes for a CdSe QD are on the order of 10 ns, while those of PbSe can be as long as 200 ns [20]. NC lifetimes tend to be much longer than those of organic fluorophors due to spin frustration in the lowest energy excited state of the fine structure [57]. Due to the decreased overlap integral, the lifetimes of Type-II materials tend to be much longer than Type-I nanocrystals. This is the result of the spatial separation of the charge in materials such as CdSe/CdTe core shell QDs (lifetime ~ 100 ns). The lifetime of the exciton can be found from fitting fluorescence decay curves with an exponential expression (Section 5.3.4.1) and is dependent upon the various decay process, radiative and non-radiative, in the QD. The fluorescence decay can be easily measured using a streak camera with resolutions of better than 50 ps. Fluorescence decay rates help determine the feasibility of using materials for light emitting devices, photovoltaic devices, emission applications or for FRET based applications. They are also integral to understanding why some NCs display low QYs.

1.2 Light Emitting Diodes

Light emitting diodes (LEDs) constructed using nanocrystals as the emitting material comprise about half the volume of this work. As such it is necessary to explore the history and physics of these devices prior to the implementation of similar devices using nanocrystals. This should enable the reader to place these recent innovations into the proper context in the field of optoelectronics in general. Further discussion is warranted on the history of using nanocrystals in LEDs, so that the innovations and new devices presented here can be understood in the context of prior work both in the Bawendi group and by others in the nanocrystals field. Finally there is some discussion of ongoing research in the field and future directions for the LED projects, including a brief discussion of our progress toward a lasing QD-LED- the "final objective" of the LED project.

1.2.1 LEDs and Physics

Optoelectronics is the study of electronic devices which either produce or make use of light. These can include LEDs, solar cells, photovoltaic devices, and even fiber optics and optocoupling devices. Light emitting devices (LED's), originally and sometimes interchangeably termed "light emitting diodes", are a product of solid state semiconductor technologies, but in recent years such devices have incorporated organic semiconductors [58-63] and semiconducting polymers, as well as QDs.

In inorganic LED (ILED) heterojunction devices [64], one material is used to conduct electrons from one metal electrode to the junction while the other conducts holes to the junction. The electron and hole recombine to emit a photon. The transport layers

are chosen so that a material with high electron mobility and low hole mobility (n–type) transports the electron and a material with high hole mobility and low electron mobility (p-type) transports the hole. This ensures that the dominant carrier in each material is the charge expected to be injected from that electrode.

The electrodes are generally low resistivity metal or metal oxide materials with work functions selected to facilitate injection of the desired charge. Hence magnesium is a good material for injecting electrons due to its low work function (3.7), while gold is a good material for injecting holes due to its high work function (5.1 eV). This reduces the amount of voltage that needs to be applied to the device in order to inject the electron (hole) into the conductive (valence) band of the electron (hole) transport layer. The charges form electron-hole pairs at the heterojunction and recombine to emit photons with a characteristic energy corresponding to the difference between the valence band of the hole transport material and that of the electron transport material. A variation on the PN junction is the PIN junction, in which the function of the p-type and n-type materials is equivalent. But in this case, the charges are transported to a thin intermediate material on which excitons are formed. These excitons recombine with the energy of the band gap of the intermediate material (the "I" in the PIN). Most LEDs are heterostructured devices, making use of the difference in transport properties to ensure that excitons recombine at the junction of the two materials. Heterojunctions allow both carriers to be transported efficiently by a material doped to increase the mobility the necessary charge while also carefully controlling the location and wavelength of emission. These devices also tend to be favored for solar cell and photovoltaic structures for similar reasons.

1.2.2 QD-OLEDs: Motivation

The QD-organic LEDs (QD-OLED) devices were the first devices in which QDs were implemented as the active emitter. The earliest devices in the Bawendi group were formed using PIN structures making use of organic transport materials and were modeled on earlier works in other groups [65,66]. Our work in this arena focused on improving the efficiency and function of existing architectures using a greater variety of materials than had previously been known [65,66].

1.2.2.1 OLED's History

Since 1987, organic LEDs (OLEDs) have gained in popularity, making use of advances in the understanding of organic semiconductors [67]. These devices are attractive to manufacturers due to the relatively low cost of materials, variety of deposition techniques, and the bright, monochromatic emission of organic dye molecules. Using either polymer materials (PLEDs) or small molecule organics (OLEDs), these devices can be made on flexible substrates [59] and are easier to scale-up for displays, using large area deposition techniques like inkjet printing [68], than are competing technologies like LCD or plasma screens [30]. The last few years have seen a number of products, such as camera and cellphones, making use of OLED displays [30,69]. Several companies, such as Sony and Samsung, have displayed OLED televisions at conferences, although none have yet been offered for sale.

Due to its advantages in manufacturing, this technology is very likely to be popular in the near future. However, organic LED's suffer from a number of setbacks. First, the organic materials tend to be air and water sensitive, requiring strict packaging in

an inert atmosphere to improve the device lifetime [70]. Secondly, these molecules tend not to be completely photostable, bleaching slowly over time and losing brightness. In fact lifetimes for these devices are rarely better than 10,000 hours [60], relegating them to technologies such as video cameras and cellphones, where screen time is kept to a minimum. Third, the emission from organic molecules is an improvement on that of conventional phosphors used in CRTs, but because of the relatively wide peak of the organic emission, they still aren't fully capable of rendering true colors.

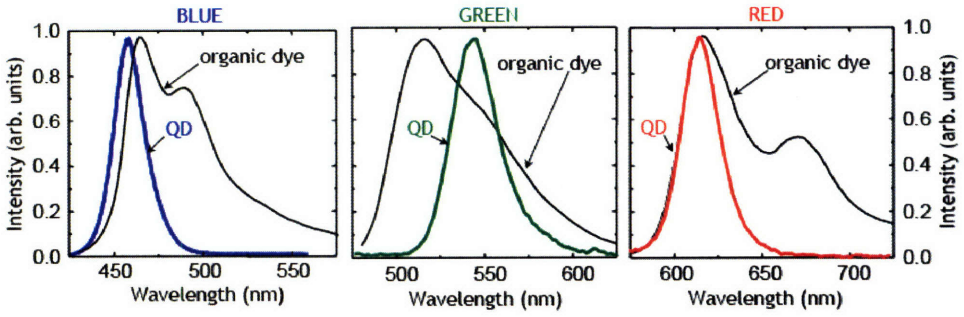

Figure 1.9: Spectra of red, green and blue (RBG) QDs superimposed over those of common organic dyes. The QD spectra have full width at half maximum (FWHM) of ~28 nm while the organics have FWHM of ~50-70 nm. [71]

1.2.2.2 QD-OLEDs History and Motivation

Quantum dot light emitting devices (QD-LEDs) have been a prominent application in nanocrystal research for several years. Although not yet as efficient as OLEDs, their superior emission characteristics allow QD-LED devices to gain access to a larger area of the Commission Internationale de l'Eclairage (CIE) coordinate diagram without much sacrifice of efficiency. QDs also exhibit improved durability over organic

flourescent dyes and can be processed easily into sandwich devices by spin-coating or micro-contact stamping monolayers [30].

The earliest QD-LEDs were fabricated in the mid 1990's using red emitting CdSe QDs, overcoated with ZnS (CdSe/ZnS), embedded in 100nm p-paraphenylene vinylene (PPV) films [72], in mixed films of polyvinylcarbazole (PVK), 2-(biphenyl-4-yl)-5-(4-*tert*-butylphenyl)-1,3,4-oxadiazole (t-Bu-PBD) and 5-10% loading fraction of QDs [73]. These devices displayed external quantum efficiencies (EQE) of below 0.01% [72,73], and either exhibited prominent electroluminescence (EL) peaks from the organic transport layers [72,73], or required low temperature operation to achieve QD color saturated spectra [73]. Improved polymer devices utilized thick layers (~25nm) of QDs, sandwiched between PPV and a magnesium/silver electrode [74]. These devices displayed poor emission characteristics, with significant EL from the polymer, but the efficiency was improved to 0.22% [74]. Another report by Mattoussi et al claimed EQE of 0.1% with a similar device using a separate organic HTL and a larger loading fraction of QDs [75]. The next generation of QD-LEDs used a sandwich structure consisting of an organic hole transporting layer (HTL) and electron transport layer (ETL) sandwiching a CdSe QD close-packed monolayer [29,30,71,76-78]. Early permutations of this design spin-cast N,N-diphenyl-N,N-bis(3-methylphenyl)-(1,1-biphenyl)-4,4-iamine (TPD) with QDs in chloroform, forming a 20-40 nm thick film of TPD with the QD monolayer on top, due to phase segregation [30]. The ETL for this device consisted of 40 nm of tris-(8-hydroxyquinoline)aluminium (Alq3), although some devices required the use of 3-(4-biphenylyl)-4-phenyl-5-t-butylphenyl-1,2,4-triazole(TAZ) as a hole blocking medium between the QD monolayer and the ETL. Devices of this type displayed improved

emission properties, with red CdSe QD emission dominating the EL spectrum. Maximum efficiencies for this style of device were 0.5%. Devices employing IR emitting PbSe dots [79] emitted IR light between 1.3-1.55 um with an EQE of ~10^{-3} %, which were reportedly less efficient than competitive IR devices utilizing a mixed CdSe/polymer emitting film, with an EQE of 0.27% [80].

Later variations of the ITO/TPD/QD monolayer/Alq3/AgMg device structure used microcontact stamping to deposit CdSe QDs [29,30,71]. In these devices, polydimethylsiloxane (PDMS) stamps coated with parylene-c were coated with a monolayer of QDs by spin-casting out of chloroform. QDs were then stamped by pressing the "inked" PDMS stamp against the surface of the TPD film. Devices of this type achieved 2% EQE [30] making use of commercial 90% QY CdSe/ZnS dots (QD Corp.). The accessible spectrum for this type of device was expanded to include green emitting ZnSe/CdSe/ZnS dots, first described by *Ivanov et al.* [81] as type-II core/shell/shell heterostructures. They were stamped into a monolayer in a device exhibiting 0.5% EQE [29], although there was some disagreement in the literature as to whether these dots were indeed true type-II materials. These stamped devices had been previously modified using a wider band-gap HTL material, 4,4 - N,N -dicarbazolyl-biphenyl (CBP), instead of TPD, and blue-emitting CdS/ZnS QDs in the active layer instead of CdSe/ZnS and TAZ as a hole blocking layer between the QDs and the Alq3 [76], with a reported EQE of 0.2%. Final variations of these devices used lithographically patterned silicon oxide to form PDMS stamps with ~20 um diameter posts, which could then be used form pixellated arrays of QDs, in RGB colors [30].

For non-monochrome (usually white) color generation, QD lumophores were utilized as a replacement for red [82,83] or green [84] color components in white-light LEDs employing organic emitters. A broad spectral emitter using a mixture of QDs has also been demonstrated using red, green and blue emitting dots embedded in polylaurylmeth acrylate [85] with a blue GaN or Hg vapor lamp for excitation. White light photoluminescence from QDs was also obtained by Bowers, *et al.* [86] and Chen, *et al.* [87], in devices in which deep trap QD luminescence was photoexcited by an external ultra-violet LED. However, deep trap emitters, generally defective CdS or ZnSe QDs, are only weakly luminescent, and the defect trap states on QD lumophores are poorly characterized and not easily reproducible from one synthesis to the next. White light LEDs have also been fabricated in this work using mixed monolayers of RGB emitting QDs [71] attained an EQE of 0.35%, but were limited by the low EQE of the current design of blue LEDs. White LEDs displayed CIE (colour international d'eclerage) coordinates of (0.35, 0.41) and a CRI of 86%, which is nominally better than "cool white" fluorescent (CRI=62) or solid state lighting (CRI>80).

Further exploration of QD-LED material design have yielded QD-LEDs using resistive NiO as an inorganic HTL [35], and fully inorganic QD-LEDs (Sections 3.2 and 3.3) which replace the HTL with a NiO thin film and the ETL layer with an SnO_2:ZnO alloyed thin film [36], or which used p- and n-doped gallium nitride as transport layers [88]. These devices both display efficiencies of 0.2%-0.1% and 0.01%-0.001% EQE, respectively, and emitted red light from commercial CdSe/ZnS QDs (QD Corp), high QY (~50%) alloyed ZnCdSe cores [89], and CdeSe/ZnS [90] also respectively. Linearly polarized LEDs have also been fabricated using partially aligned, red emitting CdSe/ZnS nanorods

(NRs) instead of QDs in organic ETL/QD-HTL devices which exhibited EQEs of 0.5% [91]. Although the range of emissive devices presented since 2002 [78] is impressive, most single monolayer devices, with a few exceptions [30,77], have failed to push far beyond the original achievement of 0.5%. Recent publications have shown improved EQEs of 0.8%, through the application of multiple hole transport materials [92], or of 2.0% [30] using red, ultra-high quantum yield (90%) commercial CdSe/ZnS dots (QD Corp). Both these results were attained in devices using red quantum dots ~620 nm.

However, with better device design, there is no theoretical barrier to 2% EQEs across the visible spectrum. Such relatively high efficiency devices would find use in RBG displays, indicator LEDs, or even solid state lighting. To improve the utility and commercializability of QD-LEDs, efficiencies of greater than 1.0% must be reliably attained at RGB wavelengths. Doing so requires using new HTL and ETL materials, now popular in OLED design [93], but not previously used in QD devices, as well as high QY materials attained with better chemistry and improved QD processing techniques.

In this work we will explore device designs with EQEs of ~2-3% across the green-red spectrum. We will also explore attempts to improve the performance of blue emitting QD-LEDs, as well as using these advances to produce reasonably efficient white light LEDs using mixed QD monolayers. Finally, we will replace the organic semiconductors with sputtered metal oxide films to form efficient quantum dot – *inorganic* light emitting devices (QD-ILEDs).

1.2.2.3 Device Structure and Function

The generalized device structure for QD-OLEDs in this work [71] consists of a hole transport material (HTL) and electron transport material (ETL), both made from semiconducting organic molecules, sandwiching a QD monolayer which is use as the active emitting layer in the device. Charges are injected into the ETL and HTL from metallically conducting electrodes with work functions chosen to facilitate injection of the respective charge into the charge transport layer. The device itself is only ~300 nm in total thickness (including the electrodes) and rests upon a glass substrate (Figure 1.10).

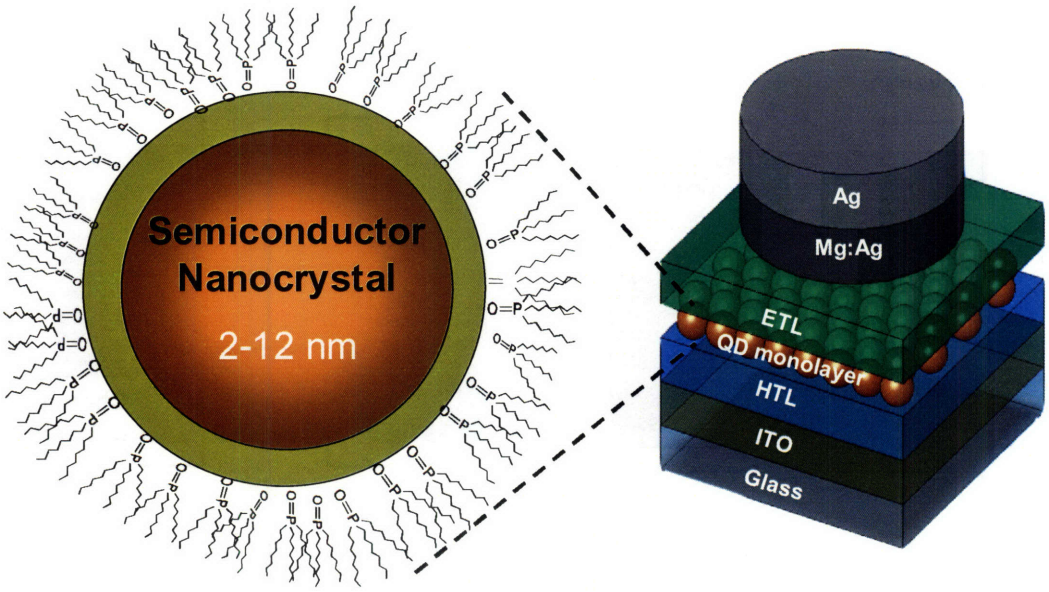

Figure 1.10: The device structure of the QD-LED, as described by Coe et al. [27]

Although no current flows at 0 V, applying a positive voltage to the high work function electrode allows the Fermi level to drop below the hole conduction band of the HTL. This allows holes to flow into the HTL and then into the valence band of the QD (Figure 1.10). Electrons are injected from the low work function electrode into the ETL

of the device where they are transported into the conduction band of the QD. The charges can then recombine across the band gap of the QD, producing electroluminescence (EL) with the QD's characteristic emission spectrum.

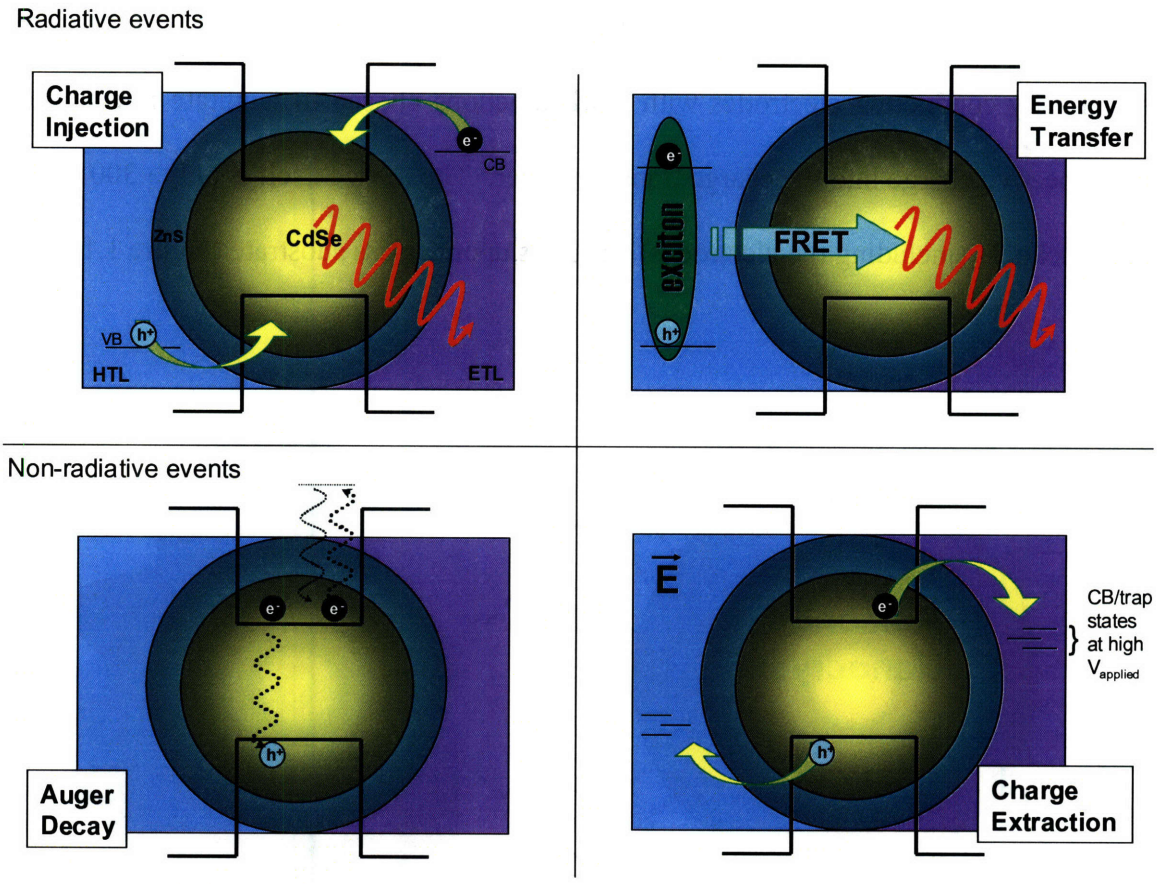

Figure 1.11: A diagram of the various processes by which excitons are formed on the QD and decay, either radiatively (top) or non-radiatively (bottom).

Alternatively, charges can form electron hole pairs in either of the two transport organics, which can themselves emit (Figure 1.11). If the emission spectrum of the organic semiconductors overlaps the absorption of the QD (i.e. the organic transport layers emit at a lower wavelength than the QD), the exciton can transfer to the QD by FRET. Although both charge injection and FRET are likely occurring in the device

during operation, FRET has been found recently to be the dominant mechanism by which excitons are formed on the QD [94].

The organic layers can be either spin-cast [78] or evaporated [30] into the device. The QD monolayer is formed either by spin-casting onto a chemically durable substrate [35,36], by phase separation from a spin-cast mixture of the QDs and HTL [77,78], or by micro-contact printing [30]. In this work, OLEDs are formed by micro-contact printing and inorganic LEDs (ILEDs) are formed by spin-casting over a metal oxide substrate.

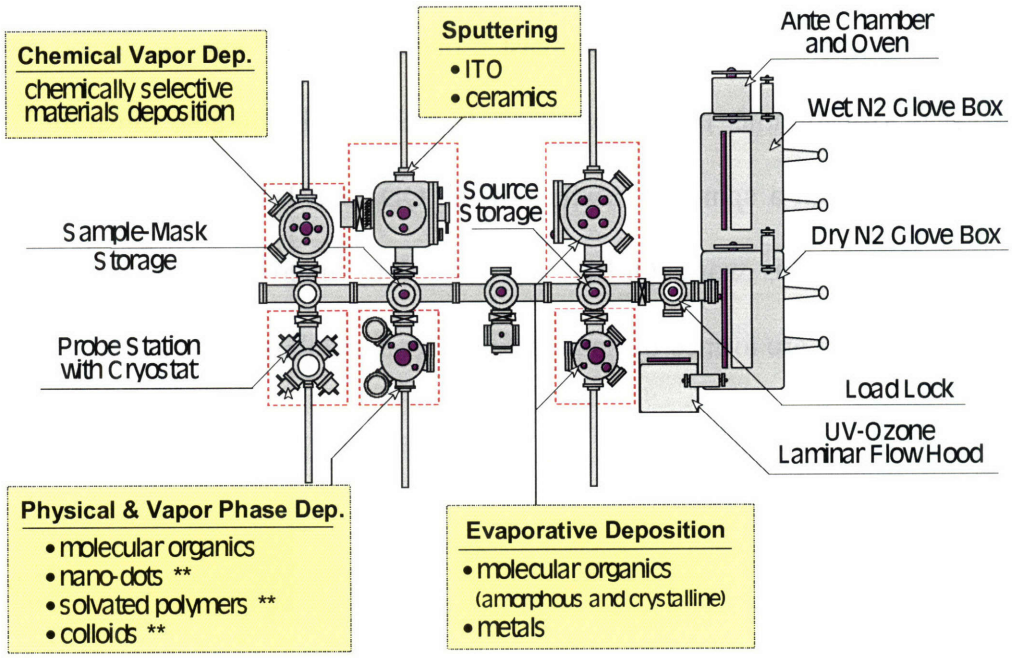

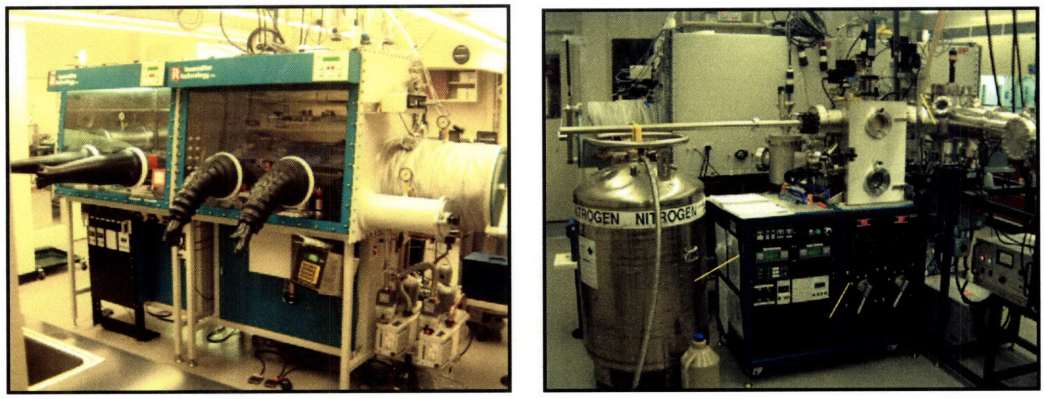

Figure 1.12: A diagram and photos of the device processing system used to make QD-LEDs. Top) A diagram of the system. Substrates are pumped down and placed under N_2 in the loadlock to the left glove box. They can be transferred to a spin-coating apparatus in the right glove box, or pumped down in a substrate holder, with or without masks, to $< 1x10^{-6}$ torr on the trolley that moves through the central conduit. From this trolley the substrates can be brought into the evaporators or sputterer for material deposition. Bottom) A photo of the glove boxes (left) and one of the evaporators (right).

Device measurements include I-V curves, EL spectra, turn-on voltage, external quantum efficiency (EQE) and luminosity (usually expressed as cd/m^2). I-V curves and spectra especially are useful for evaluating the underlying function of the device, and for troubleshooting, as shown in Figure 1.12. The turn-on voltage is the applied voltage at which photons can be detected being emitted from the device. The EQE is simply a measurement of the number of photons emitted from the device divided by the number of charges injected into the device (e.g. 1 photon per 1 electron would yield an EQE of 100%). The luminosity is a measurement of how bright the pixel appears to the human eye at a given distance.

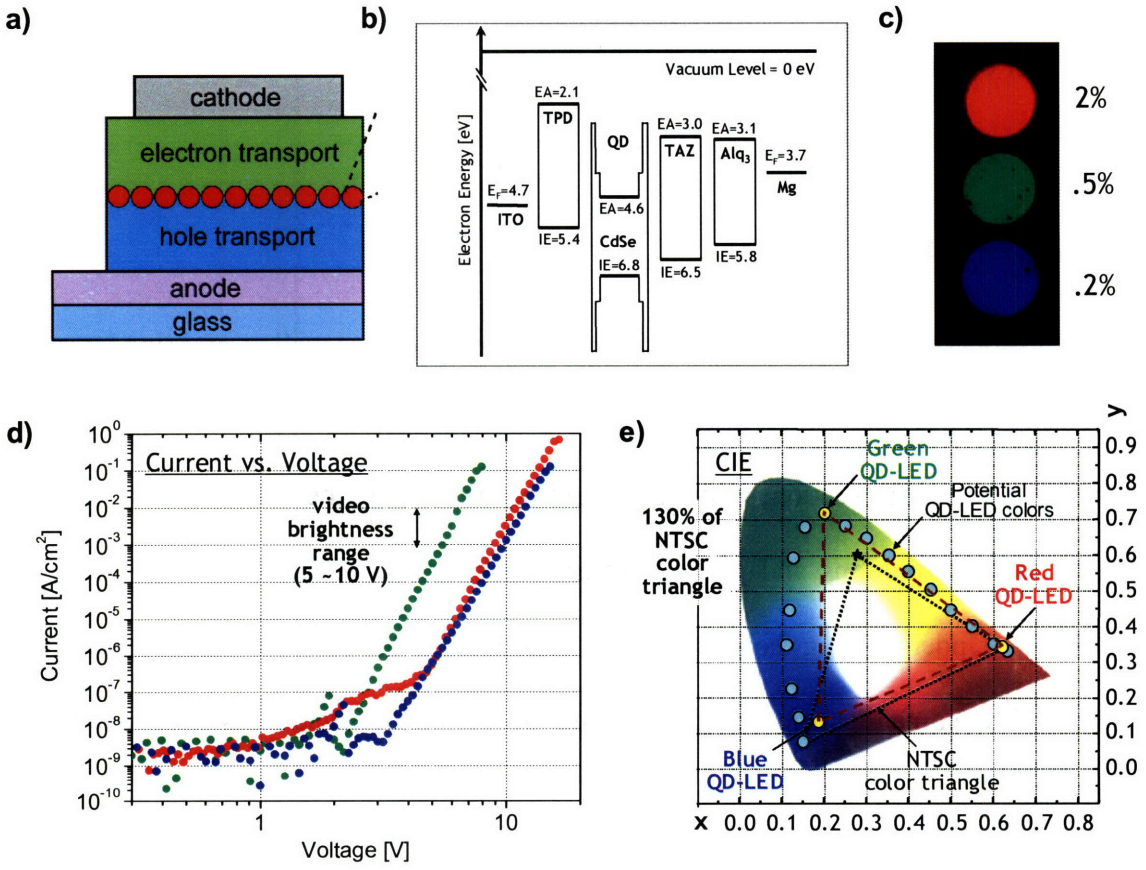

Figure 1.13: a) Device structure and b) band structure of a QD-OLED. c) Photos and peak efficiencies of RGB devices based on this structure. d) The I-V curve of a QD-OLED, the data

can be fit by a power law curve after the turn-on voltage ~3-5 V, as is generally seen in organic semiconductors employing space-limited charge transport [95,96]. e) A commission international d'eclairage (CIE) plot for the RGB devices. The color area covered by the three devices is 130% of the standard NTSC color triangle. [30,97]

Two further metrics can be calculated from the efficiency and the emission spectrum. The Commission International de l'Eclairage (CIE) coordinates, in which the relative intensity of the three colors RGB are mapped onto a two dimensional surface (Figure 1.13). The Color Reflective Index (CRI) is an measurement of how objects absorbing some portion of the visible spectrum will appear to the human eye when illuminated by a light source with defined spectral features. Finally, digital photos are generally taken of devices to visually demonstrate both the color and brightness of the pixel under operating conditions (3-10 V).

1.3 Solar Cells

Nanocrystals can be used as active absorption layers, as well as emitting layers, in optoelectronic devices. These devices, called photovoltaic (PV) devices, make use of the high absorption cross-section [98] and large surface area to volume ratio of nanocrystals to harvest incident photons and produce charges with a characteristic energy difference (voltage). Understanding how to design functional materials for these applications requires first some historical understanding of the device itself, as well as how it functions.

1.3.2 History of PV Devices and NC Solar Cells

The earliest photovoltaic cell was produced using selenium as the semiconductor by Fritts [99,100] in 1883. Modern devices used Si pn junctions to produce up to 6% power efficient devices [101]. Power efficiency (PE) at AM 1.5 (the intensity of the solar spectrum through a standard air mass) is the standard measurement of how much of the available spectral power is converted into electrical power. Power efficiency ($PE_{AM\ 1.5}$) is more appropriate than EQE when evaluating the capability of a solar cell, since a device with 5% EQE at a blue wavelength would produce electrons with a higher voltage than a device with the same efficiency at a red wavelength, and thus the first device would produce more power (voltage x current). Although p-type silicon/n-type silicon remains the standard for industrial photovoltaic cells, with PEs of > 20% for crystalline materials [102], high efficiency devices have also been produced using Cu_2S/CdS (>10%, 1980) [100], GaInP/GaAs (>30%, 1994) [103], and Cu(InGa)Se2 (19%, 1998) [104]. So called "Graetzel" cells (after their inventor) have also been produced using dye sensitized TiO_2 and liquid transport materials with PE 11% (1996) [105]. Nanocrystalline materials have also been used to produce solar cells, with reported PEs as high as 3% [106]. Materials such as CdTe [107], CdSe [108], PbS [109] and PbSe [110] have also been explored for use in PN junction devices.

Polymer PV cells have also been constructed using a "bulk heterojunction" design (see Figure 11), in which the p- and n-type materials are randomly distributed within the active region of the cell [111]. As excitons are generated within the film, the p- and n-type polymer strands, while randomly distributed, are still in contact with their respective electrodes, given an adequate concentration of both materials. Thus both the electron and hole can still be conducted toward the proper electrodes while also creating a much larger

junction area. Similar bulk heterojunction devices have been made using C_{60} [112] "Buckeyballs", or CdSe nanorods [113] embedded in a p-type polymer matrix. In chapter 4, CdSe/CdTe nanobarbells will be used to produce both a bulk heterojunction device (Section 4.4.3), and within a standard p-i-n junction device as the photoactive i-layer (Section 4.5).

1.3.3 NC Device Function

Absorption devices function in the opposite fashion from LEDs. Instead of injecting charges into the active material, which must be a relatively good emitter, in a solar cell or photodetector, the active material absorbs a photon and the band structure of the surrounding materials are designed so that the exciton will be separated and charges flow to the electrodes. The migration of charges to the different electrodes creates an internal field (voltage) across the device in open circuit operation, and the coulombic attraction between the charges gives rise to a closed circuit current. Depending on the energy levels of the bands in the device, it may or may not be necessary to apply a voltage to the device to get the charges to flow out of the absorbing layer to their respective electrodes. In the former case, the device is a photodetector and external voltage must be supplied so that the current can be used as a measure of the number of photons striking the device area. In the latter case, given good efficiency of extraction, the PV device is a solar cell and can be used to generate power.

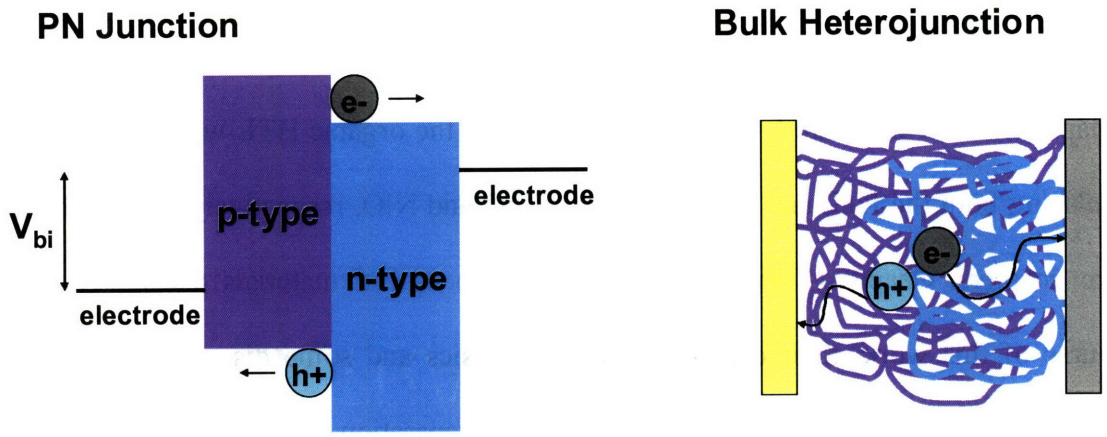

Figure 1.14, Top: A generalized band diagram for a typical bulk semiconductor solar cell. Excitons are generated when light is absorbed at the PN junction. The holes and electrons are separated into the p- and n- conduction bands then drift toward the electrodes in the field produced by the difference in the electrode work functions, called the built-in voltage (V_{bi}). Bottom: A schematic drawing of a bulk heterojunction device, in which the PN junctions are randomly distributed within the cell as the polymers strands interlace. As electron-hole pairs form at the junctions, the charges are separated, as in the standard PN-junction device, and are transported to their respective electrodes by connecting pathways of p- and n- type strands.

1.4 Overview of Thesis

The work in this thesis can be divided into two major categories: innovations in LEDs, and the synthesis of original optical materials. Chapters 2 and 3 will discuss the major innovations in LEDs made during the course of this work. Chapter 2 will focus on organic LEDs (OLEDs) while Chapter 3 focuses on inorganic LEDs (ILEDs). Unlike in previous works [CITE], these chapters will completely encompass each topic, discussing all the details of the device design and implementation, including the design, QD synthesis, production and results of each major device. Chapters 2 and 3 will largely be subdivided by the major devices accomplished during the course of the investigation.

Chapter 2 will cover the work done to create efficient blue LEDs (2.2), white emitting LEDs (2.3) and improvements in materials for blue (2.4) and red-green devices (2.5). Chapter 3 is divided mainly into devices replacing the organic HTL with NiO (3.2) and replacing both the ETL and HTL with SnO_2:ZnO and NiO, respectively (3.3). The next two chapters, Chapter 4 and 5, will examine two optical materials discovered in the course of this work, their design, synthesis, physics and some discussion of possible applications. Chapter 4 will discuss the synthetic preparation of CdSe/CdTe nanobarbells along with a description of their physics and use in solar cells. Chapter 5 will discuss the synthesis and characterization of QD-J-aggregate "constructs" made from J-aggregating cyanine dyes electrostatically bound to QDs. The FRET characteristics of these constructs will be examined, although no applications have yet been explored. The emphasis for both materials will on the original synthetic work done, more than in the LED chapters, which, with some exceptions (2.4.2) relied on altered preparations of previously reported materials. Devices for these materials tended to be more rudimentary (Chapter 4) or have yet to be applied (Chapter 5) and may warrant further discussion. Each chapter ends with a summary of the work done as well as an acknowledgement of the contributions of my collaborators to the project.

1.5 References

(1) Murray, C. B.; Norris, D. J.; Bawendi, M. G. *J. Am. Chem. Soc.* **1993**, *115*, 8706.

(2) Hines, M. A.; Guyot-Sionnest, P. *J. Phys. Chem.* **1996**, *100*, 468.

(3) Leatherdale, C. A.; Woo, W. K.; Mikulec, F. V.; Bawendi, M. G. *Journal of Physical Chemistry B* **2002**, *106*, 19-7622.

(4) Peng, Z. A.; Peng, X. *J. Am. Chem. Soc.* **2002**, *124*, 3343-3353.

(5) Mokari, T.; Banin, U. *Chem. Mater.* **2003**, *15*, 3955-3960.

(6) Kim, S.; Fisher, B.; Eisler, H.-J.; Bawendi, M. *J. Am. Chem. Soc.* **2003**, *125*, 11466-11467.

(7) Zhong, X.; Feng, Y.; Knoll, W.; Han, M. *J. Am. Chem. Soc.* **2003**, *125*, 13559.

(8) Steckel, J.; Zimmer, J.; Coe-Sullivan, S.; Stott, N.; Bulovic, V.; Bawendi, M. *Angewandte Chemie International Edition* **2004**, *43*, 2154.

(9) Streetman, B.; Banerjee, S. *Solid State Electronic Devices*; 6th ed.; Prentice Hall, 2005.

(10) Norris, D. J. In *Department of Chemistry*; MIT: Cambridge, MA, 1990, p 158.

(11) Murray, C. B. In *Department of Chemistry*; MIT: Cambridge, 1995, p 166.

(12) Efros, A. L.; Rosen, M.; Kuno, M.; Nirmal, M.; Norris, D. J.; Bawendi, M. G. *Phys. Rev. B* **1996**, *54*, 4843-4856.

(13) Ledentsov, N. N.; Ustinov, V. M.; V.A.Shchukin; Kop'ev, P. S.; Alferov, Z. I.; Bimberg, D. *Semiconductors* **1998**, *32*, 343-365.

(14) Peng, Z.; Peng, X. *J. Am. Chem. Soc.* **2001**, *123*, 1389-1395.

(15) Zhong, X.; Han, M.; Dong, Z.; White, T. J.; Knoll, W. *JACS* **2003**, *125*, 8589.

(16) Ivanov, S. A.; Nanda, J.; Piryatinski, A.; Achermann, M.; Balet, L. P.; Bezel, I. V.; Anikeeva, P. O.; Tretiak, S.; Klimov, V. *J. Phys. Chem.* **2004**, *108*, 10625.

(17) Milliron, D.; Hughes, S. M.; Cui, Y.; Manna, L.; Lin-Wang, J. L.; Alivisatos, P. *Nature* **2004**, *430*, 190-195.

(18) Dickerson, B. D.; Irving, D. M.; Herz, E.; Claus, R. O.; Spillman, W. B.; Meissner, K. E. *Appl. Phys. Lett.* **2005**, *86*, 171915.

(19) Manna, L.; Scher, E. C.; Alivisatos, A. P. *J. Am. Chem. Soc.* **2000**, *122*, 12700-12706.

(20) Hines, M. A.; Scholes, G. D. *Adv. Mater.* **2003**, *15*, 1844-1849.

(21) Puntes, V. F.; Zanchet, D.; Erdonmez, C. K.; Alivisatos, A. P. *JACS* **2002**, *124*, 12874-12880.

(22) Yin, Y.; Alivisatos, A. P. *Nature* **2005**, *437*, 664-670.

(23) Bawendi, M. G.; Jensen, K. F.; Rodriguez-Viejo, J.; Mikulec, F. V. In *US Patent Office*; MIT: USA, 2005; Vol. 6861155, p 15.

(24) Dabbousi, B. O.; et al. *J. Phys. Chem. B* **1997**, *101*, 9463-9475.

(25) Fisher, B. R.; Caruge, J.-M.; Chan, Y. T.; Halpert, J. E.; Bawendi, M. G. *Chemical Physics* **2005**, *318*, 71-81.

(26) Anikeeva, P. O.; Halpert, J. E.; Bawendi, M. G.; Bulovic, V. *Nano. Lett.* **2007**, *7*, 2196.

(27) Coe-Sullivan, S.; Woo, W. K.; Steckel, J. S.; Bawendi, M.; Bulovic, V. *Organic Electronics* **2003**, *4*, 123-130.

(28) Halpert, J. E.; Porter, V. J.; Zimmer, J. P.; Bawendi, M. G. *JACS* **2006**, *128*, 12590-12591.

(29) Steckel, J. S.; Snee, P. T.; Coe-Sullivan, S.; Zimmer, J. P.; Halpert, J. E.; Anikeeva, P. O.; Kim, L.-A.; Bulovic, V.; Bawendi, M. G. *Angewandte Chemie International Edition* **2006**, *45*, 5796-5799.

(30) Coe-Sullivan, S. In *Department of Electrical Engineering and Computer Science*; MIT: Cambridge, 2005, p 166.

(31) Bawendi, M. G.; Mikulec, F. V.; Lee, J.-K. In *US Patent Office*; MIT: USA, 2002; Vol. 6444143.

(32) Liu, W.; Choi, H. S.; Zimmer, J. P.; Tanaka, E.; Frangioni, J. V.; Bawendi, M. G. *JACS* **2007**, *129*, 14530.

(33) Sundar, V. C.; Eisler, H.-J.; Bawendi, M. G. *Advanced Materials* **2002**, *14*, 739-743.

(34) Chan, W. C.; Maxwell, D. J.; Gao, X.; Bailey, R. E.; Han, M.; Nie, S. *Current Opinion in Biotechnology* **2002**, *13*, 40-46.

(35) Caruge, J.-M.; Halpert, J. E.; Bulovic, V.; Bawendi, M. G. *Nano. Lett.* **2006**, *6*, 2991-2994.

(36) Caruge, J.-M.; Halpert, J. E.; Wood, V.; Bulovic, V.; Bawendi, M. G. *Nature Photonics* **2008**, *2*, 247-250.

(37) Porter, V. J.; Geyer, S.; Halpert, J. E.; Kastner, M. A.; Bawendi, M. G. *Journal of Physical Chemistry C* **2008**, *ASAP*.

(38) Coe-Sullivan, S.; Steckel, J. S.; Woo, W.-K.; Bawendi, M.; Bulovic, V. *Adv. Funct. Mater.* **2005**, *15*, 1117-1124.

(39) Jarosz, M. V.; Porter, V. J.; Fisher, B. R.; Kastner, M. A.; Bawendi, M. G. *Physical Review B* **2004**, *70*, 195327.

(40) Deegan, R. D.; Bakajin, O.; Dupont, T. F.; Huber, G.; Nagel, S. R.; Witten, T. A. *Nature* **1997**, *389*, 827-829.

(41) Klimov, V. I.; Bawendi, M. G. *Science* **2000**, *290*, 314-317.

(42) Chang, S.-C.; Jie Liu, J. B.; Yang, Y.; Onohara, J.; Kido, J. *Adv. Mater.* **1999**, *11*, 734-738.

(43) Yang, Y.; al., e. *Journal of Materials Science: Materials in Electronics* **2000**, *11*, 89-96.

(44) Kim, F.; Yang, P. *ChemPhyChem* **2002**, *3*, 503-506.

(45) Dabbousi, B. O.; Murray, C. B.; Rubner, M. F.; Bawendi, M. G. *Chemistry of Materials* **1994**, *6*, 216-219.

(46) Chung, I.; Witkoskie, J. B.; Cao, J. S.; Bawendi, M. G. *Physical Review E* **2006**, *73*.

(47) Shimizu, K. T.; Neuhauser, R. G.; Leatherdale, C. A.; Empedocles, S. A.; W.-K., W.; Bawendi, M. G. *Physical Review B* **2001**, *63*, 205311-205316.

(48) Nair, G.; Bawendi, M. G. *Phys. Rev. B* **2007**, *76*.

(49) Schaller, R. D.; Klimov, V. I. *Phys. Rev. Lett.* **2004**, *92*, 186601.

(50) Efros, A. L.; Rosen, M.; Kuno, M.; Nirmal, M.; Norris, D. J.; Bawendi, M. G. *Physical Review B: Condensed Matter* **1996**, *54*, 4843-4856.

(51) Norris, D. J.; Bawendi, M. G. *J. Chem. Phys.* **1995**, *103*, 5260-5268.

(52) Norris, D. J.; Efros, A. L.; Rosen, M.; Bawendi, M. G. *Physical Review B: Condensed Matter* **1996**, *53*, 16347-16354.

(53) Empedocles, S. A.; Bawendi, M. G. *Science* **1997**, *278*, 2114-2117.

(54) Forster, T. *Naturwissenschaften* **1946**, *6*, 166-175.

(55) Forster, T. *Ann Phys (Leipzig)* **1948**, *2*, 55-75.

(56) Pope, M.; Swenberg, C. E. *Electronic Processes in Organic Crystals and Polymers*; Oxford University Press: New York, 1999.

(57) Nirmal, M.; Norris, D. J.; Kuno, M.; Bawendi, M. G.; Efros, A. L.; Rosen, M. *Phys. Rev. Lett.* **1995**, *75*, 3728-3731.

(58) Bulovic, V.; et al. *Electroluminescence I* **2000**, *64*, 255-306.

(59) G. Gu; et al. *Optics Letters* **1997**, *22*, 172-174.

(60) Ke, L.; et al. *Synthetic Metals* **2004**, *140*, 295-299.

(61) Moller, S.; Forrest., S. R. *Journal of Applied Physics* **2002**, *91*, 3324-3327.

(62) Shirota, Y.; et al. *Synthetic Metals* **2000**, *111*, 387-391.

(63) Yamasaki, T.; et al. *Applied Physics Letters* **2000**, *76*, 1243-1245.

(64) Streetman, B. G. *Solid State Electronic Devices*; Prentice Hall: Upper Saddle River, NJ, 1995.

(65) Schlamp, M.; Peng, X.; Alivisatos, A. P. *J. Appl. Phys.* **1997**, *82*, 5837.

(66) Colvin, V. L.; Schlamp, M. C.; Alivisatos, A. P. *Nature* **1994**, *265*, 373.

(67) Tang, C. W.; VanSlyke, S. A. *Appl. Phys. Lett.* **1987**, *51*, 913.

(68) Lu, M.-H. M.; Sturm, J. C.; Madigan, C. F.; Kwong, R.; Office, U. P., Ed.: USA, 2006.

(69) Co., L. M. S. **2004**.

(70) Popovic, Z. D.; al, e. *Synthetic Metals* **2000**, *111*, 229-232.

(71) Bulović, V.; Bawendi, M.; Halpert, J.; Anikeeva, P.; Coe-Sullivan, S.; Woo, W.; Steckel, J.; Kim, L.; Caruge, J.-M.; Wood, V. In *SPIE Photonics West Convention*: San Jose, CA, 2007.

(72) Colvin, V. L.; Schlamp, M. C.; Alivisatos, A. P. *Nature* **1994**, *370*, 354.

(73) Dabbousi, B. O.; Bawendi, M. G.; Onitsuka, O.; Rubner, E. M. F. *Appl. Phys. Lett.* **1995**, *66*, 1316-1318.

(74) Schlamp, M. C.; Peng, X. G.; Alivisatos, A. P. *J. Appl. Phys.* **1997**, *82*, 5837.

(75) Mattoussi, H.; Radzilowski, L. H.; Dabbousi, B. O.; Fogg, D. E.; Schrock, R. R.; Thomas, E. L.; Bawendi, M. G.; Rubner, M. F. *J. Appl. Phys.* **1998**, *83*, 7965-7975.

(76) Steckel, J. S.; Zimmer, J. P.; Coe-Sullivan, S.; Stott, N. E.; Bulovic, V.; Bawendi, M. G. *Angewandte Chemie International Edition* **2004**, *43*, 2154-2158.

(77) Coe-Sullivan, S.; Woo, W.-K.; Steckel, J. S.; Bawendi, M. G.; Bulovic, V. *Organic Electronics* **2003**, *4*, 123-130.

(78) Coe, S.; Woo, W.-K.; Bawendi, M.; Bulovic, V. *Nature* **2002**, *420*, 800.

(79) Steckel, J. S.; Coe-Sullivan, S.; Bulovic, V.; Bawendi, M. G. *Adv. Mater* **2003**, *15*, 1862-1866.

(80) Konstantatos, G.; Huang, C.; Larissa, L.; Lu, Z.; Sargent, E. H. *Adv. Funct. Mater.* **2005**, *DOI:10.1002/adfm.200500379*, 1-6.

(81) Ivanov, S. A.; Nanda, J.; Piryatinski, A.; Achermann, M.; Balet, L. P.; Bezel, I. V.; Anikeeva, P. O.; Tretiak, S.; Klimov, V. *J. Phys. Chem. B* **2004**, *108*, 10625.

(82) Gao, M.; Richter, B.; Kirstein, S. *Adv. Mater.* **1997**, *9*, 802.

(83) Y. Li, A. R.; Mazzeo, M.; Carbone, L.; Manna, L.; Cingolani, R.; Gigli, G. *J. Appl. Phys.* **2005**, *97*, 113501.

(84) Park, J. H.; Kim, J. Y.; Chin, B. D.; Kim, Y. C.; Kim, J. K.; Park, O. O. *Nanotechnology* **2004**, *15*.

(85) Chen, H.-S.; Hsu, C.-K.; Hong, H.-Y. *Technol. Lett.* **2006**, *18*, 193.

(86) Bowers, M. J.; McBride, J. R.; Rosenthal, S. J. *J. Am. Chem. Soc.* **2005**, *127*.

(87) Chen, H. S.; Wang, S. J. J.; Lo, C. J.; Chi, J. Y. *Appl. Phys. Lett.* **2005**, *86*, 131905.

(88) Mueller, A. H.; Petruska, M. A.; Achermann, M.; Werder, D. J.; Akhadov, E. A.; Koleske, D. D.; Hoffbauer, M. A.; Klimov, V. I. *Nano Lett.* **2005**, *5*, 1039-1044.

(89) Zhong, X.; Feng, Y.; Knoll, W.; Han, M. *J. Am. Chem. Soc.* **2003**, *125*, 13559.

(90) Fisher, B. R.; Eisler, H.-J.; Stott, N. E.; GBawendi, M. *Journal of Physical Chemistry B* **2004**, *108*, 143-148.

(91) Hikmet, R.; Chin, P.; Talapin, D. V.; Weller, H. *Advanced Materials* **2005**, *17*, 1436 - 1439.

(92) Zhao, J.; Bardecker, J. A.; Munro, A. M.; Liu, M. S.; Niu, Y.; Ding, I.-K.; Luo, J.; Chen, B.; Jen, A. K.-Y.; Ginger, D. S. *Nano. Lett.* **2006**, *6*, 463-467.

(93) Su, S.-H.; Yokoyama, M.; Li, J.-F.; Hwang, K.-S. *Journal of the Electrochemical Society* **2006**, *153*, H51-H53.

(94) Anikeeva, P. O.; Madigan, C. F.; Halpert, J. E.; Bawendi, M. G.; Bulović, V. *Phys. Rev. B* **2008**, *Submitted.*

(95) Kozlov, V. G.; Parthasarathy, G.; Burrows, P. E.; Khalfin, V. B.; Wang, J.; Chou, S. Y.; Forrest, S. R. *IEEE Journal of Quantum Electronics* **2000**, *36*, 18-26.

(96) D'Andrade, B. W.; Holmes, R. J.; Forrest, S. R. *Adv. Mater.* **2004**, *16*, 624.

(97) Steckel, J. S. In *Department of Chemistry*; MIT: Cambridge, 2006, p 213.

(98) Leatherdale, C. A.; Woo, W. K.; Mikulec, F. V.; Bawendi, M. G. *Journal of Physical Chemistry B* **2002**, *106*, 7619-7622.

(99) Fritts, C. *Proc. Am. Assoc. Adv. Sci.* **1883**, *33*, 97.

(100) Hegedus, S. S.; Luque, A. *Handbook of Photovoltaic Science and Engineering*; Wiley and Sons: Chichester, UK, 2003.

(101) Chapin, D.; Fuller, C.; Pearson, G. *J. Appl. Phys.* **1954**, *25*, 677.

(102) Green, M.; et al. *Proc. 18th IEEE Photovoltaic Specialist Conf.* **1985**, *39-42.*

(103) Friedman, D. et al., *Prog. Photovolt.* **1995**, *3*.

(104) Contreras, M. et al., *Prog. Photovolt.* **1999**, *7*, 311-316.

(105) Hagfeldt, A.; Didriksson, B.; Palmqvist, T.; Lindstrom, H.; Sodergren, S.; Rensmo, H.; Lindquist, S.-E. *Solar Energy Materials and Solar Cells* **1994** *31*, 481-488.

(106) Gur, I.; Fromer, N. A.; Geier, M. L.; Alivisatos, A. P. *Science* **2005**, *310*, 462-465.

(107) Porter, V. J.; Geyer, S.; Halpert, J. E.; Mentzel, T. S.; Kastner, M. A.; Bawendi, M. G. *In preparation* **2008**.

(108) Oertel, D. C.; Bawendi, M. G.; Arango, A. C.; Bulovic, V. *Applied Physics Letters* **2005**, *87*, 213505.

(109) Watt, A. A. R.; Blake, D.; Warner, J. H.; Thomsen, E. A.; Tavenner, E. L.; Rubinsztein-Dunlop, H.; Meredith, P. *Journal of Physics D: Applied Physics* **2005**, *38*, 2006-2012.

(110) Mentzel, T. S.; Porter, V. J.; Geyer, S.; MacLean, K.; Bawendi, M. G.; Kastner, M. A. *Physical Review B* **2008**, *77*, 075316.

(111) Yu, G.; Gao, J.; Hummelen, J. C.; Wudl, F.; Heeger, A. J. *Science* **1995**, *270*, 1789-1791.

(112) Hoppe, H.; Sariciftci, N. S. *J. Mat. Chem.* **2006**, *16*, 45-61.

(113) Huynh, W. U.; Dittmer, J. J.; Alivisatos, A. P. *Science* **2002**, *295*, 2425-2427.

Chapter 2

Quantum Dot Organic Light Emitting Diodes (QD-OLEDs)

2.1 Introduction and Motivation

QD-OLEDs represent a significant application for QDs in the field of optoelectronics [1-11], combining the color purity and durability of QDs with the efficiency, flexibility and low cost of OLEDs. Previous efforts by *Coe et al.* culminated with the creation of red, green and blue (RGB) LED's with external quantum efficiencies (EQEs) of 1.0% [6], 0.5% [9] and 0.2% [12], respectively, patterned using PDMS micro-contact printing techniques (Section 1.1.7.2). However, OLED devices alone can be >10% efficient [13]. It is apparent that improved efficiencies are needed for the blue and green, to make the technology more marketable.

Using RGB materials also allows us to produce fluorescence that appears white to the human eye. White light OLEDs can be produced by spectrally tuning the contributions of red, green and blue light by adjusting the concentration of each nanocrystal in the device, taking into account the rate of FRET from bright blue QDs to redder QDs. Hence the efficiency of a white light device is highly dependent on creating efficient blue emitters and thus efficient blue LEDs.

Creating a white light device in turn has provided a better understanding of the mechanisms inherent in their operation. This gave rise to new material sets that could take advantage of the mechanisms of charge injection and exciton formation, and therefore greatly improve the performance of earlier red and green LEDs.

2.2 Efficient Blue QD-OLEDs using ZnCdS Cores

One of the difficulties in producing blue emitting QDs is the prevalence of interband trap states that can emit in the green to red region of the spectrum [12,14]. This trap emission appears as a long tail to the band edge emission and can change the perceived color of the emission from blue to purple, then white, yellow and even orange, as the intensity of the trap peak increases relative to the band edge peak. The traps are highly localized and can arise from either defects in the crystal lattice of the nanocrystal or from dangling bonds on the surface of the nanocrystal.

The second problem in designing blue QD-LEDs is that charge injection into wide band gap materials like CdS is not likely in the traditional TPD/QD/Alq_3 devices. Earlier works substituted CBP for TPD and added a hole blocking layer made from TAZ, but still failed to achieve better than 0.22% EQE [12]. Any replacement for the transport materials needs to be wide band gap materials, to prevent FRET from the blue QDs into the organic film.

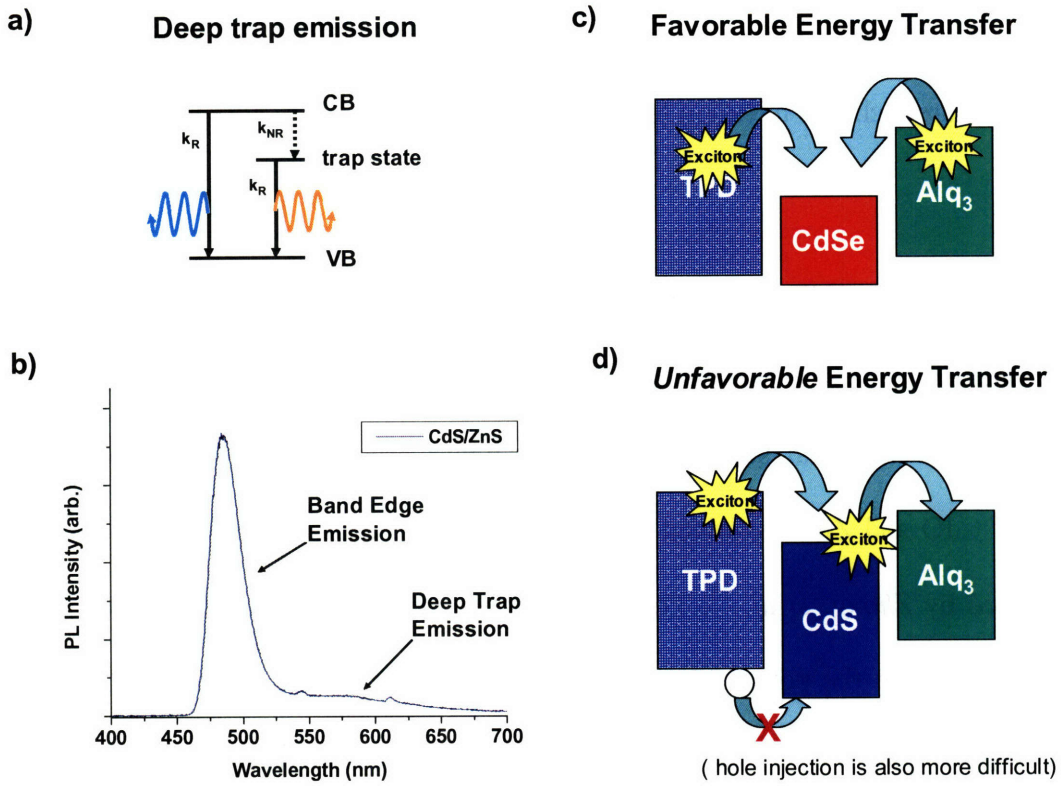

Figure 2.1: Two barriers to achieving efficient blue emitting QD-LEDs. a) A diagram of the origin of "trap emission", showing competition between the radiative and non-radiative rates of emission for the band edge and a localized trap at an energy well below the conduction band (a "deep" trap state). b) Photoluminescence spectrum of a CdS/ZnS particle showing some deep trap emission. c) A diagram describing the favorable FRET of excitons into a red emitting CdSe particle in a traditional TPD/QD/Alq_3 device, as opposed to d) a blue emitting CdS particle, wherein the exciton on the CdS nanocrystal is transferred to the green emitting Alq_3. Also shown in d) the hole transport material fails to adequately inject holes into the deep hole conduction band of CdS.

With these limitations in mind, the first step to improving the efficiency blue QD-OLEDs is to use higher quantum yield (QY) nanocrystals in their design. ZnCdS produces a much brighter nanocrystal using a more reproducible reaction. Improving the device also requires changing the hole and electron injection materials to exclude those materials that

can accept excitons from a blue emitting QD and fluoresce from the organic transport materials. Furthermore, the depth of the valence band in ZnCdS may present a further hindrance to direct charge injection for these devices.

2.2.1 Synthesis of ZnCdS Quantum Dots

Blue emitting ZnCdS QDs were prepared by injecting a degassed solution of oleylamine and elemental sulfur into a flask under argon, which contained a clear solution of CdO and ZnO dissolved into oleic acid and octadecene at 310°C, similar to that reported by *Zhong, et al.* [15]. The solution quickly turned from clear to yellow and remained stirring in the pot at 270°C for ~30 minutes. After cooling, the ZnCdS cores were then precipitated by the addition of acetone and separated from the supernatant by centrifugation. The QDs were precipitated a second time using methanol/butanol, centrifuged and redispersed in chloroform, as described above. The quantum yield for the ZnCdS QDs was found to be ~ 48% using coumarin 480 as a dye standard (99% QY in ethanol) [16].

By varying the parameters of the synthesis, several trends emerged. As expected, increasing the amount of cadmium in the pot tended to yield higher emission wavelengths. Considering that the band gaps in the alloyed particles are largely a function of the relative percentage of Zn and Cd in the nanocrystal, adding more Cd to the pot should increase the amount of Cd in the particles and therefore shift the emission to the red. Changing the injection volume also changed the emission wavelength of the final sample. Smaller injection volumes produced bluer particles while larger injection volumes favored redder particles. The reason for this is threefold. Adding a larger

volume cools the pot more quickly, causing nucleation to occur at cooler temperatures and thus fewer nuclei are likely to be formed. Secondly, the concentration of sulfur in the injection is decreased, also likely resulting in smaller nuclei. As fewer nuclei are formed, they are likely to grow larger, and therefore to be redder in emission. Finally, because cadmium oleate is more reactive, CdS should be formed preferentially, especially early in the reaction phase. As there are fewer nuclei, these particles grow larger and are less able to exchange Cd from the interior of the particle with Zn from the solution. Thus even with fairly long cooking times, the emission remains at 490 nm.

	Pot (310°C)				Injection (r.t.)	
Oleic Acid	Octadecene	ZnO	CdO	Sulfur	Injection Volume (3 ml oleylamine)	Emission Peak
2.5 ml	10 ml	64 mg	16 mg	96 mg	3 ml	415 nm
2.5 ml	10 ml	64 mg	24 mg	48 mg	3 ml	430 nm
2.5 ml	10 ml	64 mg	32 mg	48 mg	3 ml	442 nm
2.5 ml	10 ml	64mg	24 mg	48 mg	5 ml	464 nm
2.5 ml	10 ml	64 mg	32 mg	48 mg	8 ml	492 nm

Figure 2.2: A table of reaction parameters used to produce ZnCdS cores with emission wavelengths of 415 nm – 492 nm.

As can be seen in Figure 2.2, these parameters produced blue emitting particles with no deep trap emission prior to purification (sample emitting at 415 nm not shown in the figure). They appear blue to the eye when excited by a UV lamp at 365 nm (Figure

2.3b) and readily form close-packed films when stamped onto a TPD substrate (Figure 2.3c).

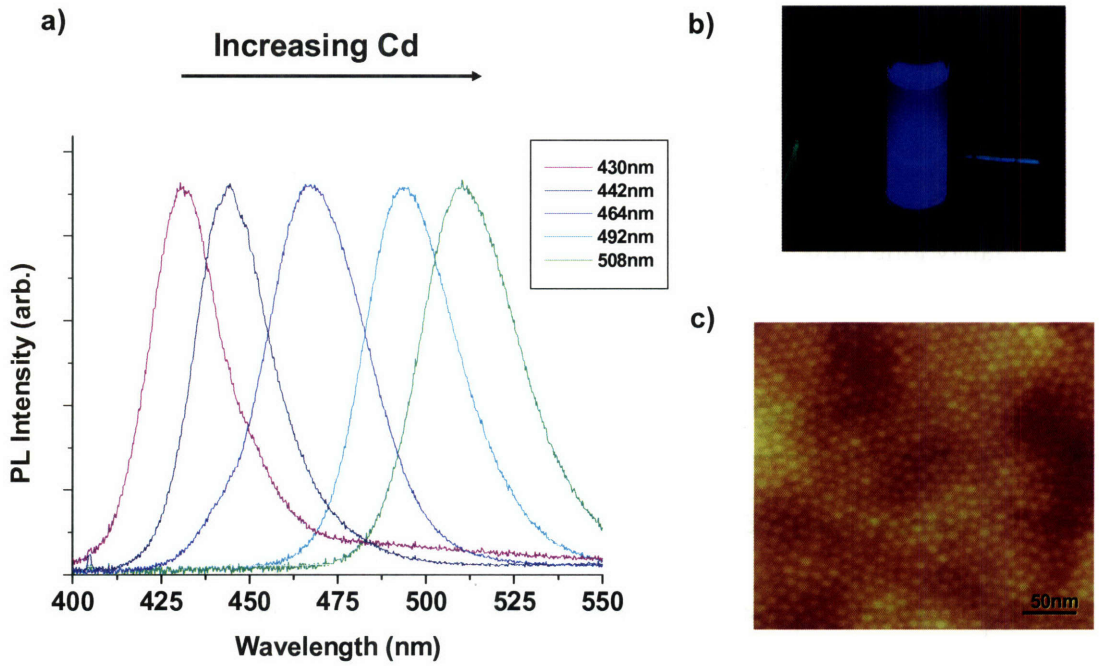

Figure 2.3: Spectra, photo and AFM of ZnCdS particles. a) Spectra of ZnCdS particles produced using a procedure modified from Zhong et al. [15]. Sample could be produced with emission peaks anywhere between 415 nm (not shown) to 508 nm. The arrow indicates particles contained an increasing percentage of Cd, as evidenced by the greener band structure, not that a larger amount of Cd was placed in the reaction pot (Figure 2.2). b) a photograph of a sample of ZnCdS QDs after two precipitations, in chloroform, and excited by a mercury UV lamp. c) An AFM of ZnCdS particles on a TPD coated glass/ITO substrate.

2.2.2 QD-OLEDs using TPD/ZnCdS/TAZ/Alq_3

The devices using the ZnCdS QD's consisted of an indium tin oxide (ITO) anode on top of a glass substrate with a layer of a 40 nm thick hole transporting layer (HTL) of

N,N'-Bis(3-methylphenyl)-N,N'-bis(phenyl)benzidine (TPD), a monolayer of colloidal ZnCdS as the emissive material, a ~30 nm thick hole blocking layer (HBL) of 3,4,5-triphenyl-1,2,4-triazole (TAZ), a 20 nm thick electron transporting layer (ETL) of tris-(8-hydroxyquinoline) aluminum (Alq_3), and a 100 nm thick cathode of magnesium silver alloy, coated with a 20 nm thick silver protective layer (see Figure 1.10).

The device characteristics displayed in Figure 2.4 show an EQE of 0.35% besting those of previously reported devices [12]. However, some emission from the Alq_3 is detected, likely due to formation of excitons in the Alq_3 layer as well as transfer of excitons from the QDs to the Alq_3. There is also some visible emission from the TPD due to formation of excitons in that material. This occurs, however, at wavelengths which are not intensely detected by the eye and does not greatly affect the purity of the color observed. Since TPD cannot absorb emission at 440 nm, FRET from the QDs into the HTL is unlikely.

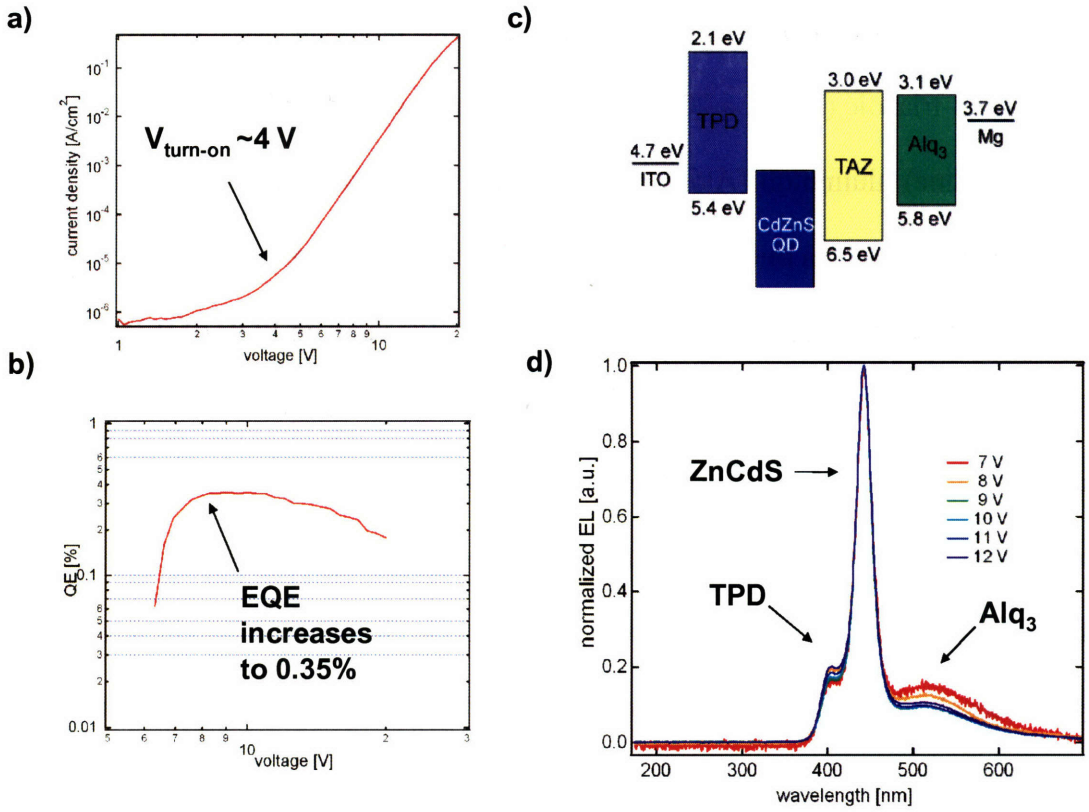

Figure 2.4: Device characteristics for ZnCdS core, blue emitting QD-OLEDs. a) IV curve for the TPD/ZnCdS/TAZ/Alq_3 device. The turn-on voltage for this device was ~4 V. b) External quantum efficiency of the device, peaking at 0.35% EQE around 7.5 V. c) a diagram of the device structure with the relevant band levels. The band structure of ZnCdS is estimated based on known values for bulk CdS and ZnS. d) The normalized EL spectrum of the device at 7-12 V. The emission profile shows three peaks originating from the TPD at 415 nm, the ZnCdS particles peaked at 440 nm and the Alq3, a broad peak at ~520 nm.

Given this data, it is clear that the charge transport layers used here are not optimal for injecting charges or FRET transferring into a blue emitting monolayer of QDs. However, the device is efficient enough at 0.4% EQE, and the material has a high enough QY to be used as the blue emitter in a white emitting, mixed monolayer device, as described in Section 2.2.1. But to boost the EQE of the blue QD-LED alone it is

sensible to find new charge transport organic materials with better performance, as is done in Section 2.4.

2.3 White Light Electroluminescence from a Mixed RGB Monolayer

Using our improvements in blue emitting QDs we demonstrate that by combining multiple QD lumophores in a standard TPD/QD/TAZ/Alq_3 QD-OLED device, an arbitrarily broad electroluminescence spectrum can be generated, with precisely controlled relative intensities of the constituent spectral components. This allows the production of a spectrum of light that appears white to the human eye, mimicking a blackbody radiator like an incandescent light bulb (CRI = 100).

There are two principle types of light sensitive cells in the eye, lining the retina, where the image is focused. These are the rods, which detect all photons and indicate brightness, and the cones which detect colors and hence occur in three distinct types: red,green and blue detectors. When only the blue detector is activated, the brain translates the signal as being blue, when both the blue and green detectors are active the brain translates the image as purple, etc. When all three are active the brain translates the image as being white. Therefore the key to optimally exciting each of the receptors in the eye is to produce a spectrum in which each color is present and peaked at the area of optimal color sensitivity of the eye, namely the wavelengths 470 nm, 530 nm and 620 nm. These wavelengths produce the most "pure" colors, and can therefore be tuned in concentration to create any arbitrary color LED.

The goal of this device was to demonstrate reproducible and efficient spectrally-broad electroluminescent QD-LEDs with spectral emission tunable across the CIE

(Commission Internationale de l'Eclairage) color space. This demonstrates that the electroluminescence spectrum can be precisely tuned in QD-OLEDs in which the mixed color electroluminescence is derived from a single QD monolayer containing QDs of multiple colors. To demonstrate spectral tunability, the relative concentrations of QD components can be adjusted in the QD monolayer to obtain white-light emitting QD-LEDs with a high color rendering index as shown in Figure 2.5.

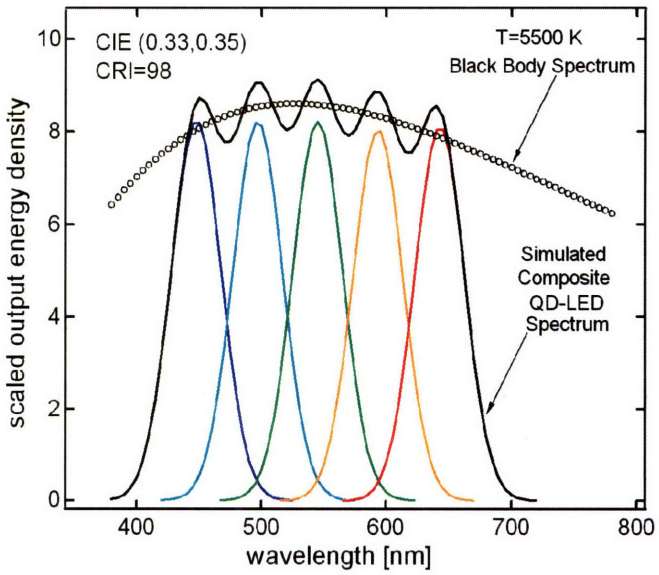

Figure 2.5: Simulated QD-LED white light source with five QD lumophores each with 40nm FWHM spectral emission. The composite emission spectrum has a color rendering index of CRI = 98, while wasting no photons in the ultra-violet and the infra-red part of the spectrum. Superimposed is the emission spectrum of a black body source with T = 5500K.

2.3.1 Synthesis of Red, Green and Blue QDs for the White Light LED

To create three colors representing red, green and blue, (RBG) we used three different types of colloidal quantum dots (QDs). The first type of QD was a CdSe/ZnS overcoated core-shell QD with a photoluminescence (PL) maximum at $\lambda = 622$ nm. The

second type was a ZnSe/CdSe/ZnS core-shell/alloy overcoated QD with a PL maximum around $\lambda = 540$ nm. The third type was a CdZnS alloy QD core with a PL maximum around $\lambda = 440$ nm. Together these three types of QDs constitute the component parts of an RGB color scheme. QD syntheses were adapted from reported preparations [15,17] to achieve specific wavelength emitters with narrow distributions and maximum quantum yield. Color emission targets were chosen to best conform to areas of maximum detection for RGB in the human eye, at $\lambda = 620$nm, $\lambda = 530$nm, and $\lambda = 470$nm, respectively, and thus to achieve the brightest possible appearance. Furthermore, to achieve arbitrary colors regardless of sample QYs (which may vary) these colors effectively form a decoupled basis set for forming all other visible colors.

Red CdSe/ZnS core-shell QDs, purchased from Quantum Dot Corporation (Invitrogen), exhibit a PL peak at $\lambda = 622$ nm, and solution PL quantum yield near 90%.

Green emitting quantum dots were prepared by synthesizing ZnSe/CdSe alloyed cores, as adapted from *Ivanov, et al.* [17], and subsequently overcoated with ZnS. To do so, ZnSe cores were first prepared by injecting a solution of diethyl zinc, trioctylphosphine selenide (TOP-Se) and TOP into a flask of hexadecylamine (HDA) at 310 °C. The cores were then grown at 270 °C for ~2 hours until the first absorption peak was at $\lambda = 354$ nm. Then the solution, still visibly clear due to the high band gap of ZnSe, was cooled to 150 °C and immediately 5ml of the growth solution was injected into a degassed solution of TOPO and hexylphosphonic acid (HPA). Immediately upon injection, a solution of dimethyl cadmium, TOP-Se and TOP was added drop-wise to the solvent/ZnSe mixture and the solution was heated at 150 °C for ~19 hours (no more than 2 days) until the emission reached a peak at $\lambda = 540$ nm. These cores, made of ZnSe and CdSe, were then

twice precipitated using methanol/butanol and redispersed in hexane. This solution was injected into a flask of degassed TOPO and HPA at 80 °C, and hexane was removed under vacuum for 1 hr. Two solutions, one containing dimethyl cadmium, diethyl zinc and TOP, the second containing TMS_2-S and TOP were added slowly to the flask at 150 °C by syringe pump at a rate of 2 ml/hr for ~2 hrs after which the solution was cooled to room temperature. The QDs were precipitated using methanol/butanol as above and redispersed in hexane. This process was performed three times, filtering after each dispersion with a 0.2 μm filter, and redissolving, in the final step, in chloroform. The quantum yield of the ZnSe/CdSe/ZnS QDs was measured to be ~65% using coumarin 540 as a standard (89% QY in ethanol) [18].

Blue emitting ZnCdS QDs were prepared as described in Section 2.2.1. The QDs were then precipitated a second time using methanol/butanol, centrifuged and redispersed in chloroform, as described above. The quantum yield for the ZnCdS QDs was found to be 48% using coumarin 480.

2.3.2 Device Fabrication

ITO substrates for QD-LEDs and for AFM samples were cleaned in a multi-step solvent cleaning process followed by a 5 min exposure to O_2 plasma. QD-LEDs were packaged in a N_2 glovebox using a glass coverslip and UV curing epoxy. The devices consisted of an indium tin oxide (ITO) anode on top of a glass substrate with a layer of conducting polymer poly(3, 4-ethylenedioxythiophene):poly(styrenesulfonate) PEDOT:PSS as the hole injection layer, a 40 nm thick hole transporting layer (HTL) of TPD, an emissive monolayer of colloidal QDs, a 27 nm thick hole blocking layer (HBL)

of TAZ, a 20 nm thick electron transporting layer (ETL) of Alq_3, and a 100 nm thick cathode of magnesium silver alloy, coated with a 20 nm thick silver protective layer. All the organic films (except PEDOT:PSS) were thermally evaporated at pressures of $<5\times10^{-7}$ torr and at rates of ~ 0.1 nm/s. PEDOT:PSS films were spin-cast onto ITO substrates, and baked at 110 C° for 15 min in a N_2 atmosphere. We used all three types of QDs (synthesis in Section 2.3.1) to generate the red, green and blue spectral components of the white LED.

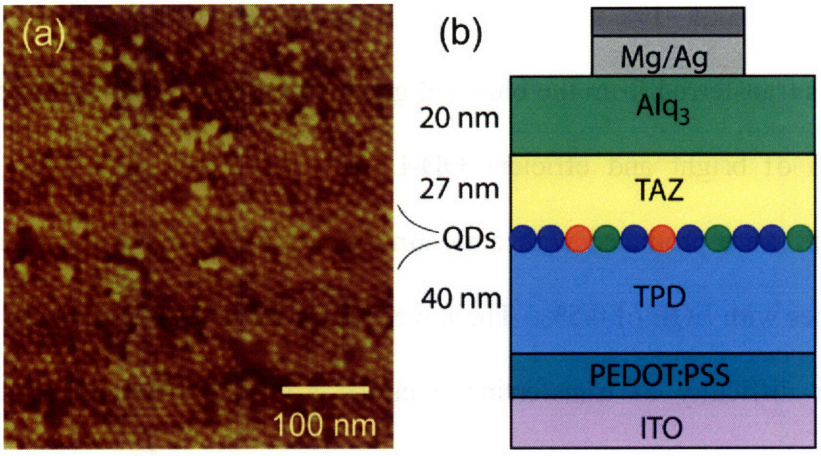

Figure 2.6: Device structure of the mixed monolayer QD-OLED. (a) Atomic force microscope phase image of blue QDs forming approximately 1.1 monolayers on top of a 40 nm thick TPD film. (b) Device cross-section of a white QD-LED. [10]

QD solutions for the white QD-LEDs were prepared by mixing red, green, and blue QD solutions so that the R:G:B QD ratio in the film is 1:2:10. The R:G:B QD ratio was chosen in part to compensate for the differences in PL efficiency of different QD samples. Additionally, QD-to-QD proximity in the electroluminescent QD monolayer enables exciton energy transfer from higher energy to lower energy QDs [18-20], red shifting

the overall emission and necessitating a higher concentration of blue QDs in the QD monolayer. Consequently, blue QDs of high luminescence efficiency are needed for efficient QD-LED operation. Solution concentrations were calibrated using atomic force microscopy (AFM) to produce a QD monolayer upon spin-casting (Figure 2.6).

2.3.3 RGB Device Characteristics

CdSe/ZnS QDs emitting at 620 nm with a QY of almost 90% produced EL devices with an EQE of ~1%, similar to those reported previously [6]. These QDs readily accept excitons transferred from the blue and green emitting transport materials allowing the production of bright and efficient QD-LEDs. Core/shell/shell QDs made from ZnSe/CdSe/ZnS were produced with emission from 510-560 nm with a QY of ~70%, enabling devices with EQE of 0.5%. The lower EQE of these green devices is likely due to the greater difficulty of transferring excitons from the blue and green emitting transport materials to the QD monolayer, which does not absorb as strongly at those wavelengths as do redder QDs. Blue devices were initially constructed using CdS/ZnS particles, as in previously published devices [12], however the QY of the QDs after processing (15%) was not high enough to allow for efficient blue emission in the film. High QY ZnCdS alloyed QDs were then synthesized instead and found to emit between 400-500nm with a QY of 40% after processing. These materials were able to produce devices with greater EQE (0.35%) than previous devices and thus enabled the production of mixed films with an adequate blue QY to create reasonably efficient white EL devices. The EQE for the blue devices was still lower than for the green and red devices, mainly because FRET transfer of excitons from the organic transport materials is either less

efficient, as in the case of TPD, or impossible, as in the case of Alq_3 (Figure 2.1). In this case the device function is more dependant than the green or red devices on the ability of the transport materials to directly inject charge into the band structure of the QD, Since it is more difficult to inject holes into the valence band of bluer QDs, these QDs tend to emit at higher voltages and as a result the white device CIE shifted to the blue with increased voltage.

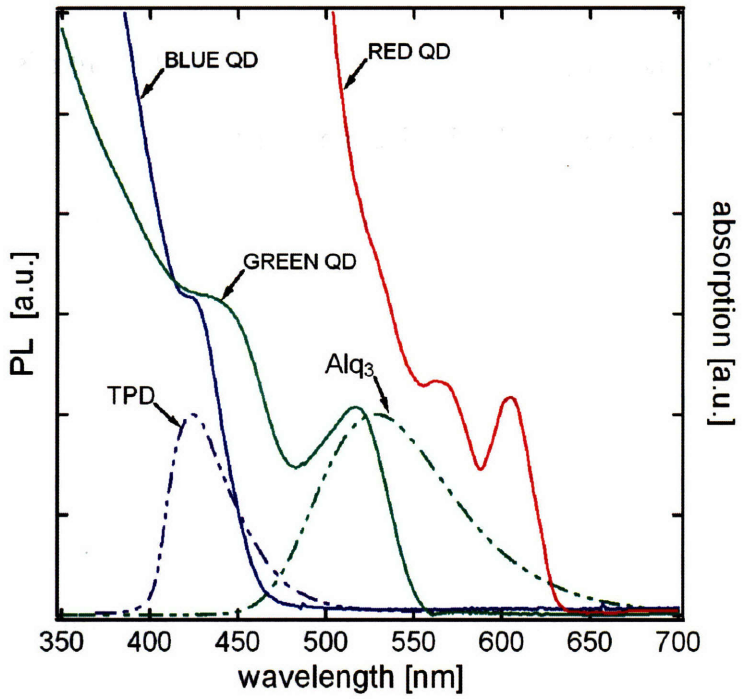

Figure 2.7: Red, green, and blue QD absorption spectra labeled with red, green, and blue solid lines, respectively, are shown together with TPD and Alq_3 PL spectra labeled with purple and green dashed lines to demonstrate spectral overlaps. [10]

EL spectra for the red, green, blue and mixed-monolayer QD-LEDs are measured at near video brightness (Figure 2.8b, next section). The EL spectra of red and green QD-LEDs correspond to the color-saturated PL spectra characteristic of colloidal QDs,

with CIE coordinates of (0.65, 0.34) and (0.31, 0.65), respectively. The blue QD-LED spectrum has a dominant QD component and weaker Alq_3 and TPD emission, consistent with energy transfer [18-20] and downconversion of the deep blue QD luminescence by Alq_3, (expected from the spectral overlap of Alq_3 absorption and blue QD PL). In contrast, spectral overlap of TPD PL and blue QD absorption is insufficient to provide complete quenching of TPD EL via energy transfer from TPD to blue QDs (Figure 2.7). CIE coordinates of the blue QD-LEDs are (0.19, 0.11). We note that the hole blocking TAZ layer should physically separate the blue QD monolayer Alq_3 film inhibiting QD-to-Alq_3 energy transfer and Alq_3 luminescence. However, the TAZ film is not planar when grown on the QD monolayer [4,21-23], allowing pinholes to form in which some QDs come into contact with the Alq_3 film. This contributes to Alq_3 EL in blue QD-LEDs.

2.3.4 White Emitting QD Devices

The emission spectrum of the white QD-LED (Figure 2.8a) shows a pronounced contribution of red, green and blue QD EL components. The TPD EL signal is largely quenched due to energy transfer to the red and green QDs. Alq_3 still appears to exhibit a weak spectral feature in the white QD-LED spectrum analogous to the blue QD-LEDs. The mixed-monolayer QD-LED pixels appear uniformly luminescent, look "white" to the eye (Figure 2.8d), with CIE coordinates (0.35,0.41) at 9 V applied bias and CRI of 86 (Figure 2.8b), when compared to the 5500K black body reference. Such high CRI compares favorably to conventional white light sources such as "cool white" fluorescent (CRI = 62), incandescent (CRI = 100), and dye enhanced InGaN/GaN solid state LEDs (CRI > 80) [16].

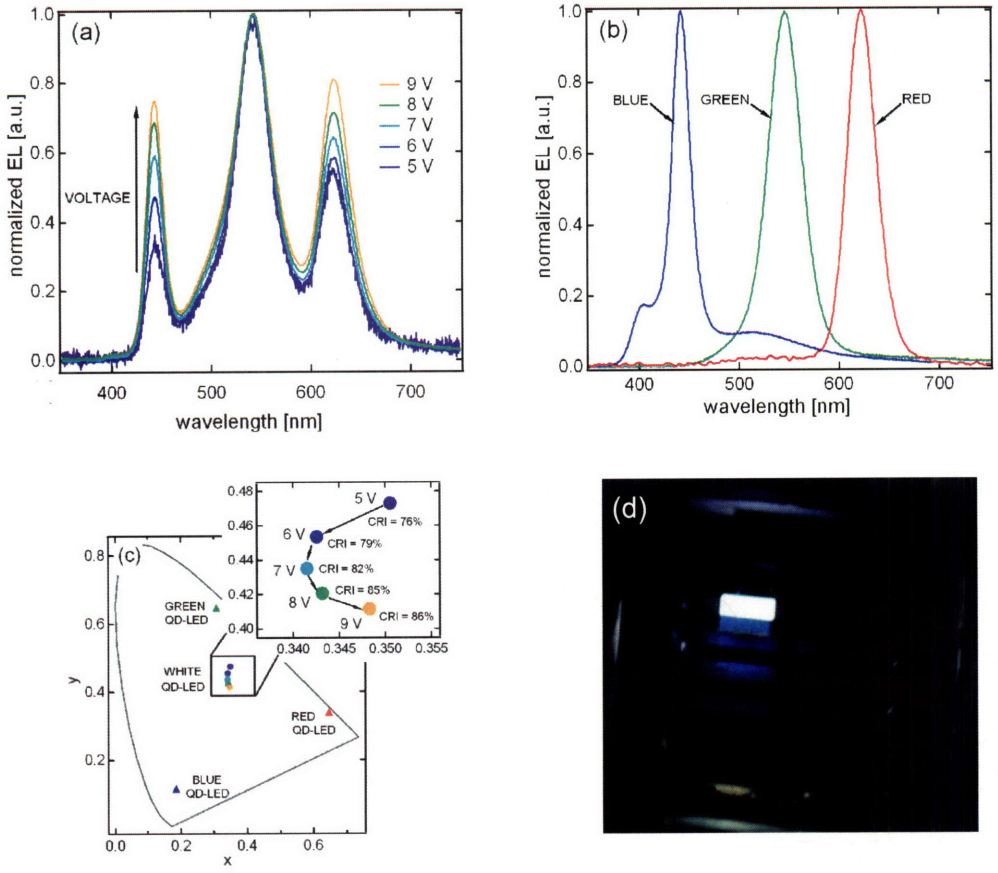

Figure 2.8 EL characteristics of the white, red, green and blue devices. (a) Normalized EL spectra of a white QD-LED for a set of increasing applied voltages. The relative intensities of red and blue QD spectral components increase in comparison to the green QD component at higher biases. (b) Normalized EL spectra of red, green, and blue monochrome QD-LEDs (red, green and blue lines, respectively). (c) CIE coordinates of the red, green, blue QD-LEDs (triangles). Circle symbols show the evolution of CIE coordinates and CRI of the white QD-LEDs upon increasing applied bias. d) a photo of the device in operation at 10V applied bias. [10]

The peak external luminescence quantum efficiencies (EQEs) of the monochrome QD-LEDs are measured to be 1.6% at 4.6 V (0.29 mA/cm^2) for red devices, 0.65 % at 5.2 V (0.63 mA/cm^2) for green, and 0.35% at 9.1 V for blue (1.73 mA/cm^2) (Figure 2.8). These values are consistent with previously reported QD-LEDs [5-7,9,10,12], and with blue

QD-LEDs, more efficient than previous reports [12]. The peak EQE of white QD-LEDs is 0.36% at 5.0 V (1.51 mA/cm^2) (Figure 2.9b), which corresponds to 0.9 cd/A and 0.57 lm/W, at a brightness of 13.5 cd/m^2. At 9 V applied bias, and optimal CIE position, the brightness was 92 cd/m^2, with efficiencies of 0.28% EQE, 0.7 cd/A and 0.24 lm/W at 13 mA/cm^2 of current. Maximum brightness exceeded 830 cd/m^2 at 14V and 230 mA/cm^2.

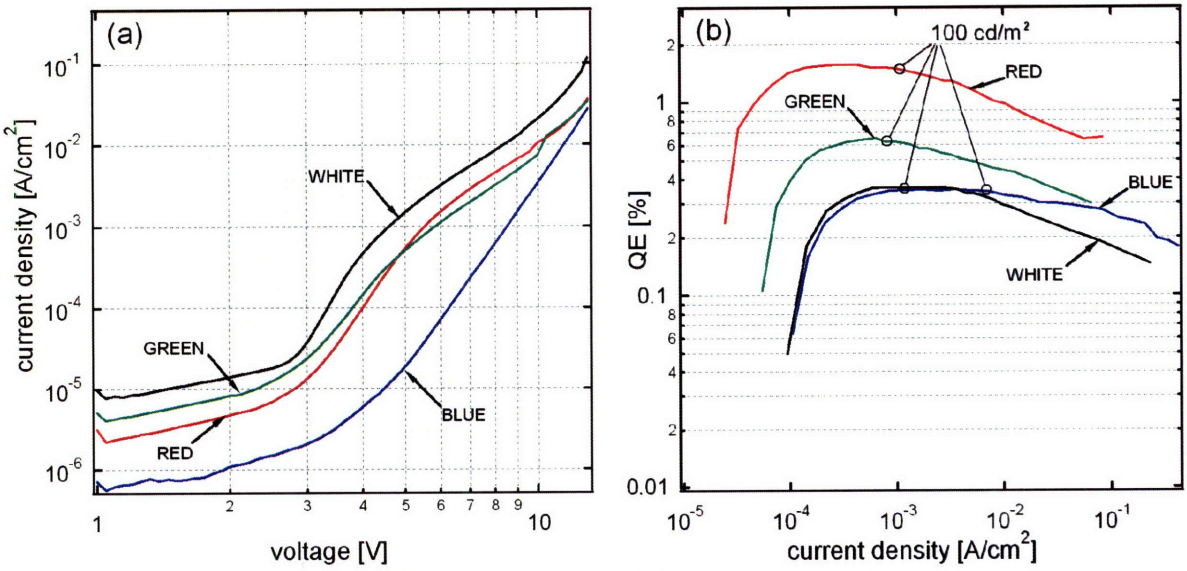

Figure 2.9: Current-voltage characteristics (a) and external electroluminescence quantum efficiency (b) measured for red, green, blue, and white QD-LEDs labeled with red, green, blue and black lines, respectively. The circled data points indicate device brightnesses of 100 cd/m^2.

Since the white QD-LEDs contain three types of QDs with different responses to charge injection, we expect the EL spectrum to change for different driving conditions. In Figure 2.8a we show the EL spectrum color shift in a white QD-LED as we change the applied bias from 5 V to 9 V, resulting in slight change of the CIE coordinates and CRI, as shown in Figure 2.8c. With increasing voltage we observe the increase of the red and blue QD spectral components in the white QD-LED spectrum relative to the initially

dominant green QD spectral component. This effect can in part be explained by analysis of the current-voltage (IV) characteristics of the red, green and blue monochrome QD-LEDs (Figure 2.8b) and the proposed energy band diagram shown in Figure 2.10. The blue QD-LED reaches video brightness at a higher voltage than the red and green devices. The higher resistance of the blue QD-LED for all currents can be ascribed to the higher energy barrier to the hole injection into the blue QDs, necessitating a higher applied voltage to generate a blue QD exciton.

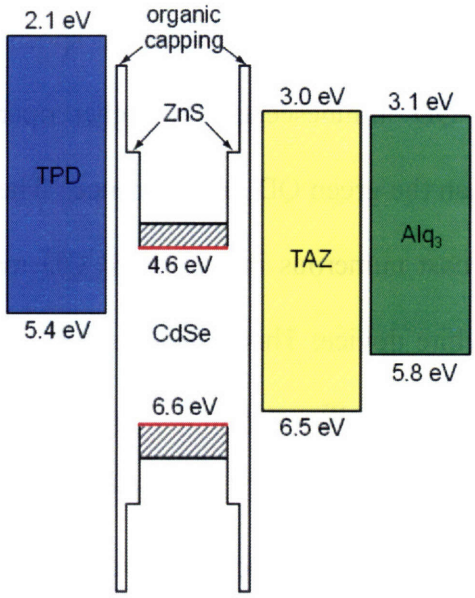

Figure 2.10: Suggested band diagram for the QD-LEDs of this study. Conduction and valence band position for the red QDs are labeled with red energy levels, the shaded area shows the range of likely energy level positions for the conduction and valence bands of the green and blue QDs. [10]

In the white QD-LED, charge injection into the mixed QD film is dominated by injection into the green and red QDs at low applied bias (5V). Since the QD mixture contained twice as many green QDs as there were red QDs, the larger fraction of the green QDs contributed to a more intense green EL component as compared to red QD EL

at low applied bias. Resonant energy transfer from green QDs to the red QDs is inhibited by the relatively small number of both red and green QDs as compared to blue QDs in the mixed QD monolayer, as the probability of locating a green QD next to a red QD is small.

At higher applied biases charge injection into blue QDs becomes more efficient, and the EL component of the blue QDs becomes more significant. Increased exciton formation on blue QDs also benefits red and green QD luminescence due to exciton energy transfer from blue QDs to red and green QDs. The energy transfer to red QDs is more efficient than to green QDs due to an increased spectral overlap. Consequently, with an increase of blue QD luminescence (at higher operating voltages), red QD luminescence rises more than the green QD luminescence. The exciton formation on the blue QDs, which are the most numerous in the mixed QD monolayer, will govern the overall efficiency of the white device. This is reflected in the efficiency data of white QD-LEDs which closely tracks the efficiency of the monochrome blue QD-LEDs.

The operation of the white QD-LED is enabled by the use of identical electron transporting, hole blocking, and hole transporting layers in all of our monochrome QD-LEDs. Akin to mixing colors in a paint shop, in an ideal device the solutions of QDs can be precisely mixed to achieve any desired spectrum. QD-LED sources have the unique capacity to surpass the tunability of the best white OLEDs. This originates from the simplicity of the QD-LED design and the color purity of QD lumophores.

2.4 Blue LEDs Using TPBi and Spiro-TPD with Alloyed QDs

In selecting new transport materials for use in the blue QD-LEDs, there are four governing criteria. First, as with any semiconducting organic material, it must be possible to be incorporate it into the device by evaporation or spin-coating. Second, the conduction (valence) band of the ETL (HTL) should facilitate injection of electrons (holes) into the conduction (valence) band of the QD (extrapolated from known bulk values [24]). Third, the material should not absorb at the wavelength of the QD emission, to prevent FRET of excitons formed on the QDs to the organic materials, and therefore to reduce emission contribution from the organic layers. Finally, materials should be identified that are significantly more robust to water and air, if possible. One of the greatest drawbacks of the TPD/QD/Alq_3 device was its propensity to degrade in air over time, limiting both device performance and longevity. Ultimately, this final problem would be better solved by switching to inorganic HTL and ETL materials (see Chapter 3).

The candidates selected were 2,2′,2″-(l,3,5-benzenetriyl)tris(l-phenyl-lH-benzimidazole (TPBi) as the ETL to replace Alq_3 and spiro-N, N'-diphenyl-N, N'-bis(3-methylphenyl)-(1, 1'-biphenyl)-4, 4'-diamine (spiro-TPD) to replace TPD. The latter material is a molecule very similar to TPD but with increased resistance to degradation in air. TPBi was selected due to its wide band gap of 3.3 eV and its ability to inject electrons into the band structure of the QDs. Its wide band gap prevents FRET from occurring between the QDs and the organic, while encouraging FRET from the organic in the QD. Armed with these improved transport materials, the next step was to improve the QY of the QDs.

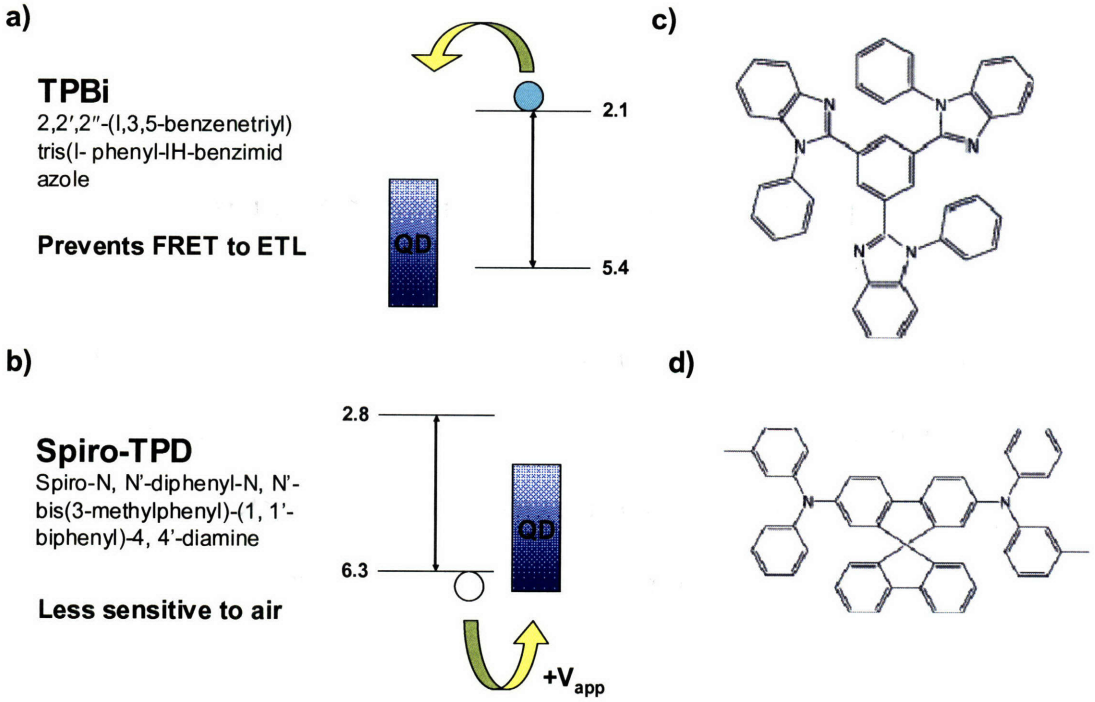

Figure 2.11: Diagram of the new organic ETL (a) and HTL (b) with band gaps of 3.3eV and 3.5eV respectively [25]. The TPBi (c) and spiro-TPD (d) molecules are pictured also.

2.4.1. Synthesis of ZnCdS/ZnS Overcoated QDs as High QY Optical Materials

The device specifications shown in Figure 2.4 show an EQE of 0.4%. However, much of the gain is realized by the increased quantum yield of the particles at 48% after purification as compared to CdS/ZnS, which had a QY of ~20% after precipitation [12]. It seems reasonable then that further increases in efficiency could be obtained using higher QY particles. The easiest way to increase the QY of any nanocrystal is by overcoating it with a higher band gap material, in a type-I configuration (Section 1.1.4). In this case ZnCdS can be overcoated with ZnS to form a type-I core/shell material.

Synthesis was achieved by precipitating ZnCdS cores twice and redispersing in hexane (Section 2.2.1. A pot of 5 ml oleylamine and 5 ml TOP was degassed at 130 °.

Blue cores were overcoated by adding core particles in hexane to the pot then removing the hexane under vacuum at 80 °C. The pot was subsequently heated to 210°C and a solution of diethyl zinc and hexamethyldisilathiane (TMS_2-S) was added dropwise. After the addition the solution was cooled to room temperature, at which point the nanocrystals spontaneously precipitated from solution. After centrifuging the solution, the precipitate was redissolved in hexane and butanol. Nanocrystals, now ZnCdS/ZnS core/shell quantum dots, were then precipitated a second time using acetone, centrifuged and redispersed in chloroform, as described above.

The quantum yield for the ZnCdS/ZnS quantum dots was found to be between 50% and 80% generally, as compared to coumarin 480, and the dots were found to be 8-10 nm in diameter after overcoating. Emission from the QDs generally did not shift significantly during the overcoating step (Figure 2.12a), in contast to traditional CdSe/ZnS QDs [26,27]. This is because some alloying can take place at 210 °C between the overcoating material and the core material, and in this case the effect of the increase in Zn in the alloy and the increase in size of the QD offset each other in terms of the band gap energy. Overcoated ZnCdS/ZnS QDs could be produced emitting from 440 nm – 510 nm and appear bright blue to blue-green to the eye (Figure 2.12b). Size dispersion was generally <10% but the FWHM of the emission peak could be as high as 34 nm, due to a distribution of both sizes and percentages of Cd in the core material. Overcoating generally increased the FWHM slightly, presumably because some particles grew slightly faster than others.

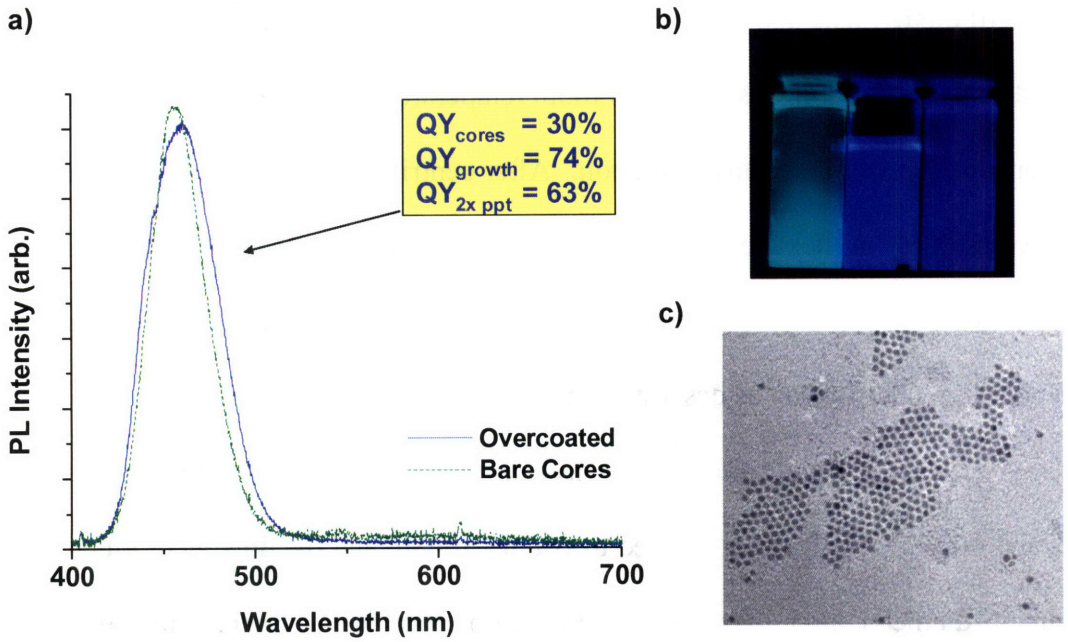

Figure 2.12: Photoluminescence, photo and TEM of ZnCdS/ZnS. a) Emission spectrum from the ZnCdS QDs before (green dashed) and after overcoating (blue solid) with ZnS. b) A photo of ZnCdS/ZnS QDs in hexane, excited with a 365 nm UV mercury lamp. The sample from (a) is shown as the center vial. c) a TEM of ZnCdS/ZnS QDs from the sample shown in (a) at 68,000x magnification.

2.4.2 Blue QD-LEDs Using Overcoated ZnCdS/ZnS

After overcoating, the QDs can be used in a device along with the new organic transport materials, TPBi and spiro-TPD. Devices were constructed as described in Section 2.3.2 with 40 nm of spiro-TPD, followed by a micro-contact printed monolayer of QDs, with a 40 nm layer of TPBi and finally a 100 nm thick Ag:Mg electrode capped with 20 nm of Ag.

Two devices are presented in Figures 2.13 and 2.14 emitting at 490 nm and 450 nm respectively. In Figure 2.13a emission was observed at 490 nm with emission primarily from the QDs in the film. Very little emission is visible from the organic films. This device shows an EQE of 0.2% at 4.5 V and 5.5 mA/cm^2. Although the efficiency is only comparable to that of previous devices (Section 2.2), the spectral purity of the device as well as its brightness in room lights (Figure 2.13c) are typical of devices utilizing these ZnCdS/ZnS particles.

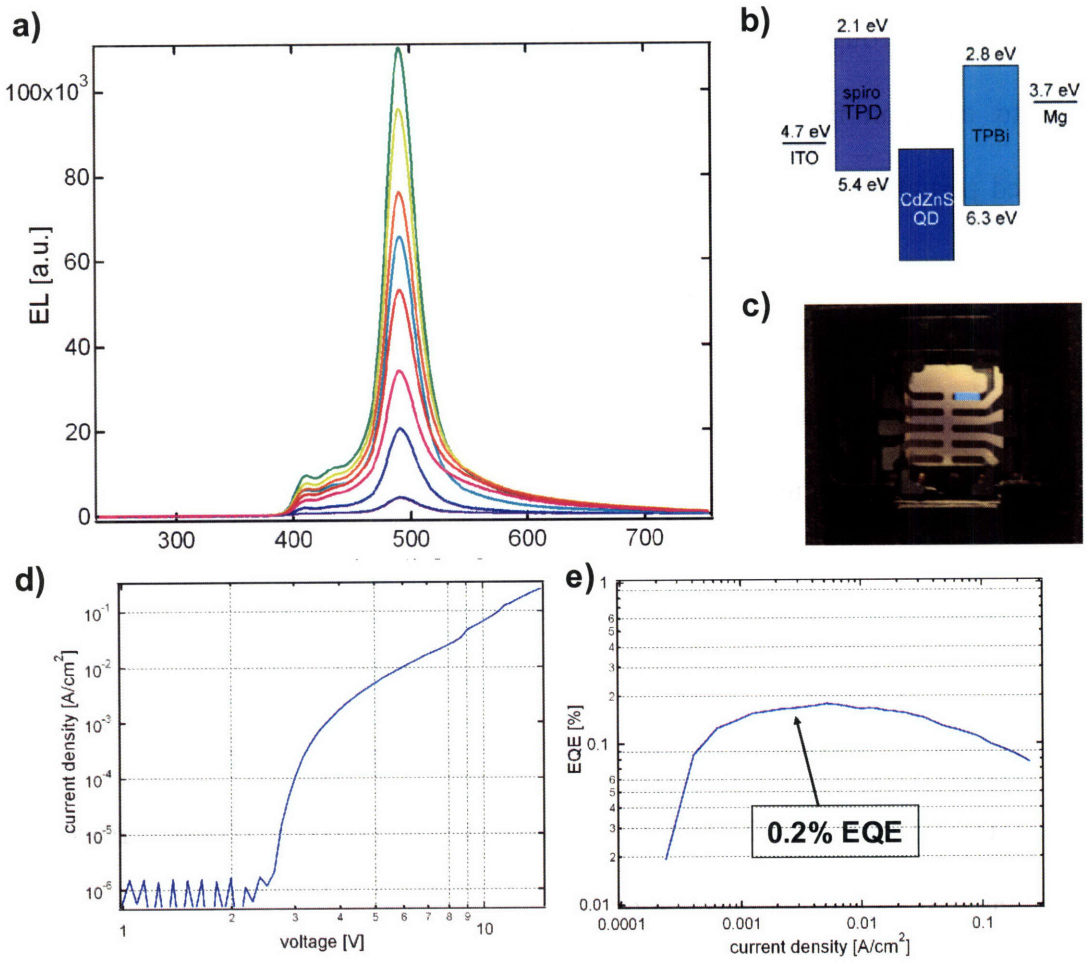

Figure 2.13: Characteristics of a 490 nm emitting ZnCdS/ZnS QD-OLED. a) EL spectrum of a blue QD-OLED using spiro-TPD/(ZnCdS/ZnS)/TPBi. The blue emission of the QDs is the main contributor to the EL. b) A diagram of the band gaps of the layers in the device. c) A photo of

the functioning device at 5V. d) The IV curve for this device. e) The EQE plotted against current density. Peak efficiency for the device occurred at ~4.5V.

However, despite their superior QY, making devices with these materials presents a significant challenge due to the difficulty of injecting charges into the wide bands of the particle. Overcoating with ZnS, while raising the QY significantly, also increases the tunneling barrier into the QD and thus raises the voltage required for injection. This increases the number of excitons formed in the transport materials, especially the ETL, and thus generally tends to increase the organic emission contribution. Furthermore, charge injection through the very thick ZnS shell coating the QD is very difficult, likely leading to emission from the organics. Devices attempting to use wide band gap overcoated particles (< 490 nm) generally emitted purely from the organic or failed to turn on.

Better transport layers or improved device structures will be required to take advantage of the excellent quantum yield of this material. However, in redesigning the organic HTL and ETL to use overcoated QDs we have in fact optimized the device to use ZnCdS cores.

2.4.3 Blue QD-LEDs using TPBi and spiro-TPD with ZnCdS Cores

Figure 2.14 presents the best device, using 450 nm emitting ZnCdS particles with quantum yield of ~40% after purification.

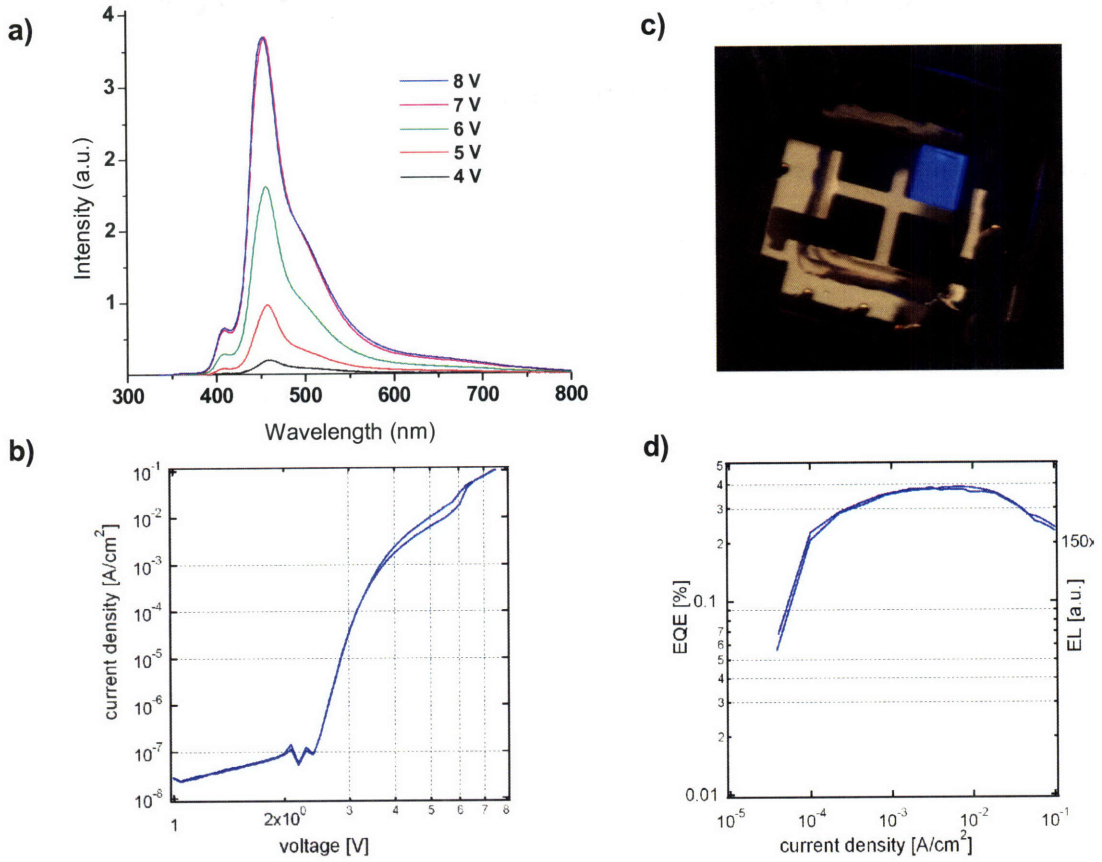

Figure 2.14: Characteristics of a 450 nm emitting ZnCdS QD-OLED. a) EL spectrum of a 450 nm emitting QD-OLED using spiro-TPD/ZnCdS/TPBi. The slight shoulder to the spectrum in this case is likely due to emission from the TPBi. b) A photo of the device functioning at 5 V. c) The IV curve for this device, turn on voltage is around ~3 V. d) The EQE plotted against current density. Peak efficiency for the device was 0.39% EQE at 6 mA/cm^2 and 4.5 V.

The device shows a slight shoulder around 500 nm, due to some contribution from the organics superimposed on a larger contribution from QDs. However, the efficiency of this device is nearly 0.4% EQE at 6 mA/cm^2 and 4.5 V, an improvement of nearly 80% in efficiency over the best CdS/ZnS devices. Coupled with the low turn on voltage of ~3.5 V and bright blue pixels (Figure 2.14c, shown in room lights), this represents one of the best efforts to date in creating a blue QD-LED.

2.5. Using TPBi and spiro-TPD for High EQE Red-Green Devices

While the new organic transport layers were not able to greatly improve the efficiency of blue devices in general, they were better able to energy transfer and inject charges through the thick ZnS tunneling barrier and into the deep valence band of the overcoated ZnCdS/ZnS particles. This was not possible using the classic TPD/QD/Alq_3 device structure. As a consequence it is then sensible to revisit the earlier work done with green and red QDs with an eye toward improving the efficiency of those devices. Since the FRET overlap between the TPBi and the QDs is now more favorable, and the spiro-TPD is more stable and easier to process than TPD, it stands to reason that these devices should be able to top the EQE of previous works which reached 0.5 % [9] and 2.0 % [7] for the green and red respectively.

2.5.1 Quantum Dot Synthesis: CdSe/ZnS

Two different types of QDs were used in this device, reflecting the range of previous work in this field and to show both the color and material versatility of our device. Green emitting devices used ZnSe/CdSe/ZnS QDs 538 nm emitting QDs with a quantum yield of 65% (see 2.3.1 for synthesis).

Red-emitting CdSe/ZnS quantum dots were synthesized by methods similar to those previously reported [21]. To prepare the CdSe cores, a pot of 6.25 g of trioctylphosphine oxide (TOPO, Aldrich 99%), 5.75 g hexadecylamine (HDA, technical grade Aldrich) and 3.4ml of trioctylphosphine (TOP, 97% Strem) was degassed at 110 °C. In a separate vial, 0.852 g hexadecanediol (Aldrich) and 0.473 g of cadmium 2,4-pentanedionate (Alfa Aesar) in 8 ml TOP were also degassed at 110 °C. After cooling to

room temperature, 2 ml of 1.5M trioctylphosphine selenide (TOP-Se) was added to the vial. The pot was then heated to 360 °C under argon and the contents of the vial were quickly injected into the pot, causing nucleation of the nanoparticles, which was then cooled to 270 °C for several minutes until aliquots of the sample revealed that the cores had grown large enough to emit at ~270 nm. The reaction was quenched by quickly cooling the pot to room temperature. The cores were precipitated twice by the addition of methanol and butanol and centrifuged for 5 minutes at 3900 RPM before being redispersed in hexane.

CdSe cores were overcoated with ZnS using established methods of overcoating [28] adapted by the use of a syringe pump instead of an addition funnel. To overcoat, a pot of 10 g TOPO and 0.4 g hexylphosphonic acid (HPA) was degassed at 140 °C, the solution of cores in hexane was added to the pot and hexane pulled off at 80 °C. The amount of nanocrystals added to the pot was estimated to contain 0.143 mmol of cadmium. The pot was then placed under argon at 80 °C and stirred for 1.5 hours after adding 0.5 ml of decylamine. The pot was heated to 155 °C after which a solution of 73 mg diethyl zinc, 18 mg dimethyl cadmium in 4 ml TOP and a second solution of 266 mg of hexamethyldisilathiane in 4 ml TOP were both added by slow injection at a rate of 2 ml/hr for about 2 hours. The pot was then cooled to 80 °C, and left stirring overnight to anneal the nanoparticle surface. CdSe/ZnS quantum dots were precipitated twice, as above, and redispersed the second time in chloroform prior to being filtered with a 0.2 um filter. Quantum yield of the sample was estimated to be ~75% after precipitation.

2.5.2 High Efficiency Device Fabrication

Devices were structured as ITO/TPBi/QD/Alq3/Ag:Mg/Ag, as used in the blue ZnCdS/ZnS devices shown in Section 2.4.2. Device fabrication steps were identical to those described in Section 2.3.2, except using red (605 nm) and green (535 nm) emitting QDs as the active layer in the device.

2.5.3 High Efficiency Device Characterization

IV curves for all devices are characteristic of organic transport QD-LEDs. These show a power law dependence of current with respect to voltage after the turn-on voltage around 2.5V. There is a noticeable decay component to this dependence beginning around 10^{-4} mA/cm^2. This is probably due to trap filling in either the hole or electron transport layers, which would then limit the current (trap-limited charge-transport) [8,29]. EQE increases with respect to voltage until the decay eventually limits the current, despite the increase in voltage. After 4 V, as the voltage, and thus the local field, rises, non-radiative recombination due to charging of the dot films becomes more prominent, decreasing the percentage of radiative excitons. Because the current is limited in this regime, fewer spare charges can escape the QD film and thus are left to participate in Auger non-radiative relaxation with excitons being formed on the QDs. This effectively begins to quench the emission, reducing the EQE as voltage increases.

Both devices displayed EQEs well over 1% with maximum EQEs of 1.8% (green) and 2.7% (red) and maximum luminosities of 20,000, and 10,000 cd/m^2 (12V), respectively. One reason for the improved EQE is the increase in QY of materials after processing. In any one QD sample, some QDs are poorly formed, or lose passivating

ligands during precipitation. This can cause either trap states on the surface due to impurities or defect sites within the nanocrystal. These defect sites create energy traps within the band gap which allow excitons a non-radiative decay pathway. Lack of a ZnS potential barrier would place bright QDs closer to neighboring non-radiative QDs, which would increase the likelihood of Forster resonant energy transfer (FRET) to non-emitting dots. This negatively impacts the QY of the film and thus the maximum EQE. It is largely due to this effect, as well as the loss of emitting device area occupied by "dead" QDs, that film QYs are relatively low and that device EQEs have rarely exceeded 1% [6,7].

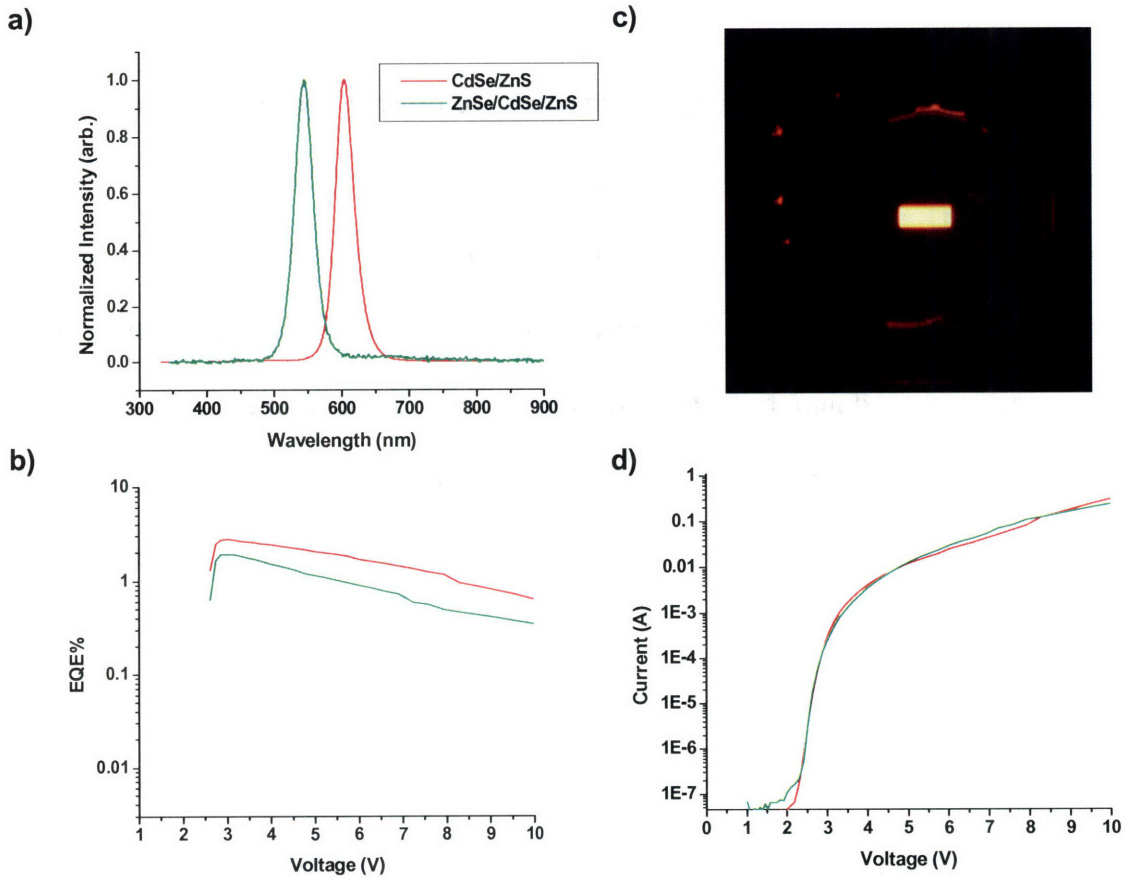

Figure 2.15: EL characteristics of red and green high efficiency QD-OLEDs. a) Electroluminescence spectrum from devices using spiro-TPD/QD/TPBi as the device structure with ZnSe/CdSe/ZnS (green curve) and CdSe/ZnS (red curve) as the QD monolayer. b) EQE% plotted against voltage for each of the two devices. The green emitting QD-OLED has peak

efficiency of 1.9% at 3.0 V and 0.27 mA/cm^2, while the red one peaks at 2.7% EQE at 3.0 V and 0.312 mA/cm^2. c) A photo of the red device in operation, the pixel appears orange-red to the eye. d) An I-V curve for the two devices, the device appears to turn-on around 2.5 V and the current begins to saturate at ~4V. The curve is similar to those presented for earlier devices [6,7,10].

The second contribution to the improved EQEs is the use of better organic ETL and HTL materials. Both are wide band gap blue emitting materials easily able to Forster energy transfer to any of the dots used in our devices, as described in Section 2.4. Improving the lifetime and reliability of the organic films necessarily improves the efficiency of the device, thus raising the EQE over previous devices. Due to the wide band gaps in both the ETL and HTL, Forster energy transfer is probable between the ETL or HTL and the QDs. Thus excitons formed in the organic layers, within the Forster radius of the QDs, can transfer to the QDs and emit across the QD band gap. This is seen in the emission spectra of the devices, where absolutely no detectable emission is derived from the organics (Figure 2.15). Similarly, with favorable band-gap alignment, charges can be directly injected into the QDs from the ETL and HTL to form excitons which then recombine across the band gap of the QD. Using materials with well matched hole and electron mobilities improves the efficiency of the device by causing the majority of excitons to be formed close to the QD layer. It also prevents charging of the QDs that can lead to Auger non-radiative decay [30]. Since both processes, FRET and direct charge injection, are likely to occur in organic QD-LEDs [6,8,10,30,31], choosing materials with appropriate band structures is paramount to achieving efficient device function. Improving the EQE requires not only better synthetic techniques to improve sample QY, but also improved processing, which, coupled with the use of a more robust HTL (spiro-TPB) and wider band gap ETL (TPBi), have increased the yield of green-red devices to

1.8% and 2.7% respectively, which is higher than any other previously published devices at these wavelengths [7,9].

2.6 Summary

This work has shown the feasibility of using a variety of QD materials as the emissive materials in a QD-OLED device. By successfully synthesizing high QY blue emitters and discovering better organic transport materials, the efficiency of the devices have been improved to 0.4%, 1.8% and 2.7% EQE for the blue, green and red devices, respectively. We have also achieved a mixed-monolayer QD-OLED, with arbitrarily tunable CIE coordinates that can be tuned to achieve a white light emitter.

In order for further progress to be made in QD-OLEDs, new materials or fundamentally new devices must be constructed to push beyond 3% EQE. Previously the maximum EQE attainable was limited mainly by the QY of the QD film. These QYs are believed to be lower than 10% in close packed films [32] and monolayers. Since the quantum yield of the QDs in solution is already very high, better processing techniques or better transport materials will be needed to increase the EQE towards the film QY. Achieving higher EQEs than that will require discarding the close-packed monolayer device structures. As of now, this work has shown that 1-3% EQE can easily, and regularly be attained in QD-LEDs using even moderately high QY (>50%) QDs. It has also found a device structure that is universally able to achieve EL from any color-emitting QD within the range of the visible spectrum. Further improvements to the efficiency of the blue emitting devices alone stands as the final barrier to achieving the

full potential of RGB QD-OLED displays with performance metrics that are competitive with commercial OLEDs.

My collaborator for the work presented in this chapter was Polina Anikeeva in the Bulovic group, who performed the bulk of the device processing.

2.7 References

(1) Colvin, V. L.; Schlamp, M. C.; Alivisatos, A. P. *Nature* **1994**, *265*, 373.

(2) Dabbousi, B. O.; Bawendi, M. G.; Onitsuka, O.; Rubner, E. M. F. *Appl. Phys. Lett.* **1995**, *66*, 1316-1318.

(3) Schlamp, M.; Peng, X.; Alivisatos, A. P. *J. Appl. Phys.* **1997**, *82*, 5837.

(4) Mattoussi, H.; Radzilowski, L. H.; Dabbousi, B. O.; Fogg, D. E.; Schrock, R. R.; Thomas, E. L.; Bawendi, M. G.; Rubner, M. F. *J. Appl. Phys.* **1998**, *83*, 7965-7975.

(5) Coe, S.; Woo, W. K.; Bawendi, M.; Bulovic, V. *Nature* **2002**, *420*, 800-803.

(6) Coe-Sullivan, S.; Woo, W. K.; Steckel, J. S.; Bawendi, M.; Bulovic, V. *Organic Electronics* **2003**, *4*, 123-130.

(7) Coe-Sullivan, S.; Steckel, J. S.; Woo, W.-K.; Bawendi, M.; Bulovic, V. *Adv. Funct. Mater.* **2005**, *15*, 1117-1124.

(8) Caruge, J.-M.; Halpert, J. E.; Bulovic, V.; Bawendi, M. *Nano Lett.* **2006**, *6*, 2991-2994.

(9) Steckel, J. S.; Snee, P. T.; Coe-Sullivan, S.; Zimmer, J. P.; Halpert, J. E.; Anikeeva, P. O.; Kim, L.-A.; Bulovic, V.; Bawendi, M. G. *Angewandte Chemie International Edition* **2006**, *45*, 5796-5799.

(10) Anikeeva, P. O.; Halpert, J. E.; Bawendi, M. G.; Bulovic, V. *Nano. Lett.* **2007**, *7*, 2196.

(11) Anikeeva, P. O.; Madigan, C. F.; Halpert, J. E.; Bawendi, M. G.; Bulović, V. *Phys. Rev. B* **2008**, *Submitted.*

(12) Steckel, J.; Zimmer, J.; Coe-Sullivan, S.; Stott, N.; Bulovic, V.; Bawendi, M. *Angewandte Chemie International Edition* **2004**, *43*, 2154.

(13) Adachi, C.; al., e. *Applied Physics Letters* **2001**, *78*, 1622-1624.

(14) Bowers, M. J.; McBride, J. R.; Rosenthal, S. J. *J. Am. Chem. Soc.* **2005**, *127*.

(15) Zhong, X.; Feng, Y.; Knoll, W.; Han, M. *J. Am. Chem. Soc.* **2003**, *125*, 13559.

(16) Krames, M. R.; J. Bhat, D. C.; Gardner, N. F.; Gotz, W.; Lowery, C. H.; Ludowise, M.; Martin, P. S.; Mueller, G.; Mueller-Mach, R.; Rudaz, S.; Steigerwald, D. A.; Stockman, S. A.; Wierer, J. J. *Phys. Stat. Sol. A* **2002**, *192*, 237.

(17) Ivanov, S. A.; Nanda, J.; Piryatinski, A.; Achermann, M.; Balet, L. P.; Bezel, I. V.; Anikeeva, P. O.; Tretiak, S.; Klimov, V. *J. Phys. Chem.* **2004**, *108*, 10625.

(18) Kuhn, H. *J. Chem. Phys.* **1970**, *53*, 101.

(19) Forster, T. *Naturwissenschaften* **1946**, *6*, 166-175.

(20) Forster, T. *Ann Phys (Leipzig)* **1948**, *2*, 55-75.

(21) Fisher, B. R.; Caruge, J.-M.; Chan, Y. T.; Halpert, J. E.; Bawendi, M. G. *Chemical Physics* **2005**, *318*, 71-81.

(22) Huang, H.; Dorn, A.; Bulovic, V.; Bawendi, M. G. *Appl. Phys. Lett.* **2007**, *90*, 023110.

(23) Huang, H.; Dorn, A.; Nair, G. P.; Bulovic, V.; Bawendi, M. G. *Nano. Lett.* **2007**, *7*, 3781-3786.

(24) Lide, D. R., Ed. *"Properties of Semiconductors", CRC Handbook of Chemistry and Physics, Internet Version 2006*; Taylor and Francis: Boca Raton, FL, 2006; Vol. 2006.

(25) D'Andrade, B. W.; Holmes, R. J.; Forrest, S. R. *Adv. Mater.* **2004**, *16*, 624.

(26) Hines, M. A.; Guyot-Sionnest, P. *J. Phys. Chem.* **1996**, *100*, 468.

(27) Dabbousi, B. O.; al., e. *J. Phys. Chem. B* **1997**, *101*, 9463-9475.

(28) Snee, P. T.; Chan, Y.; Nocera, D. G.; Bawendi, M. G. *Advanced Materials* **2005**, *17*, 1131-1136.

(29) Coe-Sullivan, S. In *Department of Electrical Engineering and Computer Science*; MIT: Cambridge, 2005, p 166.

(30) Klimov, V. I.; Mikhailovsky, A. A.; McBranch, D. W.; Bawendi, M. G. *Science* **2000**, *287*, 1011-1013.

(31) Caruge, J.-M.; Halpert, J. E.; Wood, V.; Bulovic, V.; Bawendi, M. G. *Nature Photonics* **2008**, *2*, 247-250.

(32) Klimov, V. I.; Bawendi, M. G. *Science* **2000**, *290*, 314-317.

Chapter 3

Quantum Dot-Inorganic Light Emitting Diodes (QD-ILEDs)

3.1 Introduction and Motivation

Most QD based optoelectronics, including photovoltaic cells and light emitting devices (LEDs), have combined the optical properties of QDs (absorption or luminescence) with charge transporting properties of organic semiconductors [1-10]. In Chapter 2, QDs were explored as emissive materials in LEDs for display technologies and large area planar lighting [1-10]. High performance QD-OLEDs emitting in the near infrared and visible spectral ranges have been realized in both this study and in earlier works. [2-7,9,10] [11] However, for QD-LEDs to be applicable to display and lighting applications, QD-LEDs must not only be efficient but must also have long operating lifetimes. The operating lifetime of a typical QD-OLED device (Chapter 2) are limited by the degradation of the organic layers under moisture, oxygen and the instability of the metal contacts. Furthermore, to develop color-tunable electrically pumped lasing structures, the next generation of QD-LEDs has to be designed to withstand high current density operation over a prolonged period of time.

In order to increase stability, it is necessary to replace the organic transport materials with inorganic hole and electron transport layers. In comparison to the QD_OLEDs, epitaxially-grown inorganic light emitting structures that utilize epitaxial QDs, grown by chemical vapor deposition (CVD), and used for high brightness LEDs and electrically pumped lasers have demonstrated increased robustness [12-17]. The

crystalline inorganic structure of these devices is chemically durable and can withstand high current fluxes, allowing for the facile charge transport and fast charge injection rates into the QD layers, as necessary for high exciton density in laser applications [12-17]. Hence, in this study I investigate the use of chemically inert, sputtered, amorphous inorganic semiconductors as robust charge transport layers in QD-LEDs, and demonstrate devices capable of operating at current densities as high as 3.5 A/cm^2.

As with QD-OLEDs, colloidal QDs in these devices are integrated into sandwich structures consisting of electron and hole transport layers surrounding a QD layer of one to four monolayers in thickness. Chemical and morphological stability of amorphous inorganic films enables use of solvent-rich deposition techniques on top of the transport layers, such as spin coating, dip-coating, Langmuir-Blodgett deposition, and inkjet printing of colloidal QDs. Tunable conductivity and adjustable work function of charge-transporting metal-oxide films, through doping and physical co-deposition, enables control of charge balance and charge accumulation in the QD-LEDs, facilitating device optimization.

To accomplish this, the hole transport layer (HTL) from the OLED design (Chapter 2) will first be replaced by an inorganic metal oxide film. This will allow us to tune the charge conduction properties of the p-type metal oxide to mimic those of TPD. After successfully replacing the HTL in the OLED design, the electron transport layer (ETL) will next be replaced by an n-type metal oxide film and the fully inorganic device can be assessed. The stepwise replacement of the transport layers will allow for a controlled experiment to understand how the different materials behave in the device. It

will also allow development of the several new methods necessary to sandwich the QDs between the metal oxide layers without interfering with their emission.

3.2 Inorganic/Organic Hybrid Devices Using NiO as the HTL

The first part of the study of inorganic QD-LEDs required the construction and study of hybrid inorganic/organic device. NiO was selected as the HTL for its transparency, high band gap (> 3 eV), ease of deposition, and resistance to oxidation by air or degradation by organic solvents. Earlier studies have shown that transparent p-type NiO thin films can be achieved using room-temperature reactive sputtering of NiO or Ni targets and can be used as hole-transporting/injecting layers in electro-optical devices[11,18-20]. The band structure of the NiO device is shown in Figure 3.1.

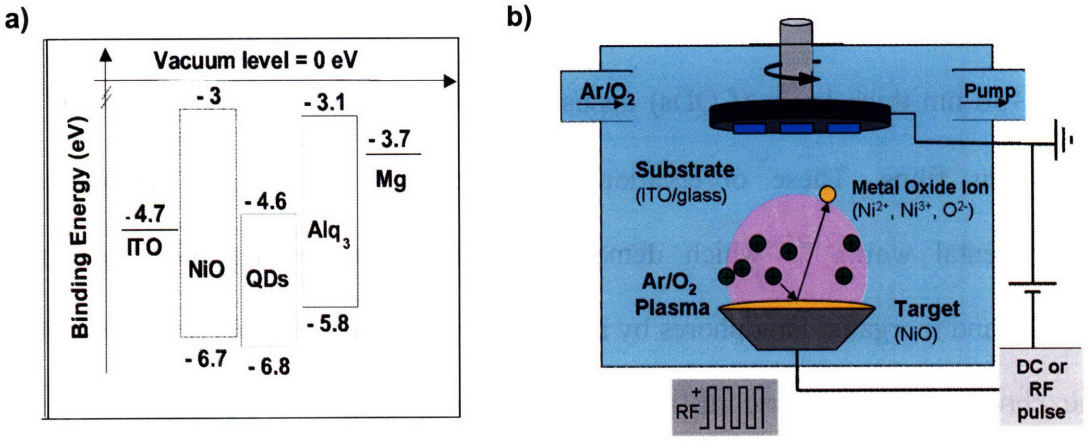

Figure 3.1: Proposed band diagram of a NiO QD-LED and means of production. a) The deep hole conduction band should allow for facile injection of holes into the hole conduction band of the QDs. b) A diagram of the sputtering system used to produce the films. A plasma creates ions from the injected argon/oxygen mix, which are then excited towards a NiO target. Charged Ni

and O ions are ejected from the surface of the target, striking the ITO/coated chips attached to a rotating stage.

There are two crucial challenges to using conductive metal oxides as the transport layer. First, quenching of the QD layer electroluminescence by the high density of free charge carriers in NiO will allow excitons to non-radiatively decay, greatly decreasing the efficiency of the device. Second, the electron and hole currents must be effectively balanced to prevent an excess of either carrier at the QD layer, preventing Auger decay of the excitons which also causes a loss of efficiency.

3.2.1 Quenching of the QD's on a NiO Surface

The issue of quenching was addressed by observing that photoluminescence intensities of single QDs (or a ~30 nm thick layer of QDs) deposited onto resistive ($\rho \approx 1\ \Omega\cdot cm$) NiO thin films remain high. This in contrast to quenched photoluminescence of single QDs (or a ~30 nm thick layer of QDs) deposited onto highly conductive ($\rho \approx 5\times10^{-4}\ \Omega\cdot cm$) NiO thin films. These observations are consistent with earlier theoretical and experimental works[21-25] which demonstrated that photoluminescence quenching of organic and inorganic lumophores by a conductive dielectric can be tuned by controlling the chromophore-dielectric distance and by tuning the electrical permitivity of the dielectric. In this case, the conductivity of the film is tuned by altering the concentration of holes present in the film through controlled doping of the NiO with oxygen.

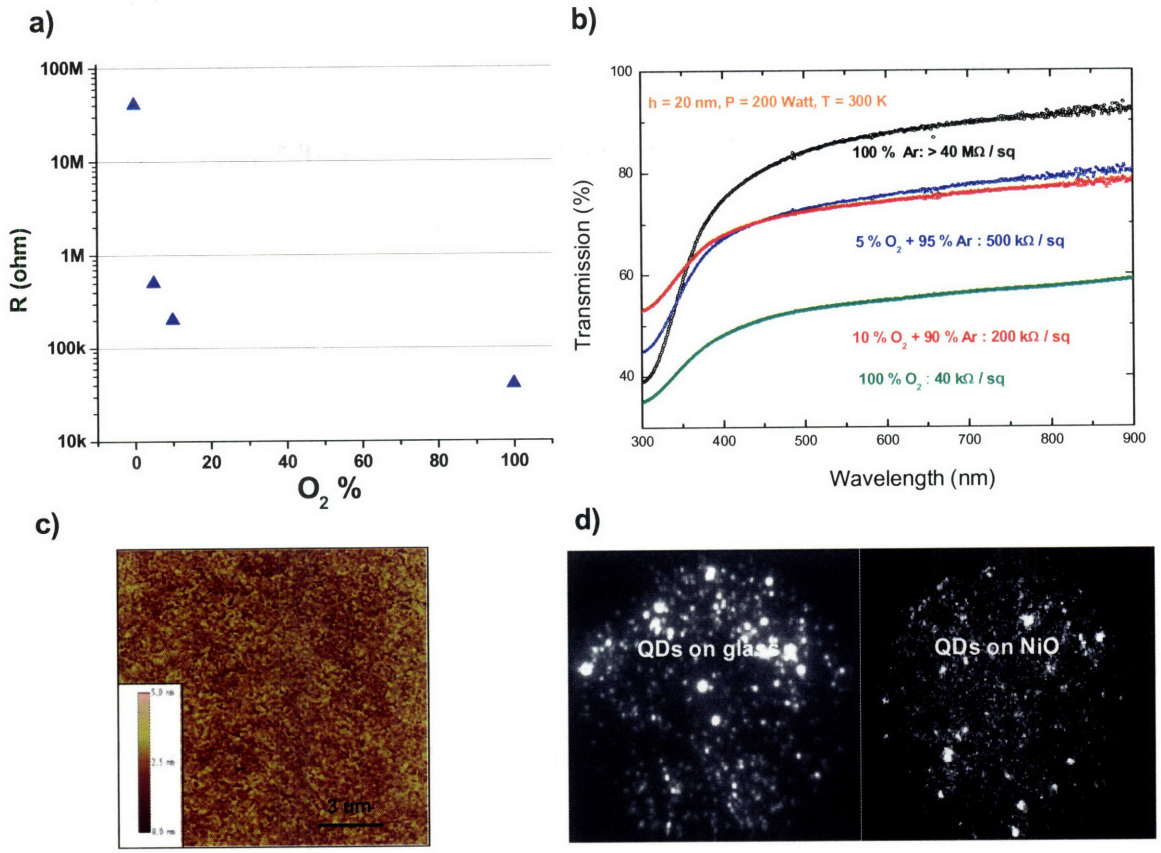

Figure 3.2: Tuning the resistivity of the NiO HTL. a) A plot of the lateral resistance with respect to oxygen percentage in the plasma. b) Optical transmission of the NiO films versus wavelength for each of the four films depicted. Due to the large band gap, films are evenly transparent in the visible spectrum. Optical absorption is derived from the color centers created by electron trap sites, effectively doping the film with holes. c) An atomic force micrograph of the surface of the NiO showing route mean square (RMS) roughness of < 0.5 nm. d) A PL microscope image (using the "single-dot microscope" described in Appendix X.X) of QD's excited using a 514 nm line of an argon-ion laser. The QD's are sitting on glass (lefthand photo) and sputtered NiO at ~0.8 Mohm (lateral resistance). The QDs on the resistive NiO are clearly not quenched by the NiO surface.

3.2.2 NiO/QD/Alq_3 Device Fabrication

To fabricate the devices, ITO coated (150 nm thick) glass substrates (with sheet resistance of 30 Ω/cm) were cleaned via sequential ultrasonic rinses in detergent solution,

deionized water, and acetone, then boiled in isopropanol for five minutes. After cleaning, the glass substrates were dried in nitrogen and exposed to UV-ozone to eliminate adsorbed organic materials. They were then inserted into a nitrogen glove box, which is connected to a sputtering and evaporation chamber via a high vacuum transfer line. In the sputtering chamber a 30 nm thick NiO thin film was deposited by reactive RF magnetron sputtering of a NiO target in an Ar/O_2 gas mixture (Figure 3.1). For our most efficient hybrid QD-LED, the base pressure before sputtering was 10^{-7} Torr, the RF power was fixed at 200 W, the plasma pressure was 6 mTorr and the ratio between the O_2 and Ar gas flow rates was 2.5 %, which, with our sputtering geometry, resulted in NiO deposition rate of 0.03 nm/s. With the above deposition parameters, the NiO thin films showed p-type conductivity with resistivity of $\rho = 5\ \Omega\cdot cm$ (sheet resistance of 2 $M\Omega/cm$), optical transmission of 80 % at wavelength $\lambda = 625$ nm (center of the QD emission peak).

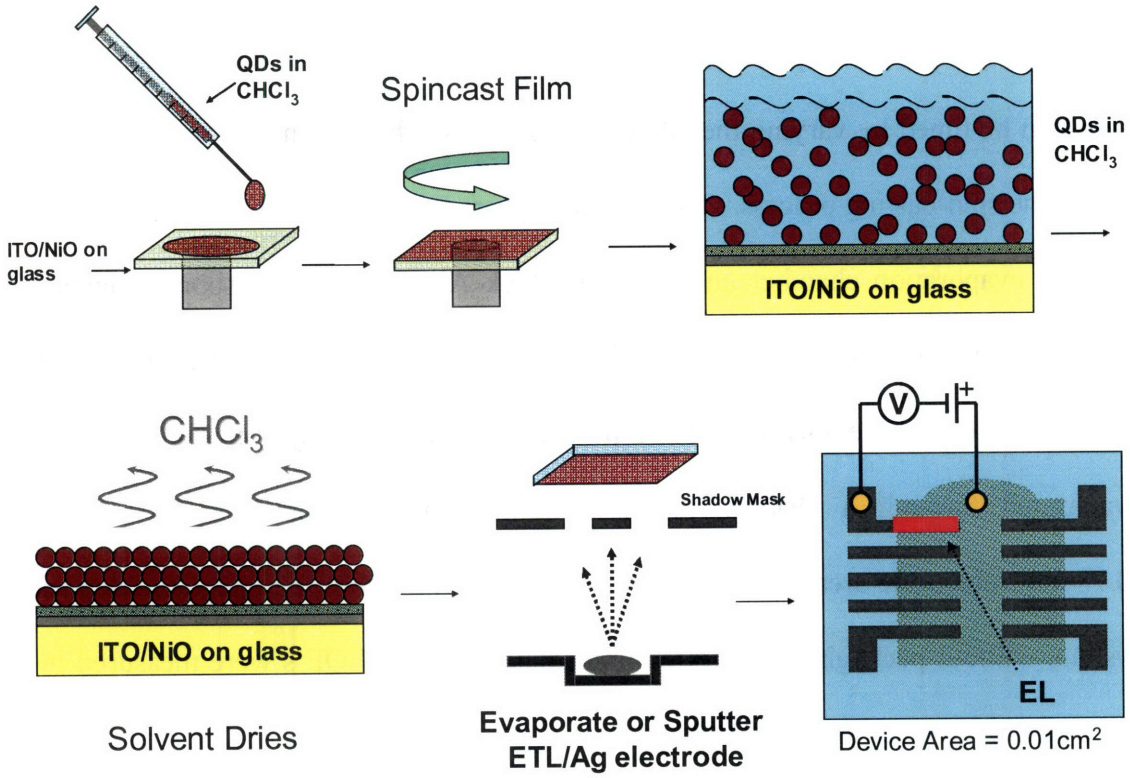

Figure 3.3: A schematic drawing of the steps required to produce the NiO/QD/Alq_3 LED.

The resistivity of the p-type NiO thin films can be accurately tuned by varying the ratio between the O_2 and Ar flow rates: higher oxygen concentration in the sputtering chamber gives lower resistivities (Figure 3.3). For instance, a 10 % oxygen to argon gas ratio gives NiO films with $\rho=5\times10^{-4}$ Ω·cm. AFM characterizations of the ITO/NiO surface reveal a rms surface roughness of ~ 3 nm. The surface roughness mainly comes from the ~ 150 nm thick commercial ITO films. Indeed, AFM characterizations of a 30 nm thick NiO thin film sputtered with the above deposition parameters onto a flat glass substrate reveal a rms surface roughness lower than 1 nm (Figure 3.2). Of paramount importance, the NiO films were highly stable in air and do not degrade in the presence of organic solvents.

Next, the glass/ITO/NiO substrates were coated with a 20 nm thick layer of CdSe/ZnS core/shell QDs that was spin-cast out of chloroform. The thickness of the spin-cast QD films can be tuned by varying the QD concentration in chloroform and/or the spin speed during the spin-casting process. The substrates were transferred, without exposure to air, into the evaporation chamber and a 40 nm thick Alq_3 electron-transporting layer was evaporated at 10^{-6} Torr, with a deposition rate of ~ 0.2 nm/s. Then a 100 nm thick Ag/Mg (1/10 by weight) and 30 nm thick Ag electron-injecting electrode were evaporated through a shadow mask, forming 1 mm diameter circular electrodes (0.78 mm^2 electrode area). The QD-LEDs were removed from the integrated deposition system, without packaging, and tested immediately in air. EQE's were measured in the same manner as were the OLEDs devices.

3.2.3 NiO/QD/Alq_3 Device Analysis

Two sets of devices,were investigated; ρ_1 =5 Ω·cm (first set) and $\rho_2=10^{-2}$ Ω·cm - (second set). Typical forward biased current-voltage (I-V) characteristics for the two sets of devices (measured with respect to the grounded Ag cathode) are plotted in Figure 3.4

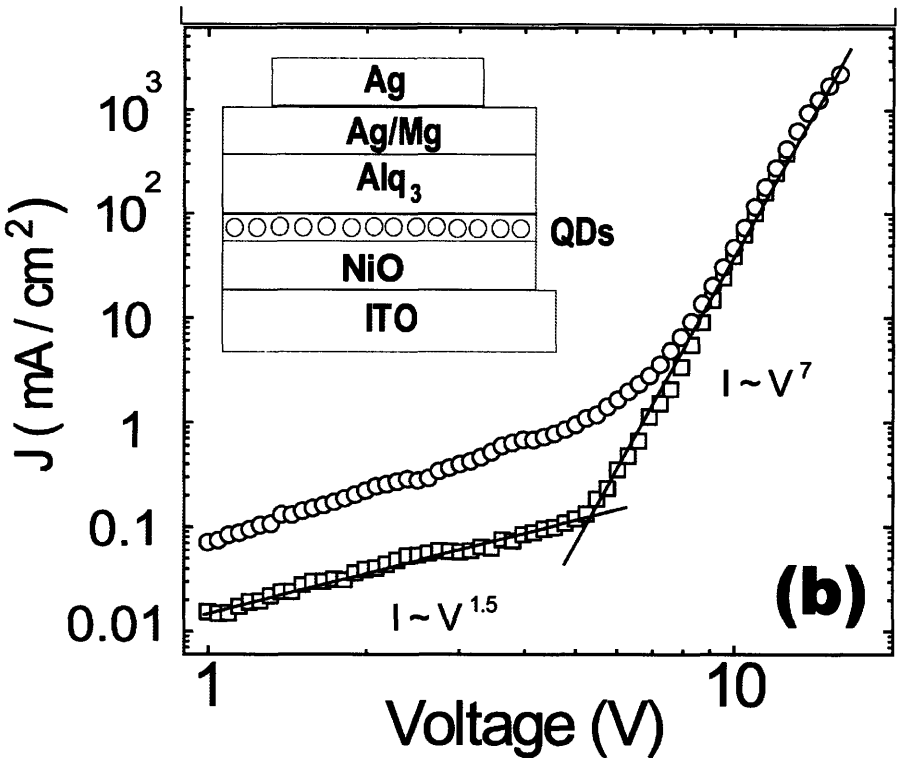

Figure 3.4. Forward-biased current-voltage characteristics for a NiO QD LED of the first (open squares) and second (open circles) set of devices. The contact area is 0.78 mm^2 for both devices. Inset: Schematic representation of the QD-LED structure. [1]

The open square and open circle curves are I-V curves for the first and second of devices, respectively. For the two sets of devices, $J \propto V^n$ with $1 < n < 1.5$ below 6 ± 1 V and $6 < n < 7$ at higher voltages. Here, n is the signature of the charge conduction mechanism and is related to the temperature, the density and the energy distribution of trap states in the organic or inorganic materials. These *I-V* curves are consistent with previous reports of trap assisted space charge limited conduction in both CdSe/ZnS closely packed films [26,27] and OLEDs.[28,29] The maximum steady-state current densities achieved in the first and second set of devices are 300 mA/cm^2 and ~4000 mA/cm^2, respectively. At these current densities 6×10^6 to 8×10^7 carriers per second can be injected into each QD forming the luminescent QD layer. Since the single exciton

recombination time in our QD devices is ≤ 10 ns[30,31], at these current levels the maximum exciton density per QD is 3 % and 40 % for the first and second set of devices, respectively.

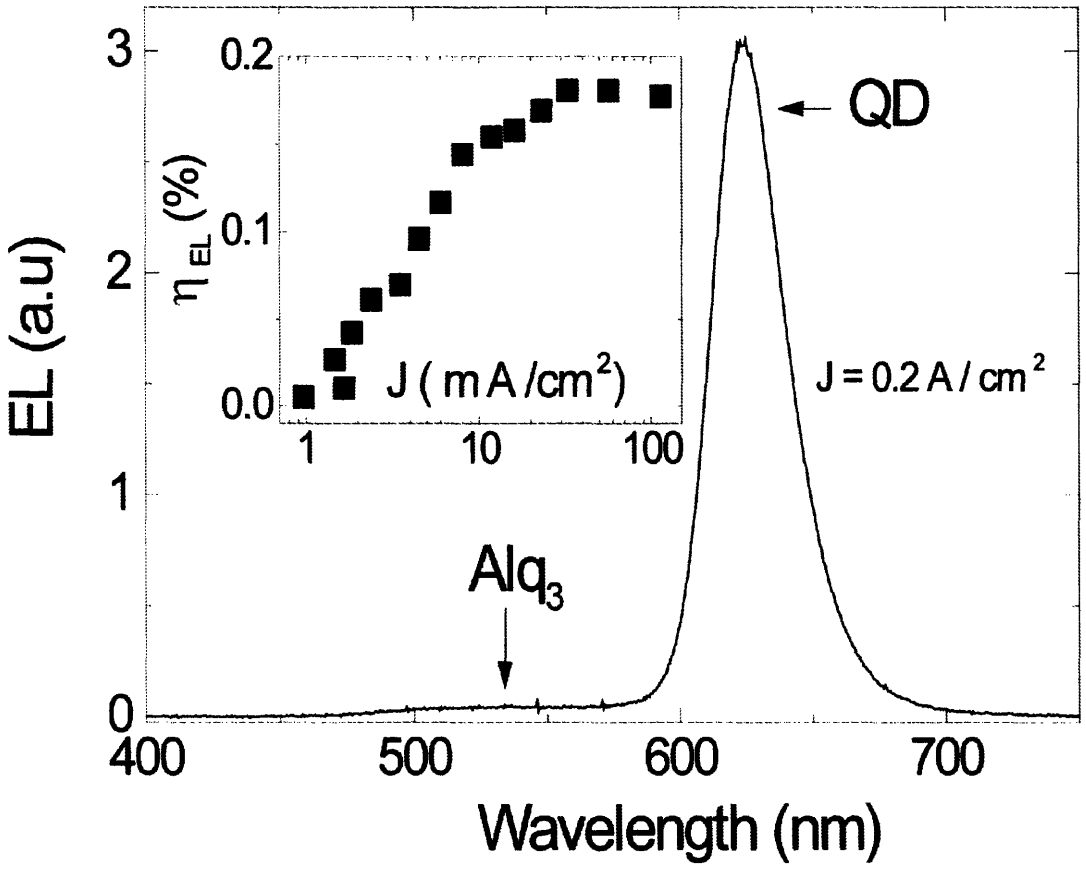

Figure 3.5. (a) EL spectrum of a NiO QD-LED taken from the first set of devices at a current density of 200 mA/cm^2. More than 95 % of the EL originates from QD luminescence. The resistivity of the NiO thin film is 5 Ω·cm. The FWHM of the QD emission peak is 30 nm. The spectral shoulder at wavelength $\lambda = 530$ nm is due to Alq_3 emission. Inset: External electroluminescence quantum efficiency versus current density for the same NiO QD-LED.

Figure 3.5 shows the EL spectrum of a NiO QD-LED, containing a resistive NiO layer (ρ_1=5 Ω·cm), at a current density of 200 mA/cm^2. The 30 nm FWHM QD emission peak centered at λ = 625 nm dominates the EL spectrum. The broader shoulder centered at λ = 530 nm is due to a weak Alq_3 emission. The 1 eV band offset (c.f. the band diagram in Figure 3.1) between the HOMO levels of the CdSe QD and Alq_3 enables hole injection into the Alq_3 film. Figure 3.5 (inset) shows the evolution of η_{EL} as a function of current density for the same device. Maximum EQE of 0.18 % and brightness of up to 40 cd/m^2 are achieved for most of the devices of the first set.

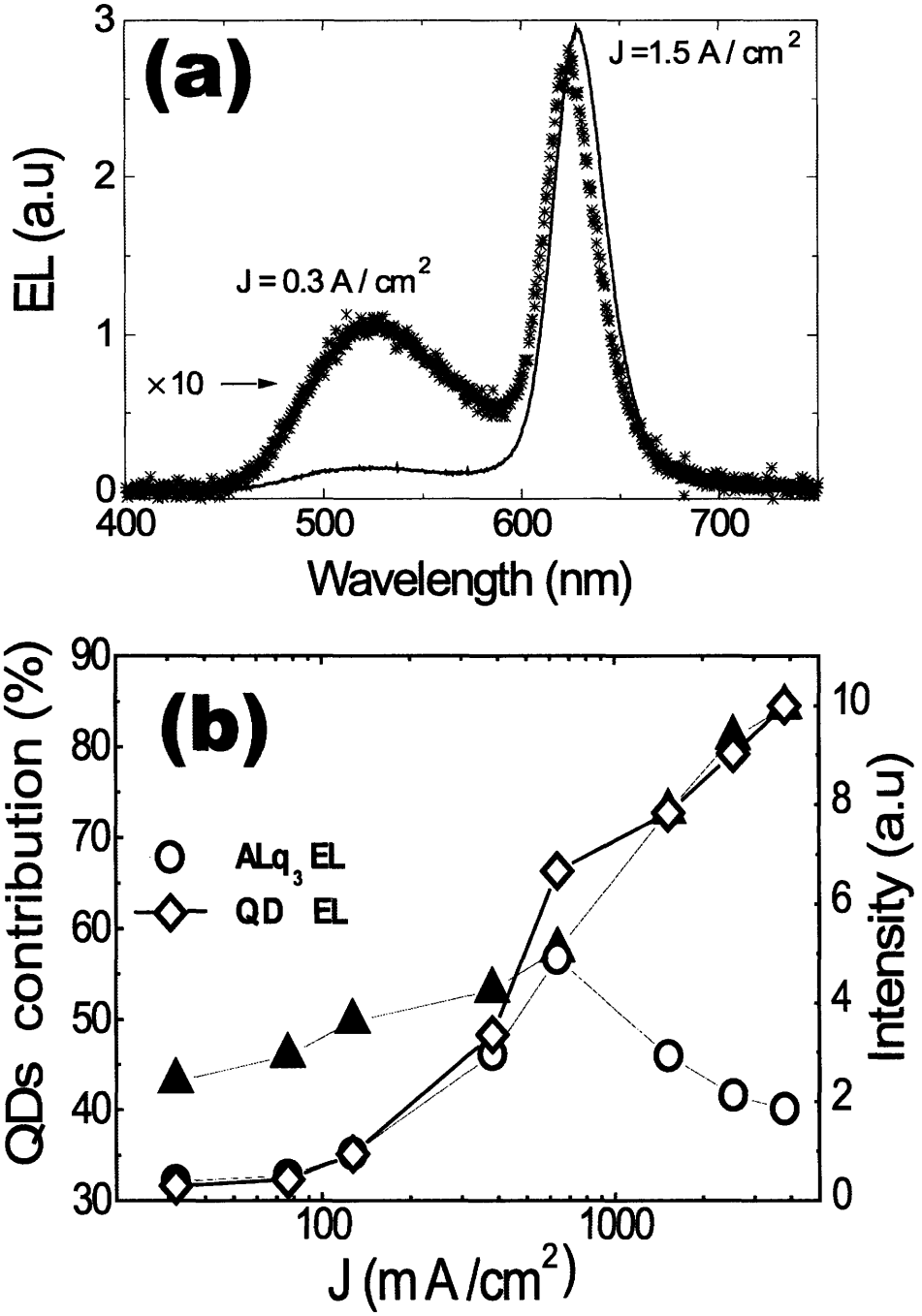

Figure 3.6. (a) EL spectra of a NiO QD-LED at 300 mA/cm2 (stars) and 1500 mA/cm^2 (solid line) using a film with a resistivity of 10^{-2} Ω·cm. (b) Contribution (solid triangles) of the QD electroluminescence to the EL spectrum versus current density (solid triangles). Integrated areas below the Alq_3 (open circles) and QD (open diamonds) emission peaks as a function of the current density. [1]

Figure 3.6 illustrates the negative impact of low resistance NiO (10^{-2} Ω·cm) on the QD-LED EL spectrum for the second set of devices. In contrast to the device in Figure 3.5, in Figure 3.6 nearly 50 % of the detected EL comes from the Alq_3 layer for current densities lower than 300 mA/cm^2 (star symbols in Figure 3.6a). This effect is attributed to (i) the imbalance of electron and hole injection at QD site due to the highly doped NiO thin films, which decreases the exciton density per QD and (ii) the quenching of the QD layer EL by the free hole in NiO via energy transfer. Additionally, numerous studies on the pholuminescence intermittency of single CdSe QDs[32-35] and charging[36] of self-assembled CdSe QD films have shown that a charged QD (i.e. a QD with an excess of hole or electron) is non-emissive, because of ultrafast (~ 100 ps) non-radiative Auger relaxation[32,36-38] processes. Furthermore, the increased hole injection shifts the exciton recombination region into the Alq_3 layer, which leads to more emission from the organic layer. At 1.5 A/cm^2 (solid line in Figure 3.6a) 85 % of the EL originates from the QDs. The increase in the QD spectral contribution with current is attributed to a reduction in the imbalance of charge carrier densities in the device combined with the 60 % decrease in the Alq_3 emission from 600 mA/cm^2 to 3000 mA/cm^2. In Figure 3.6b the open-circles and -diamonds illustrate the evolution of the integrated areas below the Alq_3 and QD EL peaks, respectively. As a consequence of the quenching and the charge imbalance, the EQE was $< 10^{-3}$ % for most of the devices of the second set.

3.2.4 Using NiO as a Stable Substrate for Deposition

Whereas QD-OLEDs fabrication was limited to the use of either phase separation or micro-contact printing techniques to create the QD monolayer, having NiO as the HTL enables the use of new deposition techniques that were incompatible with an organic HTL. As shown above, spin-casting QDs out of chloroform enables the production of fairly efficient QD-LEDs at 0.18%. However, NiO can also enable the use of more sophisticated deposition techniques including inkjet printing and Langmuir-Blodgett deposition (Figure 3.7).

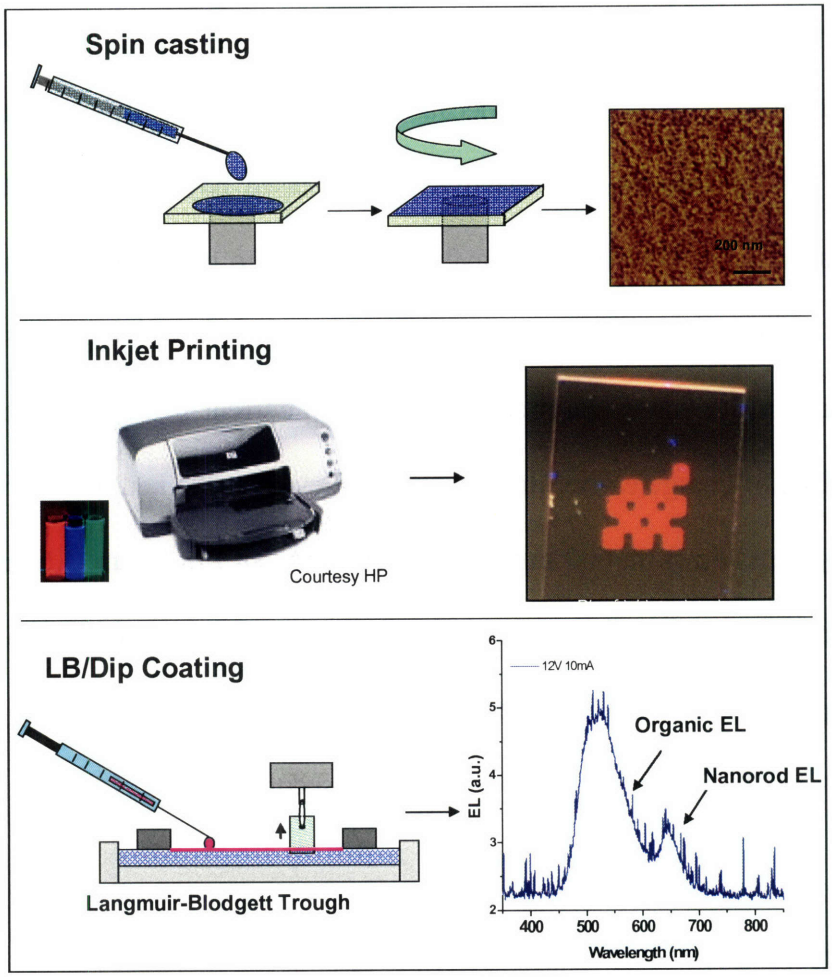

Figure 3.7: Several deposition techniques for the production of QD-LEDs that are enabled by the use of NiO as a hole transport layer. They include: (top) spin-casting, shown in a diagram with an AFM of QDs spin-cast onto NiO. (center) Inkjet printing is illustrated with a photo of an

inkjet printer (actually performed using a prototype HP "drop on demand" printhead) and a photo of an inkjet printed film of CdSe/ZnS nanorods. (bottom) A diagram of a Langmuir trough used to produce a film of CdSe/ZnS nanorods which are then Langmuir-Schaeffer transferred to a NiO coated substrate to produce an ITO/NiO/NC/Alq3/Ag:Mg/Ag LED. The device EL shows a large organic contribution, due to inconsistent monolayer deposition and some quenching of the NRs from contact with the subphase. However there is a distinct NR EL peak present, making this the first Langmuir-Schaeffer produced QD-LED.

3.3 A Fully Inorganic Device

Having successfully replaced the organic HTL in the QD-OLED design, the next step was to replace the organic ETL material, typically Alq_3, with inorganic films. As before, the required material needs to be i) a wide band-gap semiconductor with ii) tunable conductivity and controlled film morphology but now iii) must also be able to be deposited onto the QD surface without chemically or thermally degrading the QDs. This presents an additional challenge in that the QDs are sensitive enough to heat and oxidation that exposure to plasma, heat or charged oxygen during the deposition is enough to quench the luminescence. The electronic band structure of the constituent layers are shown in Figure 3.8.

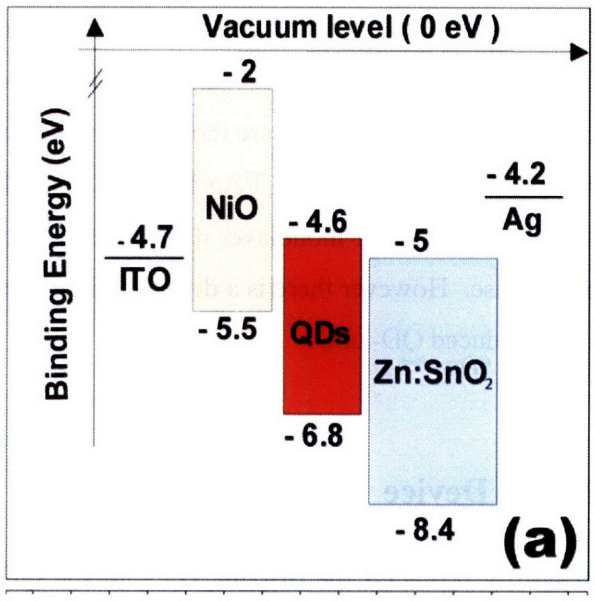

Figure 3.8: (a) An energy band diagram of the constituent QD-ILED layers.

The films that formed the QD-LED charge transport layers also needed to be mechanically smooth and compositionally amorphous to prevent formation of preferred current channels through the film, as this can cause shorting of the device.

3.3.1 All-inorganic Device Fabrication

Fabrication of the device was accomplished using cleaned glass substrates that were then patterned with a 60 nm thick ITO anode deposited via RF sputtering in an inert Ar environment at a rate of 0.06 Å/s. Heating of the substrate during deposition allowed control of the ITO resistivity and contributed to film smoothness. Any mechanical roughness of the ITO electrode was seen to propagate as roughness in the HTL overlayer. As with the NiO/organic devices [1] in Section 3.2, the HTL of the all-inorganic QD-LED is a 20 nm thick layer of resistive p-type NiO, sputtered onto the ITO at a deposition rate of 0.2 Å/s in a 1:100 O_2 to Ar atmosphere at 6 mTorr pressure and using 200 W of

RF power. As before, the oxygen concentration in the plasma during sputtering determines the concentration of carriers and, therefore, the resistivity of the NiO [39,40], which is 5 Ω·cm for the above sputtering conditions. AFM characterizations of the NiO layer on top of the ITO electrodes reveal a root mean square roughness of less than 0.5 nm, which enables deposition of monolayers of self-assembled QDs onto the NiO. This marks a significant improvement over the previous efforts [1], where surface roughness prevented QD monolayer formation and often led to short circuits, low device yield, and limited efficiency.

3.3.2 ZnCdSe Tertiary II-VI Quantum Dots

The luminescent layer of these inorganic/QD hybrid LEDs consists of ZnCdSe alloyed QDs with colloidal solution photoluminescence quantum yields of 40-60%, an emission peak at $\lambda = 638$nm, and a full width at half-maximum (FWHM) of 40 nm. ZnCdSe was chosen as a material because it was possible to quickly and easily scale up the procedure to create the large quantities of QDs needed to spin coat four monolayer thick films. Furthermore, the size and high QY of the material should decrease the prospect of Auger decay and non-radiative decay of excitons, respectively. Finally, the lack of a significant ZnS tunneling barrier, as found in Type I core/shell QDs, was expected to improve the chances of direct charge injection. In a device where the HTL and ETL do not appear to form radiative electron-hole pairs, FRET appears to be an unlikely mechanism of forming excitons on the QDs and hence the system must be designed around a charge injection model.

Building upon work by Zhong *et al.* [41,42], the colloidal QDs were synthesized by injecting trioctylphosphine selenide into a pot of ZnO, CdO, oleic acid, and 1-octadecene at 310°C. The ZnCdSe QDs were precipitated twice with acetone and redispersed in chloroform. This solution was then spin-coated in a nitrogen atmosphere onto the NiO substrate so as to form about three to four close-packed monolayers in a 30 ± 5 nm thick film. The highest electroluminescence efficiencies were measured for QD-LEDs containing ZnCdSe QDs, however devices containing CdSe/ZnS QD lumophores showed comparable efficiencies, within an order of magnitude. Thus the choice of lumophore seems irrelevant in for red emitting devices, probably because the band levels of the ZnCdSe and CdSe/ZnS are fairly similar. Attempts to make green and blue devices using ZnSe/CdSe/ZnS and ZnCdS/ZnS in this device structure were wholly unsuccessful and the devices failed to emit.

Pot (310°C)				Injection (r.t.)			
Oleic Acid	ODE	ZnO	CdO	TOPSe (1.5M)	TOP	Cook at 310°C for	Emission Peak (1 hr)
2.5 ml	10 ml	64 mg	24 mg	3.0ml	0.0ml	2 hrs	565nm
2.5 ml	10 ml	64 mg	24 mg	3.0ml	0.0ml	30 min	576nm
2.5 ml	10 ml	64 mg	24 mg	3.0ml	0.0ml	14 min	588nm
2.5 ml	10 ml	64 mg	16 mg	1.0ml	2.0ml	30 min	616nm
2.5ml	10 ml	64 mg	24 mg	0.5ml	2.5ml	25 min	632nm
2.5 ml	10 ml	64 mg	32 mg	0.5ml	2.5ml	15 min	647nm

Figure 3.9: A chart detailing the experimental conditions used to produce ZnCdSe emitters at various wavelengths.

The ZnCdSe QD's are tunable, according to reaction conditions during their synthesis. The full range of emission wavelengths from 550-680 nm could be produced by altering the reaction parameters, as shown in Figure 3.9. The resulting nanocrystals had quantum yields of > 50% after two precipitation steps and formed ideal monolayer films when stamped onto a TPD surface (Figure 3.10d). Absorption features tended to be more broad than CdSe/ZnS, with a typical emission FWHM of ~30-34 nm. It is likely that this is due to both a distribution of sizes and relative concentrations of Zn and Cd in each particle. Together, these two distributions account for the wider emission peak. Particle sizes ranged from 6-10 nm in diameter, somewhat larger than standard CdSe cores.

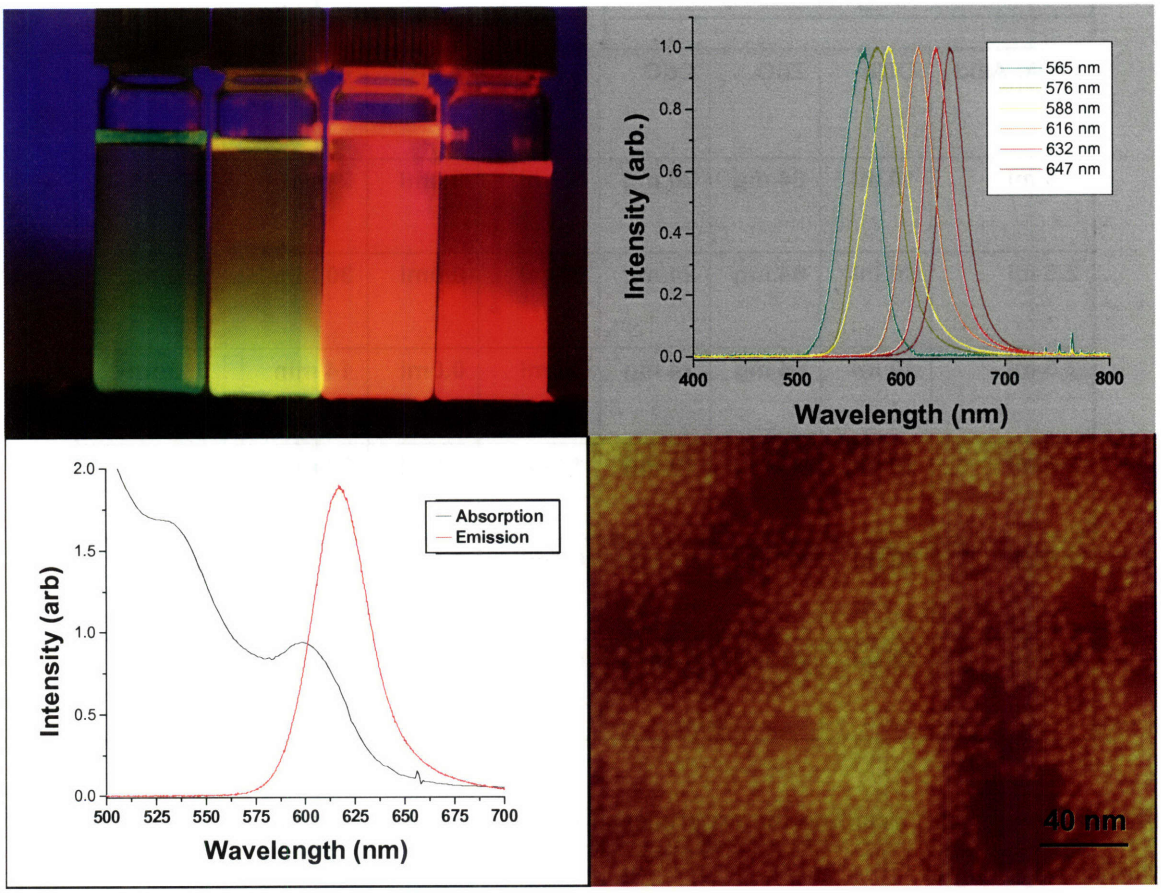

Figure 3.10: ZnCdSe QDs of varying emission wavelengths in vials excited by a 365 nm UV lamp in photos (top left), and spectra (top right). A single sample of ~620 nm emitting ZnCdSe QDs absorption and emission spectra (bottom left) and an atomic force micrograph of this sample micro-contact printed onto a spiro-TPD coated ITO/glass surface (bottom right).

The reaction dynamics for this system are somewhat different from those of CdSe cores. The band gap for ZnCdSe is a function both of the size and of the concentration of Zn versus that of Cd in each particle. Thus by correctly varying the initial conditions, particles of equivalent size could be produced with different band gaps, making ZnCdSe both size and composition tunable. As can be seen in Figure 3.9 and Figure 3.10, increasing the amount of Cd in the initial pot tended to increase the wavelength of

emission. This is expected since the conduction and valence band levels can be approximated as a contribution from ZnSe band levels and CdSe band levels. And unlike in CdSe cores, where increased time at growth temperatures produced redder particles, these particles tend to blueshift after 15 minutes. This is caused by the slower reaction of the Zn-oleate than Cd-oleate. At first, the CdSe grows with only slight amounts of Zn in the crystal. After five minutes, most of the Cd has reacted and the Zn and Se precursors begin to overcoat the particles, increasing the quantum yield. After five more minutes, Zn begins to be incorporated into the crystal lattice, raising the band gap even as the particle seems to grow. After a long time at high temperature, large amounts of Zn are able to diffuse throughout the nanocrystal producing nanocrystals that are greatly blueshifted from their emission after fifteen minutes of growth (Figure 3.9, first three experiments).

Although they are bright and tunable across a fairly large range, these particles tend to degrade over time when exposed to oxygen. Although redder particles were more resistant to oxidation, all ZnCdSe particles synthesized lost quantum yield within just a few minutes of exposure to air (in hexane solution), as seen in Figure 3.11.

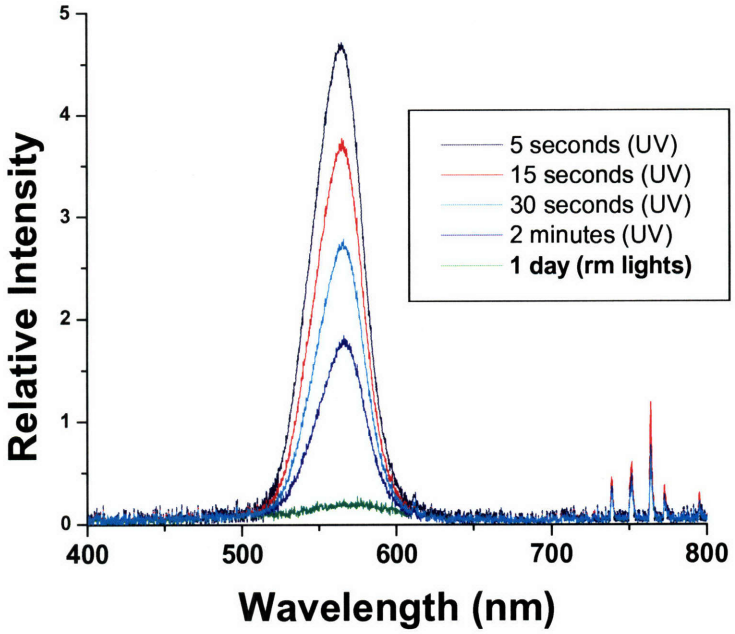

Figure 3.11: A sample of yellow emitting ZnCdSe quantum dots excited with a 365 nm UV lamp upon exposure to air. The emission intensity is clearly decreasing in a short period of time.

This feature of the ZnCdSe limits their use to air-free applications. Fortunately the QD films in the QD-LEDs were produced in a nitrogen environment and the ZnCdSe films appeared to be more stable in close-packed films than in solution. Thus QD films used in the QD-ILED devices were found to largely retain their luminescence over several days.

3.3.3 Incorporating ZnCdSe into QD-OLEDs

Having successfully synthesized ZnCdSe particles as an efficient means of producing bright, red emitters in large quantity, ZnCdSe QDs were used in a QD-OLED structure to compare them to CdSe/ZnS. These devices performed almost identically to

standard CdSe/ZnS OLED devices, with a slightly lower turn-on voltage. This could be due to the lack of a resistive ZnS overcoating layer on the particles, allowing more facile charge injection with less of a tunneling barrier. From the results in Figure 3.12, it seems clear that ZnCdSe could be used almost interchangeably with CdSe/ZnS.

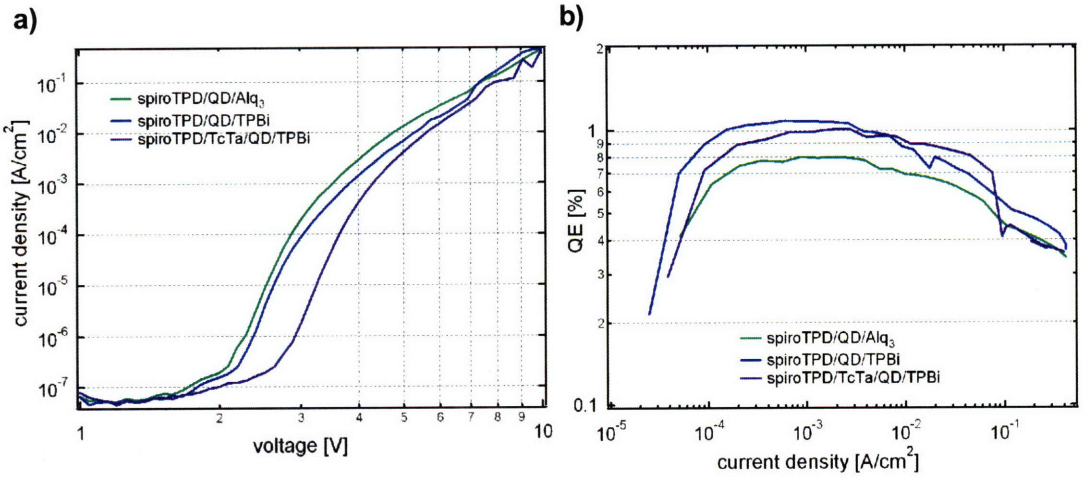

Figure 3.12: Performance characteristics for a series of devices using ZnCdSe QDs as the active layer in the standard QD-OLED structure, ITO/HTL/QD monolayer/ETL/Ag:Mg, described in Chapter 2. Devices were constructed using spiro-TPD/QDs/Alq_3 (green), spiro-TPD/QDs/TPBi (blue), and spiro-TPD/TcTa/QDs/Alq_3 (purple). 4,4',4''-tris(*N*-carbazolyl)-triphenylamine (TcTa) serves as an electron blocking layer [43]. The IV curves (a) and EQEs (b) are comparable to devices constructed using standard CdSe/ZnS QDs with EQEs of 0.7 %-1.0 % with a turn-on voltage ~2.5 V for the devices without TcTa and ~3.0 V for those with. Emission from the device (not shown) was primarily from the QD peak (as in PL, in Figure 3.15, bottom left) with no observed organic emission.

3.3.4 Using SnO_2:ZnO as the Electron Transport Layer

For the electron transport layer (ETL), we selected a 50 nm thick, optically transparent film of alloyed ZnO and SnO_2, with resistivity of 10 Ω·cm. The ZnO:SnO_2 film is both chemically and mechanically stable, and energy alignment of its conduction

band level allows injection of electrons into the ZnCdSe conduction band. Whereas pure SnO_2 films tended to be polycrystalline with pronounced grain boundaries, AFM and X-ray diffraction measurements reveal that ZnO:SnO_2 films are relatively smooth (with less than 0.5 nm rms roughness) and amorphous, reducing the likelihood of morphologically-induced electrical shorts in the device. Since the ZnO to SnO_2 ratio determines the film conductivity, the excess oxygen is not needed in the sputtering process as in the NiO case. The O_2 plasma can easily oxidize the organic ligands capping the QDs and produce trap sites that facilitate non-radiative recombination of QD excitons.

The ETL was deposited by simultaneously sputtering ZnO at 15 W RF power and SnO_2 at 9 W RF power in a pure argon environment at 5 mT pressure, corresponding to a combined deposition rate of 0.1 Å/s. In this process ZnO:SnO_2 is sputtered directly onto the QD layer with some damage to the underlying QDs, where for NiO/QD/ZnO:SnO_2 structures I measured a 40% drop in UV-excited QD photoluminescence intensity as a result of the sputtering process.

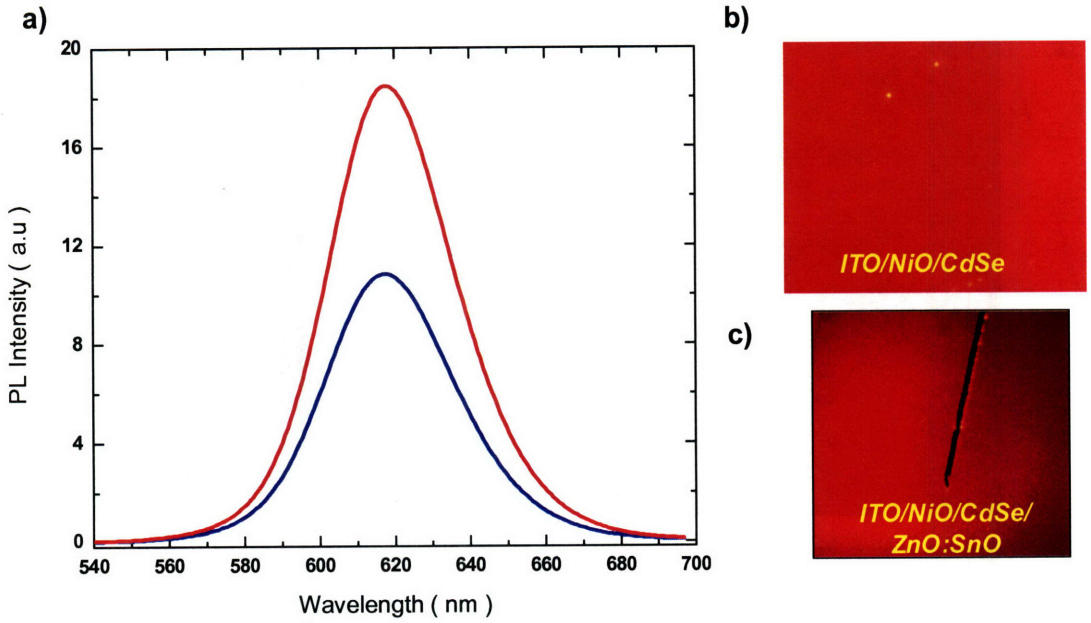

Figure 3.13: PL characteristics of ZnCdSe films in the QD-ILED device. a) PL spectra of the ITO/NiO/QD films before (red) and after (blue) sputtering 50 nm of ZnO:SnO onto the QD film. As can be seen in a microscope photos, using identical integration time and gain settings (b-c), the film loses about 40% of its PL after sputtering (c). The final layer (c) is scratched for comparison to the background ITO/glass.

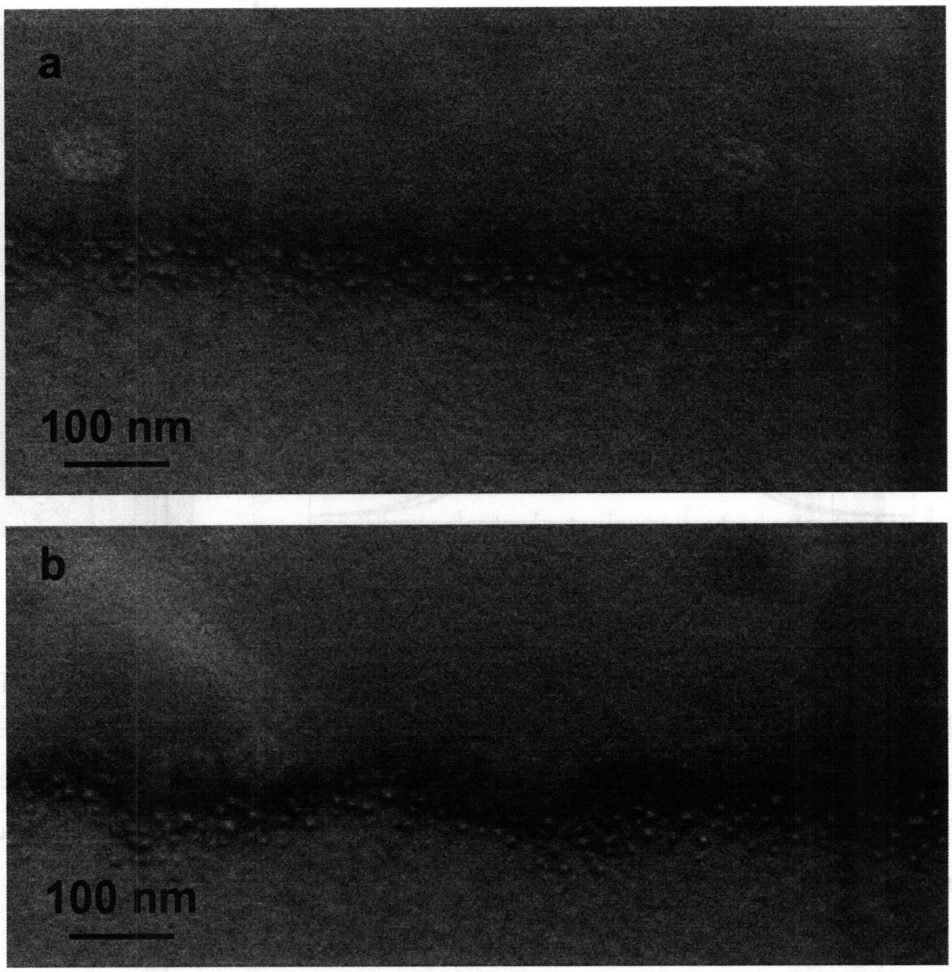

Figure 3.14: A scanning electron micrograph of a QD-ILED at the device junction of the NiO/ZnCdSe/SnO_2:ZnO. The QDs are clearly visible in the center of the device as round ~10 nm nanoparticles. The device junctions can be smooth as in (a) but as often as not have irregular borders (b). This is generally a feature of the film morphology at a particular location on the glass chip, as well as a function of the speed of the sputtering process. If material from the ETL goes on too quickly it can form spikes through the QD layer and short the device. Because the device process is very sensitive to minor surface fluctuations, shorting occurs in roughly 70% of pixels.

This indicates that sputtering the ETL on the QDs still largely preserves their passivating ligands and that radiative recombination of excitons inside the QDs is competitive with the PL quenching of excitons by the free carriers in the ETL and HTL.

The inorganic/QD hybrid structure is completed by thermally evaporating a 40nm thick silver cathode onto the ZnO:SnO_2 at a rate of 1.5 Å/s to allow for electron injection into the conduction band of the ZnO:SnO_2 layer.

3.3.5 All-inorganic Device Analysis

All our devices were tested in air over several days without packaging. Figure 1b shows a typical forward biased current-density-voltage (*J-V*) characteristic of the QD-LED described above, which was recorded using a computer controlled Keithley 2612 current/voltage source-meter.

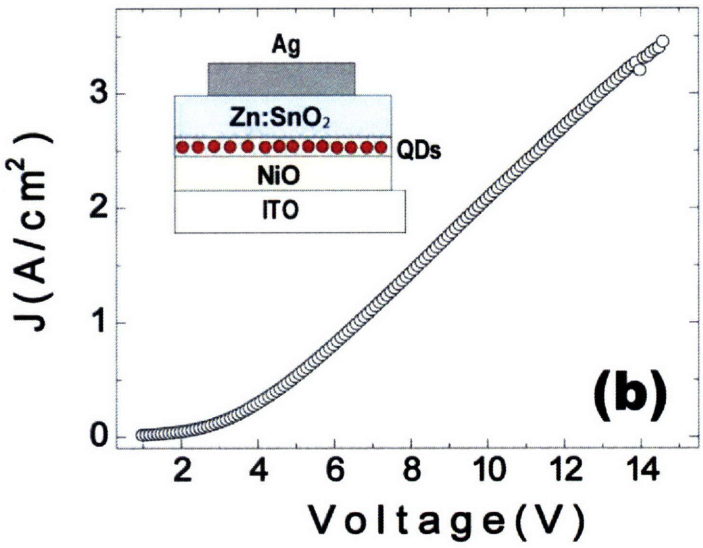

Figure 3.15: The I-V curve for the QD-ILED device under forward bias is shown along with a schematic of the structure of the device showing the heterostructure composed of the ITO anode, the p-doped NiO HTL, the QD active luminescent layer, and the ZnO:SnO_2 ETL.

Below 5 V applied bias a mean least square fit leads to a current density $J(V) = a + b\times \exp(\alpha V)$, with $\alpha = 0.8\ V^{-1}$. Above 5.5 V we find a linear conduction regime where J(V)

$= c + \beta \times V$ with $\beta = 0.3\ \Omega^{-1}\cdot cm^{-2}$, which gives a calculated device resistance in the range of 300 Ω to 500 Ω, using an effective device area of 0.012 cm^2. The initial exponential rise is likely due to the efficiency of tunneling/transport through the QD layer and by potential barriers for charge injection at the NiO/QD and ZnO:SnO_2/QD interfaces. Above 5.5 V the conduction is limited by the drift of carriers inside the thin QD multilayer. The linear regime indicates that the electron and hole mobilities are independent of voltage above 5.5 V. This regime can be reached when the tunneling rate of electrons from QD to QD becomes field independent, i.e. the displacements of the conduction and valence bands by the applied electric field are such that electron tunneling takes place with no significant energy barrier to overcome. A similar linear conduction regime was reported in photoconductivity measurements of CdSe QD films [26,27]. In devices where the CdSe/ZnS core-shell QDs were used, we observed the trap-assisted space charge limited conduction mechanism that was previously observed in neat CdSe/ZnS films [26] and QD-OLEDs [2,4,26]. The absence of the ZnS QD shell, which decreases the tunneling distance for injected charges, is at the origin of the difference in the *I-V* behavior.

The QD-LEDs are able to sustain current densities of up to 3.5 A /cm^2, which corresponds to a carrier injection rate of $\phi = 6x10^7$ carriers per second per QD and a maximum exciton (hole + electron) density per QD of 0.2, using a QD lifetime of 5 ns in a close-packed film, and assuming equal hole and electron currents [44]. It should be noted that the gain threshold for QDs is ~1.5 excitons per QD [45].

Figure 3.16 illustrates the evolution of the electroluminescence (EL) spectrum as a function of voltage. The spectral data was taken with an Ocean Optics spectrometer.

The turn-on voltage, at which EL is detected, is 5.5V. At 9 V there is a clearly observable characteristic QD EL peak centered at wavelength λ = 642 nm with a FWHM of 38 nm.

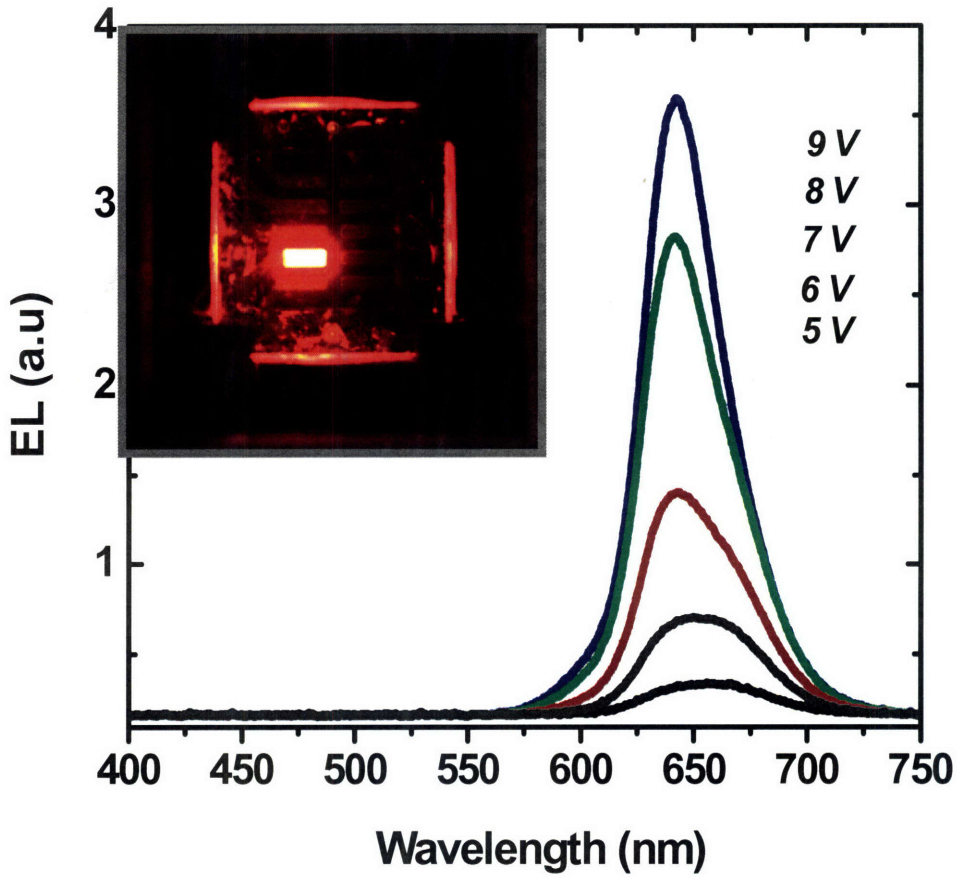

Figure 3.16: Increasing relative intensity of a series of EL spectra of the QD-ILED device, shown in Figure 1, with the increasing applied voltage from 5V to 9V. The inset shows a photograph of a bright and uniform pixel.

Excitons are formed in the QD layer when holes and electrons are injected into the valence and conduction bands of the QDs, respectively. The electrons and holes then

recombine across the QD band gap with the emission spectrum characteristic of the QDs in solution. The electroluminescence efficiency of the devices is strongly dependent on the carrier concentration in the HTL and ETL, which is controlled by film doping. The resistivities of the NiO and $ZnO:SnO_2$ layers must be adjusted so that carriers recombine in the active QD region and not in the charge transport layers. For the most efficient operation, a balance of electron and hole injection into the QD layer is desirable. If the charge injection is not in balance, the preponderance of one type of carrier in the QD

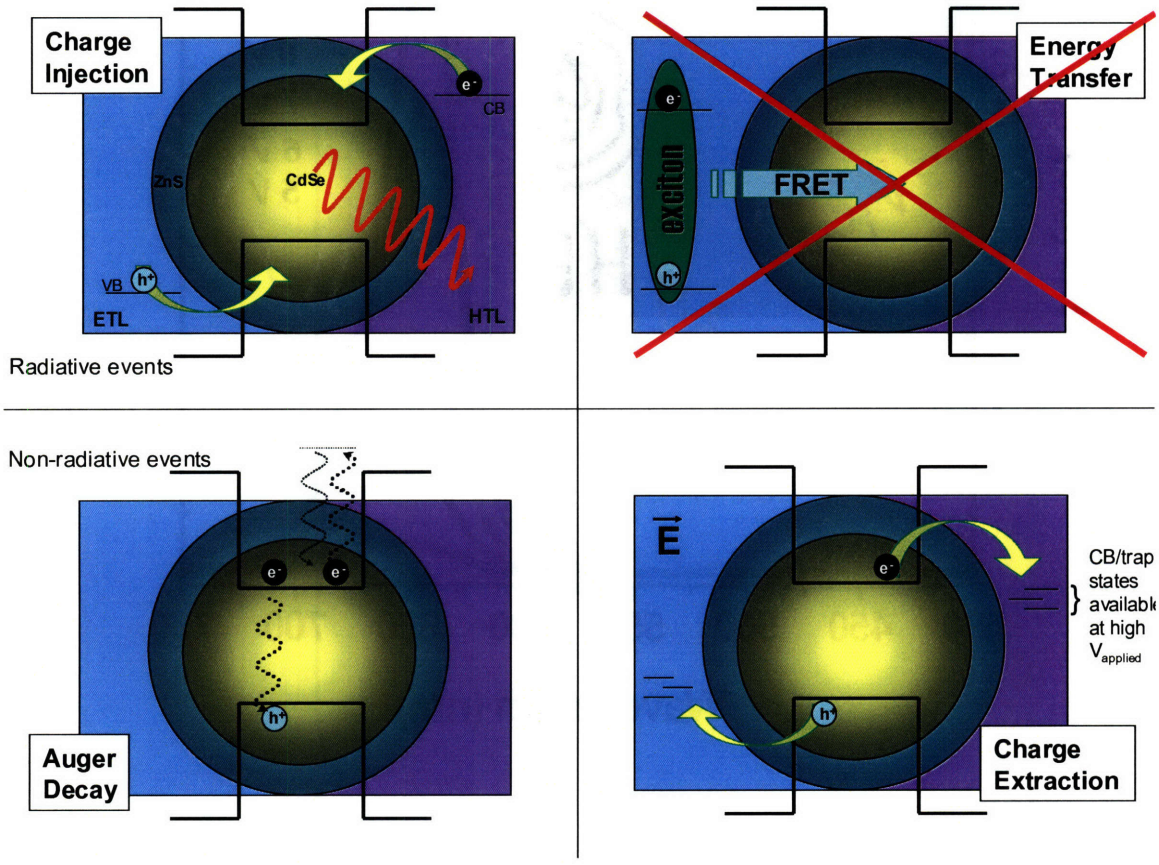

Figure 3.17: A schematic diagram of the mechanisms of exciton formation on the QD and either radiatively or non-radiatively decay, or are separated into charges. This diagram is a refrain to Figure 1.11, in which FRET is in fact a major component [47] of the QD-OLED operating mechanism .

region will result in QD charging and Auger decay [46], thus decreasing the electroluminescence efficiency [1,11]

Figure 3.18 shows EQE as a function of current density, which reaches the maximum of 0.1 %, almost two orders of magnitude higher than previous reports of devices embedding QDs between doped inorganic transport layers [48].

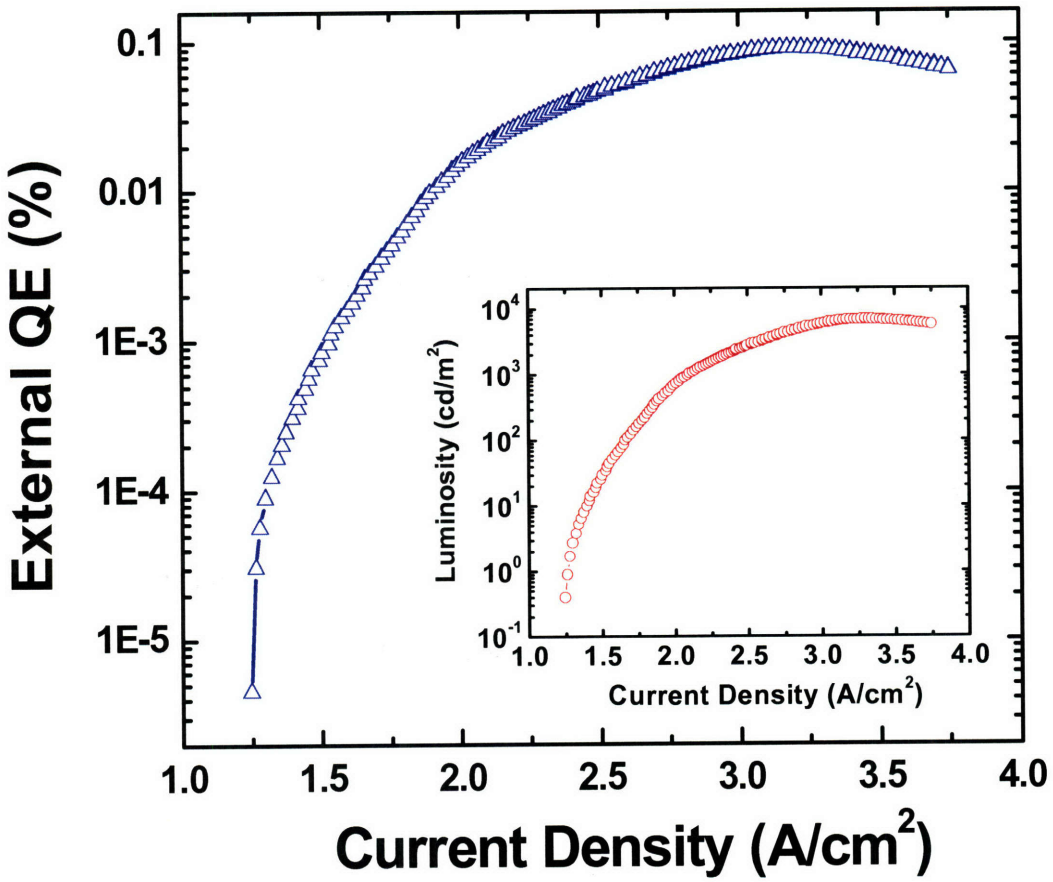

Figure 3.18: QD-ILED external quantum efficiency (EQE) as a function of current density. Maximum EQE for this device is 0.09%. The inset shows that a maximum luminance of 7000 Cd/m^2 is reached at 3.2 A/cm^2, which corresponds to 0.2 cd/A.

Furthermore, this device has bright, uniform pixels even at low voltage as shown in the inset of Figure 3.16. The luminosity is measured to be 1950 cd/m^2 at current density of 3.5 A/cm^2. Comparable brightness was observed when the devices were tested after being stored in air for four days, in contrast to unpackaged organic QD-LEDs that can not withstand prolonged atmospheric exposure [49].

Two competing mechanisms are potentially responsible for QD exciton formation in these devices (Figure 3.17). The first mechanism is direct charge injection from the transport layer, and the second is energy transfer from the weakly bound Wannier excitons that are formed in the transport layers. Time resolved measurements taken with a 10 ps resolution streak camera show no PL emission from 50 nm thick NiO and ZnO:SnO_2 thin films that were grown with the same deposition parameters as for the devices presented here, and that were excited with 100 fs long and λ = 400 nm optical pulses generated by a Titanium-Sapphire regenerative laser amplifier. This indicates that ultrafast (faster than 10 ps) non-radiative processes dominate exciton relaxation in the inorganic transport layers. This leads to the conclusion that the dominant mechanism for generating electroluminescence in our inorganic/QD hybrid LEDs is direct charge injection into the QD layer. The exciton creation rates in the QD layer may, in fact, compete with non-radiative processes, such as the Auger decay, that have to be overcome to achieve biexciton lasing in colloidal QD films [45,46]. Considering the biexciton lifetime of 1.3 ns [50] to 0.3 ns [51] (8×10^8 Hz to 3×10^9 Hz) for these CdZnSe QDs, our QD-LED average maximum carrier injection rate of $\phi = 6\times10^7$ electrons per second per QD, at ~13 V and 3.5 A/cm^2, is still 10 to 50 times slower than needed for gain to occur (or ASE in a cavity). In addition, AC-voltage measurements show that the response cut-off frequency

of our devices is 10 MHz, on average. The instantaneous carrier injection rate per QD should be increased by driving the QD-LEDs with a series of square wave pulses of high intensity and short duration to limit device heating and enable high instantaneous current density. In such high current measurements additional optical absorption due to high carrier density in QD layers might necessitate further increase in drive currents, emphasizing the need for robust inorganic/QD hybrid devices as the first step towards the demonstration of electrically pumped colloidal QD lasers.

3.4 Summary

These efforts have demonstrated that semiconducting metal oxides and colloidal QDs can be combined in fabrication of bright monochrome LEDs with uniform pixel emission of saturated color and high peak luminance. Although the electroluminescence efficiency of the presented devices is an order of magnitude lower than that of the best hybrid organic QD-LEDs, the inorganic/QD hybrid's maximum brightness, of 1950 cd/m^2, a significant improvement on previously reported QD-ILEDs. As such, the QD-ILED presented here represents an important step in achieving robust large-area-processable LEDs for a variety of applications. Furthermore, with demonstrated high QD-LED carrier injection rates that are approaching the biexciton Auger relaxation rates in colloidal QD systems, we can begin considering QD-LED designs and operating modes that will be needed to demonstrate electrically pumped colloidal QD lasers. Such lasing devices would be able to take full advantage of the tunability and the ease of fabrication and processing of colloidal QDs to provide simple, tunable, coherent light sources.

My collaborators for the work presented in this chapter were Jean-Michel Caruge in the Bawendi group, who did the bulk of the device processing, and Vanessa Wood from the Bulovic group, who contributed the smoothed ITO films. I'd also like to thank Gerry Chen who performed the inkjet printing.

3.5 References

(1) Caruge, J.-M.; Halpert, J. E.; Bulovic, V.; Bawendi, M. *Nano Lett.* **2006**, *6*, 2991-2994.

(2) Coe, S.; Woo, W. K.; Bawendi, M.; Bulovic, V. *Nature* **2002**, *420*, 800-803.

(3) Coe-Sullivan, S.; Steckel, J. S.; Woo, W.-K.; Bawendi, M.; Bulovic, V. *Adv. Funct. Mater.* **2005**, *15*, 1117-1124.

(4) Coe-Sullivan, S.; Woo, W. K.; Steckel, J. S.; Bawendi, M.; Bulovic, V. *Organic Electronics* **2003**, *4*, 123-130.

(5) Schlamp, M.; Peng, X.; Alivisatos, A. P. *J. Appl. Phys.* **1997**, *82*, 5837.

(6) Steckel, J.; Zimmer, J.; Coe-Sullivan, S.; Stott, N.; Bulovic, V.; Bawendi, M. *Angewandte Chemie International Edition* **2004**, *43*, 2154.

(7) Zhao, J.; Bardecker, J. A.; Munro, A. M.; Liu, M. S.; Niu, Y.; Ding, I.-K.; Luo, J.; Chen, B.; Jen, A. K.-Y.; Ginger, D. S. *Nano Lett.* **2006**, *6*, 463.

(8) Mueller, A. H.; Petruska, M. A.; Achermann, M.; Werder, D. J.; Akhadov, E. A.; Koleske, D. D.; Hoffbauer, M. A.; Klimov, V. I. *Nano Lett.* **2005**, *5*, 1039-1044.

(9) Colvin, V. L.; Schlamp, M. C.; Alivisatos, A. P. *Nature* **1994**, *265*, 373.

(10) Hikmet, R. A. M.; Talapin, D. V.; Weller, H. *J. Appl. Phys.* **2003**, *93*, 3509.

(11) Caruge, J.-M.; Halpert, J. E.; Wood, V.; Bulovic, V.; Bawendi, M. G. *Nature Photonics* **2008**, *2*, 247-250.

(12) Grundmann, M.; Heinrichsdorff, F.; Ribbat, C.; Mao, M.-H.; Bimberg, D. *Appl. Phys. B* **1999**, *69*, 413-416.

(13) Ledentsov, N. N.; Ustinov, V. M.; V.A.Shchukin; Kop'ev, P. S.; Alferov, Z. I.; Bimberg, D. *Semiconductors* **1998**, *32*, 343-365.

(14) Arakawa, Y.; Sakaki, H. *Appl. Phys. Lett.* **1982**, *40*, 939.

(15) Asada, M.; Miyamoto, Y.; Suematsu, Y. *IEEE Journal of Quantum Electronics* **1986**, *QE-22*, 1915.

(16) Lott, J. A.; Ledentsov, N. N.; Ustinov, V. M.; Maleev, N. A.; Zhukov, A. E.; Kovsh, A. R.; Maximov, M. V.; Volovik, B. V.; Alferov, Z. I.; Bimberg, D. *Electronics Letters* **2000**, *36*, 1384.

(17) Mirin, R.; Gossard, A.; Bowers, J. *Electronics Letters* **1996**, *32*, 1732.

(18) Yamada, S.; Yoshioka, T.; Miyashita, M.; Urabe, K.; Kitao, M. *J. Appl. Phys.* **1987**, *63*, 2116.

(19) Kitao, S. Y. M. *J. Appl. Phys.* **1988**, *63*, 2116-2119.

(20) Caruge, J.-M.; Halpert, J. E.; Bulovic, V.; Bawendi, M. G. *Nano. Lett.* **2006**, *6*, 2991-2994.

(21) Chance, R. R.; Prock, A.; Silbey, R. *J. Chem. Phys.* **1974**, *60*, 2744

(22) Drexhage, K. H.; Fleck, M.; Khun, H.; Schaffer, F. P.; W. Sperling *Ber. Bunsenges. Phys. Chem.* **1966**, *70*, 1179.

(23) H. Morawitz *Phys. Rev. B* **1969**, *187*, 1792

(24) Kuhn, H.; Mobius, D. *Angew. Chem.* **1971**, *10*, 620.

(25) Larkin, I.; Stockma, M. I.; Achermann, M.; Klimov, V. *Phys. Rev. B* **2004**, *69*, 121403(R).

(26) Jarosz, M. V.; Porter, V. J.; Fisher, B. R.; Kastner, M. A.; Bawendi, M. G. *Physical Review B* **2004**, *70*, 195327.

(27) Leatherdale, C. A.; Kagan, C. R.; Morgan, N. Y.; Empedocles, S. A.; Kastner, M. A.; Bawendi, M. G. *Phys. Rev. B* **2000**, *62*, 2669.

(28) Burrows, P. E.; Forrest, S. R. *Appl. Phys. Lett.* **1994**, *64*, 2285.

(29) Burrows, P. E.; Shen, Z.; Bulovic, V.; McCarty, D. M.; Forrest, S. R.; Cronin, J. E.; Thompson, M. E. *J. Appl. Phys.* **1996**, *79*, 7991.

(30) Kagan, C. R.; Murray, C. B.; Bawendi, M. G. *Phys. Rev. B* **1996**, *54*, 8633.

(31) Kagan, C. R.; Murray, C. B.; Nirmal, M.; Bawendi, M. G. *Phys. Rev. Lett.* **1996**, *76*, 1517.

(32) Krauss, T. D.; Brus, L. E. *Phys. ReV. Lett.* **1999**, *83*, 4840.

(33) Neuhauser, R. G.; Shimizu, K. T.; Woo, W. K.; Empedocles, S. A.; Bawendi, M. G. *Phys. ReV. Lett.* **2000**, *85*, 3301.

(34) Nirmal, M.; Dabbousi, B. O.; Bawendi, M. G.; Macklin, J. J.; Trautman, J. K.; Harris, T. D.; Brus, L. E. *Nature* **1996**, *383*, 802.

(35) Tang, J.; Marcus, R. A. *J. Chem. Phys.* **2005**, *123*, 054704.

(36) Woo, W. K.; Shimizu, K. T.; Jarosz, M. V.; Neuhauser, R. G.; Leatherdale, C. A.; Rubner, M. A.; Bawendi, M. G. *AdV. Mater.* **2002**, *14*, 1071.

(37) Guyot-Sionnest, P.; Wehrenberg, B.; Yu, D. *J. Chem. Phys.* **2005**, *123*, 074709.

(38) Kharchenko, V. A.; J., R. M. *Lumin.* **1996**, *70*, 158.

(39) Yamada, S.; Yoshioka, T.; Miyashita, M.; Urabe, K.; Kitao, M. *J. Appl. Phys.* **1987**, *63*, 2116.

(40) Yoshimura, K.; Miki, T.; Tanemura, S. *Jpn. J. App. Phys.* **1995**, *34*, 2440.

(41) Zhong, X.; Feng, Y.; Knoll, W.; Han, M. *J. Am. Chem. Soc.* **2003**, *125*, 13559.

(42) Zhong, X.; Han, M.; Dong, Z.; White, T. J.; Knoll, W. *JACS* **2003**, *125*, 8589.

(43) Xia, Y.-J.; Lin, J.; Tang, C.; Yin, K.; Zhong, G.-Y.; Ni, G.; Peng, B.; Gan, F.-X.; Huang, W. *J. Phys. D: Appl. Phys.* **2006**, *39*, 4987-4991.

(44) Given a QD radius of 4nm and a ligand length of 1nm, this calculation uses the current density and QD cross sectional area to find the current density per QD in a hexagonally close packed film. This assumes that all charge carriers flow through the QD and not the ligands bounding it.

(45) Klimov, V. I.; Bawendi, M. G. *Science* **2000**, *290*, 314-317.

(46) Klimov, V. I.; Mikhailovsky, A. A.; McBranch, D. W.; Bawendi, M. G. *Science* **2000**, *287*, 1011-1013.

(47) Anikeeva, P. O.; Madigan, C. F.; Halpert, J. E.; Bawendi, M. G.; Bulović, V. *Phys. Rev. B* **2008**, *Submitted.*

(48) Mueller, A. H.; Petruska, M. A.; Achermann, M.; Werder, D. J.; Akhadov, E. A.; Koleske, D. D.; Hoffbauer, M. A.; Klimov, V. I. *Nano Lett.* **2005**, *5*, 1039.

(49) Popovic, Z. D.; al, e. *Synthetic Metals* **2000**, *111*, 229-232.

(50) Biexciton lifetimes in ZnCdSe found by time resolved measurements using the 400 nm band of a pulsed Titanium:Saphire laser and a streak camera with 10 ps

resolution. PL decay curves were fit with an exponential function by varying parameters to find the lifetime.

(51) Fisher, B. R.; Caruge, J.-M.; Chan, Y. T.; Halpert, J. E.; Bawendi, M. G. *Chemical Physics* **2005**, *318*, 71-81.

Chapter 4

Synthesis and Application of CdSe/CdTe Nanobarbells

4.1 Introduction and Motivation

Nanocrystals (NC) have been employed as photoconductors in numerous previous works [1-7]. Generally these nanocrystals have been used as the active absorbing material in thick close-packed films in either sandwich [1,2,8] or parallel device structures [3-6,9]. CdSe[8], CdTe[6], PbS[7] and PbSe[10] cores have all served as active functional materials. However, solar cells produced from these materials have generally suffered from low power efficiencies [1,11], without sintering [2]. One of the likely causes of this has been the difficulty of transmitting charges from the absorbing NCs, through the film and to the electrode. This difficulty is compounded by the fact that NC films usually conduct one charge much better than the other. The solution, described in this chapter, has been to use heterostructured nanocrystals that can both absorb, and also separate, the exciton into spatially separated conduction bands. From these bands they can percolate out of the film by hopping between nearest neighbors. The challenge described here was both to synthesize a useful heterostructured material and to incorporate that material into a device structure able to take advantage of the heterostructured NC's unique composition.

4.1.1 Synthesizing Heterostructures to Achieve Conduction and Charge Separation

Considerable research has focused on the synthesis, shape control and physics of heterostructured nanocrystals. Non core-shell heterostructures using Group II-VI nanocrystals, such as CdSe, have been of particular interest [12-14]. For example, CdSe rods have been used to nucleate the growth of gold nanocrystals (dots) onto one or both ends. These CdSe/Au nanobarbells (NBs) have shown unique physical properties relating to the interaction between the two materials [12]. The method of their synthesis suggests that it may be possible to nucleate many other types of materials on the tips of semiconductor nanorods.

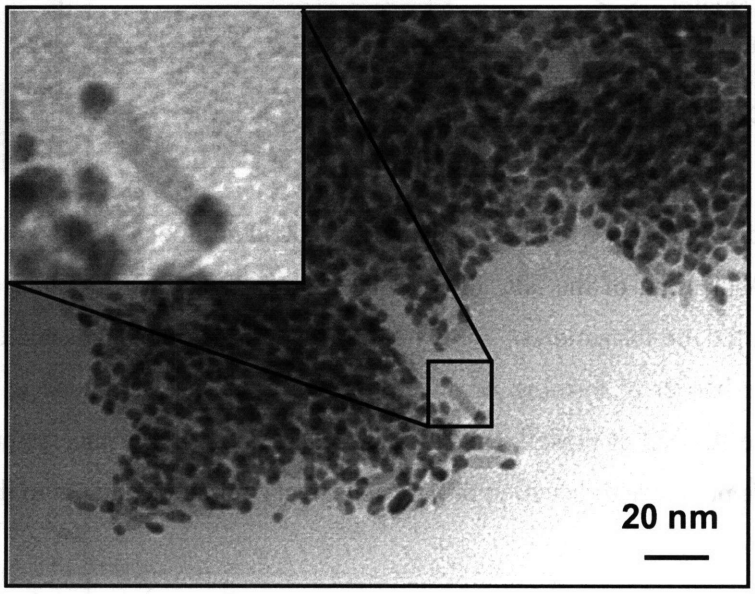

Figure 4.1: A TEM image of Au tipped CdSe nanorods, produced using a preparation reported by Banin et al. [14] NCs were produced by the slow addition of Au NC precursors at temperatures below the Au NC nucleation temperature [14]. This work served as a model for the synthesis of CdSe/CdTe NBs.

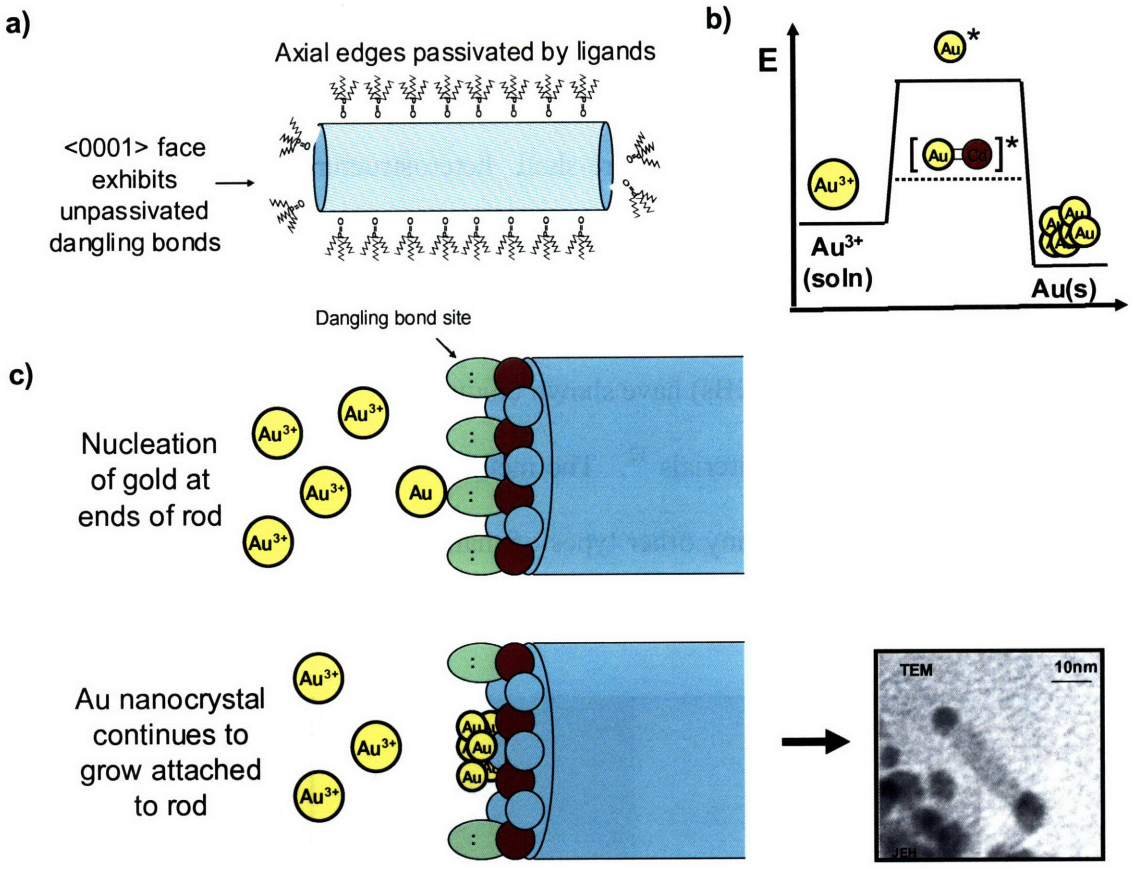

Figure 4.2: A diagram of the reaction dynamics of the addition of Au NCs to the tips of a CdSe nanorod. a) A diagram of the NR, illustrating the greater reactivity of the end facets. b) an energy diagram for the formation of Au-Cd bonds that allow subsequent nucleation of Au sites. By lowering the barrier to forming Au in the crystalline phase, the dangling bond sites enable formation of the Au NC at those locations rather than elsewhere in the system. c) A cartoon illustrating the approach and reduction of Au^{3+} ions to crystalline Au bound to the NR.

Conjoining two materials with a Type-II band gap offset in a nanostructure spatially separates photogenerated carriers (Figure 4.3) within the nanostructure such that the wavefunction of the electron largely resides in one material and the wavefunction of the hole in the other [15,16]. CdSe/CdTe heterostructures are predicted to be ideal for separation of 1D excitons (1DEs), despite their large binding energies [17], when the structure lies within the "wide wire" regime (where the rods and dots are of comparable thickness) [15].

These materials could find potential applications in photovoltaic devices, including solar cells and photodetectors, by reducing the applied voltage required to turn excitons into free charge carriers.

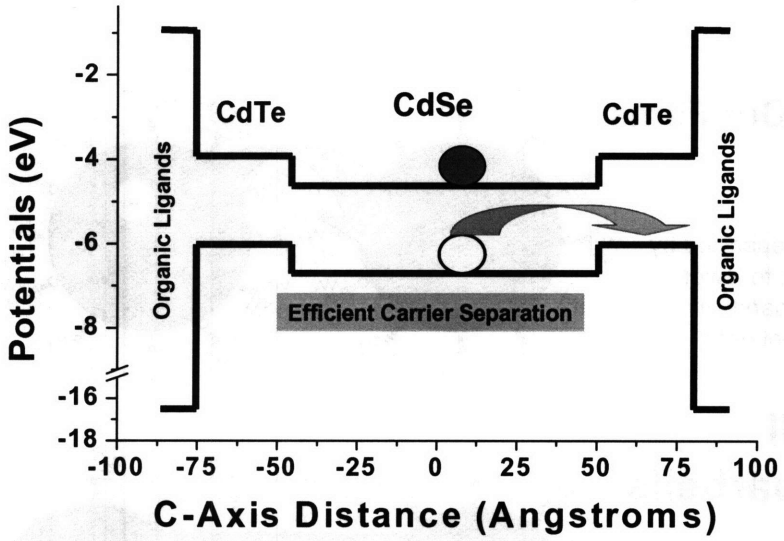

Figure 4.3: Band structure of the CdSe/CdTe nanobarbells. The band offsets of more than 500meV in the bulk between valence (4.6eV, 4.1eV) and conduction (6.7eV, 5.9eV) bands of CdSe and CdTe driving exciton separation in the nanocrystal. [16]

Heterostructures have been produced in many previous works. Type-I heterostructures are commonly used in emission applications, such as LEDs [18-25] or biological applications [26-29]. Type-II materials have also been produced, such as CdTe/CdSe core/shell nanocrystals [16] and CdTe branches grown off of CdSe tetrapods [30]. However these structures are not ideal for photoconduction because once the excitons are separated, the charges cannot easily move through the film. Tetrapods leave empty volume when deposited into a film while core/shell particles trap one of the carriers in the core. This chapter presents the synthesis for CdSe/CdTe rod/dot "nanobarbells" (NBs) designed to be of interest for photoconduction or photovoltaic applications. This particle is uniquely

suited to photovoltaics since the Type-II electronic structure will separate the exciton and the rod-like particle allow it to pack tightly into a film [31]. These nanobarbells should both allow exciton separation within the nanocrystal and separate conduction of electrons through CdSe rods and holes through CdTe dots.

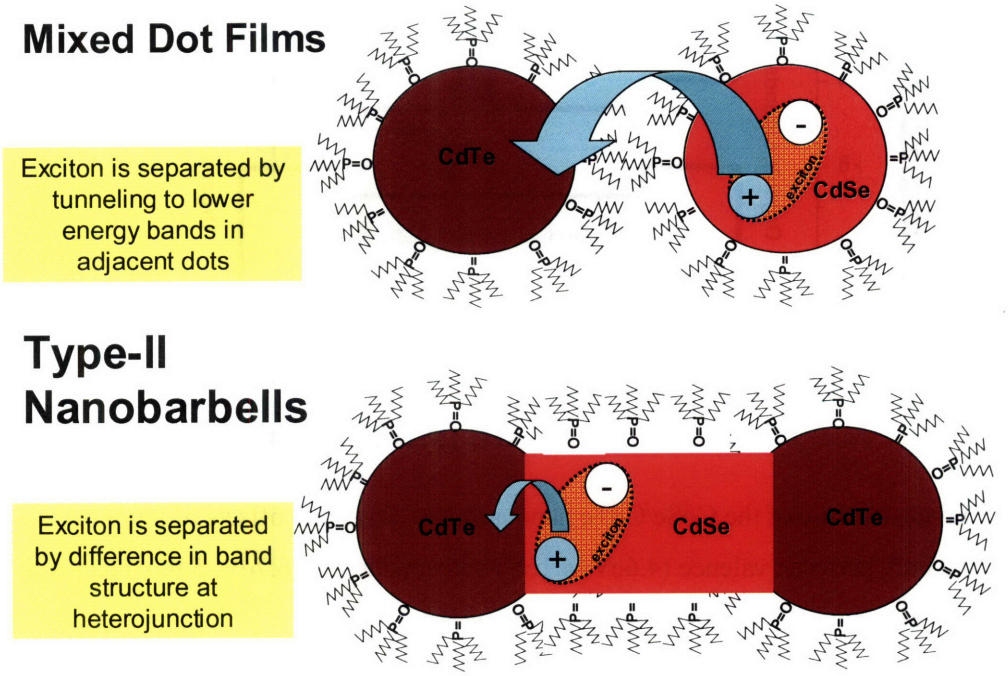

Figure 4.4: A cartoon comparing exciton separation in mixed films, which could conduct either charge through perculation pathways but presents a tunneling barrier to charge separation (top) to that of a single nanocrystal incorporating both materials, which achieves both dual charge transport and charge separation (bottom).

4.2 Synthesis of CdSe/CdTe Nanobarbells

The first step to creating the material is the synthesis of the CdSe nanorods (NRs). This was first achieved in pursuit of their linearly polarized emission properties (Appendix A.2). The second step is the attachment of CdTe QDs to the tips of the NRs.

Finally the CdSe/CdTe "nanobarbells" (NBs) are characterized by TEM, STEM, and PL and absorption spectroscopy.

4.2.1 Preparation of Nanobarbells

To synthesize the CdSe/CdTe rod/dot nanobarbells, CdSe rods were synthesized by heating 0.2054 g cadmium oxide (CdO), 1.2946 g octadecylphosphonic acid (ODPA) and 2.500 g trioctylphosphine oxide (TOPO) to 300 °C in a 3-neck 25ml flask, until the solution was clear, then heating to 320 °C and injecting a solution of 0.300 g toluene, 1.290 g trioctylphosphine (TOP) and 0.410 g of 3.5 M trioctylphosphine selenide (TOP-Se),. Next, the rods were grown at 260 °C for fifteen minutes. The rods were then precipitated from solution twice by adding ~5 ml butanol and ~20 ml methanol, the solution was centrifuged at 3900 RPM and redispersed in hexane. After the second precipitation, rods were redispersed in hexane with a few drops of octylamine and allowed to sit for several days until a significant increase in quantum yield occurred. Introducing a mild etchant to the solution of nanorods, such as octylamine, at room temperature and letting it sit over a period of ~ 1 week prior to the introduction of CdTe precursors reduced the number of CdTe "warts" grown along the shaft of the rods. Rods were then precipitated as above, redispersed in hexane and filtered.

To create CdSe/CdTe nanobarbells, 3.125 g TOPO, 2.875 g hexadecylamine (HDA) and 0.2825 g hexylphosphonic acid (HPA) were degassed at 140 °C in a 4-neck 50 ml flask with an attached addition funnel, cooled to 80 °C at which time rods, containing approximately 1 mmol of Cd total as estimated by optical absorption, and were dispersed in hexane were added to the pot.The hexane was removed under vacuum.

Meanwhile a solution of 0.078 g cadmium 2,4-pentadionate, 0.285 g 1,2-hexadecanediol, and 4 ml TOP was degassed at 110 °C in a separate vial. After degassing, the solution was cooled to room temperature and 2ml of 1.0M trioctylphosphine telluride (TOP-Te) was added to the vial, the contents of which were transferred to the addition funnel and added to the pot at 260 °C dropwise at a rate of 1 drop/3 seconds. These conditions were identical to, excepting the presence of the rods, the dropwise addition and the temperature, to the formation of CdTe dots. The total reaction time after the start of the addition of the precursor solution did not exceed 15 minutes, after which the resulting solution was cooled to room temperature and transferred under argon to a nitrogen glovebox to avoid oxidization of the CdTe tips.

It may be noted that the temperature at which the tips were grown is not high enough to cause the CdSe nanorods to become spherical. This is probably because they were not kept at this temperature long enough to achieve the thermodynamically lowest energy state (a sphere), and also because the addition of CdTe precursor in solution drives the general reaction towards the deposition of material onto the ends, and thus away from the "ripening" effect of material leaving the ends and being deposited on the sides. Furthermore, were deposition of CdSe on the side of the rod favorable at this temperature, it seems unlikely that tip formation would occur at all, since most CdTe would also form isotropically. At higher temperatures (or given more time and no precursors), the CdSe rods would be expected to deform and become spheres.

After formation, the CdSe/CdTe nanobarbells were precipitated from the growth solution by the addition of toluene, and centrifuged at 3900 RPM, after which the supernatant, containing CdTe dots (usually accounting for less than 10% of total CdTe

added in second step) was discarded. The resulting precipitate was sonicated into a suspension in hexane from which immediately precipitated and could be centrifuged. Once again the supernatant was discarded. These steps extracted, in the supernatant, any CdTe dots formed during the synthesis from the solid CdSe/CdTe nanobarbells. After this CdSe/CdTe nanobarbells were redispersed in chloroform and precipitated several times using butanol/methanol in order to remove any excess organic material from the solution. CdSe/CdTe nanobarbells appear to be light sensitive and stay dispersed in solution for several days only if stored under nitrogen in the dark.

4.2.2 Mechanism of Formation

The mechanism for the formation of nanobarbells is similar to that suggested by Banin et al. [14], to explain the formation of gold tipped CdSe rods. In that work, the higher reactivity facets, the [000±1] facets perpendicular to the crystalline c-axis, served as nucleation points for the formation of a gold "dot" attached to the rod. By adding the CdTe precursor slowly and below nucleation temperature, the precursors in solution obtain the necessary free energy, as their concentration increases, overcoming the thermodynamic barrier to nucleation at the ends of a CdSe rod well before any appreciable homogeneous nucleation can occur (as illustrated in Figure 4.2).

Given an adequate number of nucleation sites in solution, nucleation on the end of a CdSe rod becomes the dominant pathway for CdTe dot formation, as only a small number of "free" dots are produced. After nucleation, growth then occurs primarily on the CdTe dots due to the preferential reactivity of the precursor. Evidence for this mechanism can be found in the formation of CdTe dots attached to defect sites along the

body of imperfectly shaped rods and in the minimal overcoating of the rod with CdTe seen in STEM measurements of CdSe/CdTe nanobarbells. It is noteworthy that the formation of these heterostructures simply requires modifying the CdTe dot synthesis only by (1) the presence of rods that serve as nucleation sites and (2) adding precursors dropwise at a temperature high enough for growth, but low enough to suppress homogeneous nucleation. This synthesis shows that the mechanism of rod-nucleated growth may be generally applicable for creating other non-core/shell heterostructures with unique physical properties.

4.3 Characterization of Nanobarbells

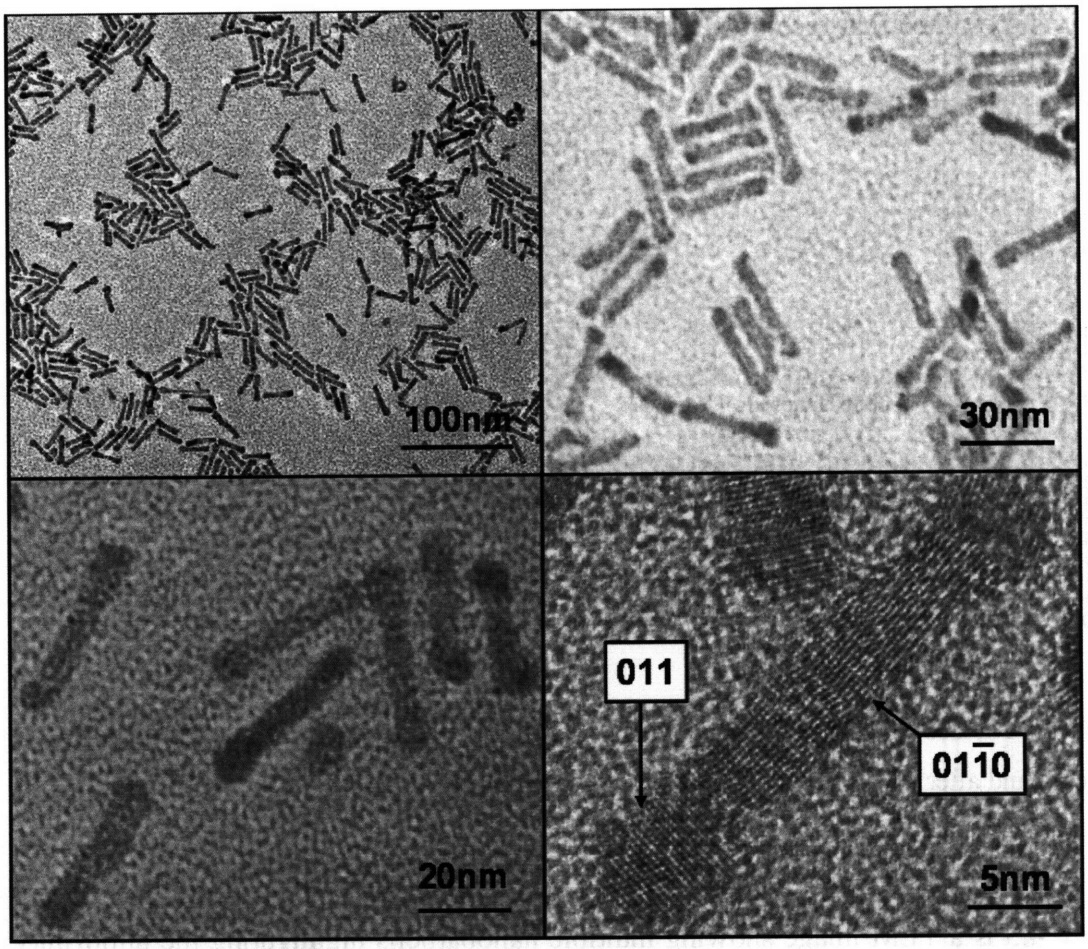

Figure 4.5: Transmission electron microscope images of nanobarbells taken on a JEOL 200 TEM and expanded (top) and JEOL 2010 HR-TEM (bottom) showing CdSe/CdTe nanobarbells. High res. images show that the CdTe dots are neither Wurtzite nor oriented along the c-axis of the rod. [32]

Nanobarbells exhibit absorption spectra (Figure 4.6) typical of Type-II heterostructures [16], with significant absorption across the visible spectrum. This is expected as the photon can be absorbed either by the CdSe rod, the CdTe dot, or intermediate states that exist at the junction between the two materials. However, unlike in core/shell Type-II heterostructures, there is no observed emission. Since the carriers are spatially well-separated and the nanobarbell is not overcoated with a higher band gap material (such as

ZnS), it is presumed that recombination occurs primarily through non-radiative pathways involving surface trap states.

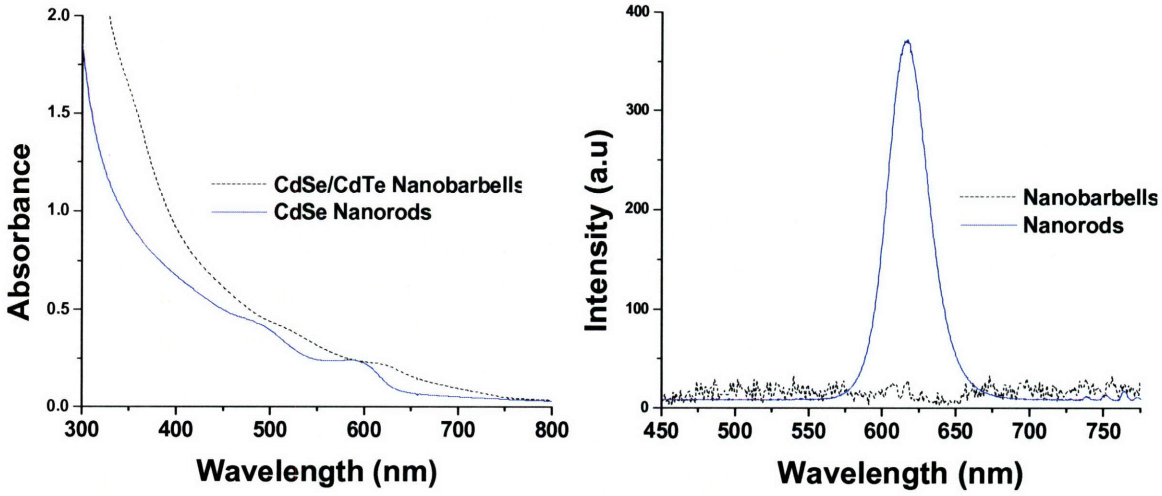

Figure 4.6: The absorption (left) and emission (right) spectra of a sample of nanobarbells before (nanorods) and after the addition of CdTe tips (nanobarbells). [32]

Figure 4.5 is a TEM image showing multiple nanobarbells highlighting the uniformity of the material. The CdTe dots grow symmetrically on either end without branching or other deviations that may increase "empty" volume in a film. Nanobarbells synthesized in this manner should show packing properties similar to CdSe rods [31]. As transport in nanocrystal films is generally limited by a carrier tunneling mechanism [33-35], obtaining good conductivity and high photocurrent requires minimizing the distance between adjacent particles. This requires the particles to form close-packed films, which in turn illustrates the need for well formed rodlike nanocrystals. Using a two step synthesis significantly improves the quality of the heterojunction by minimizing contamination of the CdTe dots with Se. A low growth temperature minimizes overcoating of the CdSe rods with CdTe. STEM measurements confirm this in Figure 4. Although the spatial

precision of the instrument is limited, spots measured in the center of the rod indicate a concentration of CdTe that is less than 30 %, which corresponds

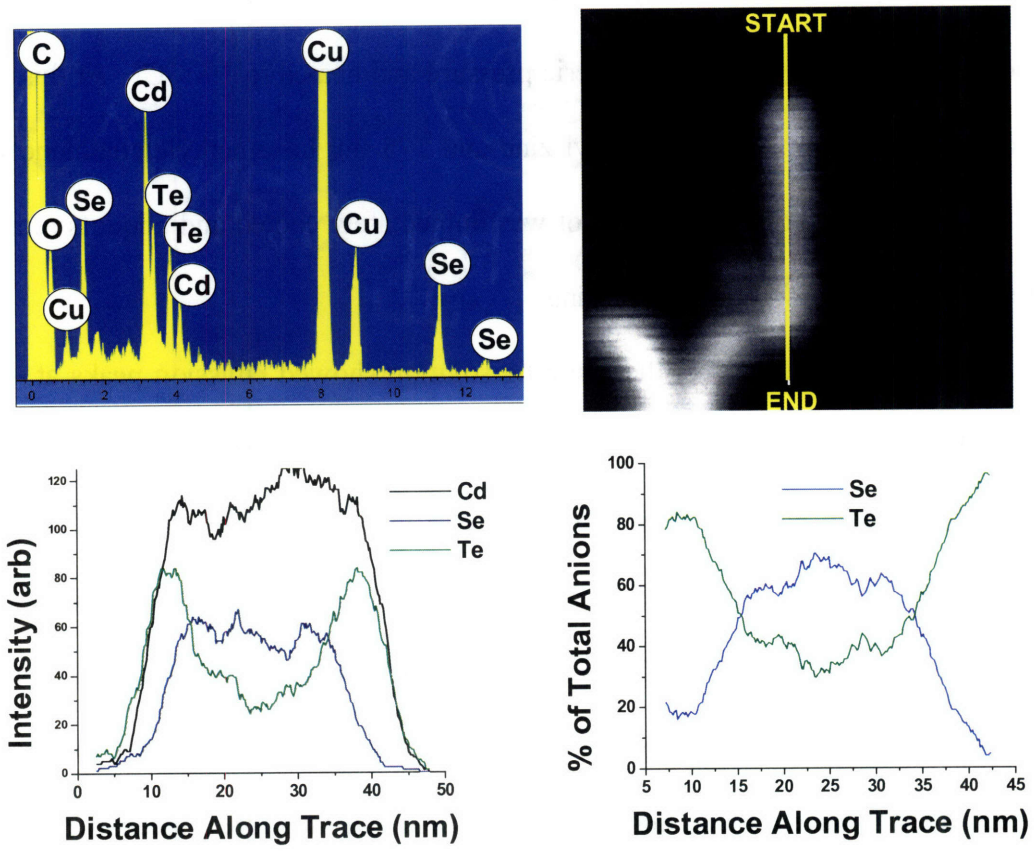

Figure 4.7: Electron energy loss data (example top left) from a scanning transmission electron microscope (STEM) trace of a single CdSe/CdTe nanobarbell (image top right). Concentration is plotted for all three elements (bottom left) and the anion ratio is assessed (bottom right). [32]

to a CdTe thickness of about two monolayers around a rod with radius ~3 nm. However, the proximity of the Cd and Te peaks in the x-ray spectrum leads to over-counting of tellurium, and no discernable shell can be seen in HR-TEM images (Figure 4.5).

4.3.1 Overcoating CdSe/CdTe Nanobarbells

Emission from nanobarbells is observed only once the material is overcoated with a ZnCdS layer. Overcoating was achieved by degassing a pot of 10g TOPO and 0.4 g

HPA at 160°C (as for CdSe QDs in Chapter 2). The NBs, representing about 0.42 mmol of Cd as determined from the absorption at 600 nm, were then added in chloroform, after purification, to the pot under vacuum at 80 °C. Once the chloroform was removed, the pot was placed under argon at atmospheric pressure and heated to 190 °C. At this point 6 mg dimethyl cadmium, 54 mg diethyl zinc and 175 mg hexamethyldisilathiane were added dropwise in 5ml of TOP. The pot was immediately cooled and aliquots removed to determine the success of the overcoating.

As is seen in Figure 4.8, the resulting solution showed emission peaks at ~ 700 nm and ~ 950 nm. This result was typical for most of the NB overcoated samples. The first peak is likely to be CdTe/ZnS core-shell QDs formed either from CdTe cores left over from the purification process, or from CdTe QDs formed during the overcoating from nucleation of excess Cd and Te in solution or from CdTe QDs which have broken away from the NB core. These represent a minority of the NCs in solution, however they can be expected to have a much higher quantum yield and therefore appear more intense than their population would warrant. The second peak is consistent with the expected emission from a Type-II CdSe/CdTe nanocrystal and could not be produced by any other species (such as CdSe/ZnS, CdTe/ZnS, etc.). The emission is somewhat redder than previous studies on Type-II CdTe/CdSe QDs, as would be expected for an anisotropic Type-II CdSe/CdTe NC.

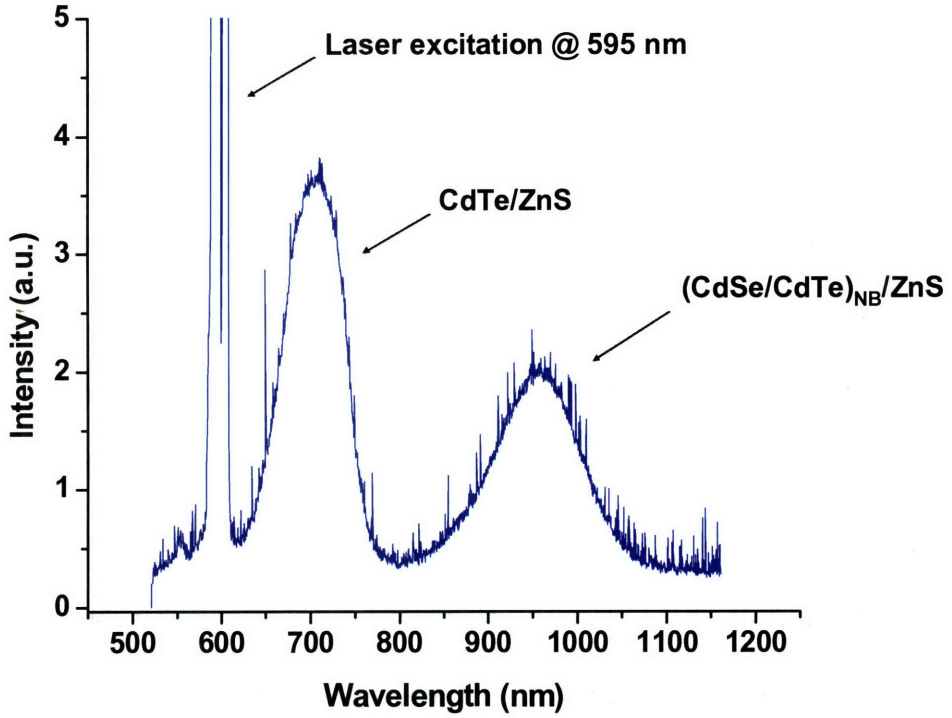

Figure 4.8: An emission spectrum of the nanobarbell solution after overcoating with ZnS. The two emission peaks can be attributed to the presence of two different species in solution and are unlikely to emanate from a single NC. The second peak at ~ 950 nm is most likely emission from the NBs themselves.

The best way to determine the source of each emission peak for the sample would be through single NC spectroscopy. However, the experimental setup necessary was not available nor could not be easily assembled. Furthermore, although the overcoated NBs are interesting spectroscopically, they are not ideal for photoconduction as they possess yet another tunneling barrier in the form of the ZnS shell. As such this species may warrant further characterization.

4.4 Conductivity in CdSe/CdTe Nanobarbell Films

Prior to construction of a functional absorption device, it is necessary to determine the physics of conductance in films made from CdSe/CdTe. Determining the mechanism of conduction, and the dominant charge carriers involved in conduction, will yield insight into the possible use of the material in a solar cell structure[36].

Previous works have shown that charges flow through a close-packed film of QD by tunneling from the conductive bands of one QD into those of a neighboring QD [4,37]. For a given sample of QDs, one charge is generally more mobile than the other, although it may be either the hole or the electron. Conduction can occur either through the band structure of the QD [37] or be mediated by traps on the QD surface [6]. It is generally dependent both on the material type [6,37,38], the quality of the sample or surface treatments [37,39,40]. As an example, previous work on CdSe films have shown that these films primarily conduct electrons [37], while CdTe films primarily conduct holes [6].

4.4.1 Conductivity: Device Processing and Measurement

The field effect transistor (FETs) devices, for testing conductivity, were fabricated by lithographically patterning gold bar electrodes 200 x 800 x 0.1 μm^3 on 330 nm thick silicon oxide (Figure 4.9). The electrodes were separated by 1 or 2 μm. Solutions of CdSe/CdTe nanobarbells solutions were then spin coated onto the planar device structures.

The planar FETs were attached to a 28-pin chip carrier and electrical contacts were made from the electrodes to the chip carrier by gold wire bonds. Devices were tested for

leakage before film deposition by applying high voltage (100 V) to the source, drain, and gate electrodes. Devices with leakage greater than 0.5 pA were discarded.

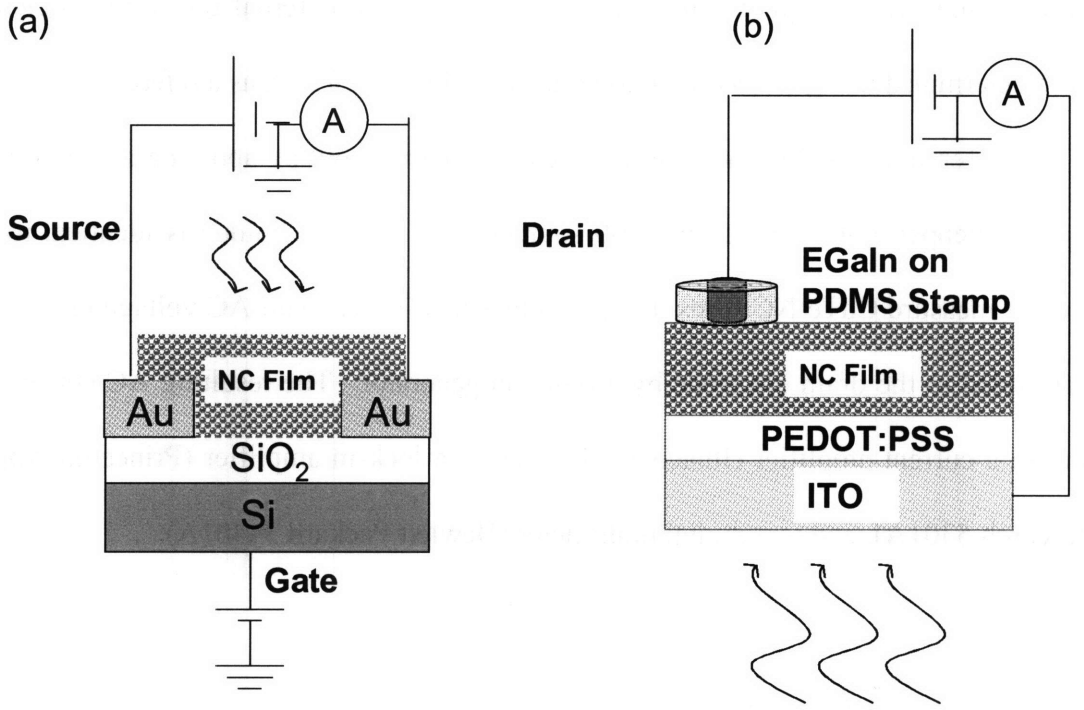

Figure 4.9: a) The device structure used for conductivity measurements on CdSe/CdTe films [6]. The film here is drop-cast between the two Au electrodes. b) A sandwich structure device used to construct a solar cell using NC films of either CdTe or CdSe/CdTe [6]. This device is described in greater detail in 4.5.

Conductivity measurements on planar devices were performed in a Janis VPF-100 cryostat under vacuum. Samples were loaded into the cryostat in the glovebox and never exposed to air. A Keithley 6517 electrometer was used to measure current, I, and apply voltage across the source and drain electrodes, V_{ds}. An Agilent 6614C DC power provided the gate voltage, V_g. An Ar^+ laser at 514 nm was used to photoexcite the samples. It has been shown previously that photocurrent is not a result of photoinjection from the electrodes.[35] The NCs were photoexcited with an Ar^+ laser at 514 nm for I-V

curve measurements. For photocurrent action (PCA) spectra measurements in which the photocurrent is measured as a function of the wavelength of the excitation light, the samples were photoexcited with a 150 W ozone free xenon arc lamp through a monochrometer. The photovoltaic and photoconductive external quantum efficiencies were determined using a silicon photodiode, Thor Labs DET210, as a reference.

The differential conductance measurements are carried out by applying a constant V_{ds}. V_g was stepped with a Keithley 2400 sourcemeter. This technique is identical to that used to measure CdTe NC films in a previous study [41]. A small AC voltage (13Hz, 5V) was added to the drain electrode by a function generator. The resulting AC current was sent to a current amplifier (Ithaco 1211), then to a lock-in amplifier (Princeton Applied Research 5301A), and to a digital multimeter (Hewlett Packard 34401A).

4.4.2 Results and Discussion

Differential conductance measurements were performed to find the mobile carrier in the NB films (Figure 4.10). For both values of V_{ds} the current increased with negative gate voltage. This indicates that holes are the majority carrier. The activation energy of the dark current in the CdSe/CdTe NB film was also measured in the same manner as the activation energy of the dark current in CdTe NC films.[41] Current, as a function of voltage, was measured at 87, 110, 140, 170, 200, 230, 260, and 295 K. The current at each voltage is plotted against the temperature (Figure

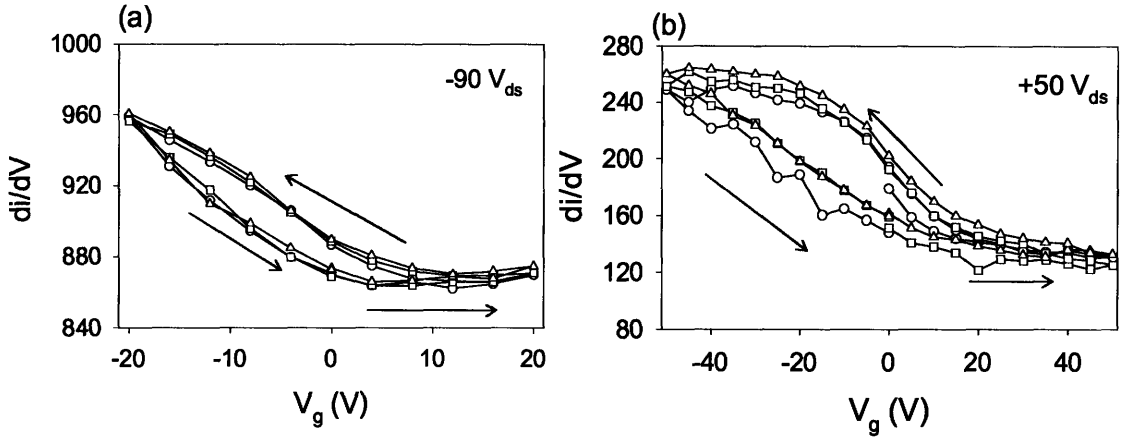

Figure 4.10. Room temperature differential conductance di/dV plotted as a function of gate voltage for a CdSe/CdTe NB film held at (a) -90 V_{ds} and (b) + 50V_{ds}. V_g wasapplied for 5 s and followed by a recovery of 5 s at 0 V_g before V_g was stepped to the next value. In (a) V_g was swept from 0 to + 20 V, from + 20 V to – 20 V, and back to 0 V while in (b) V_g was swept from 0 to + 50 V, from + 50 V to – 50 V, and back to 0 V. For both (a) and (b) the open circles represent the first sweep, open squares the second sweep, and open triangles the third sweep. The solid line serves as a guide to the eye.[6]

4.10) and each curve is fit with an Arrhenius equation. The activation energy at a given voltage is extracted and that value is plotted versus field (Figure 4.11, inset) to extract the zero field activation energy. The zero field activation energy of the CdSe/CdTe NBs was found to be 0.33 eV.

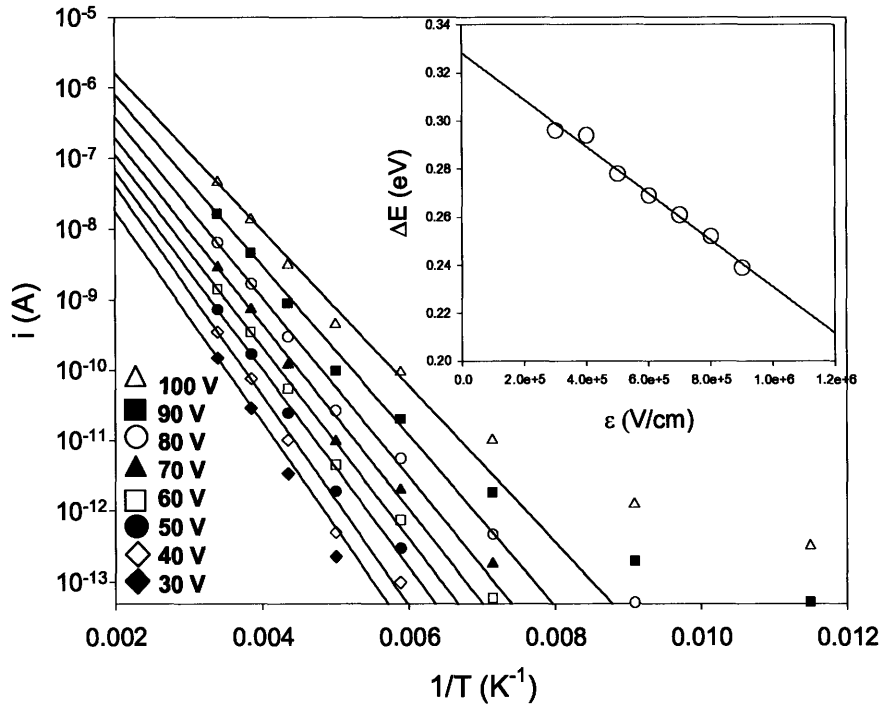

Figure 4.11: Temperature dependence of the dark current for a CdSe/CdTe NB film plotted at different values of V_{ds}. An Arrhenius fit to each data set is given by a solid line. Field dependent activation energies are extracted from the fit and plotted verses electric field in the inset. A solid line gives a linear fit to the data in the inset. The temperature was monitored with a Lakeshore 330 temperature controller. [6]

In CdSe/CdTe NBs, the CdTe QD is connected to the CdSe NRs, which should increase the probability of Type-II exciton separation. In addition, the ratio of CdTe to CdSe is uniform throughout the film, eliminating potential difficulties stemming from segregation of CdTe and CdSe NCs. However, the photocurrent vs. electric field dependence for films of CdSe/CdTe NBs (Figure 4.12) is identical to that of a film composed entirely of CdTe NCs [6] with the same absorbance, as in *Porter et al.*[6]. Also, the field dependence is nearly identical for both CdSe/CdTe NBs and CdTe QDs, which

have a field dependent mobility of 3.0 x 10^5 V/cm for the NB films and 3.1 x 10^5 V/cm, respectively, using Equation 4.4.2:

$$I = \frac{\varepsilon}{R_0} \exp(\frac{\varepsilon}{\varepsilon_o}) \qquad (4.4.2)$$

where ϵ is the electric field, I is current, R_o is characteristic resistance, and ϵ_o is a characteristic field dependence.

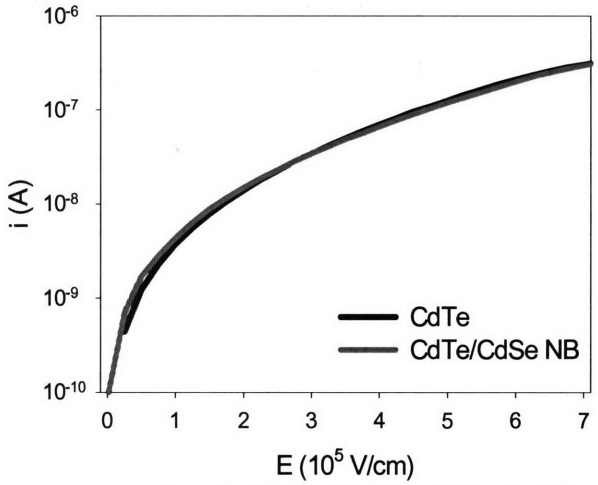

Figure 4.12. Photocurrent verses electric field with 32 mW/cm2 514 nm excitation for a CdTe NC film (black line) and a CdSe/CdTe NB film (grey line). The magnitude of the photocurrent has not been scaled for either of the films but they were matched to have a similar absorbance value at 514 nm. [6]

4.4.3 Conclusions on Nanobarbell Conduction and Bulk Heterojunction Device

Electron trapping on the CdTe QD surface appears to dominate charge transport through the films in CdSe/CdTe NBs, as was found in earlier studies of mixed CdTe films and CdSe films [6]. Even if excitons are separated at the Type-II interface, electron transport does not appear to be segregated to the CdSe NRs, and electrons appear to be deeply trapped at the CdTe surface. This implies that CdSe/CdTe nanobarbells may still

suffer from the same inherent problems as CdTe films; namely that they conduct mainly holes through a trap mediated conduction mechanism, and that electrons are still effectively "stuck" in the film, never making it to the electrode. Amplification is observed in the NB films, similar to CdTe films, as holes cycle through the film several times prior to recombining with a trapped electron. Unfortunately, this does not make it much more effective as a solar cell material than CdTe on its own, as it suffers from many of the defects of that material, while also being more difficult to produce.

In Figure 4.13, a trial device produced using ITO/PEDOT-PSS/NBs (~80 nm)/Au was tested with a chopped 514 nm line of an argon-ion laser. As expected, the device showed very low open circuit voltage of 72 mV and closed circuit current around 9 nA. The fill factor was 33%. The main difficulty with these devices was the large dark current due to the hole conduction of the CdTe tips, and the propensity to short due to penetration of the Au electrode into the NB film. The low current shows that charges, probably electrons, are stuck in the film, while the low open circuit voltage indicates that the charges are not migrating towards their respective electrodes. If NBs are to be used in a solar cell, it must be designed as in more of a "p-i-n" junction device, surrounded by electron and hole blocking layers and not as a simple bulk heterojunction device.

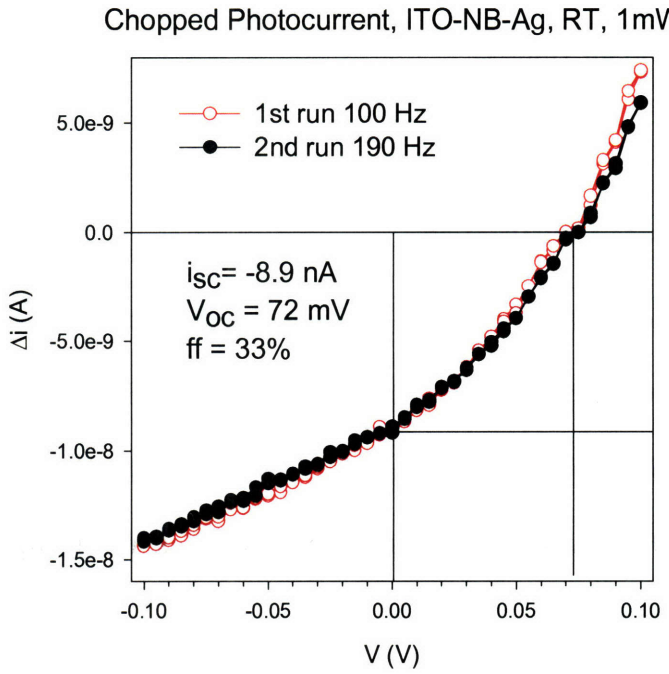

Figure 4.13: A PV device using ITO/PEDOT-PSS/NBs/Au. Although the device is slightly rectifying, the short circuit current (I_{sc}) and open circuit voltage (V_{oc}) are much too low, under 514 nm laser excitation for this device to be efficient.

4.5 CdSe and CdTe QDs as Transport Layers in an NB Solar Cell

Although the NBs did not have the initially desired transport properties, their ability to absorb strongly throughout the visible spectrum and the possibility of exciton separation without tunneling render it feasible to create an efficient solar cell device. Instead of percolation through a thick NB film, as was initially proposed, the device was designed using CdSe as an ETL layer, and CdTe as an HTL layer with the active CdSe/CdTe NBs sandwiched between them. The built-in field in this device still originates from the difference in the work functions of the electrodes and therefore it is not a true p-i-n device. However the CdSe and CdTe blocking layers should greatly decrease the dark

current, allowing greater charge to build up at either electrode and significantly improving the open circuit voltage.

4.5.1 Solar Cell Device Construction

The NB solar cell consists of a glass slide coated with 80 nm of sputtered, conductive ITO, a 25 nm CdTe QD layer, a 25 nm thick CdSe/CdTe NB layer, a 25 nm thick CdSe QD layer, and an EGaIn semi-liquid electrode [6] (Figure 4.14). Devices were constructed as with previous QD sandwich photovoltaic devices [8] by spin-casting QDs onto an ITO surface, heating the substrate to 70 °C for several minutes to anneal the film, then cooling to room temperature prior to spin-coating the next layer. This prevents the solvent from subsequent layers from dissolving the previous QD films. Deposition of the NC films, the device was treated with a butylamine solution in order to remove the native capping groups and decrease the tunneling barrier, as in *Jarosz et al* [34]. The liquid electrode is applied by injecting a little of the liquid metal from the tip of a syringe into a circular PDMS mold with dimensions of 1 mm in diameter. [36]

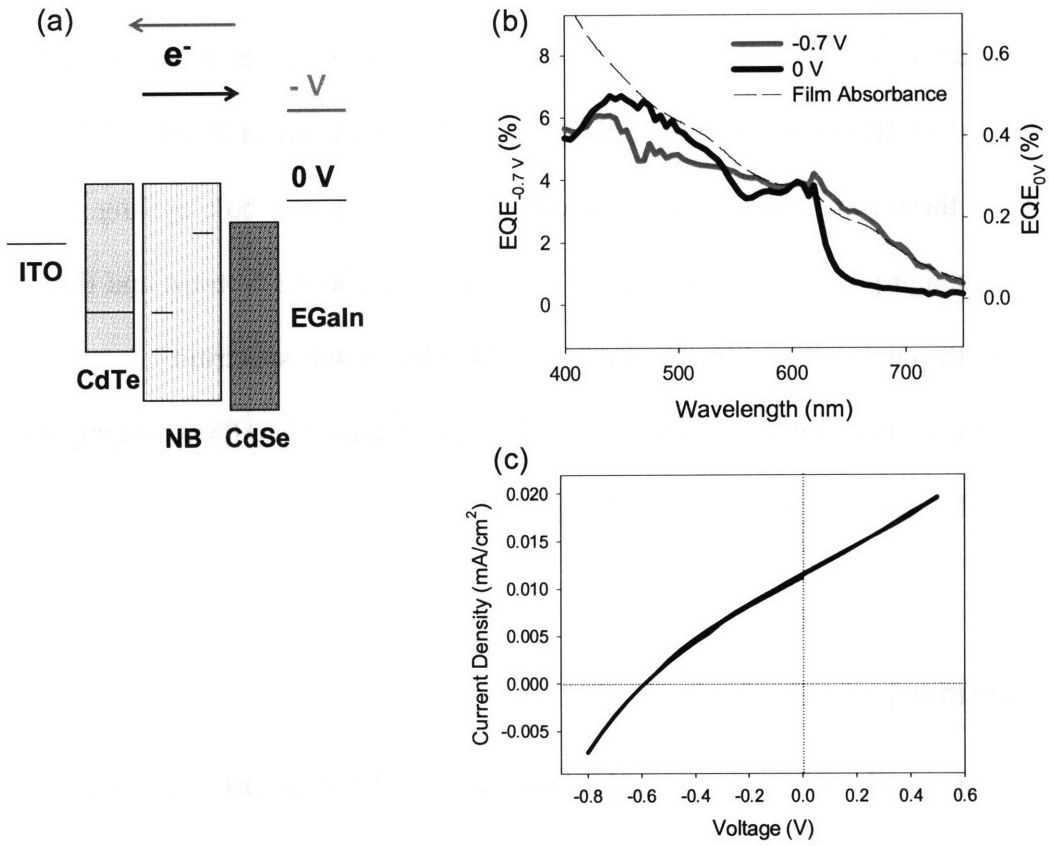

Figure 4.14. a) A diagram of the relative energy levels of the ITO/CdSe/NB/CdTe/EGaIn solar cell. The direction of the flow of electrons in the device at each voltage is designated by the arrows and color coded with the label for the bias. The black arrow indicates electrons flow from the ITO to the EGaIn (reverse/positive bias) and the grey arrow indicates electrons flow in the opposite direction (forward/negative bias). (b) The PCA spectra for this device is displayed at 0 V (black line) and at -0.7 V (grey line). The absorbance is given by the dotted line. (c) Current verses voltage plot for this device in which the voltage was swept from 0 to + V, from + V to – V, and back to 0 V. Devices were measured at room temperature and photoexcited with 27 mW/cm^2 of 514 nm light.

The device shows EQEs of nearly 0.3 % to 0.5 % at 0V (Figure 4.14b), similar to those of previous close-packed NC devices [8]. The open circuit voltage (V_{oc}) was ~0.60 V while the short circuit current (I_{sc}) was 12uA/cm^2. The fill factor (FF) was found to be ~30% for the best devices.

The photocurrent action spectrum (Figure 4.14b) clearly shows that most of the photocurrent arises from the CdSe QD film at 0V. This makes sense in light of the trapping of electrons in the CdTe QD and NB layers shown in Section 4.4. Excitons formed in these films cannot contribute current, except through hole cycling. At 0.7 V, there is enough potential to pull those electrons out of the 0.3 V traps and through the film, thus the contribution from the CdTe and NB films in this spectrum.

The estimated power efficiency for this device was only 0.06%, roughly 40 times less than the best reported devices utilizing NCs [2].

4.6 Summary

This work successfully synthesized CdSe/CdTe nanobarbells, adding another heterostructured NC to those available for use in device design. They have been characterized by TEM and STEM, and show type-II photonic behavior in their absorption spectra. Furthermore they can be overcoated with ZnS to produce near IR emission spectra, as expected. Although they do not appear to conduct electrons through the CdSe NRs, and thus are not suited for bulk heterojunction devices, they have been successfully implemented in a pseudo-p-i-n junction device with V_{oc} = 0.6V, I_{cc} = 12 uA/cm2 and FF = 30 %. The PE of this device was very low however, and was estimated to be ~ 0.06%.

Although this device is not as efficient as other devices in the field, it does represent a significant step toward understanding how to design NCs for these types of applications. While anisotropic type-II materials may still be useful in solar cell applications, it is now understood that the transport function of the materials is equally as important as the material's photonic properties. The electron trapping function of CdTe

simply makes the NBs unfeasible as a solar cell material, without significant alterations to the surface. Future work in this area is likely to use PbS instead of CdTe, with its near IR band edges and somewhat greater durability. Conductivity and device testing with these new materials are now being investigated by several researchers in the field.

Although the devices produced by this work were not efficient, both silicon and polymer solar cells were much less efficient in the early stages of their development than they are today. It is possible then that NCs of this sort could still play an important role in future innovations in the field.

My collaborators in this chapter were Venda Porter, who performed the conductivity measurements, and Scott Geyer, for processing and testing the second solar cell.

4.7 References

(1) Gur, I.; Fromer, N. A.; Alivisatos, A. P. *Journal of Physical Chemistry B* **2006**, *110*, 25543-25546.

(2) Gur, I.; Fromer, N. A.; Geier, M. L.; Alivisatos, A. P. *Science* **2005**, *310*, 462-465.

(3) Jarosz, M. V.; Porter, V. J.; Fisher, B. R.; Kastner, M. A.; Bawendi, M. G. *Physical Review B* **2004**, *70*, 195327.

(4) Leatherdale, C. A.; Kagan, C. R.; Morgan, N. Y.; Empedocles, S. A.; Kastner, M. A.; Bawendi, M. G. *Phys. Rev. B* **2000**, *62*, 2669.

(5) Porter, V. J.; Geyer, S.; Halpert, J. E.; Kastner, M. A.; Bawendi, M. G. *Journal of Physical Chemistry C* **2008**, *ASAP*.

(6) Porter, V. J.; Geyer, S.; Halpert, J. E.; Mentzel, T. S.; Kastner, M. A.; Bawendi, M. G. *In preparation* **2008**.

(7) Watt, A. A. R.; Blake, D.; Warner, J. H.; Thomsen, E. A.; Tavenner, E. L.; Rubinsztein-Dunlop, H.; Meredith, P. *Journal of Physics D: Applied Physics* **2005**, *38*, 2006-2012.

(8) Oertel, D. C.; Bawendi, M. G.; Arango, A. C.; Bulovic, V. *Applied Physics Letters* **2005**, *87*, 213505.

(9) Yang, Y.; et al. *Journal of Materials Science: Materials in Electronics* **2000**, *11*, 89-96.

(10) Mentzel, T. S.; Porter, V. J.; Geyer, S.; MacLean, K.; Bawendi, M. G.; Kastner, M. A. *Physical Review B* **2008**, *77*, 075316.

(11) Huynh, W. U.; Dittmer, J. J.; Alivisatos, A. P. *Science* **2002**, *295*, 2425-2427.

(12) Steiner, D.; Mokari, T.; Banin, U.; Millo, O. *Physical Review Letters* **2005**, *95*, 056805(056804).

(13) Kudera, S.; Carbone, L.; Casula, M. F.; Cingolani, R.; Falqui, A.; Snoeck, E.; Parak, W. J.; Manna, L. *Nanoletters* **2005**, *Vol. 5*, 445-449.

(14) Mokari, T.; Rothenberg, E.; Popov, I.; Costi, R.; Banin, U. *Science* **2004**, *304*, 1787-1790.

(15) Franceschetti, A.; Lang, L. W.; Bester, G.; Zunger, A. *Nano Lett.* **2006**, *6*, pp 1069 - 1074.

(16) Kim, S.; Fisher, B.; Eisler, H.-J.; Bawendi, M. *J. Am. Chem. Soc.* **2003**, *125*, 11466-11467.

(17) Shabaev, A.; Efros, A. L. *Nanoletters* **2004**, *4*, 1821-1825.

(18) Anikeeva, P. O.; Halpert, J. E.; Bawendi, M. G.; Bulovic, V. *Nano. Lett.* **2007**, *7*, 2196.

(19) Caruge, J.-M.; Halpert, J. E.; Bulovic, V.; Bawendi, M. *Nano Lett.* **2006**, *6*, 2991-2994.

(20) Caruge, J.-M.; Halpert, J. E.; Wood, V.; Bulovic, V.; Bawendi, M. G. *Nature Photonics* **2008**, *2*, 247-250.

(21) Coe, S.; Woo, W. K.; Bawendi, M.; Bulovic, V. *Nature* **2002**, *420*, 800-803.

(22) Coe-Sullivan, S.; Steckel, J. S.; Woo, W.-K.; Bawendi, M.; Bulovic, V. *Adv. Funct. Mater.* **2005**, *15*, 1117-1124.

(23) Coe-Sullivan, S.; Woo, W. K.; Steckel, J. S.; Bawendi, M.; Bulovic, V. *Organic Electronics* **2003**, *4*, 123-130.

(24) Steckel, J.; Zimmer, J.; Coe-Sullivan, S.; Stott, N.; Bulovic, V.; Bawendi, M. *Angewandte Chemie International Edition* **2004**, *43*, 2154.

(25) Steckel, J. S.; Snee, P. T.; Coe-Sullivan, S.; Zimmer, J. P.; Halpert, J. E.; Anikeeva, P. O.; Kim, L.-A.; Bulovic, V.; Bawendi, M. G. *Angewandte Chemie International Edition* **2006**, *45*, 5796-5799.

(26) Chan, W. C.; Maxwell, D. J.; Gao, X.; Bailey, R. E.; Han, M.; Nie, S. *Current Opinion in Biotechnology* **2002**, *13*, 40-46.

(27) Chan, Y. T.; Snee, P. T.; Caruge, J.-M.; Yen, B. K.; Nair, G. P.; Nocera, D. G.; Bawendi, M. G. *JACS* **2006**, *128*, 3146-3147.

(28) Liu, W.; Choi, H. S.; Zimmer, J. P.; Tanaka, E.; Frangioni, J. V.; Bawendi, M. G. *JACS* **2007**, *129*, 14530.

(29) Liu, W.; Howarth, M.; Greytak, A. B.; Nocera, D. G.; Ting, A. Y.; ., M. G. B. *Submitted* **2007**.

(30) Milliron, D.; Hughes, S. M.; Cui, Y.; Manna, L.; Lin-Wang, J. L.; Alivisatos, P. *Nature* **2004**, *430*, 190-195.

(31) Li, L.-s.; Alivisados, A. P. *Advanced Materials* **2003**, *15*, 408-411.

(32) Halpert, J. E.; Porter V. J..; Zimmer, J. P.; Bawendi, M. G. *JACS* **2006**, *128*, 12590-12591.

(33) Drndic, M.; Jarosz, M. V.; Morgan, N. Y.; Kastner, M. A.; Bawendi, M. G. *Journal of Applied Physics* **2002**, *92*, 7498-7503.

(34) Jarosz, M. V.; Porter, V. J.; Fisher, B. R.; Kastner, M. A.; Bawendi, M. G. *Physical Review B* **2004**, *70*, 195327.

(35) Leatherdale, C. A.; Kagan, C. R.; Morgan, N. Y.; Empedocles, S. A.; Kastner, M. A.; Bawendi, M. G. *Physical Review B* **2000**, *62*, 2669-2680.

(36) Porter, V. J.; Geyer, S.; Halpert, J. E.; Mentzel, T. S.; Kastner, M. A.; Bawendi, M. G. *Physical Review Letters* **Submitted 2008**.

(37) Jarosz, M. V.; Porter, V. J.; Fisher, B. R.; Kastner, M. A.; Bawendi, M. G. *Physical Review B* **2004**, *70*, 195327.

(38) Wehrenberg, B. L.; Yu, D.; Ma, J.; Guyot-Sionnest, P. *J. Phys. Chem. B* **2005**, *109*, 20192-20199.

(39) Hagfeldt, A.; Didriksson, B.; Palmqvist, T.; Lindstrom, H.; Sodergren, S.; Rensmo, H.; Lindquist, S.-E. *Solar Energy Materials and Solar Cells* **1994** *31*, 481-488.

(40) Porter, V. J.; Geyer, S.; Halpert, J. E.; Kastner, M. A.; Bawendi, M. G. *Journal of Physical Chemistry C* **2008**, *ASAP*.

(41) Porter, V. J., T. Mentzel, S. Charpentier, M.A. Kastner, M.G. Bawendi *Phys. Rev. B* **2006**, *73*, 155303.

Chapter 5

Forster Resonance Energy Transfer from Quantum Dots to J-aggregates in Aqueous Solution

5.1 Introduction and Motivation

J-aggregates are a class of fluorophors that exhibit intense narrowband absorption and emission bands (~12 nm FWHM) from the coherent excitation of tens to thousands of aligned molecules. In this work, J-aggregates are attached to the QDs via electrostatic attraction between the ionically charged dye and a charged polymer that coats water solubilized QDs. The resulting QD/J-aggregate conjugates exhibit efficient Forster Resonant Energy Transfer (FRET) from the QDs to the J-aggregates, with essentially complete quenching of the QD photoluminescence and the consequent sensitizing of the J-aggregate fluorescence to UV excitation. These hybrid constructs combine the broadband UV absorption of a colloidal QD with the ultra-narrow emission band of J-aggregates. A QD/J-aggregate construct could find use in optoelectonic applications such as LED [1-5] and LCD displays [6-8], and also in biological marker applications involving fluorescence multiplexing [9,10]. These materials could also be useful for fundamental studies of electro-optic effects in hybrid nanostructures, for example, investigating strong coupling effects between Wannier and Frenkel excitons [11-13]

5.1.1 Introduction to J-aggregate Dyes

Cyanine dyes have been synthesized and used for many years in photography and biology, with applications ranging from silver halide sensitizers and staining agents to fluorescent markers for DNA sequencing [14-16]. Certain cyanine dyes have been extensively studied for their ability to J-aggregate in solution and at liquid-solid interfaces, induced by changes in solution conditions such as solvent polarity, salinity, and temperature [17-19]. The J-aggregation effect is made possible by the flat, elongated morphology of the cyanine dye, which controls packing, and the presence of a strong dipole formed from a conjugated pi system that forms the backbone of the molecule. The dye 1,1',3,3'tetraethyl5,5',6,6'tetrachlorobenzimidazolo-carbocyanine chloride (TTBC), which is investigated here, has been proposed to occur in a "herringbone" or "staircase" type arrangement [20]. When the dye monomers are positioned and aligned such that their optical transition dipoles couple strongly and constructively, the aggregates form the collectively emitting J-band state, whose signature photoluminescence (PL) spectrum is red-shifted and considerably narrower than the PL of the monomer [21,22].

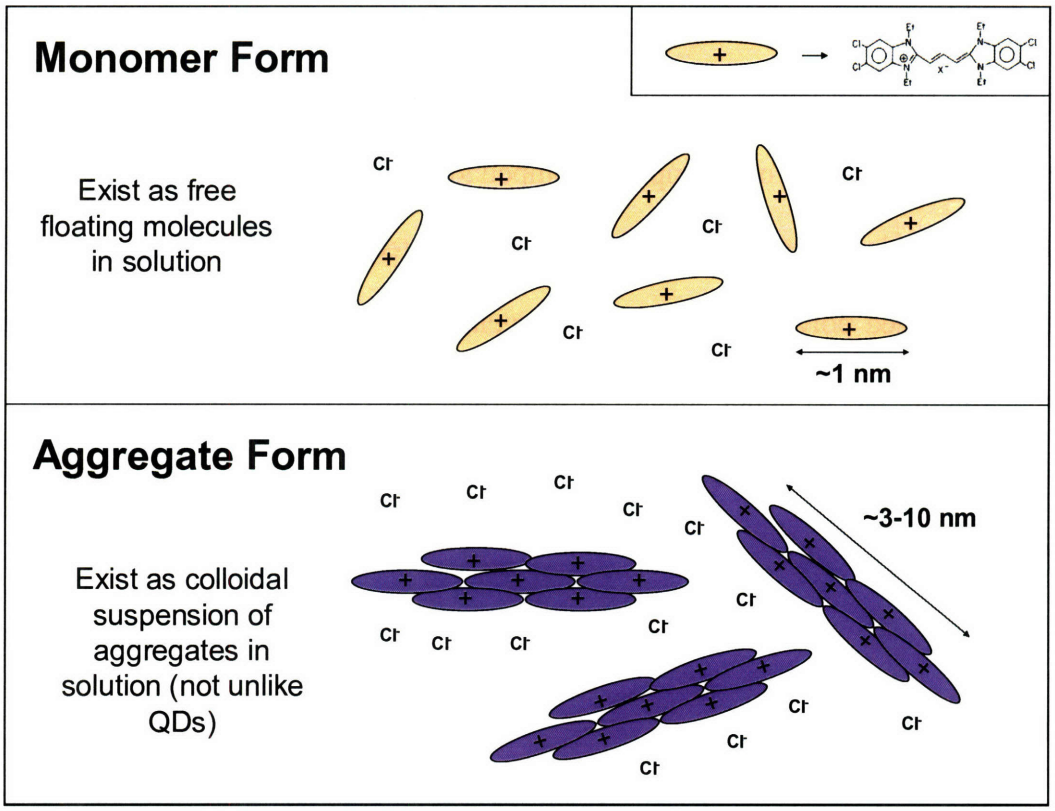

Figure 5.1: A cartoon representation of J-aggregating cyanine dye 1,1',3,3'-tetraethyl-5,5',6,6'-tetrachlorobenzimidazolocarbo-cyanine (TTBC) as monomers in methanol solution (top), and as aggregates in water (bottom).

Cyanine dyes often occur as organic salts [15]. Typically, the lumophore component is positively charged due to the partial positive charge on the amine moieties that are coupled to the conjugated pi system that forms the color center of the molecule (Figure 1). However, the lumophore may also be negatively charged overall, depending on the presence of charged pendant groups. The resulting J-aggregates are nanoscale charged species dispersible in a number of polar solvents including water and alcohols, although solvent choices are often limited by the conditions required to cause aggregation. These ionic species have been previously shown to adsorb readily onto a charged surface [23,24], to AgBr nanocrystalline grains [25], and to charged Au nanocrystals in solution [26]. They

have also been shown to be efficient FRET acceptors and donors when assembled above a film of layer-by-layer deposited polyelectrolyte-CdSe/ZnS QD monolayers [27]. Electrostatic synthesis of complex compounds involving QD's has also been demonstrated using dihydrolipoic acid (DHLA) coated, negatively charged QD's and positively charged polypeptides such as a leucine zipper [28]. QD-dye conjugates are, in general, finding use as donor species in near field and FRET based applications [29]. In particular, QD-dye FRET pairs find ready applications in sensing [30], for example as pH probes [31].

5.1.2 Methodology

This work explores the synthesis of QD/J-aggregate constructs in aqueous solution (Figure 5.1). First in Section 5.2, negatively charged polymer-coated CdSe/ZnS QDs, previously reported, [32] are ionically conjugated to positively charged cyanine dye monomers in methanol. The remaining dye in solution is then aggregated by the addition of water, using conditions optimized to create uniform aggregates [33] that are ionically bound to the QD polymer coating. In Section 5.3, similar constructs are formed using a positively charged quantum dot bound to a negatively charged cyanine dye (BIC) in order to demonstrate the general utility of electrostatic assembly. Control experiments were performed to discount other binding mechanisms by using identically charged species. conjugation was confirmed using emission, absorption and photoluminescence excitation spectroscopy, as well as transient photoluminescence.

5.2 Synthesis of QD_{555nm}(-)/ J-$aggregate_{TTBC}$(+) Construct

ZnSe/CdSe/ZnS QDs emitting at 555 nm were synthesized using methods adapted from those reported previously [34,35]. To make ZnSe QDs, hexadecylamine (HDA, Alrich) was degassed in a 3-neck roundbottom flask at 110 °C, after which it was heated under Ar to 300 °C and a solution of 96 mg of diethyl zinc (filtered using a 0.2 um PTFE filter, Strem), 0.28 ml of trioctylphosphine selenide and 4.72 ml of trioctylphosphine (TOP, 98% Strem) was injected into the flask and heated at 270 °C for 1.5 hrs before cooling to 150 °C. Meanwhile, a 4-neck flask with 8 g of trioctylphosphine oxide (TOPO, 99% Aldrich) and 0.4 g of hexyphosphonic acid (HPA, 99% Alpha Aesar) was degassed at 160 °C before cooling under Ar to 150 °C and injecting 4 ml of the ZnSe QD solution. Immediately upon injection, a solution of 78 mg of dimethyl cadmium (filtered using a 0.2 um PTFE filter, Strem), 0.16 ml of TOP-Se and 4.84 ml of TOP was added to the flask dropwise at a rate of 1 drop per second. The solution was then held at 150 °C for 19 hours until the emission peak was stable at 532 nm. The QDs were precipitated twice by addition of butanol and methanol, and then redispersed after each precipitation in hexane. This solution was added to a 4-neck flask containing a solution of 10 g TOPO and 0.4 g HPA which had been degassed at 160 °C, then cooled to 80 °C. After removing hexane (solvent grade, Aldrich) by vacuum, the flask was heated under Ar to 155 °C and two solutions, one of 6 mg dimethyl cadmium, 49 mg diethyl zinc in 5 ml of TOP and the other of 160 mg hexamethyldisilathiane (TMS_2-S, Aldrich) in 5 ml of TOP, were simultaneously added at a rate of 1.5 ml per hour by syringe pump. After this, the QDs were cooled and precipitated twice from solution by the addition of butanol (solvent grade, Aldrich) and methanol (solvent grade, Aldrich), and then redispersed in

chloroform (anhydrous, Aldrich). Quantum yield of the completed QDs in chloroform was found to be ~50% using to Coumarin 540 (from Exciton, QY=89% in ethanol) as a reference. The size of the inorganic core/shell nanocrystals from TEM measurements was found to be 2.8 nm in radius, with a standard deviation of ~ 5%.

An anionic polyacrylic acid polymer was used to water solubilize the QD555s. The synthesis was adapted from those previously reported [32]. In a 250 ml 1-neck flask, 1.000 g of polyacrylic acid (2000 MW, Aldrich) was dissolved in 10 ml of DMF prior to adding a solution of 1.333 g of 1-Ethyl-3-[3-dimethylaminopropyl]carbodiimide hydrochloride (EDC, 99% Fluka) in 60 ml of DMF (anhydrous, Aldrich). Slowly, while stirring, 0.91 ml of octylamine was added dropwise to the flask and the solution stirred overnight. DMF was removed by vacuum until the total amount of solvent in the pot was ~5 ml. At this time, DI water was added until the polymer precipitated from solution and the supernatant was removed and discarded. Then 30 ml of DI water was added to the pot and stirred with 4 g of tetramethylammonium hydroxide. 30 ml of ethyl acetate (solvent grade, Alrich) was added to form two phases and the solution was stirred overnight. The mixture was placed in a separation funnel, allowed to separate and the aqueous fraction was retained. Any remaining ethyl acetate in the aqueous solution was removed under vacuum. Approximately 10 ml of 3 M HCl (diluted from 12M concentrated acid, Alrich) was added to precipitate the polymer, which was next centrifuged at 3900 RPM to remove the precipitate and redisperse it in 30 ml solution of DI water containing 800 mg of NaOH (pellets, Aldrich). The solution was vortexed and left to sit for a day to redisperse. Again ~10 ml of 3 M HCl was added to precipitate the polymer which was centrifuged at 3900 RPM and washed several times with DI water to remove excess HCl.

The resulting powder was then dried and crushed to form the amine modified polymer reagent. Water solubilization of the QDs was accomplished by adding 10 mg of QD550s, dried by vacuum, in 20 ml of chloroform. This solution was added dropwise to a stirring solution of 60 mg of amine modified polymer in 20ml of chloroform and stirred for 0.5 hours before the chloroform was removed by vacuum. 10 ml of pH 9 borate buffered solution was added to the dried polymer coated QDs to redisperse and store them as a stock solution (1mg/ml of QDs in buffered aqueous solution).

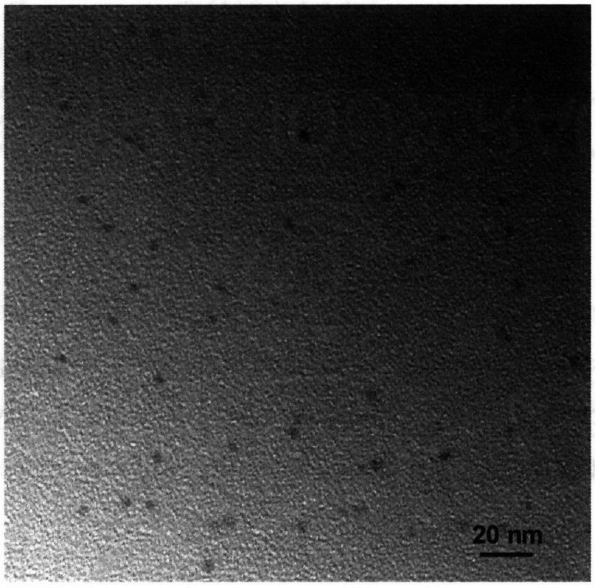

Figure 5.2: Transmission electron micrographs (using a JEOL 200 TEM) of polymer coated nanocrystals (ZnSe/CdSe/ZnS) at 80,000x magnifications. QD's averaged 5.6 nm in diameter with ~5 % standard deviation. The TEMs presented here are of QDs coated with the water solubilizing polyacrylic acid polymer. The initial decylamine capping ligand are calculated to add ~0.7 nm to the radius of the inorganic QD, as calculated using average bond lengths and angles, giving a total particle size of ~3.5 nm prior to coating with the polymer.

Formation of QD/J-aggregate using cationic 1,1',3,3'-tetraethyl-5,5',6,6'-tetrachlorobenzimidazolocarbo-cyanine (TTBC) was performed by adding 0.2 ml of a

solution of 0.1 mg/ml TTBC in methanol to 0.5ml of methanol in a glass vial. 0.1 ml of stock solution of anionic polymer coated QD555 (1mg/ml QDs in buffered aqueous solution) was added to the vial for the monomer to associate to the QDs prior to aggregation. 5 ml of DI water was then added quickly to the vial to cause the TTBC to aggregate (Figure 5.3).

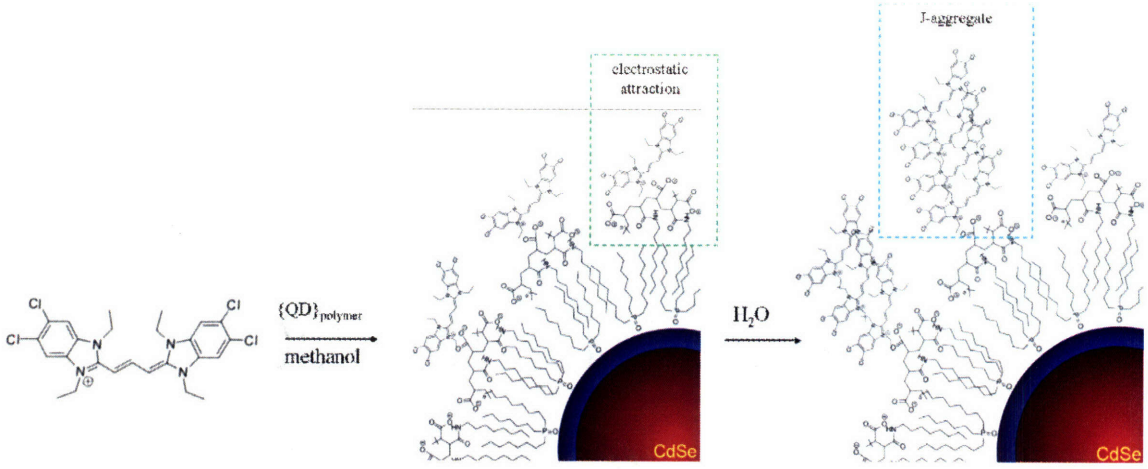

Figure 5.3: A representation of the reaction steps leading first to association of the TTBC monomer with the the anionic polymer coating and second to the aggregation of excess TTBC monomers with the anchoring TTBC molecules. The modified polyacrylic acid molecules are represented in a simplified fashion for clarity; in reality they may represent a bulkier interface with the solution.

5.3 Characterization of QD_{555nm}(-)/ J-$aggregate_{TTBC}$(+) Construct

5.3.1 Photoluminesence Spectroscopy

Steady state measurements of emission for the QD/TTBC constructs exhibit characteristic evidence of FRET transfer from the QD550s to TTBC J-aggregates, indicating electrostatic binding between the QD and J-aggregates. As can be seen in Figure 5.4, the QD/TTBC constructs emit light at λ = 585 nm with a FWHM of 12 nm when excited in

the UV. The QD emission is almost completely quenched by the dye aggregates and the emission intensity of the solution is significantly larger than for dye aggregated in the absence of QDs, with identical monomer concentrations (Figure 5.4).

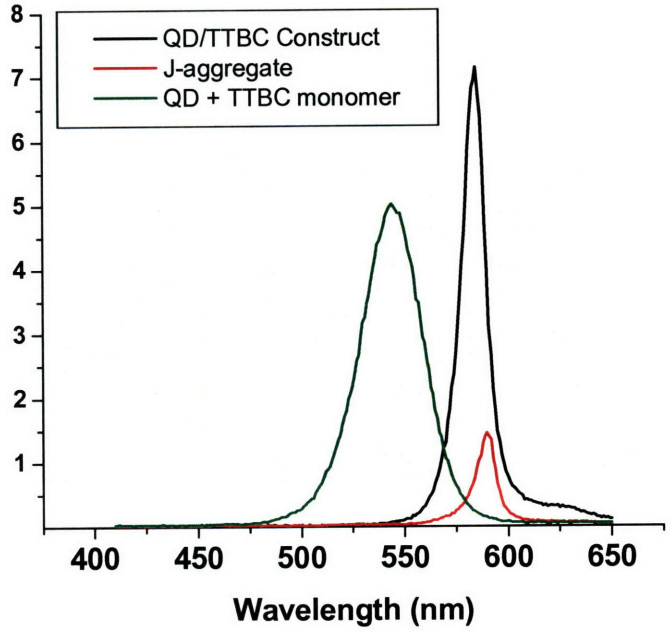

Figure 5.4: Emission of the QD/TTBC solution before aggregation (green curve), of the QD/J-aggregate constructs (black curve) and of J-aggregates in the absence of QDs (red curve). All species present are at equivalent concentrations for each measurement. Spectra were taken of solutions prepared simultaneously in quartz cuvettes, using a Fluoromax-3 (HORIBA Jovin Yvon) spectrometer.

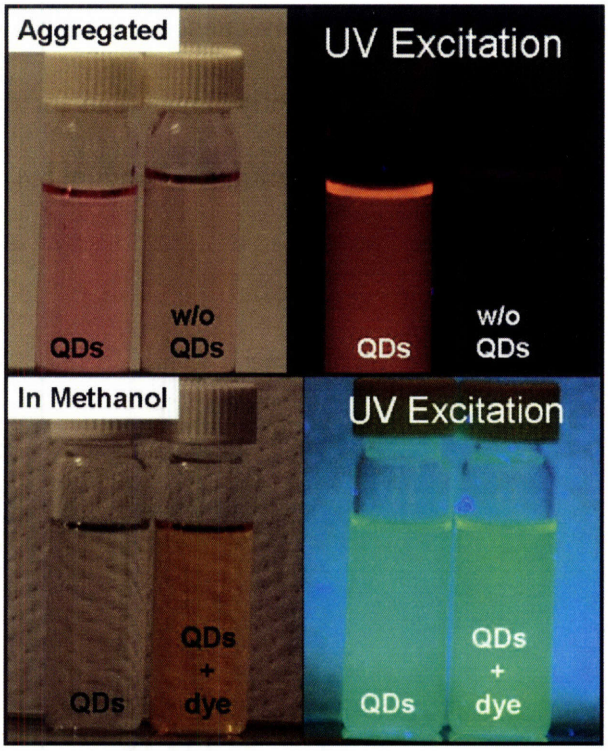

Figure 5.5: (Top) Photograph of two solutions, one of TTBC aggregated in the presence of QDs (left hand vial), and the other of TTBC aggregated in the absence of QDs (right hand vial). All other conditions were equivalent. The left hand vial displays significantly greater emission intensity when excited at 365 nm. (Bottom) A photograph of two more solutions, one of QDs in methanol and another of QD's in methanol with TTBC dye (monomeric form). Under UV excitation both solutions emit with the characteristic emission of quantum dots. There is no J-band emission from the right hand vial.

The quantum yield of the construct was measured to be 40% when excited at 365 nm using a reference sample of QDs (QY=70%) emitting at ~590 nm, which were in turn calibrated using rhodamine 610 (QY=95% in methanol) as a reference.

5.3.2 Absorption Spectra

The absorption spectrum of the constructs show both QD and J-band absorption features. The J-band of the construct is slightly blue-shifted and broadened compared to the J-band of dyes aggregated in the absence of QDs (Figure 5.6). These discrepancies are likely due to the difference in size of the aggregate formed on the QD's as opposed to those formed independently of the QD's. However, it is also possible that the dye emission is solvatochromically shifted, to some degree, due to the different local field

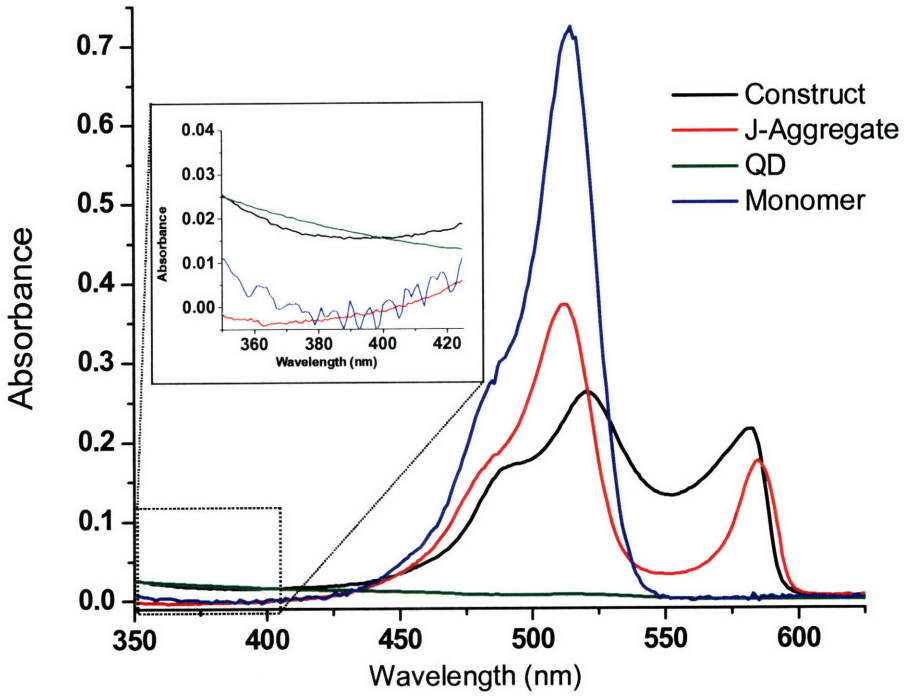

Figure 5.6: Absorption spectrum of the TTBC monomer (blue curve), TTBC aggregated in the absence of QDs (red curve), in the presence of QDs (black curve), and the absorption spectrum of the QDs alone (green curve). Concentrations of reactants are kept constant for all experiments (unless omitted). Inset: a close-up of the absorption spectrum at near UV wavelengths, demonstrating the role of the QDs in enhancing the solution absorption at those wavelengths (up to 25x).

environment of the negatively charged polymer as opposed to that of the solution. There is also a significant contribution of what appears to be monomer dye absorption after the aggregation steps are performed. The increased absorption of the construct due to the QDs as shown in Figure 5.6 (inset) is responsible for the increased PL of the construct at excitation wavelengths shorter than 400 nm.

5.3.3 Photoluminescence Excitation (PLE)

Evidence of FRET is also seen in the PLE spectra (Figure 5.7), further confirming the close association of the QD and J-aggregates. Emission from samples was collected at 590 nm and the excitation wavelength was scanned for QD/J-aggregate pairs (black curve) and J-aggregates (red curves). At wavelengths longer than 450 nm, the excitation spectra (Figure S1) show similar features for the J-aggregates and QD/J-aggregate pairs, since these peaks are due to absorption peaks in the monomer and J-aggregate forms of TTBC. The increased emission intensity in the range of 350-400 nm is consistent with UV absorption by the QDs followed by FRET into the J-band of the J-aggregates. The QD/J-aggregate constructs (black curve) show significantly greater emission intensity when excited in the UV, as shown by the ratio of the QD/J-aggregate pair emission to the normalized J-aggregate emission (purple curve). For ease in comparison due to the lower concentration of J-aggregates formed in the absence of QD's, the J-aggregate curve is rescaled (by a factor of ~8) to match the QD/J-aggregeate curve at ~500 nm, where only the J-aggregates are contributing to the emission intensity.

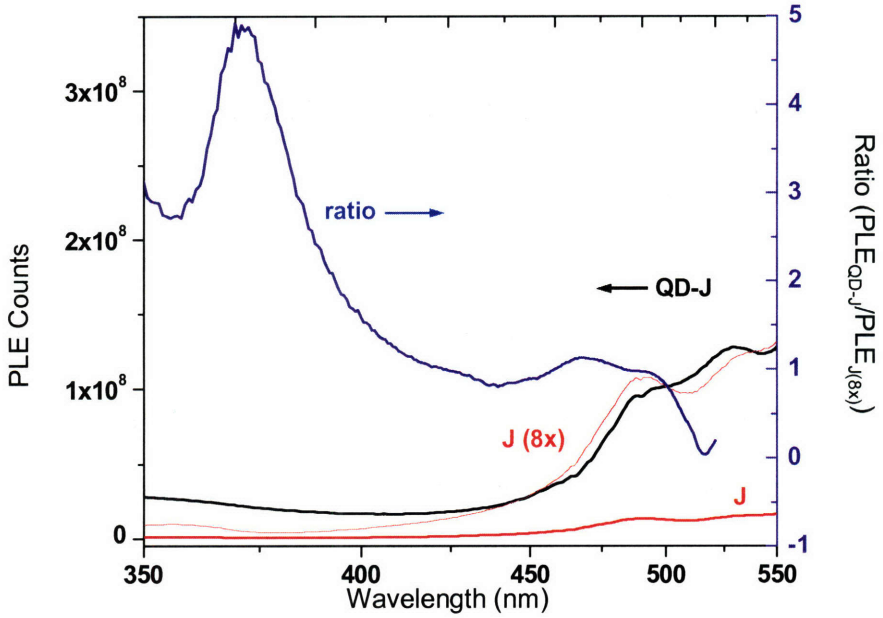

Figure 5.7: Photoluminescence excitation spectra of the QD/J-aggregate construct, collecting J-aggregate emission at ~590 nm while the excitation wavelength (x-axis) is scanned for QD/J-aggregate pairs (black curve), J-aggregate (red curve) and rescaled J-aggregate (scaled by a factor of ~8, also red). The purple curve is the ratio of the excitation spectra for the J-aggregate construct and the J-aggregate alone (rescaled).

The UV excitation creates excitons in the QD, which then transfer to the J-band of the J-aggregate, quenching the PL intensity of the quantum dot but increasing that of the J-aggregate. The relatively low optical density (~0.3) of the solution at 555 nm and the low emission intensity of non-conjugated J-aggregates when excited in the UV, ensures that the J-band emission observed cannot be attributed to absorption and re-emission of photons from nearby QDs or to direct UV excitation of the J-aggregates.

5.3.4 Transient Photoluminescence Measurements

While the steady state spectroscopic measurements point to FRET and hence close conjugation of the QD and J-aggregates, fluorescence lifetime measurements (Figure 5) are required to confirm these conclusions. To do so the quantum dot and the dye aggregate were excited separately, and the J-band emission was collected in each case in order to confirm the occurrence of FRET and to estimate the FRET rate. Samples were excited with 400 nm or 570 nm pulses obtained by second harmonic generation or opical parameteric amplification (Coherent OPA) of a 250 kHz amplified Ti:sapphire laser (Coherent RegA 9000). Emission was dispersed with a spectrometer (Acton) and time resolved with a streak camera (Hamamatsu C5680).

5.3.4.1 Exponential Fitting of Photoluminescent Decays to Find Lifetime, τ

QD and J-aggregate PL decays (QDs absent) were fitted using an exponential decay curve of the form:

$$y = y_0 + A_1 e^{-x/\tau_1} \qquad (5.3.4.1a)$$

where y_0 is the baseline (usually fixed to zero to start), A_1 represents the magnitude, and τ_1 is the lifetime. The single exponential curve used in Figure 5 (in the main text) to fit the QD PL decay gives a lifetime of 5.6 ns while a double exponential curve of the form:

$$y = y_0 + A_1 e^{-x/\tau_1} + A_2 e^{-x/\tau_2} \qquad (5.3.4.1b)$$

yields 7.0 ns as the lifetime (discarding the short time component $\tau_2 \sim 0.6$ ns). Although double exponentials are routinely used to fit QD PL decays, [36] a single exponential fits reasonably well to the curve in this case. For the QD/J-aggregate exponential decays, a

multi-exponential decay is expected and equation (5) is used to fit these curves. In this case fitting is performed by setting y_0 and A_2 to 0.0 to start, finding the best fit single exponential then slowly releasing these terms to find a truer fit. In this case the short time components ($\tau_2 \sim 0.1$ ns in most cases) are merely useful fitting parameters while the lifetime of the constructs are reported as the longtime component τ_1.

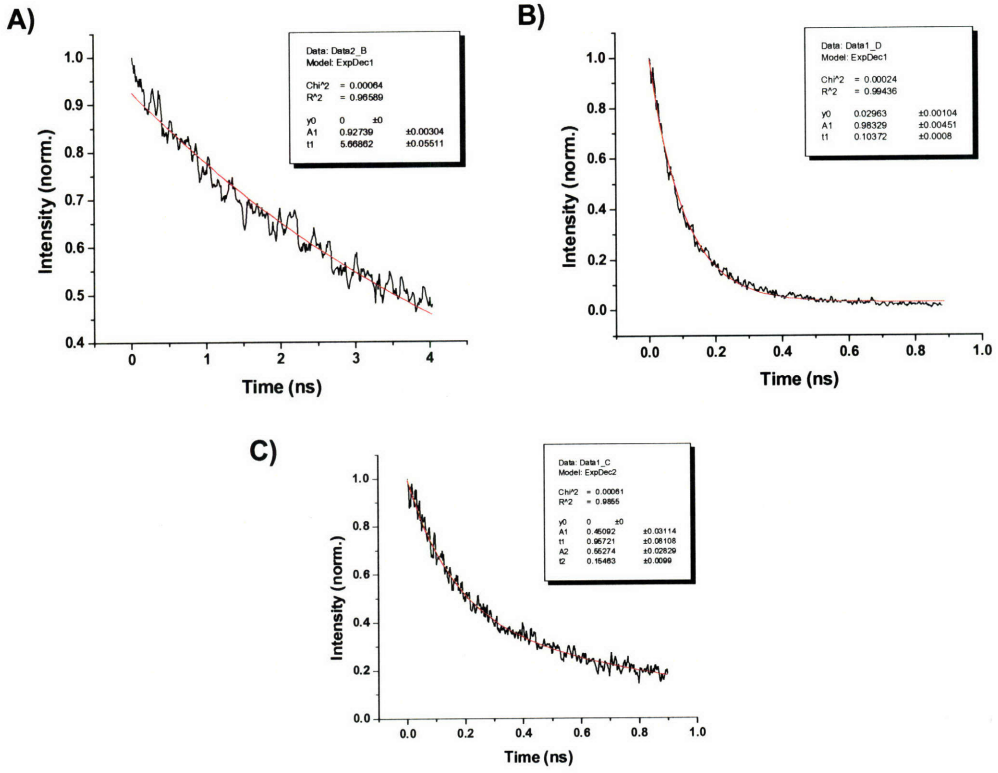

Figure 5.8. Single exponential fits of A) QD B) J-aggregate PL decays using Equation 5.3.4.1a. The C) QD/J-aggregate construct decay curve is fit using a double exponential as in Equation 5.3.4.1b.

5.3.4.2 Analysis of Transient Photoluminescence Data

The fluorescence lifetime of the construct was found to be ~700 ps when excited at 570 nm (direct excitation of the J-aggregate), while that of the non-conjugated J-aggregates is ~100 ps [36] (Figure 5.9).

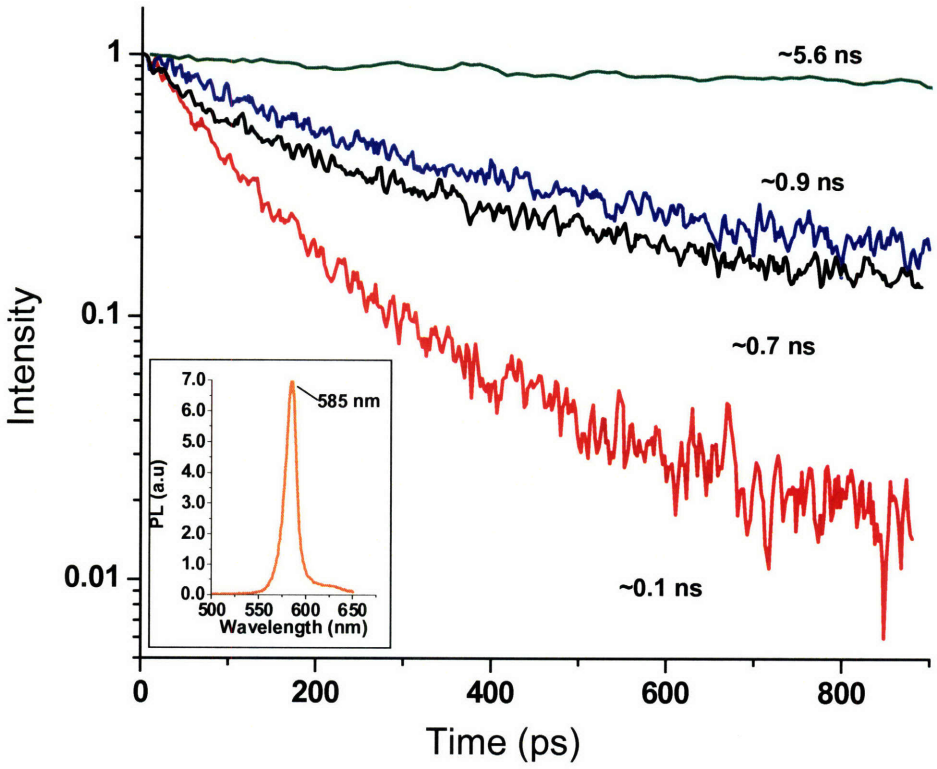

Figure 5.9: Time resolved measurements of exciton lifetimes as detected by collecting spectrally resolved emission at the J-aggregate peak (inset). The decay curves are plotted for 570 nm excitation of TTBC aggregated in the absence of QDs (red curve) and QD/J-aggregate conjugates (black curve), as well as for 400 nm excitation of the QD/J-aggregate conjugate (blue curve) and the QDs with no dye present (green curve).

The difference in rate between these two species supports the conclusion that construct J-aggregates are indeed significantly smaller than those formed separately, in agreement with the earlier DLS conclusions. Meanwhile, the lifetime of the construct excited at 400 nm (where QD absorption is dominant) is 900 ps while that of the non-conjugated QD is 5.6 ns (measured at the peak of the QD emission). As expected, we see no indication of absorption and re-emission, where the emission at the J-band would follow the lifetime of the QD. The fact that the fit lifetimes of the construct excited at both 400 nm (exciting

the QDs) and 570 nm (exciting the J-aggregates) are so close in value indicates that the FRET rate must be fast relative to the lifetime of the acceptor (the J-aggregate). The lack of an observable risetime within the resolution of the instrument, ~50 ps, indicates that the FRET rate must be at least that fast.

5.3.5 Calculating the FRET Rate

We can calculate the FRET in two ways: (i) by using modified forms of the generalized Forster equations discussed in Section 1.8.1.1 and (ii) by estimating the efficiency of FRET between the QD and dye aggregate from the static PL measurements.

5.3.5.1 Derivation of the Useful Forster Equation

For a donor/acceptor pair consisting of a single QD and a single acceptor molecule A, the FRET rate, Γ_{ET}, is determined using Forster's equation:

$$\Gamma_{ET} = \frac{1}{\tau_D}\left(\frac{R_F}{R}\right)^6 \qquad (5.3.5.1a)$$

Where τ_D is the QD fluorescence lifetime measured in the absence of the acceptor, R is the distance between the QD center and molecule A, and R_F is the Forster radius characterizing the transfer process for the specific donor/acceptor pair [37,38].

R_F itself is determined from the integral expression:

$$R_F^6 = \frac{9}{8\pi}\frac{c^4}{n^4}\kappa^2\eta_D\int\frac{S_D(\omega)\sigma_A(\omega)}{\omega^4}d\omega \qquad (5.3.5.1b)$$

Where c is the speed of light, n is the refractive index of the medium between the donor and acceptor, η_D is the quantum yield of the donor photoluminescence, κ^2 is the geometric factor describing the relative orientation of the donor and acceptor transition dipoles, σ_A is the acceptor absorption cross-section, and S_D is the donor PL spectrum normalized such that the integral of S_D over frequency is unity.

In applying Equation (5.3.5.1b) to the QD/TTBC constructs, we set κ^2 equal to 2/3, the value used for randomly oriented donor/acceptor pairs [39]. Even though the QD cannot freely rotate within the construct, setting $\kappa^2 = 2/3$ is justified because there is no predetermined orientation of the TTBC acceptor relative to the QD. We set $n = 1.4$, as in [40-42], because the constructs are immersed in aqueous solution with a polymer (polyacrylic acid) separating the QD and TTBC components. Based on quantum yield measurements of QD's prior to conjugation (~50%), we assume $\eta_D = 0.5$ for the conjugated QD donor.

To derive σ_A, we need to determine the average absorption coefficient of a single TTBC molecule when situated in the construct. We start by taking absorption spectrum of the construct solution and then subtract from it the QD contribution. From dilution experiments, we know that nearly all of the TTBC in the solution is conjugated to the QDs, so the remainder is the absorption spectrum of TTBC situated in the constructs. We then divide this by the number of TTBC molecules in the solution to find σ_A.

In deriving σ_A, we include both the monomer and J-aggregate features of the TTBC absorption spectrum. From the dilution experiments, we know that both forms of the dye are situated on the constructs, so the description of an average construct TTBC

molecule must capture both of these possibilities. With this composite σ_A in Equation Equation (5.3.5.1b), the overlap integral accounts for energy transfer occurring from the QD to either species.

The Forster radius for FRET from a QD to a single conjugated TTBC acceptor that is in either monomeric or J-aggregate form from this calculation gives R_F = 5.1 nm. The net energy transfer rate from the QD to surrounding acceptor dyes will depend on the number of acceptor molecules as well as the distance between them and the QD donor. In this section, the equation describing FRET between a QD and a single acceptor described by Equation (5.3.5.1a) is expanded upon to account for situations where the QD is surrounded by either a monolayer-thick or thicker shell of acceptor dye (Figure 5.10b and Figure 10c, respectively). This derives Equation (5.3.5.1f) below.

When the QD donor is surrounded by a thin shell of acceptor molecules, separated by the same distance, *R,* from the QD center, the net transfer rate increases with an increased number of acceptor molecules. The surface area of the shell is $4\pi R^2$. So for a shell of thickness *dR*, the total volume is given by $4\pi R^2(dR)$. Consequently, if the volume density of dye in the shell is ρ_A, the total number of dye molecules is given by $4\pi R^2(dR)\rho_A$. Hence the net FRET rate is:

$$\Gamma_{ET} = \frac{1}{\tau_D}\left(\frac{R_F}{R}\right)^6 4\pi R^2(dR)\rho_A \qquad (5.3.5.1c)$$

Note that Equation (5.3.5.1c) possesses the $1/R^4$ dependence characteristic of FRET from a point to a plane [43], as both plane and shell are topologically similar.

When the QD donor is instead surrounded by a thick shell of acceptor dye, the net transfer rate again depends on the total number of acceptor molecules. In this case,

however, care must be taken to account for the variation in the distance R between donor and acceptors. The net transfer rate is therefore the integral of Equation (5.3.5.1c) over the thickness of the shell. If the shell extends from radius R_1 to R_2, then the net transfer rate is given by the integral:

$$\Gamma_{ET} = \int_{R_1}^{R_2} dR \frac{1}{\tau_D}\left(\frac{R_F}{R}\right)^6 4\pi R^2 \rho_A \quad (5.3.5.1d)$$

which yields:

$$\Gamma_{ET} = \frac{1}{\tau_D}\left(\frac{R_F}{\sqrt{R_1 R_2}}\right)^6 \frac{4}{3}\pi\left(R_2^3 - R_1^3\right)\rho_A \quad (5.3.5.1e)$$

We can simplify this expression by recognizing that $4/3\,\pi\left(R_2^3 - R_1^3\right)\rho_A = N_A$. Hence, the transfer rate from a single QD to a thick shell of acceptors is:

$$\Gamma_{ET} = \frac{1}{\tau_D}\left(\frac{R_F}{\sqrt{R_1 R_2}}\right)^6 N_A \qquad (5.3.5.1f)$$

Conceptually, Equation (5.3.5.1e) is similar (in form) to the expression for transfer from a QD to a single acceptor. For the thick acceptor shell, an effective radius characterizes the average distance separating the QD and acceptors, which is given by the

geometric mean of R_1 to R_2 ($\overline{R} = \sqrt{R_1 R_2}$). This "average" transfer rate is then multiplied by the number of acceptor molecules in the shell, N_A, to give the total transfer rate, Γ_{ET}.

There are two key assumptions in the derivations of Equations (5.3.5.1b-e). Firstly, the orientation of the acceptor molecules is not fixed relative to the QD surface. Hence, the same geometric prefactor, κ^2, that is used to average the FRET rate over all possible donor-acceptor orientations in the single acceptor case can be applied to the multiple acceptor thin and thick shell cases. The second key assumption is that the FRET rate is linearly dependent on the dye density, ρ_A, within the shell. This assumption holds when the percent absorption of the shell, had it been unfolded into a thin film, is less than a few percent [44,45]. Otherwise, the FRET process is altered via near field effects within the densely packed acceptor layer. In the scenarios presented in this paper, the dye density appears to fall within the safe low loading limit. There are 150 dye molecules per QD within a polymer shell volume of ~2000 nm^3 and the absorption cross section per dye molecule is $\sigma = 1.2 \times 10^{-16}$ cm^2. Hence, the absorption coefficient for the acceptor shell is $\alpha \sim 9 \times 10^3$ cm^{-1}. The thickness of this shell is only 4.5 nm, and if the shell were unfolded into a thin film, it would absorb only 0.4% of the incident light. Therefore, it is valid to assume the FRET rate is linearly dependent on the dye density for the constructs in consideration.

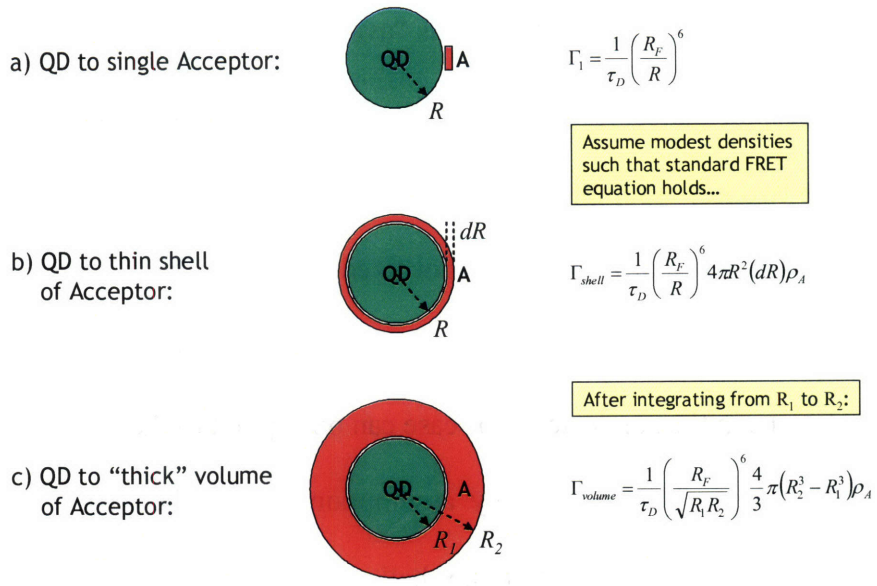

Figure 5.10: Three different energy transfer scenarios consisting of FRET from a single QD to either (a) a single acceptor molecule, (b) a thin shell of acceptor or (c) a thick volume of acceptor.

5.3.5.2 Summary of the Useful Forster Equations

The FRET rate from a spherical donor (i.e. the QD) to a surrounding shell of acceptors (i.e. the J-aggregates) extending from inner radius R1 to outer radius R2, (as derived above):

$$\Gamma_{ET} = \frac{1}{\tau_D}\left(\frac{R_F}{\sqrt{R_1 R_2}}\right)^6 N_A \qquad (5.3.5.2a)$$

Where RF is the characteristic FRET radius of a single donor/acceptor pair using the standard Forster formalism [37,38], τD is the donor lifetime prior to conjugation, and NA is the number of acceptors within the shell.

The second useful equation in determining the FRET rate can be inferred from the energy transfer efficiency, E (no derivation is necessary):

$$E = 1 - \frac{\int PL_{DA}(E)dE}{\int PL_{D}(E)dE} = 1 - \frac{\tau_{DA}}{\tau_{D}} = \frac{\Gamma_{ET}}{1/\tau_{D} + \Gamma_{ET}} \qquad (5.3.5.2b)$$

where PLDA(E) [PLD(E)] corresponds to the donor PL spectrum in the presence [absence] of the acceptors, and likewise τDA is the donor lifetime in the presence of the acceptors.

5.3.5.3 Calculation of the FRET Rate

We can quantify the FRET rate, Γ_{ET}, based on the PL quenching of the QD emission. In the presence of TTBC acceptors, the PL intensity of the QD spectrum is reduced by a factor of 100 or more. To calculate the FRET transfer efficiency for the QD/J-aggregate constructs, it is necessary to determine the degree to which the PL intensity of the QD donor has been quenched by the presence of the TTBC acceptor. Figure 5.11a shows that in a linear plot of QD/J-aggregate construct PL, no QD emission is discernable at 555 nm, suggesting 100% transfer efficiency. However, Figure 5.11b shows that on a logarithmic scale it is possible to identify where a QD spectral feature could exist hidden in the J-band peak and thus to determine the maximum possible contribution from QD emission intensity. To determine the degree of quenching, we compared the intensity level of these features to the spectrum of the construct-free QD sample, and we determined that if the PL data of the stand-alone QD is scaled down by a factor of 100, then it matches the intensity level of the QD features in the construct. The scaled QD spectrum is included (in blue) in Figure 5.11b to illustrate this point. Hence, we conclude that the quenching ratio is at least 100, leading to a minimum FRET efficiency E = 99.0%.

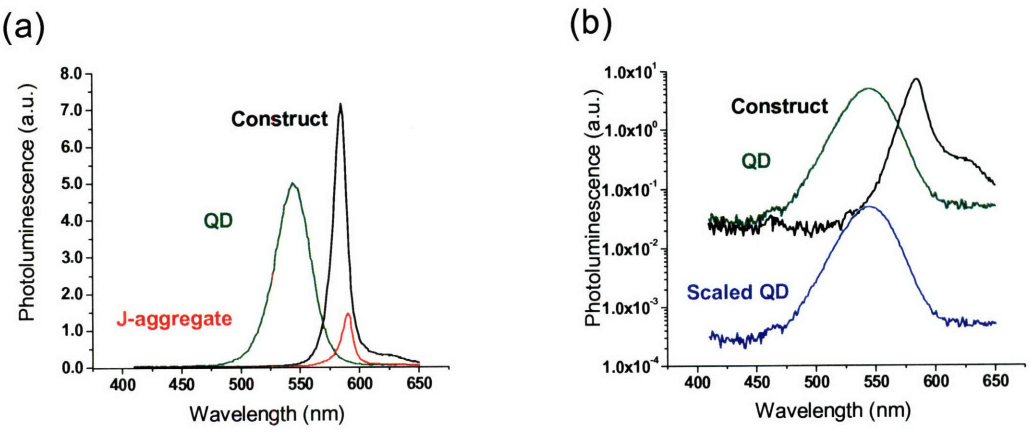

Figure 5.11: Photoluminescence spectra of the construct, J-aggregate and QD, samples. (a) PL data depicted with linear vertical axis. (b) PL data plotted with logarithmic vertical axis and copy of QD spectrum scaled down by a factor of 100.

Using (5.3.5.2b), this means that the quenching efficiency, E, is at least 99%, and equivalently, that the FRET rate is at least 99 times faster than the QD lifetime of 5.61 ns. Hence the "lifetime" associated with the FRET process, $1/\Gamma_{ET}$, is at most 57 ps. This timescale is in agreement with the observations found by transient photoluminescence in which the rise time of the PL decay was less than 50ps (the resolution of the instrument).

5.3.4 Characterization of J-aggregate Formation on QD_{555nm}(-)

Addition of water to the QD/monomer solution causes aggregation of the dye onto the QD as illustrated in Figure 5.3. Prior to aggregation, no FRET is observed, due to a combination of (i) smaller spectral overlap between the QD donor and the dye monomer acceptors, and (ii) weaker association between the monomers and the polymer shell around the QDs. Conjugation is driven by electrostatic attraction of opposite charges on

the dye and the QD coating. This is evident from the observation that FRET pairs form only when the QD and the J-aggregate are oppositely charged, but not when they are both

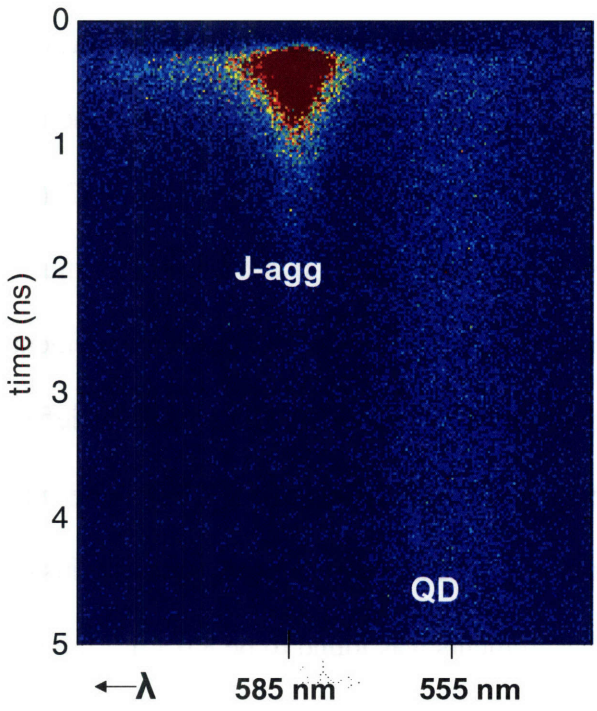

Figure 5.12: Spectrally resolved photoluminescence decay of negatively charged polyacrylic acid coated QDs along with negatively charged BIC dye aggregates. The samples were prepared by aggregating BIC monomer in the presence of carboxylic acid coated QD's (aggregation conditions described in Section 5.4). As can be seen in Figure S4, the emission peaks of both the QD's and the BIC J-aggregates are plainly visible. The QD peak at 555 nm clearly has a lifetime on the order of several nanoseconds, as is expected for QD's, while the BIC J-aggregate's lifetime is close to a few hundred picoseconds, similar to those measured for BIC J-aggregates alone. There is no indication of FRET between the QD's and the BIC dye aggregates, despite the favorable overlap of their emission and absorption bands. This indicates that the two species are not likely to be bound together, as would be expected for two negatively charged species, consistent with our hypothesis that electrostatic attraction is the dominant binding mechanism.

negatively charged (Figure 5.12). In the latter case, emission from both the QD and the aggregate can be seen simultaneously, and the independent lifetimes of each can be spectrally resolved.

The size of the aggregates formed in the construct species can be estimated by comparing hydrodynamic radii of the QDs before and after the aggregation step using dynamic light scattering (DLS) measurements. In Figure 5.13 (top left), the polymer coated QDs are easily identified with a hydrodynamic radius of 5.9 nm in this measurement. The average radius obtained over three measurements was 5.6 ± 0.6 nm. The dye aggregates formed in the absence of QD's (bottom left) show a single large species with an average hydrodynamic radius of 55 ± 5 nm over multiple measurements (49 nm in the example shown). The average hydrodynamic radius of the QD/J-aggregate species over multiple measurements was found to be 8.0 ± 1.7 nm (9.3 nm in the example shown) with a second, smaller peak at 29 nm probably from a small number of J-aggregates formed independently from QD's or possibly from aggregates remaining from the polymer coating process (a similar small peak can be seen in the QD DLS data). These larger particles made up on average less than 20% of the material detected (17.6% ± 2% in the example). The observation of FRET implies that J-aggregates are attached to the QD. However, the measured change in apparent radius of the QD's after aggregation is 2.4 ± 1.8 nm which is not statistically significant. The fact that the attached aggregates are not directly observable by DLS makes it reasonable then to conclude they are small enough to be masked by a combination of the error of the measurement (2 nm) and the change in size of the polymer shell hydrodynamic radius due to charge passivation upon aggregation. This change cannot be larger than the total hydrodynamic of the polymer

shell itself, which is found to be ~4 nm using measurements of hydrodynamic radius, known core size and the calculated length of the ligand.

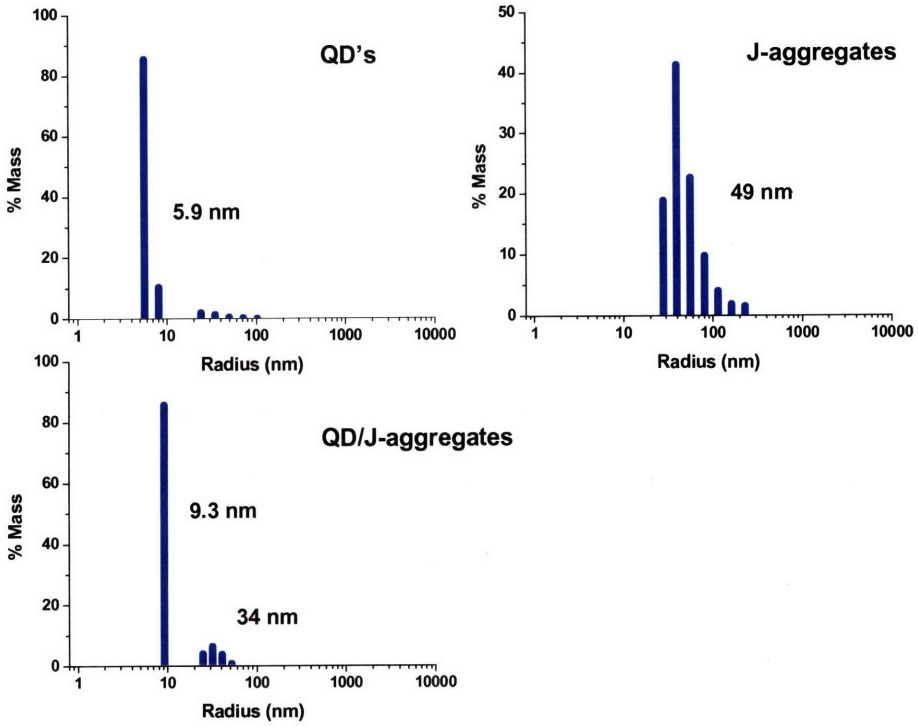

Figure 5.13: Examples of Dynamic Light Scattering measurements (DLS) of three species: (top left) QDs coated with polyacrylic acid, (top right) J-aggregates formed in the absence of QD's, and (bottom left) QD/J-aggregate construct.

The lack of significant change in the size, as measured in DLS, despite the presence of attached aggregates, as indicated from FRET, is due to two factors. First the aggregates formed are much smaller than those formed in the absence of QD. Secondly, the addition of positively charged dye molecules decreases the overall negative charge of the construct, which results in smaller size for the solvation shell around the construct. Furthermore if the boundary between the polymer and solution is diffuse, dye aggregates could be embedded within the polymer shell. Considering the measurement error (±2 nm) and the size of the polymer shell (~4 nm), we can safely surmise that the aggregates must then be less than 6 nm in length on average.

A lower bound for the size of the J-aggregates can be established by estimating the area across which the exciton is delocalized. This area, known as the coherence domain, is described by the number of participating molecules, N_c, and is given by the expression [46]:

$$N_c = (\Delta M / \Delta J)^2 \qquad (4)$$

where ΔM and ΔJ are the FWHM of the absorption peaks of the J-aggregate and monomer, respectively. From the absorption spectra, we find $N_c > 5$ molecules, setting a lower bound of ~1 nm for the size of the aggregates. This allows us to estimate a maximum diameter of the aggregates as ~6 nm, giving a range of 1-6 nm for the diameter, with the coherence length calculated from the emission spectrum of the QD/J aggregate construct as a the minimum size.

In contrast, large aggregates which are 55 nm in hydrodynamic radius are measured by DLS when formed in the absence of QDs (Figure 5.13) [47]. Thus the available anionic carboxylic acid sites on the QD appear to serve as nucleation points for J-aggregate formation, resulting in many more J-aggregates of significantly smaller size.

Aggregating in the presence of the oppositely charged QDs also confers a greater degree of stability to the J-aggregate compared to those formed in the absence of QDs. Unlike free aggregates in solution, J-aggregates in the QD/aggregate construct can be diluted several times without redissolving, indicating a stronger attachment of the monomers within the aggregates bound to the QD. In Figure 5.14, PL spectra of QD/J-aggregate pairs and J-aggregate samples are taken as a function of dilution. Samples were

diluted by addition of a buffer/methanol/water mixture identical to that in which the species were formed. The PL spectra on the right show as series of dilutions for QD/J-aggregate pairs (top) and J-aggregates (bottom) relative to the undiluted samples. The plots, on the left, show the integrated area of the PL spectra versus the relative concentration (%) for both species.

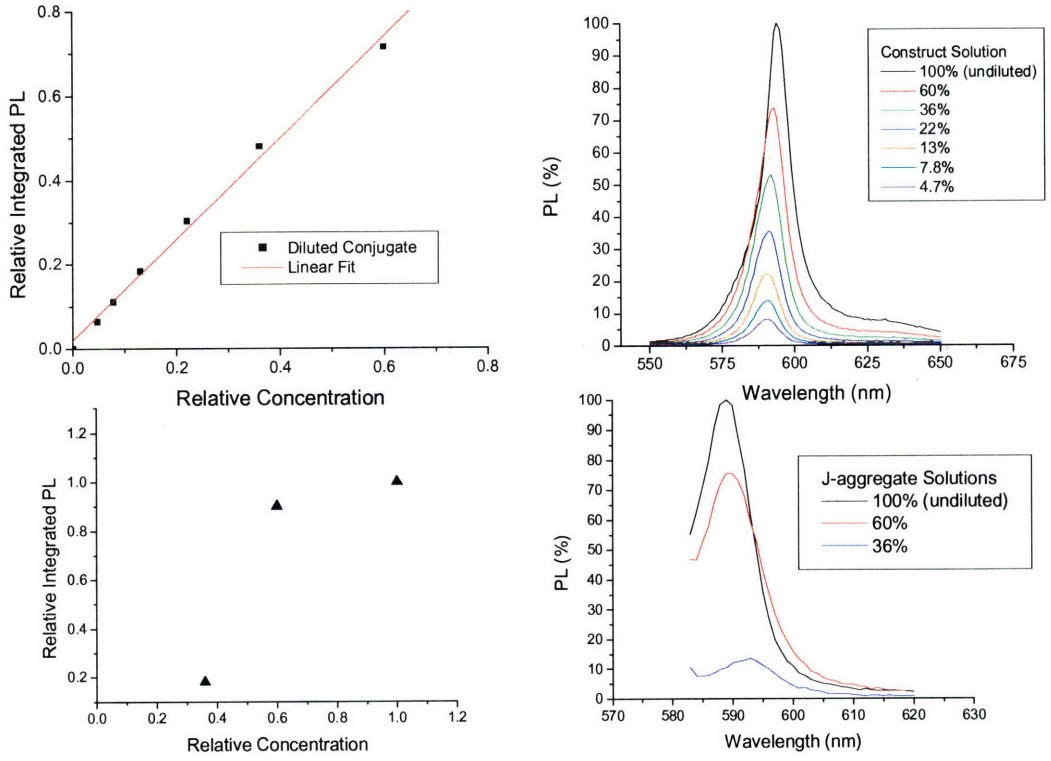

Figure 5.14: Serial dilutions of the QD/J-aggregate construct (top, right and left), along with that of the J-aggregates formed in the absence of QDs (bottom, right and left).

The top left plot shows that diluting the construct solution results in a linear decrease in PL intensity as would be expected from a molecular species or a stable construct. The bottom left plot shows a non-linear decrease in integrated intensity with dilution, consistent with dissolution of the aggregates into monomers, which do not emit from the J-band. J-aggregates that are part of the QD/J-aggregate construct are therefore more

stable, providing further evidence that the J-aggregates are bound to the QDs. This also suggests that QD/J-aggregate pairs could prove to be more robust than J-aggregates alone.

5.4 QD_{570nm}(+)/ J-$aggregate_{BIC}$(-) Construct

To examine the generality of electrostatic assembly observed in the TTBC/QD system, we select a negatively charged dye, BIC, and couple it in the same fashion to a positively charged, aminoPEG [48] coated QD.

5.4.1 Synthesis of QD_{570nm}(+)/ J-$aggregate_{BIC}$(-) Construct

CdSe/ZnS QDs emitting at 570 nm were synthesized [34,49] by methods adapted from those previously reported. In a 3-neck 50ml roundbottom flask, 3.25 g of TOPO (99%), 3.0 g of TOPO (tech.) and 5.75 g of HDA, and 0.28 g of hexylphosphonic acid (HPA, 99% Alpha Aesar) were degassed at 160 °C before heating under Ar to 360 °C. A solution of 0.31 g of cadmium 2,4-pentadionate ("cad-AcAc", 99% Strem), 0.5 ml of DDA, in 8 ml of TOP was degassed at 110 °C prior to cooling and adding 2 ml of 1.5 M TOP-Se. This solution was then injected into the flask at 360 °C and immediately cooled. Then the CdSe QDs were precipitated from solution twice with butanol and methanol, redispersing each time in hexane. This solution was added to a 4-neck flask containing a solution of 10 g TOPO and 0.4 g HPA which had been degassed at 160 °C, then cooled to 80 °C. After removing hexane by vacuum, the flask was heated under Ar to 100 °C and 0.5 ml of decylamine (96% Aldrich) was added and the solution stirred for 1 hour. After

this, the flask was heated to 170 °C and two solutions, one of 18 mg dimethyl cadmium, 72 mg diethyl zinc in 5 ml of TOP and the other of 252 mg TMS2-S in 5 ml of TOP, were simultaneously added at a rate of 1.5 ml per hour by syringe pump. The QDs were then cooled and precipitated from solution by the addition of butanol and methanol, and then dried under vacuum to remove all solvent. Quantum yield of the completed QDs in chloroform was found to be ~30% using Rhodamine 590 (from Exciton, QY=89% in ethanol) as a reference.

Synthesis of cationic aminoPEG with a dithiol ligand functionality has been reported previously [48]. Cationic solubilization of the QD570s was accomplished by adding approximately 2 mg of QD570s, dried by vacuum then dispersed in 100ul of hexane, to 50 ul of DHLA-amino-PEG in 100 ul of methanol and stirred at room temperature. for 45 minutes before adding 2 ml of ethanol and 2 drops of chloroform to stabilize the particles before precipitating them with hexane. The particles were then centrifuged at 3900 RPM and the supernatant discarded before redispersing the QD's in 2 ml of DI water to form a stock solution (~1mg/ml of QDs in water).

Formation of the QD(+)BIC(-) QD/J-aggregate was accomplished by adding 0.2 ml of a solution of BIC (0.1 mg/ml in water) to 0.1 ml of stock solution of DHLA-amino-PEG coated QD570s (~1mg/ml in water) and 2 ml of DI water, in a glass vial. One to two drops of concentrated NaCl solution were then added to cause immediate aggregation of the BIC onto the QDs.

5.4.2 Characterization of QD_{570nm}(+)/ J-$aggregate_{BIC}$(-) Construct

For this BIC(-)/QD(+) system we observe nearly identical FRET characteristics as those observed in the TTBC(+)/QD(-) system. The absorption spectrum of the conjugate species in Figure 5.15 shows that the BIC dye has in fact aggregated in solution from the appearance of the characteristic J-band peak.

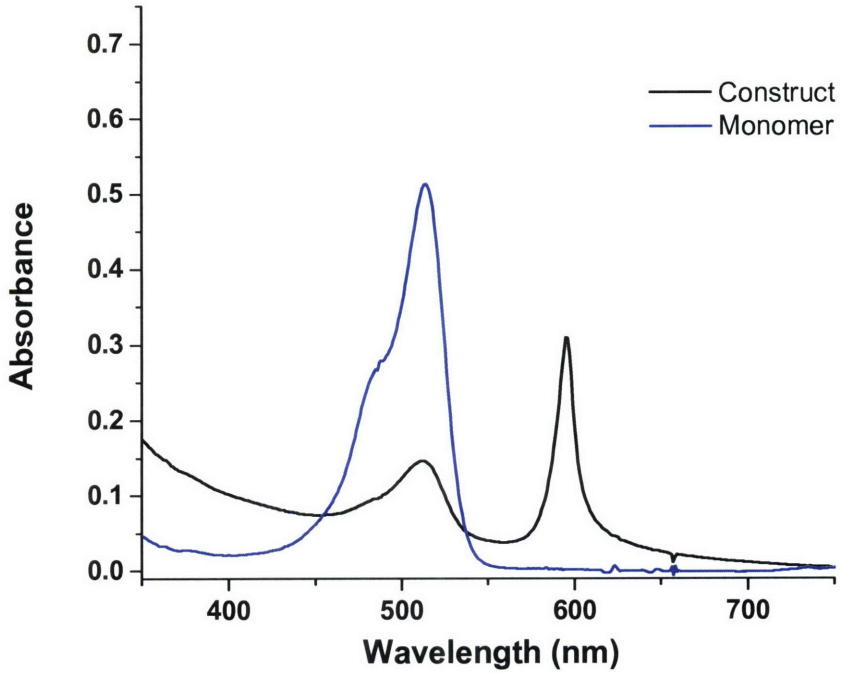

Figure 5.15: Absorption spectra of the BIC dye monomer (blue curve, no QDs) and after the addition of QDs, and aggregation of the dye (black curve). The J-band absorption peak is clearly visible ~590 nm and the QDs absorb strongly in the UV.

Once conjugated to the QD, the emission of the QDs is completely quenched. As can be seen in Figure 5.16, the emission spectrum of the conjugate is completely dominated by emission from the BIC aggregate, which has a FWHM of 12 nm. It has been observed that BIC aggregates at significantly lower salt concentration in the presence of the QDs than without. The overall enhancement of the conjugate emission over that of the

aggregate alone is nearly a factor of 100, due to the increased absorption of the conjugate species at 400 nm and the greater number of aggregate species formed in the presence of the QDs.

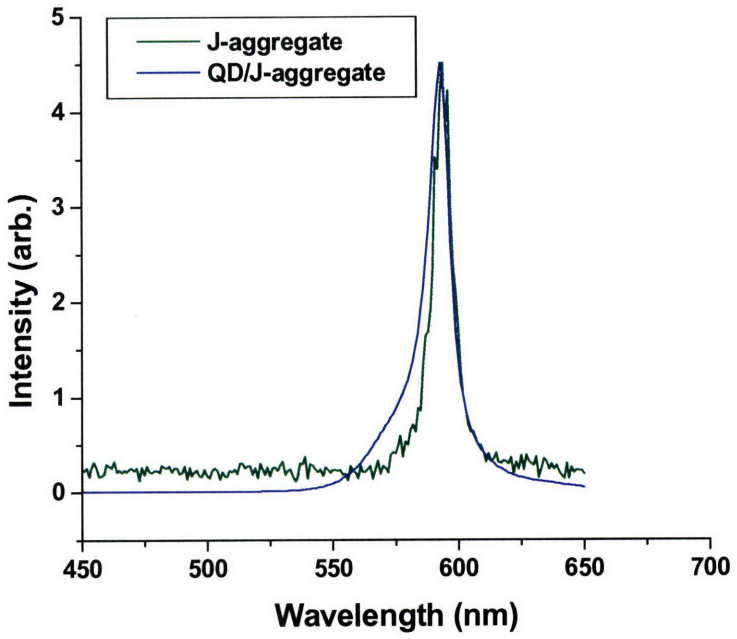

Figure 5.16: Normalized PL spectra of the QD/BIC construct (blue curve) and BIC aggregated in the absence of QDs when excited at 365 nm. Both species are emitting from the J-band state but the integrated intensity of the construct emission is ~100x that of the BIC aggregate alone under equivalent excitation intensity. This is due both to the increase in absorption in the UV due to the presence of the QDs and also the much greater concentration of aggregates that forms when the QDs are present.

The PL lifetime decay (Figure 5.17) for this species shows no QD emission and a fast risetime (resolution limited) of the construct lifetime curve coupled with a decay constant similar to that of the J-aggregate alone. As in the case of the TTBC/QD construct, this indicates that the FRET rate is much faster than the acceptor excited state lifetime.

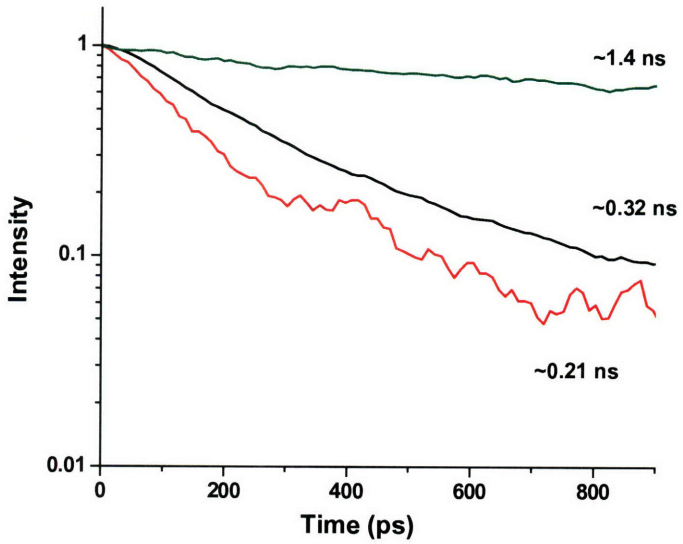

Figure 5.17: Time resolved measurements for the QD/BIC construct. The QD lifetime (green curve) is observed to be very long compared to that of the dye aggregated onto the QD in the construct (black curve) and the dye aggregated in the absence of QDs (red curve). Once again no rise is observed in either peak, and the lifetime of the aggregate dye is nearly equivalent in both cases indicating a transfer rate faster than the resolution of the instrument (~50 ps).

Thus the TTBC/QD system does not appear to be unique to any one specific dye or any one particular ligand system for dispersing QDs in water. We expect that this method of binding may work generally for any system where the QD and the monomers are oppositely charged and the aggregation conditions can be replicated in the presence of the QD.

5.5 Summary

This work demonstrates the synthesis of QD/J-aggregate constructs formed from conjugating positively and negatively charged cyanine dye aggregates onto an oppositely charged QD. Spectroscopic evidence of FRET is observed within the construct such that the species are in fact closely bound in solution. The observed FRET characteristics of the system are in agreement with calculations yielding reasonable results for the energy transfer rate and the Forster radius. The spectral features of this material could make it useful in optical down-conversion devices or for biological multiplexing applications.

My collaborators on the work presented in this chapter was Jonathan Tischler, who did the theory calculations, and Gautham Nair, who performed the lifetime decay measurements. I'd also like to thank Brian Walker, who contributed the dilution experiments, and Wenhao Liu, for his help with the DLS measurments.

5.6 References

(1) Coe, S.; Woo, W.-K.; Bawendi, M. G.; Bulovic, V. *Nature* **2002**, *420*, 800.

(2) Coe-Sullivan, S.; Steckel, J. S.; Woo, W.-K.; Bawendi, M. G.; Bulovic, V. *Adv. Funct. Mater.* **2005**, *15*, 1117.

(3) Era, M.; Adachi, C.; Tsutsui, T.; Saito, S. *Chemical Physics Letters* **1991**, *178*, 488-490.

(4) Era, M.; Adachi, C.; Tsutsui, T.; Saito, S. *Thin Solid Films* **1992**, *210*, 468-470.

(5) Achermann, M.; Petruska, M. A.; Koleske, D. D.; Crawford, M. H.; Klimov, V. I. *Nano Lett.* **2006**, *6*, 1396-1400.

(6) Springle, I.; Bayley, P.; Crossland, W.; Needham, B.; Davey, A. *Macromolecular Symposia* **2000**, *154*, 37-44.

(7) Montali, A.; Bastiaansen, G.; Smith, P.; Weder, C. *Nature* **1998**, *392*, 261-264.

(8) Vecht, A.; Newport, A. C.; Bayley, P. A.; Crossland, W. A. *Journal of Applied Physics* **1998**, *84*, 3827-3829.

(9) Clapp, A. R.; Medintz, I. L.; Uyeda, H. T.; Fisher, B. R.; Goldman, E. R.; Bawendi, M. G.; Mattoussi, H. *J. Am. Chem. Soc.* **2005**, *127*, 18212-18221.

(10) Somers, R. C.; Bawendi, M. G.; Nocera, D. G. *Chemical Society Reviews* **2007**, *36*, 579-591.

(11) Agranovich, V.; Atanasov, R.; Bassani, F. *Solid State Communications* **1994**, *92*, 295-301.

(12) Scholes, G. D. *Chemical Physics* **2002**, *275*, 373-386.

(13) Agranovich, V. M.; Basko, D. M.; Rocca, G. C. L.; Bassani, F. *Journal of Physics: Condensed Matter* **1998**, *10*, 9369-9400.

(14) Tani, T. *Imaging Science Journal* **2007**, *55*, 65-79.

(15) Mishra, A.; Behera, R. K.; Behera, P. K.; Mishra, B. K.; Behera, G. B. *Chem. Rev.* **2000**, *100*, 1973-2011.

(16) Waggoner, A. *Current Opinion in Chemical Biology* **2006**, *10*, 62-66.

(17) Kirstein, S.; Daehne, S. *International Journal of Photoenergy* **2006**.

(18) Struganova, I. A.; Hazell, M.; Gaitor, J.; McNally-Carr, D.; Zivanovic, S. *Journal of Physical Chemistry A* **2003**, *107*, 2650-2656.

(19) Yao, H.; Sugiyama, S.; Kawabata, R.; Ikeda, H.; Matsuoka, O.; Yamamoto, S.; Kitamura, N. *J. Phys. Chem. B* **1999**, *103*, 4452-4456.

(20) Birkan, B.; Gulen, D.; Ozcelik, S. *Journal of Physical Chemistry B* **2006**, *110*, 10805-10813.

(21) Vanburgel, M.; Wiersma, D. A.; Duppen, K. *Journal of Chemical Physics* **1995**, *102*, 20-33.

(22) Knoester, J. *Journal of Chemical Physics* **1993**, *99*, 8466-8479.

(23) Fukumoto, H.; Yonezawa, Y. *Thin Solid Films* **1998**, *327-329*, 748-751.

(24) Bradley, M. S.; Tischler, J. R.; Bulovic, V. *Adv. Mater.* **2005**, *17*, 1881.

(25) Rubtsov, I. V.; Ebina, K.; Satou, F.; Oh, J.-W.; Kumazaki, S.; Suzumoto, T.; Tani, T.; Yoshihara, K. *J. Phys. Chem. A* **2002**, *106*, 2795-2802.

(26) Lim, I.-I. S.; Goroleski, F.; Mott, D.; Kariuki, N.; Ip, W.; Luo, J.; Zhong, C.-J. *J. Phys. Chem. B* **2006**, *110*, 6673-6682.

(27) Zhang, Q.; Atay, T.; Tischler, J. R.; Bradley, M. S.; Bulovic, V.; Nurmikko, A. V. *Nat Nano* **2007**, *2*, 555-559.

(28) Mattoussi, H.; Mauro, J. M.; Goldman, E. R.; Anderson, G. P.; Sundar, V. C.; Mikulec, F. V.; Bawendi, M. G. *J. Am. Chem. Soc.* **2000**, *122*, 12142-12150.

(29) Zhang, C. Y.; Yeh, H. C.; Kuroki, M. T.; Wang, T. H. *Nature Materials* **2005**, *4*, 826-831.

(30) Somers, R. C.; Bawendi, M. G.; Nocera, D. G. *Chem. Soc. Rev.* **2007**, *36*, 579-591.

(31) Snee, P. T.; Somers, R. C.; Nair, G. P.; Zimmer, J. P.; Bawendi, M. G.; Nocera, D. G. *J. Am. Chem. Soc.* **2006**, *128*, 13320-13321.

(32) Wu, X.; Liu, H.; Liu, J.; Haley, K. N.; Treadway, J. A.; Larson, J. P.; Ge, N.; Peale, F.; Bruchez, M. P. *Nature: Biotechnology* **2003**, *21*, 41-46.

(33) Birkan, B.; Gulen, D.; Ozcelik, S. *J. Phys. Chem. B* **2006**, *110*, 10805-10813.

(34) Hines, M. A.; Guyot-Sionnest, P. *J. Phys. Chem.* **1996**, *100*, 468.

(35) Ivanov, S. A.; Nanda, J.; Piryatinski, A.; Achermann, M.; Balet, L. P.; Bezel, I. V.; Anikeeva, P. O.; Tretiak, S.; Klimov, V. I. *J. Phys. Chem. B* **2004**, *108*, 10625-10630.

(36) Fisher, B. R.; Eisler, H.-J.; Stott, N. E.; GBawendi, M. *Journal of Physical Chemistry B* **2004**, *108*, 143-148.

(37) Forster, T. *Naturwissenschaften* **1946**, *6*, 166-175.

(38) Forster, T. *Ann Phys (Leipzig)* **1948**, *2*, 55-75.

(39) Baumann, J.; Fayer, M. D. *J. Chem. Phys.* **1986**, *85*, 4087.

(40) Lakowicz, J. R. *Principles of fluorescence spectroscopy*; Kluwer Academic/Plenum: New York, 1999.

(41) Zhang, C.-Y.; Yeh, H.-C.; Kuroki, M. T.; Wang, T.-H. *Nature Materials* **2005**, *4*, 826-831.

(42) Zhang, C.-Y.; Yeh, H.-C.; Kuroki, M. T.; Wang, T.-H. *Nature Materials* **2005**, *4*, Supporting Information.

(43) Kuhn, H. *J. Chem. Phys.* **1970**, *53*, 101.

(44) Andrews, D. L.; Juzeliunas, G. *J. Chem. Phys.* **1992**, *96*, 6606.

(45) Juzeliunas, G.; Andrews, D. L. *Phys. Rev. B* **1994**, *49*, 8751.

(46) Knapp, E. W.; Scherer, P. O. J.; Fischer, S. F. *Chemical Physics Letters* **1984**, *111*, 481-486.

(47) Hydrodynamic radius measurements tend to overestimate the size of highly charged particles as these measurements rely on the speed with which a particle diffuses in water, and charged polyacrylic acid functionalities effectively "drag" water molecules as they diffuse.

(48) Liu, W.; Howarth, M.; Greytak, A. B.; Nocera, D. G.; Ting, A. Y.; ., M. G. B. *Submitted* **2007**.

(49) Fisher, B. R.; Eisler, H. J.; Stott, N. E.; Bawendi, M. G. *J. Phys. Chem.* **2004**, *108*, 143 (supplemental information).

Appendix A

Other Projects

A.1 Semiconductor Nanocrystals for Use in Fluorescence Multiplexing

Recent trends in pharmaceutical research have emphasized a "systems based" approach to understanding cellular function [1]. However, using this approach requires large amounts of data about protein and/or RNA expression in cells [2]. Current microsphere-based proteomics measurements are limited to <50 proteins at one time by two factors: i) the number of available "cross-talk" free antibodies and ii) the ability to encode more than 100 distinguishable micron sized microspheres. Several organizations are currently working to add nearly 100 antibodies yearly to their cross-talk free library.

The second issue is due to the wide spectral peaks typical of organic dyes currently used in micromicrosphere multiplexing. Semiconductor nanocrystals exhibit peaks nearly half the width of organic dyes (below) and are therefore ideally suited to creating libraries of tens of thousands of codes, an improvement of two orders of magnitude over existing technologies. This technology can thus enable experiments in which thousands of different proteins (a large fraction of the functional proteome of the cell) can be simultaneously detected.

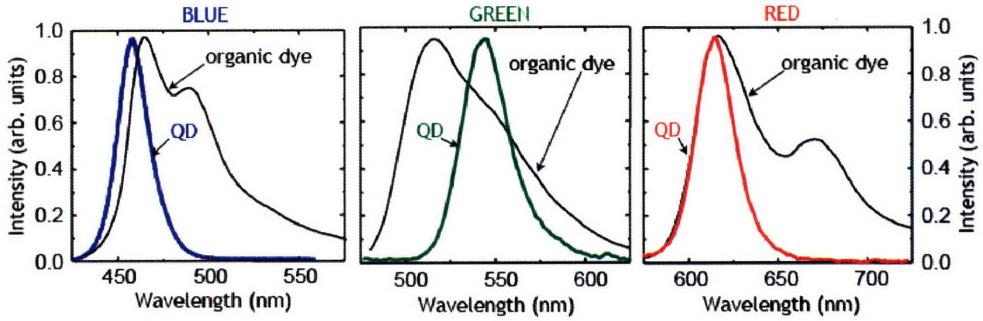

Figure A.1.1: Nanocrystal quantum dot (QD) spectra superimposed over common organic dyes.

Aside from the immediate benefit to pharmaceutical and proteomics research communities, this technology could also eventually find use as a diagnostic tool in medical applications. We have therefore developed a means to implant semiconductor nanocrystals into micron sized microspheres to demonstrate

1. Using nanocrystal emitters to detect protein concentrations
2. Demonstrate a coding scheme that be used to create >1000 distinguishable particles and can be reasonably scaled up to produce these particles (Fig. A.1.2)
3. Demonstrate a detection system capable of distinguishing each particle and accurately and reproducibly determine the protein concentration of a given sample

These steps should provide adequate evidence that a nanocrystal based labeling system provides a significant advantage over existing dye based products. Although nanocrystals have been previously used to detect a few nucleotides or proteins in a single experiment, a practical system to detect thousands of analytes simultaneously has never

been reported. Furthermore, no system using a spectrally resolved CCD has been practically demonstrated for flow through detection of proteins.

A.1.1 Modeling a Code for Multiplexing with QDs

A QD based multiplexing system must be designed to distinguish over one thousand coded microspheres, so the first step is to find the minimum number of spectral peaks and intensity levels. The number of spectral peaks may vary with the working range of the detector (UV-visible-nIR) and by the properties of the coding agents themselves. QD's have a larger working range and thinner emission linewidths than organic dyes - enabling more spectral peaks - and a greater range of intensities, to be resolved by the detector. Thus assuming a working range and a full width, half-maximum (FWHM) for each peak, the maximum number of peaks and their intensities can be mathematically determined.

A.1.1.1 Coding Using Fixed Color Channels

Upon cursory examination we have determined that six QD peaks spaced by 30 nm from 480-680 nm, with a 30 nm FWHM, will be able to code up to four intensity levels (corresponding to levels 0-3 for each peak). This code has up to 4096 individual combinations from 000000-333333.

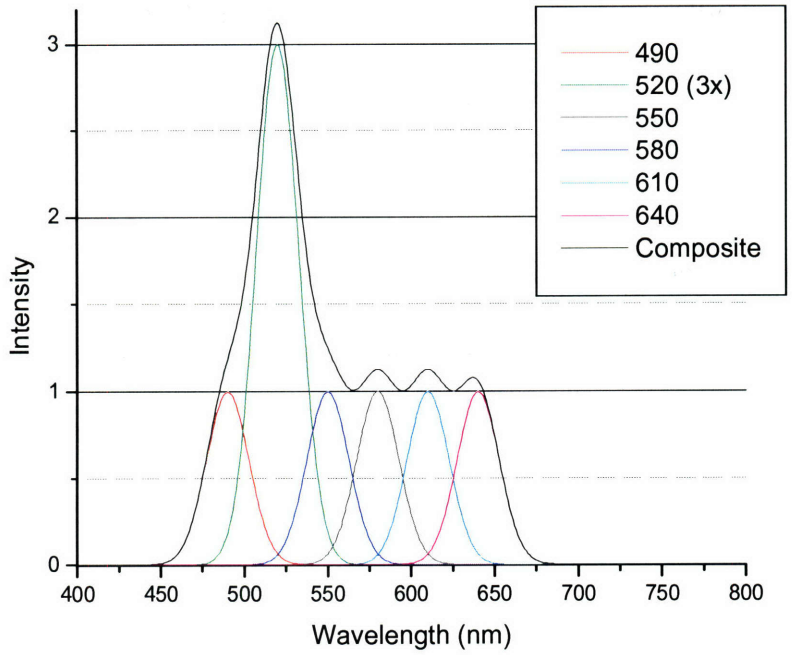

Figure A.1.2: Theoretical modeling of Gaussian peaks (FWHM = 30 nm) showing that even at Level=3 for the 520 peak, the intensity of the neighboring peaks is still less than a discernable threshold (in this case intensity threshold=1.5). Using 6 colors and a four level system 0,1,2,3 we can generate over 2000 distinct codes.

To ensure that these codes are distinguishable, the spectra must be refined. To distinguish between spectra which may not be equally as intense, (due to shifts in position in the flow cytometer or changes between QY of separate microsphere batches) each spectrum will be normalized before decoding. This will eliminate some code multiples, as 000002 will appear identical to 000001. Similarly it makes sense to discard codes for which the normalized intensity for a level=1 may not be clear. In order to determine the relative magnitude of levels 1,2, and 3 after normalization, it is preferable for a level 1 to be present in the code as a reference. Codes without such a reference are discarded. These restrictions will cull the number of distinguishable codes from the set

of possible numeric combinations. For the example of six peaks and four levels, the number of distinguishable codes is around 2500.

To further expand the number of codes, the maximum level may be increased beyond 3 for some cases. The number of levels is restricted to avoid overlap from neighboring Gaussian emission peaks; however, some codes contain peaks without neighbors (e.g. 102131 and 010231). Such stand-alone peaks will not interfere with signals on either side, and thus can increase their level to 4, 5 or higher. When the analysis software recognizes the high amplitude for these peaks, it will automatically set the neighboring peak levels to 0, thus avoiding confusion between the shoulder and a nonexistent neighbor's signal. This strategy may be easily extended for codes that contain peaks separated by two intervals or more (e.g. 100212, 001002, 100002), allowing the amplitude of the stand-alone peaks to increase even more. The analysis software will include a scale for these super levels that automatically clears an appropriate range of neighbors. For instance, a signal corresponding to 411210 will be interpreted as 401210, and the software will read 931001 as 900001. Using this model codes could be distinguished 100% of the time, even with errors on the intensity of nearly ±15%, and on wavelength of ± 3 nm.

The incorporation of QDs as the coding agent offers several key advantages. The great coding efficiency in this scheme is due to the narrow, Gaussian lineshape of QD emission. Schemes using molecular fluorophors are intrinsically limited by their irregular lineshape and large FWHM, and a set of one thousand distinguishable codes would require a much larger spectral range. Unlike organic dyes, QDs don't

photobleach, so QD based codes will maintain their readability longer. Also the broad absorption in the UV will allow the entire microsphere to be excited by a single source.

A.1.1.2 Wavelength Coding of Microspheres

Microspheres could also be coded by wavelength alone, without the need for intensity levels. This could be accomplished by spectroscopically analyzing each microsphere rather than finding the emission intensity at set wavelengths. From the spectrum, the peaks of the QD emission Gaussians could be found for the emission from several (in this case three or four) populations of QDs, provided those peaks are separated by about 20 nm or more. Since the peaks would be fit using a Gaussian fitting program, the assessment of the peak average would be extremely accurate even under less than optimal conditions. Coding would be accomplished by creating up to forty samples of QDs with peaks spaced by as little as 5-10 nm apart. Although the spectrometer could never distinguish between peaks 5 nm apart in a single microsphere, it would easily be able to do so for two such populations in two separate microspheres. Therefore the two microspheres could be identified as belonging to different groups.

If each microsphere contained as few as three separate populations, with a possible range of wavelengths from 30 different QD samples, the resulting opportunities for coding would be that of picking from 30 objects to fill 3 slots, or 30 choose 3. Since the range starts at 500 nm and ranges up to 650 nm, with samples of [500, 505, 510, 515, ...650], we must eliminate, after each pick, the five points corresponding to the four closest to the peak already chosen and the identical peak. Hence if the first is 550 nm, then the peaks at 540, 545, 550, 555, 560 must be removed from choice from

consideration for the second pick. So the maximum discernable, different, combinations using 3 picks would be (30*25*20)/3! = 2500 distinct combinations. (The exclamation point corresponds to the factorial function). In the case of 40 QD samples and 3 picks, there are 7,000 combinations. For the case of 30 QD samples and four picks, there are 9,375 combinations. For 40 samples and four picks there are 43,750 distinct combinations.

There are several advantage for this system over the coding scheme presented in Section A.1.1.1. From a manufacturing standpoint, QD's samples, unlike dye molecules, can have variable quantum yield's that cannot be precisely controlled between samples even using similar recipes. This interferes with the manufacturing of microspheres whenever one "550 nm" (for example) sample runs out and needed to be replaced. The replacement sample would have a different QY and the concentration of QDs needed at each intensity level would need to be reassessed and calibrated. Since QD's are made by small batch processes, this could be a time consuming and laborious process that adds undue complications to the microsphere coding reaction.

Similarly, QY can be difficult to maintain or to predict after several reaction steps or even after a long periods of time in cases where they have been exposed to heat or ligand exchange. Using different channels with absolute intensities would be nearly impossible under these circumstances, but even relative doping may not be robust since different sizes of QDs can respond differently to these treatments. The most robust system is one in which QDs are allowed have a range of different intensities (ie quantum yields, the least controlled factor), but required to have fixed wavelengths (which is an absolutely controlled of the QD). Tolerances on wavelength could be more relaxed than

for intensity and the issue of interference by neighboring peaks would be largely eliminated. Since organic dyes cannot be tuned so precisely to specific wavelengths, this coding scheme would play into the particular advantages of using quantum dots and could not likely be replicated by non-QD technologies (although it should be protected therefrom).

The downside is of course that many more samples of QDs must be produced. However, in terms of volume of QDs required for mass production, the number of samples needed is equivalent. Although more recipes would be required, fewer samples would need to be discarded for errors in wavelength. Aiming for 550 nm emitting sample may yield a sample at 555; this is still a useful sample under a wavelength coding scheme but not for a fixed channel/intensity scheme. Hence the overall effort required to create a viable product is approximately equivalent for either technique, but wavelength coding solves the problem of variable QY in nanocrystals from batch to batch.

A.1.2 Synthesizing Coded Microspheres

Currently we have been able to implant nanocrystals into polystyrene microspheres (Figure A.1.3) with arbitrarily selected emission peaks (Figure A.1.4). NCs with various emission spectra can be synthesized from CdSe/ZnS, ZnSe/ZnCdSe/ZnS and ZnCdS/ZnS as described in Sections 2.3.1 (red and green) and 2.4.1 (blue). QDs are purified by precipitation using methanol and butanol prior to redispersing them in hexane or chloroform. The QDs are purified twice and finally dispersed in chloroform in the final step.

Carboxylic acid coated polystyrene microspheres with diameter of 5 um (Polysciences) arrived in water and were dispersed in butanol/methanol by centrifuging the microsphere solution at 1500 rpm, then removing the clear supernatant and redispersing the precipitate (microspheres) with first 0.5 ml of methanol and then adding 2.5 ml of butanol. QDs were embedded in the polystyrene microspheres in a method similar to Xing et al. [3] by adding 100 ul of QDs in chloroform (absorbance ~ 0.1 at first absorption peak) to ~$1.5x10^7$ microspheres in 2.5 ml of butanol and 0.5 ml methanol. The QDs were incubated with the microspheres while sonicating for 45 minutes. After this, the microspheres were removed from the butanol/methanol solution by centrifuging at 1500 rpm, removing the relatively clear supernatant and drying the microspheres on a Schlenk line under vacuum. After drying for ~30 minutes, the microspheres were redispersed in pH = 9 borate buffered solution.

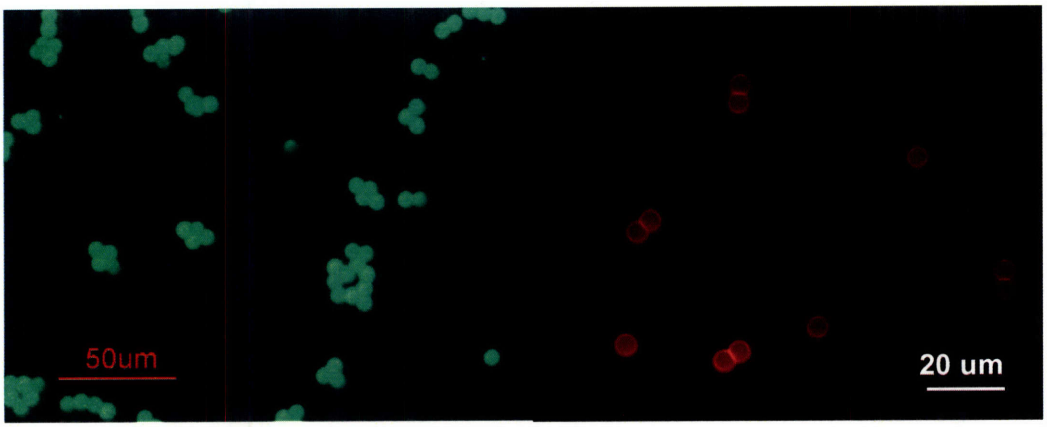

Figure A.1.3: Microspheres embedded with ~5 nm diameter nanocrystals emitting at ~550 nm (left) and ~610 nm (right) under excitation with a 365 nm UV lamp under magnification (20x, 50x).

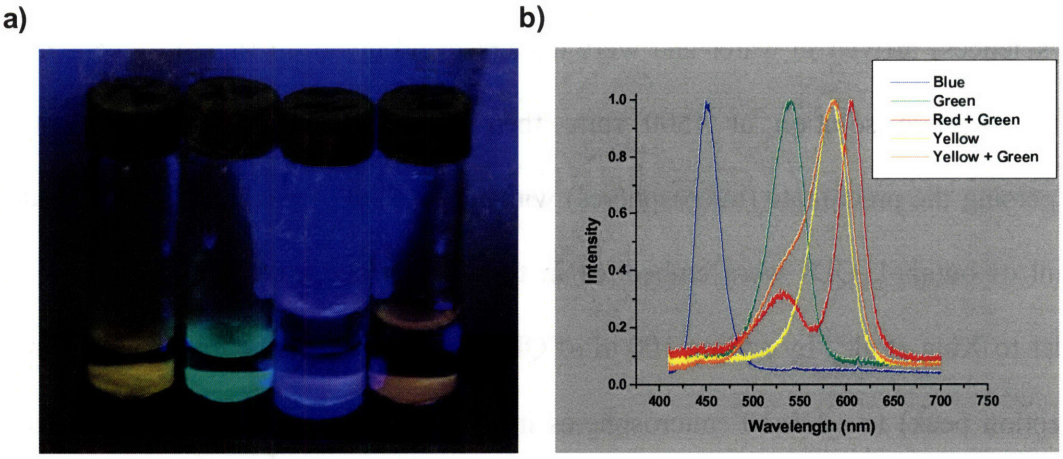

Figure A.1.4: Photographs (a) and spectra (b) of polystyrene microspheres embedded with one or two types of nanocrystals in vials.

Microspheres could be coded with any high QY (>50%) QD sample and appeared bright to the eye (Figure A.1.5). Spectra show features as linear combinations of the emission spectra of the embedded QDs, thus allowing spectral coding using combinations of QD populations in the incubation step. The spectral contribution of each QD population was found to be directly related to the ratio of the number of QD of each type added.

A.1.3 Detecting Coded Microspheres

Coded microspheres can be "read" by flowing them through a 250 um microcapillary tube and detecting the spectrum of each microsphere. A syringe pump was used to push microspheres through the tube at 10 - 0.1 ml/hr. Microspheres were imaged using a "single QD" microscope setup [4] (originally designed to view single NCs on a slide as in Section A.2) shown in Figure A.1.5.

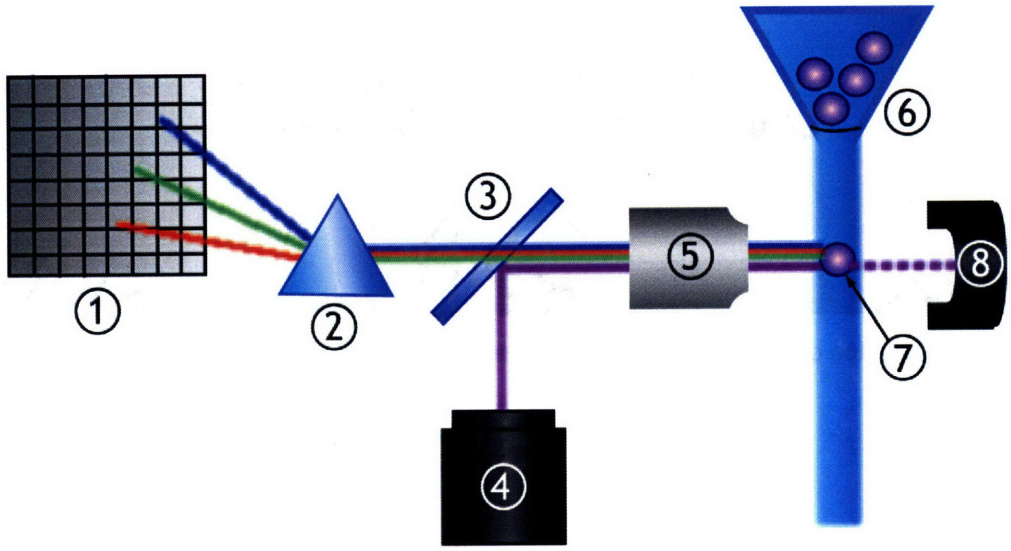

Figure A.1.5: A method of detecting the fluorescence signal from each microsphere (7) as it passes through the excitation beam. All visible emitting semiconductor nanocrystals absorb broadly in the UV and require only a single excitation source (4). Emission is detected by focusing the emission through an objective microscop lens (5), separating it from the excitation beam (3) and spectrally resolving (2) the emission onto CCD chip (1).

Each sphere could be individually detected and its emission spectrum read at 1 - 50 ms intervals. Microspheres could be recorded either as images (Figure A.1.6) or as spectra (Figure A.1.7). Microspheres could be detected as large increases in the integrated emission intensity and the spectra could be fitted with Gaussian curves.

This allows, in principle, for two different coding schemes to be used. In the first, modeled in section A.1.1, the fixed emission peaks are known thus enabling multiple Gaussians to be fitted to determine the intensity at each peak. In the second, the Gaussian is fitted to determine the peak emission wavelength which can correspond to one of multiple samples with emission peaks separated by ~10 nm. Flow through detection also enables microspheres to be read quickly and accurately with a fixed objective lens.

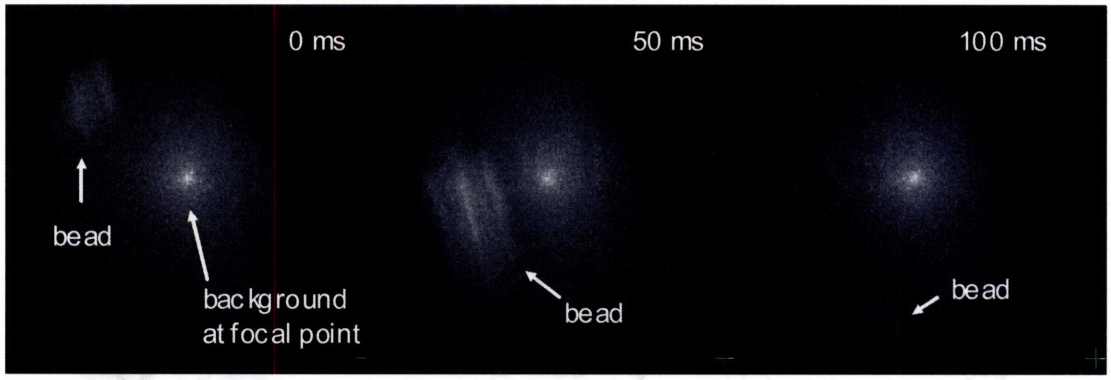

Figure A.1.6: A video of a microsphere moving through the focal volume at slow speed (0.1ml/hr).

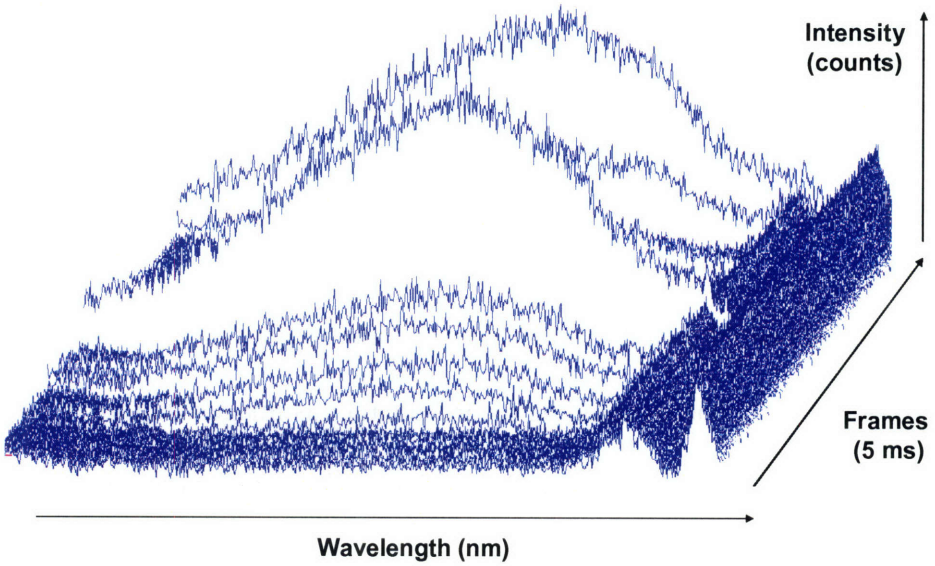

Figure A.1.7: A trial of the spectroscopic system using a green emitting microspheres flowing through a 250 um cylindrical microcapillary tube at 1 ml/hr. Spectra were captured with 5 ms integration times.

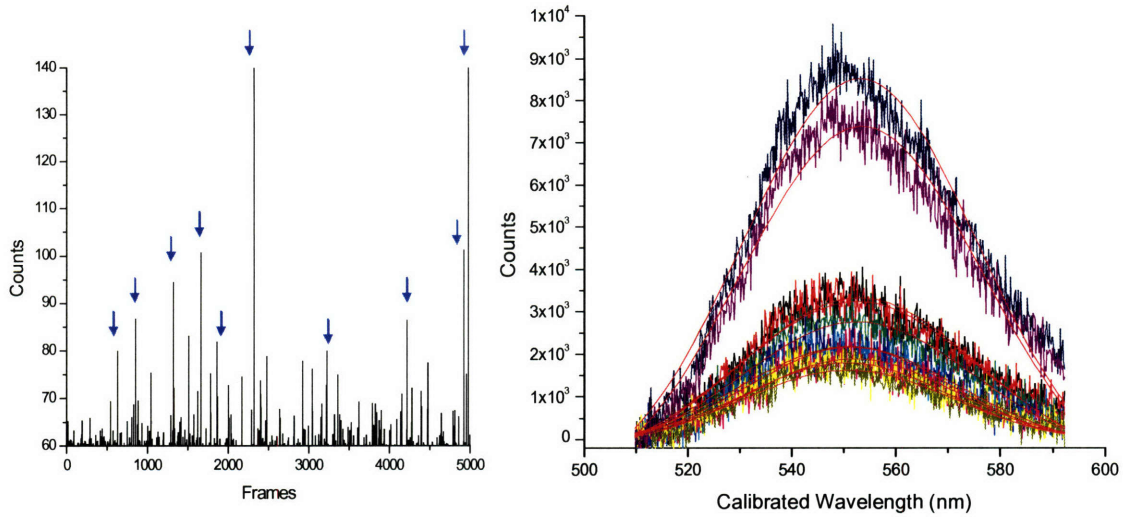

Figure A.1.8: Analysis of the spectral data from Figure A.1.7. The total signal measured in each frame determines whether a spectrum has been captured (left), while the spectra for each microsphere detected is fitted with a Gaussian curve. The spectra are peaked at 552 nm with a standard deviation of ± 1 nm.

Optimum detection was achieved at a flow rate of 1 ml/hr and 5 ms integration times. At a concentration of ~ $1x10^7$ microspheres in 10 ml of solution, we could detect nearly 1 microsphere per second. This would allow almost 30,000 microspheres to be read in an 8 hour period (overnight). By concentrating the microspheres, this could be improved by a factor of nearly 50, to more than 1 million microspheres overnight, without losing resolution of individual microspheres. Furthermore the emission wavelength of the microspheres flowing through the microcapillary tube were found to be 552 nm ± 1 nm making this method extremely attractive for wavelength coded microspheres.

In future we expect to etch, in silica, three input channels into an imaging channel. The central channel will be used to slowly inject microspheres into the imaging channel while the two side channels flow, at a faster rate, solution (water) with no

microspheres. These side channels should help to "focus" the microspheres into the center of the imaging channel so that fewer microspheres pass by the detector without being read (ostensibly because they don't enter the focal volume).

A.1.4 Next Step: Detecting Proteins

The chemistry for attaching antibodies to polystyrene microspheres is available commercially (Polysciences). However standard treatments generally create a number of possible attachment sites on the protein. These sites can attach in a variety of conformations to polystyrene microspheres, whose surface conjugates with the primary amine groups on the antibody. These groups appear at relatively random intervals on a particular antibody, although each antibody is uniform in its distribution. Thus some antibodies will tend to bind desirably through its end of the "Fc region", while others may have a greater propensity for an undesirable random binding to the microsphere, such that the Fab regions are unavailable for protein binding.

Quantitation of proteins in solution will be enabled through the secondary detection antibody. The secondary detection antibody, which will be conjugated to a fluorescent marker is a second antibody specific to the protein. Excitation and emission wavelengths of small fluorescent dyes must be outside the range of the QD coding emission peaks. It is also possible that a QD could be used as the dye marker.

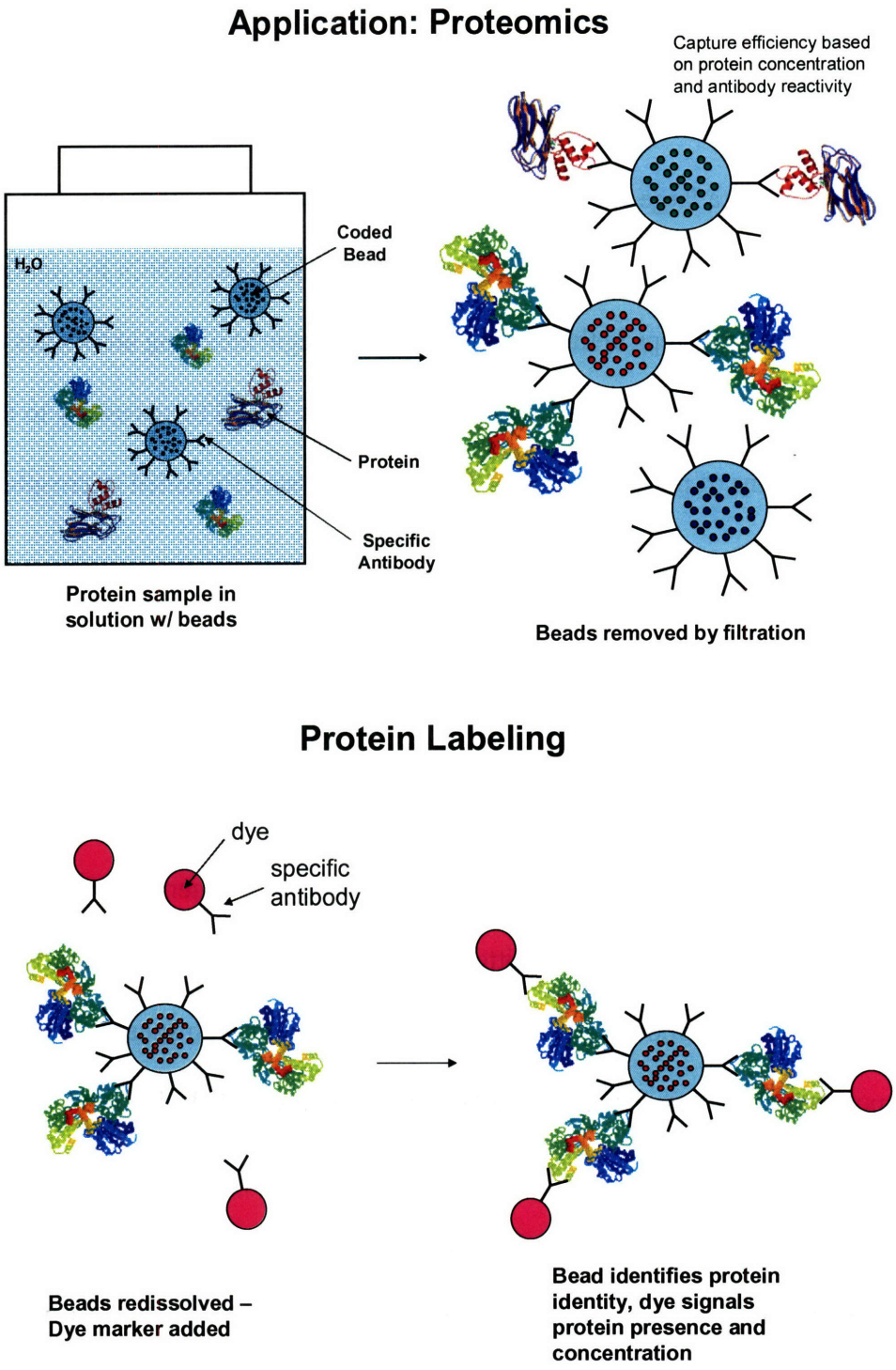

Figure A.1.9: Cartoons of the next step for using coded microspheres to capture proteins in cell lysate solution. The captured proteins are labeled with a dye prior to detection.

A.1.5 Nancrystal Multiplexing: Conclusion

While protein multiplexing can be accomplished rapidly using NC generated spectral codes, it remains to be seen if such a system can accurately measure protein concentrations using a large variety of coded microspheres. If so, this may present a significant improvement in microsphere-based assays and in using NCs for multiplexing applications. The next steps in this experiment are to begin attaching antibodies to microspheres and attempt to capture proteins. After this, it will be necessary to construct an automated means of producing 1000s of batches of distinctly coded microspheres.

A.2 Polarized CdSe Nanorod Films

Spherically shaped semiconductor nanocrystals (NCs) known as quantum dots (QDs), have been studied for their novel photonic properties. Similarly rod shaped nanocrystals (nanorods, NRs) have been found to display confinement properties similar to quantum dots, except the light emitted is linearly polarized [5-8]. Linearly polarized light finds use in applications such as polarization coding in high speed communications, and as polarized emitters for LCD displays or for optocoupled electronic components. Previous work on the physics of single nanorods suggests the presence of a 1-D transition dipole parallel to the length of the rod [5-8]. If these rods could be aligned at the nanoscale level but over a large macro-sized field, they could be used to create a linearly polarized nanorod LED (NR-LED). To date only one such device has been realized [9].

The production of a linearly polarized NR-LED will open up new avenues of investigation into the physics of the NC-LED. Given that the amplified stimulated emission (ASE) threshold for rods has been found to be significantly lower than dots [10]

and that rod alignment will increase the relative reabsorption rate of the rods in a film [10,11], it was believed to be possible to achieve electrically pumped ASE emission from an all inorganic, aligned NR-LED.

A.2.1 Synthesis of CdSe Nanorods

As with QDs, nanorods are prepared by injecting a solution of concentrated selenium precursor into a hot solution of concentrated cadmium precursor. NR synthesis also requires the presence of a long chain phosphonic acid bound to the cadmium as a phosphonic acid/cadmium complex [11,12] in order for growth to proceed preferentially along the [001] Wurtzite crystal facet. This 1D growth elongates the rod along the axis perpendicular to the [001] face, called the c-axis (z-axis), [11,12]. Uniform, monodisperse rod growth can be obtained using procedures adapted from Peng [11], involving periodic additions of selenium precursor during the 1D growth phase. Current synthetic methods for producing colloidal CdSe NRs allow controllable growth with emission properties of tunable peak emission wavelength from 600-680 nm, narrow peak width of ~28nm (FWHM) and band edge photoluminscent (PL) quantum yield as high as 40% when over-coated with ZnS [13].

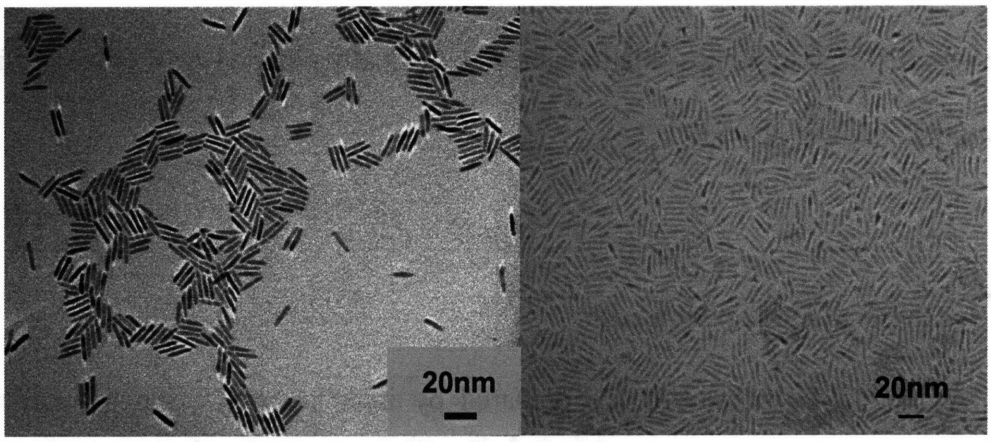

Figure A.2.1: TEM of CdSe rod cores (left) grown with length ~22nm and width ~3nm exhibiting moderate nematic self assembly. Overcoated rods (right) with similar dimensions show similar properties.

A.2.2 Physics of CdSe Nanorods

The electronic structure of a nanorod is similar to that of a QD, however, while QDs are 3-dimensionally confined, rods exhibit confinement only along their diameter (a-axis, x and y dimensions). From effective mass approximation calculations the exciton energy levels can be expressed as discrete states. These calculations predict that the states closest to the valence band edge chiefly originate from the Se 4p atomic orbitals and that states closest to the edge of the conduction band originate mainly from the Cd 5s orbitals. The lowest energy excited state of a QD is derived from the nearly degenerate Se $4p_x$ and $4p_y$ atomic orbitals, but not the p_z atomic orbitals. This is due to the crystal field anisotropy of the Wurtzite structure. Since most photoluminescence (PL) comes from allowed transitions between conduction and valence band states near the bandgap edge, the light emitted by a QD is circularly polarized. For nanorods (Figure A.2.1), the lowest excited state contains a large degree of $4p_z$ character because states with nodes

lying in the z direction will decrease their energy more quickly due to changes in the rod length [7]. Thus, for a rod, transitions from the lowest energy excited state to the ground state will be primarily polarized in the z direction. The effect is enhanced by the greater electric field in the z direction which is due to the shape anisotropy of the dielectric material. This also increases the overall probability of a transition from states with greater p_z character. Thus the recombination of excitons in a high aspect ratio rod will tend to produce photons linearly polarized with electric fields parallel to the c-axis [8]. If the rods can be nematically ordered, the light emitted should be polarized in parallel with respect to the common director.

The presence of a nematic (orientationally ordered) phase for hard-body spherocylinders (non-interacting rods) is predicted by Onsager's Theory [14] which solves the Helmholtz free energy equation by minimizing the energy density with respect to the entropy. This shows that stability can be achieved for some concentrations by maximizing the orientational order parameter, S, related to all the rods at angle Ω to a common director where:

$$S = \frac{1}{2}\langle 3\cos\Omega - 1\rangle$$

An isotropic solution will have order parameter S=0 while a perfectly aligned nematic phase has order parameter S=1. The Onsager model can qualitatively yield a number of strategies by which to obtain a nematic monolayer. Increasing rod volume fraction, increasing the rod-rod attraction, and increasing the aspect ratio all decrease the free energy and allow the spontaneous formation of a nematic phase to occur. It is also predicted that monodisperse samples will form more rigid phase boundaries with smaller areas of phase coexistence [15]. Of all these parameters, the easiest means of controlling

the ability of a sample to form a nematic phase is by forming monodisperse, cylindrical, high aspect ratio rods.

A.2.3 Polarization Studies on Single Nanorods

Although theory predicts a 1-D transition dipole for high aspect ratio rods [5,7,8], real rod samples are not perfect ellipsoids and must be tested for polarized emission. It is necessary then to find the degree of polarization (DOP), ρ, which is equivalent to the fraction of emitted light that is linearly polarized. DOP is described by the equation [16]:

$$\rho = \frac{(I_{\max} - I_{\min})}{(I_{\max} + I_{\min})}$$

where I_{max} and I_{min} correspond to the maximum and minimum intensity for a plot of intensity versus polarizer angle.

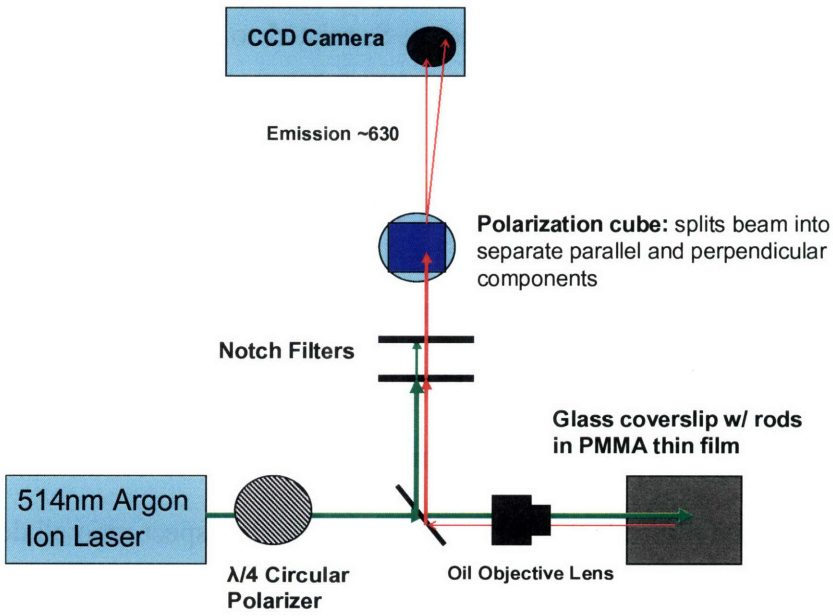

Figure A.2.2: A diagram of the polarization spectroscopy setup used to measure degree of polarization in single NCs and in NC films.

In order to measure DOP, NRs are dispersed in a very thin polymer film and excited with the 514nm line of an Argon ion laser. The resulting emission is split with a polarization cube into parallel and perpendicularly polarized intensity which is collected in two separate images of a sample of about 40 individual rods. By collecting the perpendicular and parallel intensities a comparison can be made between different images regardless of integration time or incidental rod intensity since the ratio allows us to plot normalized intensities versus polarizer angle. This plot (Figure A.2.4) can then be used

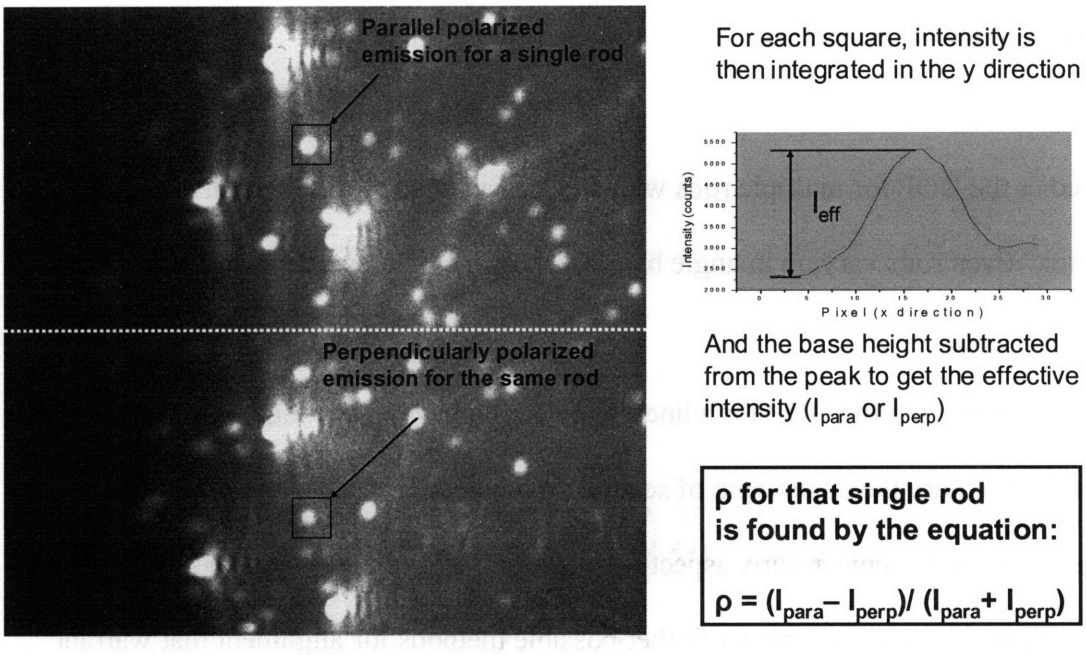

Figure A.2.3: Sample data for the determination of the polarization, p, for a single nanocrystal. The polarization cube (Figure A.2.2) splits the image into two parts corresponding to parallel and perpendicular polarizations. The intensity (I_{eff}) is found from the peak height compared to the background after integrating in the y direction in a standard area near the emission peak. These effective intensities are collected for both images and used to find the degree of polarization, p.

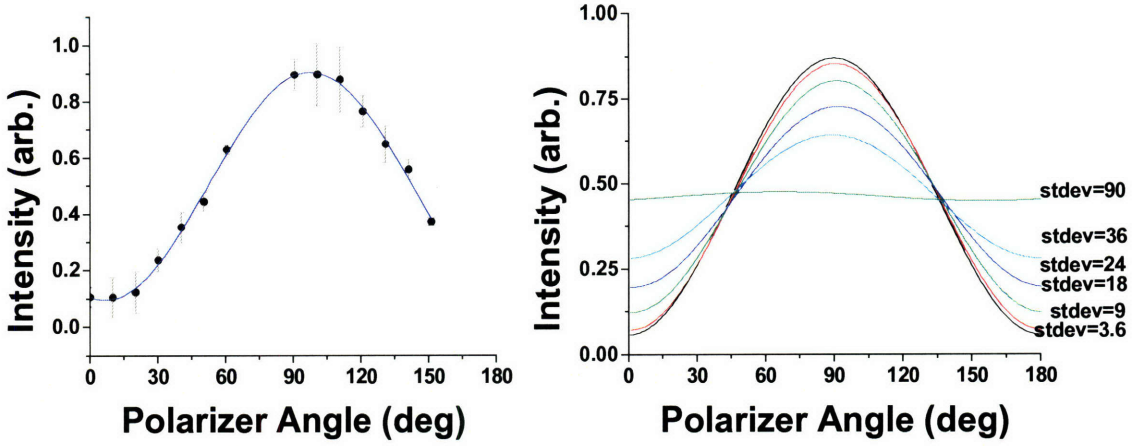

Figure A.2.4: Measured intensity versus polarizer angle for a single CdSe nanorod (left). The curve is fit to by cosine squared function, the DOP for this rod is ~80% and the c-axis is at ~97°. Theoretical intensity versus polarization angle (left) for several orientational distributions (standard deviations in degrees).

to predict the DOP for multiple rods with a Gaussian angular distribution around a mean director. Even rods varying in angle by ±20° show a significant degree of polarization (Figure A.2.4).

Maximizing the DOP for a linearly polarized device, and thus the orientational order, will require the adjustment of several parameters. Not only can the solvent systems, pressure, temperature, aspect ratio and uniformity all be adjusted by Langmuir-Blodgett, but there are a variety of other possible methods for alignment that warrant further investigation.

A.2.4 CdSe/ZnS Nanorod LEDs

Previous work has shown that a well ordered monolayer of CdSe/ZnS QDs can be used to produce LEDs with up to 1.1% external quantum efficiency (EQE) [17,18], as

described in Chapters 1 and 2. Nanorod LEDs were created using the same ITO/TPD/NC/Alq_3/Ag:Mg/Ag device structure described in Chapter 2. This device structure can be reasonably shown to work using nanorods in place of quantum dots (Figures A.2.5 and A.2.6). NR-LEDs to date have exhibited lower external quantum efficiency than QD LEDs. This likely arises from energy transfer effects and the difficulty of attaining a close packed rod

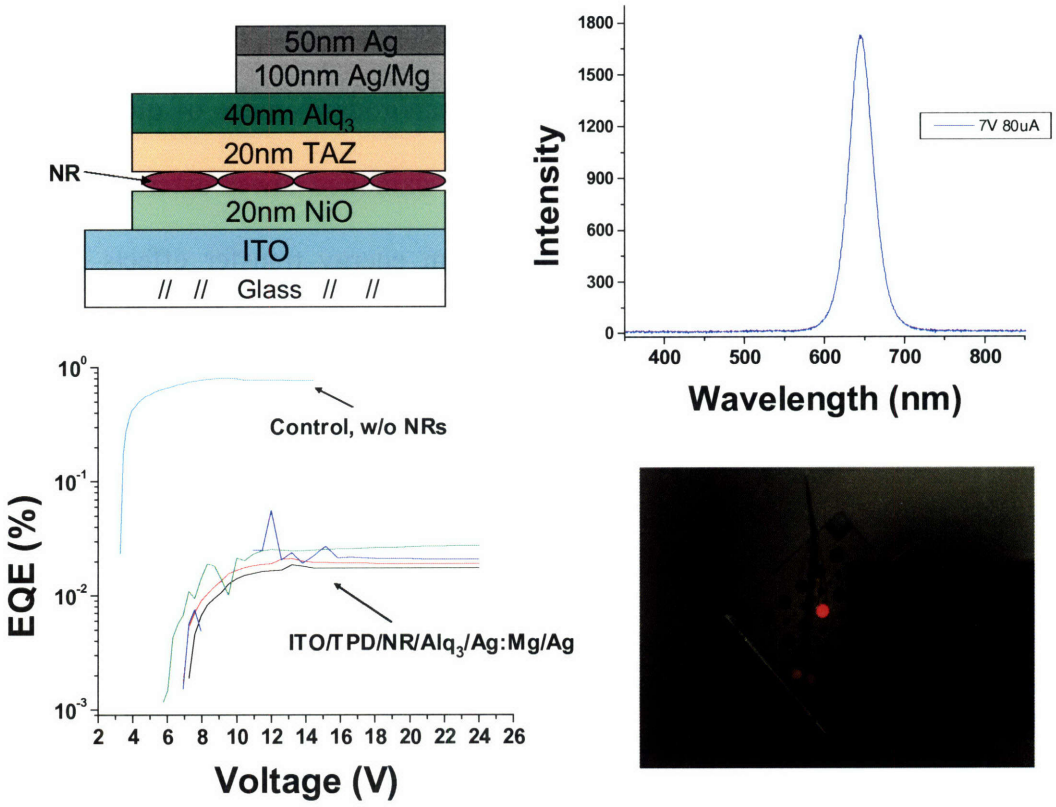

Figure A.2.5: Device characterization for an NR-OLED. Top left) device structure of the NR-OLED. EQE (bottom left) and EL spectrum (top right) show emission solely from the NRs, but with low EQE ~ 0.1%. The device appears red to the eye (bottom right) and is brightly visible in room lights.

film with current deposition techniques. Both of these effects likely cause the NR monolayer to have a lower QY in the thin film than do QDs, which also decreases the efficiency. The use of organic hole conducting thin films limits the available deposition techniques since organic materials are sensitive to air, water, and most organic solvents. Thus the use of NiO as a hole conducting material [19-21] was investigated as a viable replacement for TPD. Although the precise mechanism by which carriers are formed in NiO is unknown, it has been proposed that sputtering in oxygen allows nickel (II) oxide films to form doped with a small concentration of nickel (III) incorporated into the crystal

structure [19]. The excess charge on the nickel (III) site traps electrons and effectively removes them from the valence band, providing a hole. It was found that NiO sputtered with 2.5% oxygen in argon, forms films with a resistivity approaching 10 Ω•cm, could

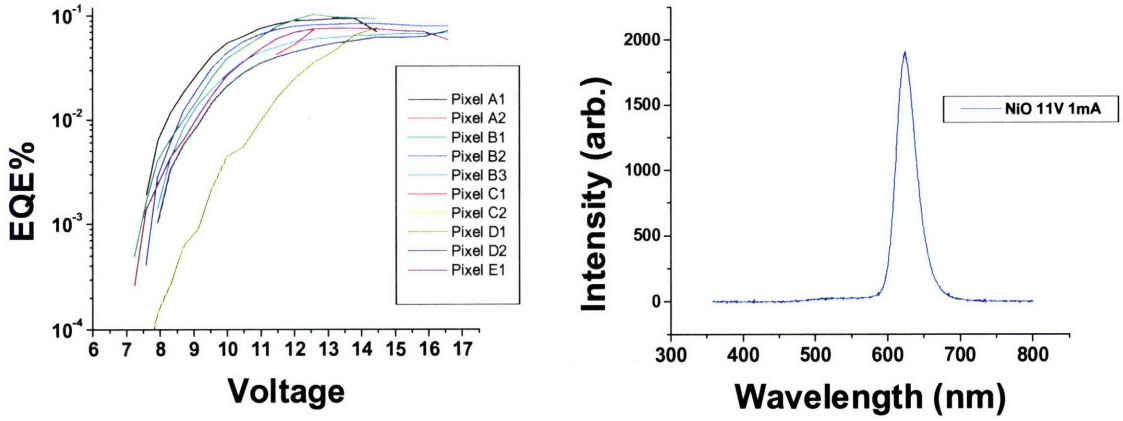

Figure A.2.6: Efficiency and emission spectrum of NiO/NR/Alq3 device.

be used in "hybrid" inorganic/organic QD and NR LED devices with EQE regularly approaching 0.1% (Figure A.2.6). Since NiO is resistant to degradation by air, water, and most solvents, it would allow access to a wider range of deposition techniques to attain nematic alignment. Emissive devices using NiO as a water resistant hole conducting layer have already been produced using a Langmuir trough. This proves the feasibility of using LB to produce an aligned monolayer that can then be used to produce a linearly polarized LED (Figure A.2.7).

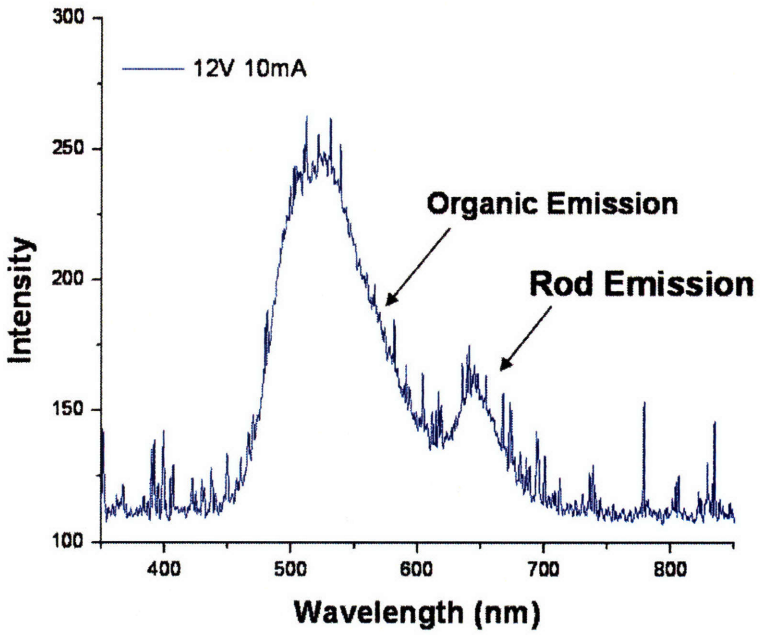

Figure A.2.7: Emission spectrum from an LS-stamped NiO/rod/Alq3 hybrid device shows modest rod electroluminescence, proving the feasibility of using LB monolayers for LEDs.

A.2.5 Unidirectional Rubbing for Polarized Nanorod Films

However, LB techniques are not ideal for use with nanocrystals due to the sensitivity of the NC surface to water and the possibility of aggregation on the subphase. CdSe/ZnS nanorod films created with LB were not found to be significantly polarized and showed significant losses in PL efficiency. Recently unidirectional rubbing has been suggested as a superior means of achieving alignment of CdSe rods in a film [9].

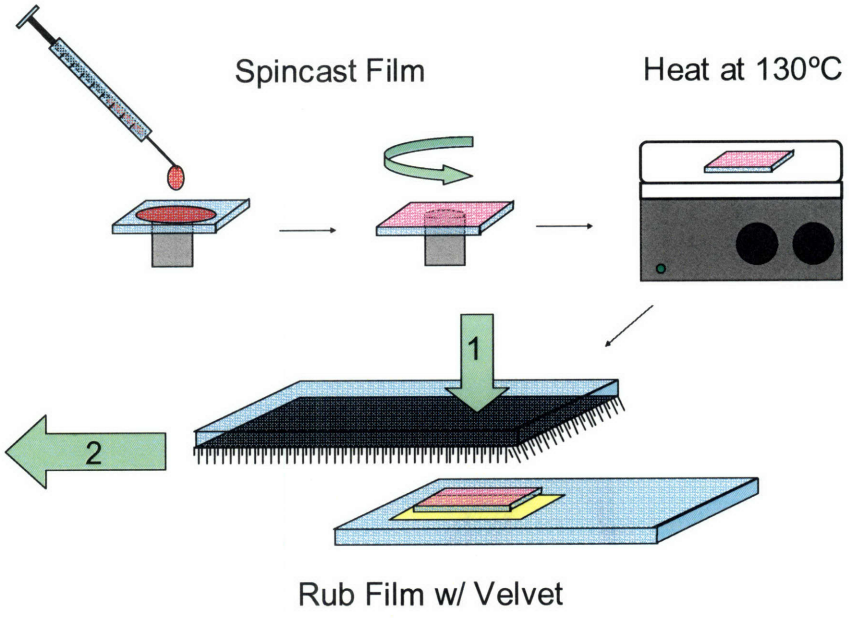

Figure A.2.8: Procedure for forming polarized films using unidirectional rubbing with velvet.

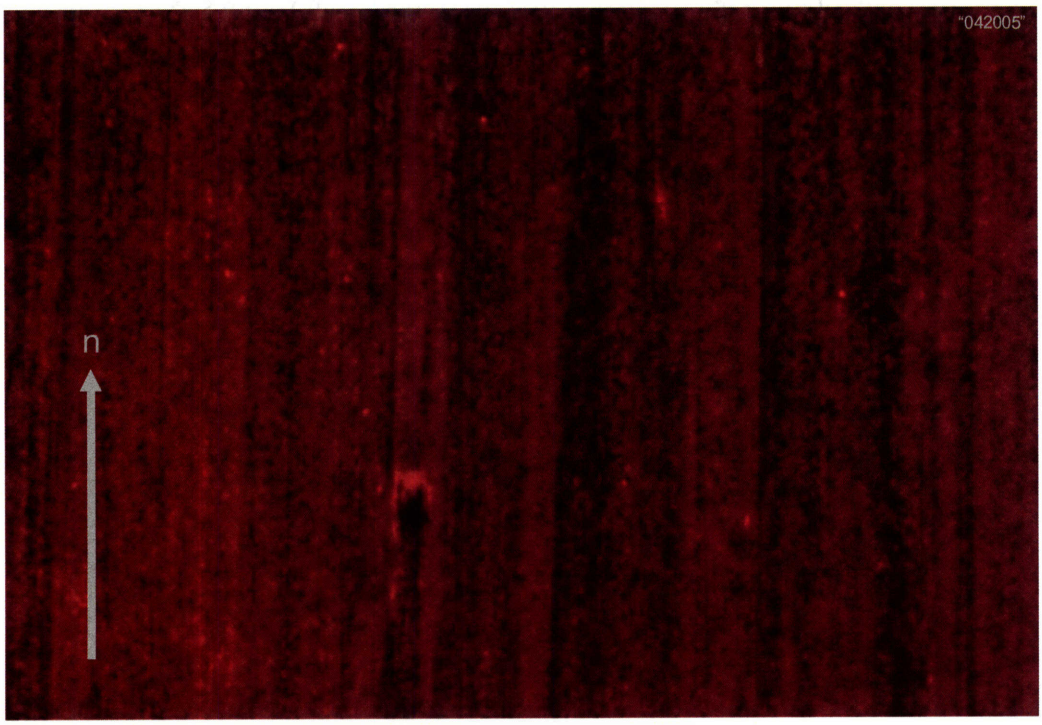

Figure A.2.9: NR monolayer unidirectionally rubbed with velvet at 100 mag under UV excitation. While the film does appear to have some directionality imposed by the rubbing, and

therefore possibly some alignment of the nanorods, it also has introduced several defects and pinholes which are likely to cause shorting in a prospective device.

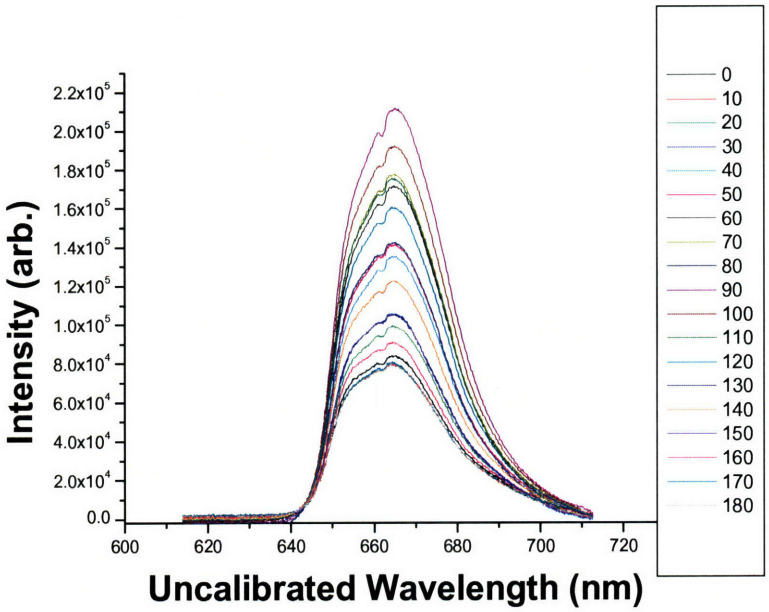

Figure A.2.10: Intensity profile of emission from the rubbed film with respect to wavelength at different polarizer angles.

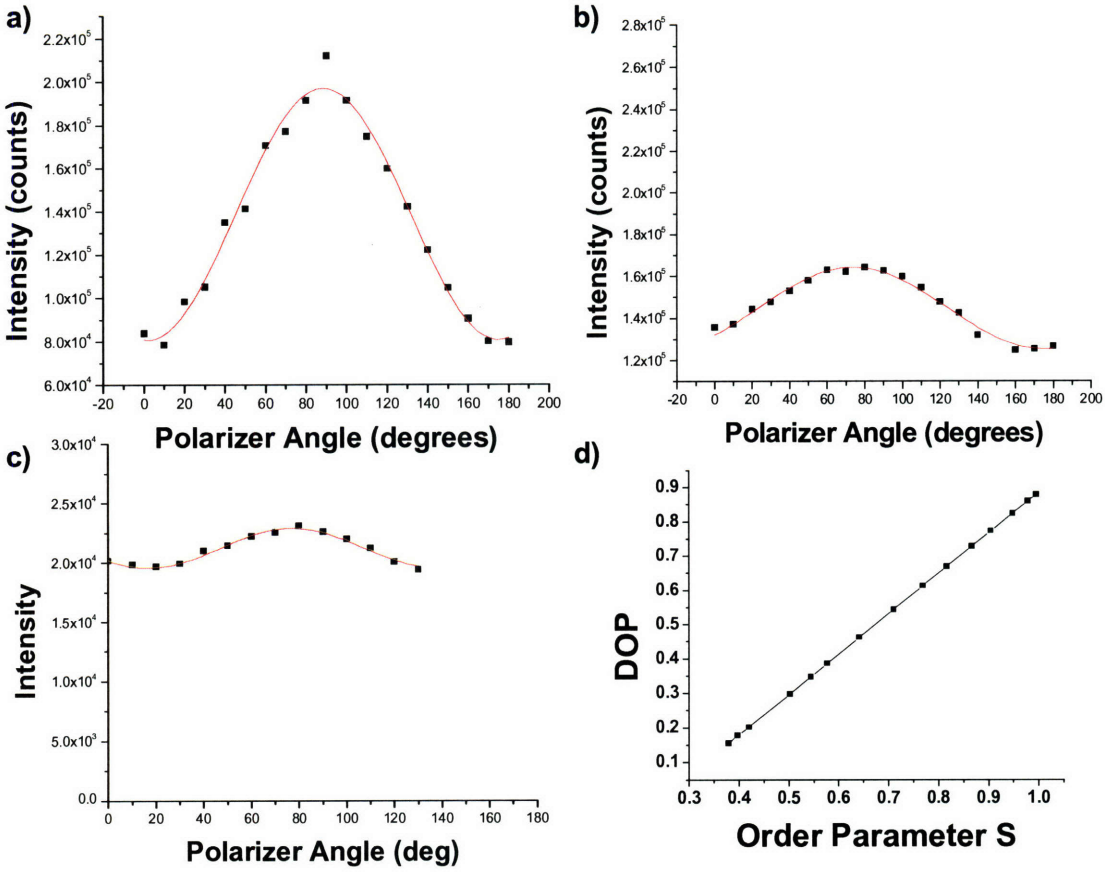

Figure A.2.11: PL intensity v. polarizer angle for three films a) a rubbed NR monolayer, b) a non-rubbed NR monolayer and c) a rubbed QD monolayer. All three are fit with a $\cos^2 \theta$ dependence, after subtracting the background, to find the degree of polarization. d) Shows a theoretical correlation of degree of polarization (DOP or p from Figure A.X) with S, the order parameter. Both b) and c) show no DOP < 10%, indicating an S ~ 0.3. Only a) shows significant polarization, with S ~ 0.6.

A.2.6 Conclusions for Polarized Nanorod LEDs

It appears that with some improvements to the film processing, it will be feasible to create a linearly polarized, all inorganic NR LED using unidirectional rubbing (Figures A.2.8-A.2.11). Inorganic materials will not only increase the number of available deposition techniques but will also be able to handle much higher current densities than organic transport layers and allow more rapid injection of carriers into the rods.

Achieving optical gain in CdSe nanocrystals is dependant on the formation of more than one exciton per crystal so a device that is able to achieve a significant population of biexcitons could also exhibit ASE. In the presence of an optical cavity, lasing could be achieved by coupling the NR ASE to the modes of the cavity. Rod lasing has already been found to occur at a lower pump threshold than dots, most likely due to decreased non-radiative (Auger) rates for biexcitons in rods [22]. Since rod lasing is also known to be linearly polarized [10] it was surmised that alignment of nanorods will increase the optical gain characteristics [10,23,24], and thus decrease the current density threshold required for lasing to occur.

A.3 Doped Nanocrystals for AC Driven LEDs

Several publications have suggested synthetic routes towards doping QD's with d-orbital emitters such as Cu, Mn, Ni and Fe [25-27]. Generally doping NC's are of two types. The first type is not really doping (which implies a minute addition of another material, as in addition of boron to silicon to create p-type silicon) but rather the creation of tertiary materials of the type $M_xD_{1-x}E$ where the "dopant", D, is another group II metal cation which is present in fairly large quantity [28,29]. This creates either a homogeneous or graded structure with band gap characteristics that appear to be an intermediate of those of ME and DE II-VI nanocrystals. Examples of these types of cores are ZnCdS tertiary structures exhibited in Chapter 2.

The second form of doping (true doping) is the doping of nanocrystals materials with a minute amount of a second material, usually a transition metal which is not common to the formation of II-VI (e.g not Zn, Cd or Pb). These dopants are generally of

the form $MD_{<<1}E$, where the concentration of D is very low compared to M and E which are nearly equivalent. These dopants are transition metals like Fe, Ni, Mn, Cu, and even lanthanides like Eu, Er, Tm, Tb. Doping by simple addition of the second material during the reaction generally does not work since the dopants will often prefer to form a second type of nuclei rather than be incorporated into the ME crystal structure. Instead the material must be introduced after nucleation, to prevent nucleation with the dopants to form DE. Once introduced, the cores must generally undergo an overcoating either with a different material, to form a type-I nanocrystals, or with more of the core material to secure the dopant metal ions inside the core. Doping is useful either to change the conductivity of the core, or to impart magnetic or optical properties of the dopant to the nanocrystals. Specifically phosphorescent dopants, which emit from a d to d (or f to f) orbital transition within the unbound atomic states of the dopant [25-27], can be used to create emitters which are independent of the band gap of the host material. A good example is the ZnSe/ZnMnS/ZnS doped core-shell nanocrystals which can phosphoresce from the Mn d-d transition at 590 nm, even though the host particle's first (lowest energy) absorption peak occurs at ~355 nm. This creates the unusual situation of a clear solution of nanocrystals that emit orange light when exposed to a UV lamp, and could find use in transparent displays.

A.3.1 Synthesis of ZnSe/ZnMnS/ZnS and ZnSe/ZnCuSe

The synthesis was adapted from Thakar et al.[30] ZnSe cores were prepared by injecting 96 mg of diethyl zinc and 0.67 ml of TOP-Se into a flask of 10 ml oleylamine which has been degassed at 140 °C. After heating at 270 °C for ~90 minutes, the pot was

cooled to 170 °C and a solution of 45 mg of manganese stearate, 76 mg of diethyl zinc and 160 mg of hexamethyldisilathiane in a solution of 6 ml TOP was added dropwise to the pot at 1 drop/second. This was then cooled to room temperature. The ZnSe/ZnMnSe particles were precipitated twice using methanol and butanol and redispersed in hexane. This solution was then added to a degassed pot of 10 g TOPO and 0.4 g HPA (as in Section 2.3.1) at 80 °C and the hexane removed under vacuum. The pot was then placed under argon and heated to 170 °C. A solution of 80 mg diethyl zinc and 160 mg hexamethyldisilathiane in 5 ml TOP was added dropwise and the pot cooled to room temperature and 4 ml of hexane and 4 ml butanol were added. The ZnSe/ZnMnS/ZnS QDs were then precipitated twice using methanol and butanol and redispersed in hexane then chloroform. The resulting QD solution had QY of ~ 70 % as compared to a solution of orange emitting QDs (~70%) calibrated to a solution of rhodamine 610. Although the accuracy of the measurement is compounded by using an intermediate calibrated solution, a direct comparison to an organic dye is not possible to the large difference (>200 nm) between the first absorption peak (~355 nm) and the emission peak of the ZnSe/ZnMnS/ZnS particles at 570 nm.

The high quantum yield of these particles is largely due to the ability of Mn to effectively be incorporated into a Zn site in the ZnSe and ZnS crystal lattice. The thick shell of ZnS then effectively localizes the excited state on the Mn dopant atom by preventing energy transfer to surface states or the surrounding medium. A d-orbital phosphorescent transition then accounts for the orange emission from the NCs [26]. These particles showed an excited state lifetime in excess of 1 ms, consistent with a phosphorescent emission decay mechanism.

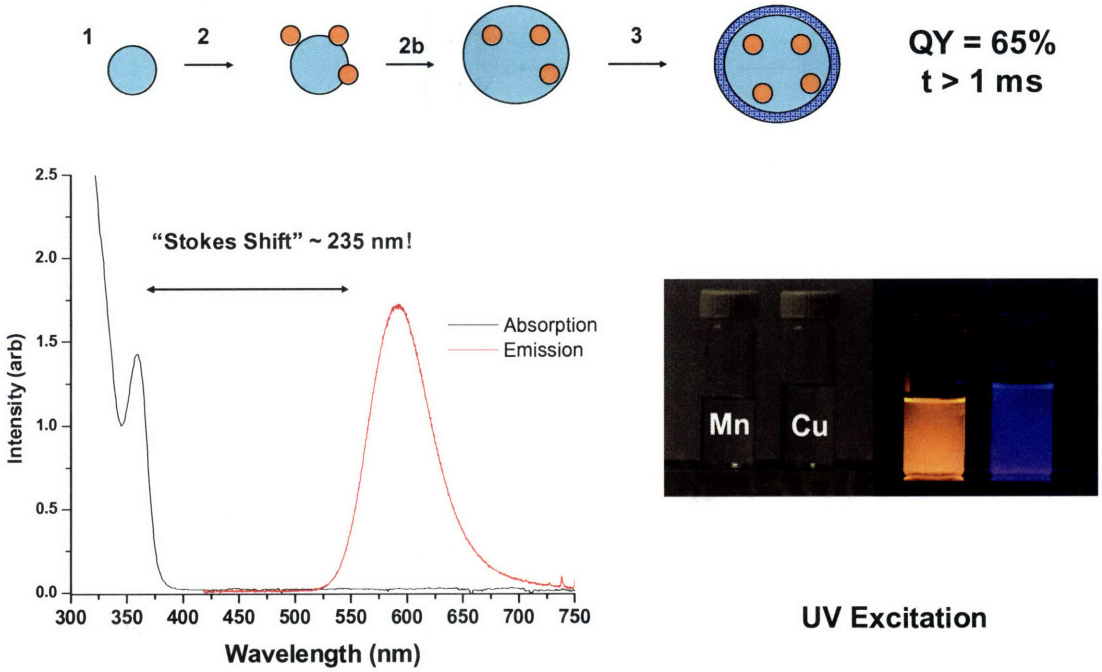

Figure A.3.1: Doping of ZnSe with Mn and Cu. Top) the mechanism of reaction as (1) ZnSe cores are formed (2) the cores are surface doped with Mn^{2+} ions (3) the particle is overcoated with more ZnSe, burying the Mn ions beneath the surface of the NC and (4) the particle is overcoated with ZnS. Bottom) the emission spectrum (left) and photos of the Mn (right, orange vial) doped ZnSe QDs. The ZnSe:Cu particles are also shown in the bottom right photo (blue vial).

Cu doped MnSe could be prepared using a similar scheme as reported by Peng et al [25]. However, these particles could not be easily overcoated with ZnS and proved to be much less stable in air. Furthermore, many trials resulted in incomplete doping of the ZnSe, giving rise to both band edge and Cu phosphor emission (Figure A.3.2).

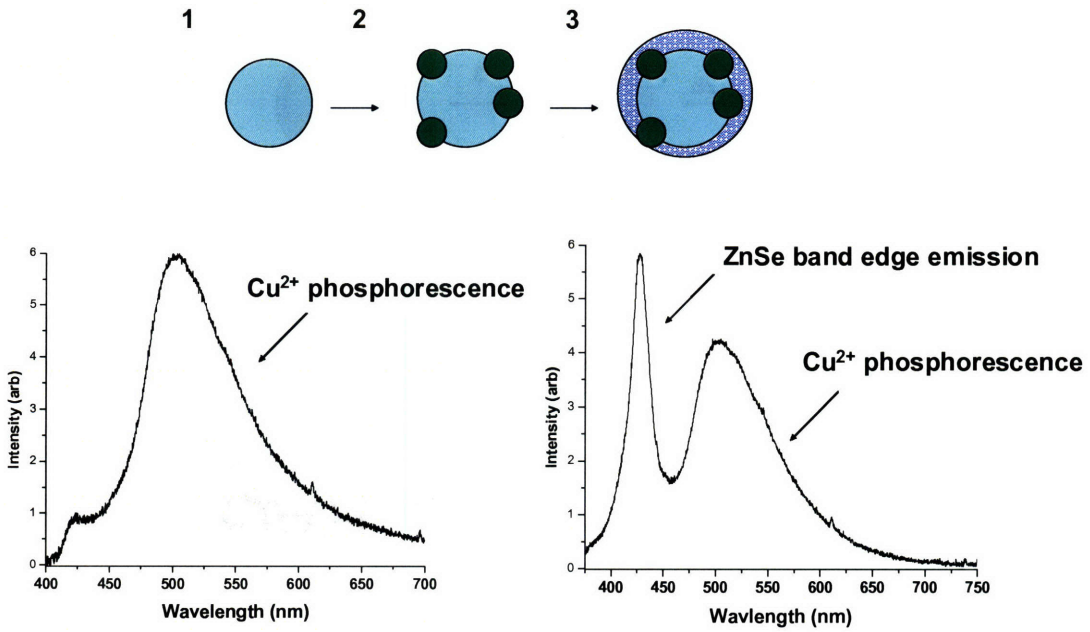

Figure A.3.2: Doping of ZnSe with Cu. Top) Reaction steps consisting of (1) creating the ZnSe core (2) surface doping it with Cu and (3) overcoating the core with ZnS. Bottom) A successfully doped ZnSe:Cu emission spectrum, the d-orbital triplet emission of the Cu creates a broad green peak (left). In many cases the impantation of Cu did not occur uniformly, leaving undoped ZnSe/ZnS which emits from the ZnSe band edge at ~ 420 nm (right).

A.3.3 AC Devices Using ZnSe/ZnMnS/ZnS d-Doped Nanocrystals

As a result of these experiments, it was clear that Mn doped ZnSe appeared to be the most promising candidate material for use in an LED. However, QD-OLED structures, like those used in Chapter 2 proved extremely inefficient. This is likely due to the difficulty in injecting charges into the bands of the ZnSe and the impossibility of FRET into either the ZnSe core band structure, which is too wide, or the Mn d-orbital state manifold, which has an extremely small absorption cross-section.

An AC driven device, on the other hand, does not require charge injection, relying instead on the fast acceleration of charges to excite the dopant atoms by impact

ionization. To construct an AC device, materials with high dielectric constant were placed between two conductive electrodes. The devices required a high series resistance to reduce the AC current and thus raise the power efficiency. Similar devices have been constructed using micron sized ZnS particles doped with Cu, as in Appendix A.4. Our devices were constructed using layers of ZnSe/ZnMnS/ZnS particles interspersed with layers of sputtered ZnS. These were sandwiched between two layers of resistive hafnium oxide with conductive ITO electrodes on either end.

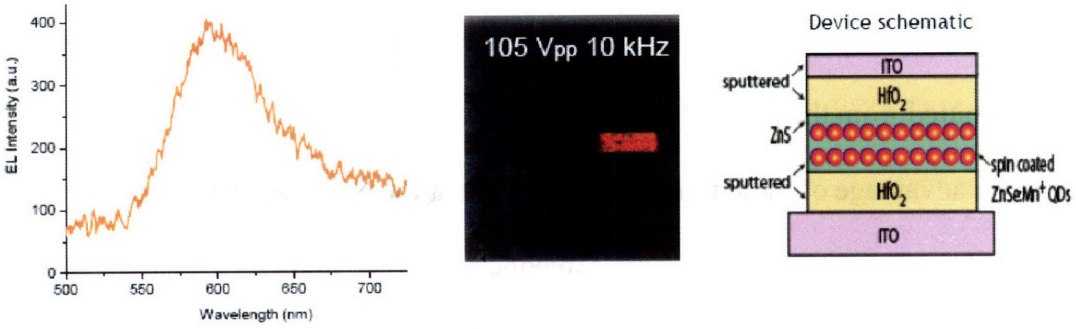

Figure A.3.3: A trial AC device using (ZnSe:Mn)/ZnS NCs. The device is run at 105 V and 10kHz. The emission from the device is clearly from the Mn^{2+} d-orbitals as the spectrum (left) matches the emission of the QDs in the vial (Figure A.X), and appears orange to the eye (center). The device structure (right) is constructed by sputtering insulating HfO_2 onto conductive ITO, sputtering on ZnS, then spin coating this with QDs and sputtering ZnS onto the monolayer. After three layers of QDs have been deposited, a final HfO_2 insulating layer is sputtered onto the device along with an ITO electrode. An AC voltage is applied (V_{pp}) to the two ITO electrodes. (Photo and figures courtesy Vanessa Wood)

Although the power efficiency of the device was low, orange emission from the Mn dopant atoms is clearly visible in the spectrum and photo (Figure A.3.3) at 105 $V_{pp,AC}$. While ZnSe/ZnMnS/ZnS particles may have other applications, such as in biological

labeling or LCD applications, this effort represents an attempt to find a replacement for the direct current QD-LED structures described in Chapters 2 and 3.

A.4 Inkjet Printed Downconversion LEDs

The final light emitting device produced during this work was a downconversion LED using semiconductor nanocrystals as the emissive material. Downconversion devices work by emitting at a blue wavelength using an efficient DC ILED or OLED or an AC excited blue emitting phosphor. This blue or UV emission is then absorbed by the QD layer which then "downconverts" the light, energetically, into a redder wavelength which is emitted from the band edge of the QDs.

The advantage of these types of devices is that the NCs themselves are not being used to conduct current as an electronic component. Earlier studies [31-33], have shown that NCs generally do not make good electronic materials in that they have low electron or hole mobilities, tend to trap charges, and generally do not form uniform films when compared with organics molecules or crystalline inorganic films.

The disadvantage of downconversion devices is that they tend to be inefficient since the efficiency of the blue LED is then "filtered" through an inefficient absorption re-emission step. For example, if the functional LED has an EQE of 10%, and the QD film has a QY of 10% then the ultimate EQE of the device cannot be better than 1%, even if 100% of the light from the blue LED is absorbed by the film. However, since DC QD-LEDs are have nearly 1% EQE anyway, it may be possible to create LEDs with comparable efficiency that are much easier to produce, more robust and longer lived than previously QD-OLEDs.

A.4.1 Inkjet printed IR AC-LEDs

In this iteration of a downconversion LED, a paste of micron sized ZnS particles doped with Cu (purchased from and encased in thin polymer capsules, is excited using an AC field of nearly 400 V_{AC} and 10 kHz is applied to the two ITO electrodes. A thick layer of PbS (>100 nm) in polyisobutylene (PIB) polymer is deposited on top of the paste using a prototype "drop-on-demand" inkjet print head (Hewlett-Packard), as described in Chapter 3.

PbS is synthesized [34] by injecting 90 mg of hexamethyldisilathiane into a 150 °C solution of 5 ml oleic acid, 5 ml octadecene (ODE) and 380 mg of lead oleate which has been previously degassed for 4 hours at 110 °C. The solution is cooled to 100 °C and the QDs grown for 6 minutes prior to cooling to room temperature. The QDs are then precipitated twice with acetone and redispersed in hexane. Prior to printing, 1% btw polyisobutane (PIB) polymer is added to the hexane solution.

Upon application of the field, charges in the ZnS impact the Cu dopant atoms causing excitation by impact ionization. The excited state in the Cu relaxs to emit a blue photon which is absorbed by the PbS nanocrystals embedded in a polyisobutylene polymer (PIB). The PbS then emits an IR photon which passes through a 900 nm filter (silicon) and is detected using a spectrally resolved InGaAs detector.

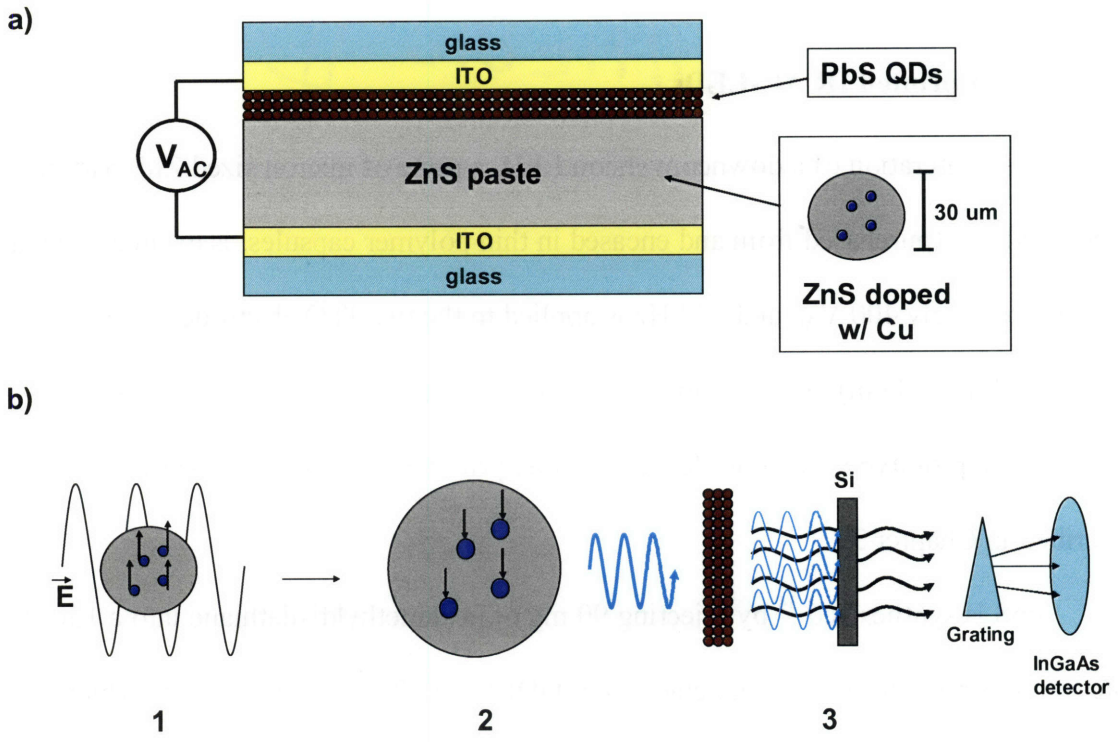

Figure A.4.1: A diagram of an IR downconversion device showing a) device structure and b) the mechanism of operation. An electric field (1) is used to excite Cu^{2+} dopants in the um sized ZnS particles (not nanocrystals, available commercially). These excited states relax, emitting blue light (2), which then strikes the nearby QD monolayer and is absorbed, causing IR photoluminescence (3). The emission is filtered through a silicon substrate and detected using an InGaAs detector equipped with a spectrometer grating.

As shown in Figure A.4.2, the electroluminescent spectrum of the composite device is identical to that of the PbS sample, with an emission peak at 1430 nm. The device itself appears black under operation, since the PbS layer is thick enough to absorb all of the blue light emitted from the ZnS:Cu layer.

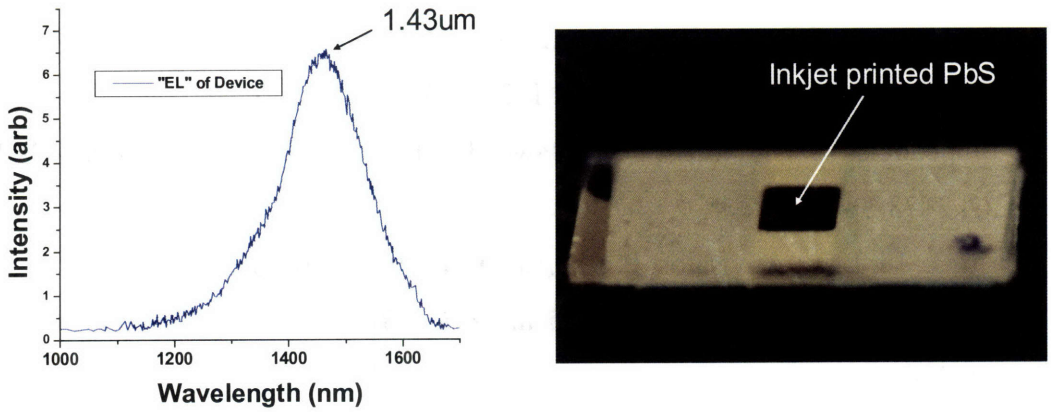

Figure A.4.2: The EL operating spectrum of the IR downconversion LED, emitting at 1.43um (left) and a photo of the device at rest (right). The square pixel is deposited by an inkjet process identical to that described in Chapter 3.

Although the power efficiency was likely low (<0.1%), due to the inefficiency of the AC excitation process and the low QY of the PbS materials (~10%), this method did produce an IR EL spectra with very simple air stable processing. Furthermore, application of the inkjet printing process allowed easily defined pixels to be created using thick films of QDs in polymer. The simple method of processing may in fact be useful for the production of cheap IR emitting devices if a more suitable form of excitation can be found.

A.5 References for Appendix A

(1) Yan, W.; Lee, H.; Yi, E. C.; Reiss, D.; Shannon, P.; Kwieciszewski, B. K.; Carlos Coito2, X.-j. L.; Andrew Keller1, J. E.; Galitski, T.; Goodlett, D. R.; Aebersold, R.; Katze, M. G. *Genome Biology* **2004**, *5*, R54.

(2) Pearson, H. In *Nature News (online)*, 2008; Vol. doi: 10.1037/452920a.

(3) Xing, Y.; Chaudry, Q.; Shen, C.; Kong, K. Y.; Zhaus, H. E.; Chung, L. W.; Petros, J. A.; O'Regan, R. M.; Yezhelyev, M. V.; Simons, J. W.; Wang, M. D.; Nie, S. *Nature Protocols* **2007**, *2*, 1152-1165.

(4) Empedocles, S. A.; Norris, D. J.; Bawendi, M. G. *Physical Review Letters* **1996**, *77*, 3873-3876.

(5) Hu, J.; Li, L.-s.; Alivisatos, P. *Science* **2001**, *292*, 2060-2063.

(6) Chen, X.; Xiao, M.; Peng, X. *Physical Review B* **2001**, *64*, 245304-(245301-245304).

(7) Hu, J.; Li, L.-s.; Alivisatos, P. *J. Phys. Chem. B* **2002**, *106*, 2447-2452.

(8) Shabaev, A.; Efros, A. L. *Nanoletters* **2004**, *4*, 1821-1825.

(9) Hikmet, R.; Chin, P.; Talapin, D. V.; Weller, H. *Advanced Materials* **2005**, *17*, 1436 - 1439.

(10) Kazes, M.; Banin, U. *Advanced Materials* **2002**, *14*, 317-321.

(11) Peng, Z. A.; Peng, X. *J. Am. Chem. Soc.* **2002**, *124*, 3343-3353.

(12) Peng, Z. A.; Peng, X. *J. Am. Chem. Soc.* **2001**, *123*, 1389-1395.

(13) Mokari, T.; Banin, U. *Chem. Mater.* **2003**, *15*, 3955-3960.

(14) Wensink, H. H.; Vroege, G. J. *J. Chem. Phys.* **2003**, *119*, 6868-6882.

(15) Sollich, P.; Speranza, A. *Journal of Chemical Physics* **2003**, *118*, 5213-5223.

(16) Chung, I.; Shimizu, K.; Bawendi, M. *PNAS* **2003**, *100*, 405-408.

(17) S. Coe , W. K. W., M. Bawendi, V. Bulovic *Nature* **2002**, *420*, 800-803.

(18) Coe-Sullivan, S.; Woo, W. K.; Steckel, J. S.; Bawendi, M.; Bulovic, V. *Organic Electronics* **2003**, *4*, 123-130.

(19) Hotovy, I.; Rehacek, V. *Sensors and Actuators B* **1999**, *57*, 147-152.

(20) Bandara, J.; Weerasinghe, H. *Solar Energy Materials & Solar Cells* **2005**, *85*, 385-390.

(21) Shoji Yamada, M. K., et al. *J. Appl. Phys.* **1988**, *63*, 2116-2119.

(22) Htoon, H.; V.I.Klimov *Applied Physics Letters* **2003**, *82*, 4776-4778.

(23) Klimov, J. H. V. I. *Applied Physics Letters* **2003**, *82*, 4776-4778.

(24) Rothenberg, E.; Banin, U. *J. Phys. Chem. B* **2004**, *108*, 2797-2800.

(25) Li, L.; Pradhan, N.; Wang, Y.; Peng, X. *Nano Letters* **2004**, *4*, 2261.

(26) Norris, D. J.; Yao, N.; Charnock, F. T.; Kennedy, T. A. *Nano Lett.* **2001**, *1*, 3.

(27) Peng, X.; Wickham, J.; Alivisatos, A. P. *J. Am. Chem. Soc.* **1998**, *120*, 5343.

(28) Zhong, X.; Feng, Y.; Knoll, W.; Han, M. *J. Am. Chem. Soc.* **2003**, *125*, 13559.

(29) Zhong, X.; Han, M.; Dong, Z.; White, T. J.; Knoll, W. *JACS* **2003**, *125*, 8589.

(30) Thakar, R.; Chen, Y.; Snee, P. T. *Nano Lett.* **2007**, *7*, 3429-3432.

(31) Jarosz, M. V.; Porter, V. J.; Fisher, B. R.; Kastner, M. A.; Bawendi, M. G. *Physical Review B* **2004**, *70*, 195327.

(32) Porter, V. J.; Geyer, S.; Halpert, J. E.; Kastner, M. A.; Bawendi, M. G. *Journal of Physical Chemistry C* **2008**, *ASAP.*

(33) Porter, V. J.; Geyer, S.; Halpert, J. E.; Mentzel, T. S.; Kastner, M. A.; Bawendi, M. G. *In Preparation* **2008**.

(34) Hines, M. A.; Scholes, G. D. *Adv. Mater.* **2003**, *15*, 1844-1849.

Curriculum Vitae

Education

Ph.D., Physical Chemistry, Massachusetts Institute of Technology (MIT), 2008
Concentrations: Nanocrystal Synthesis, Device Engineering
Dissertation: Design and Synthesis of Nanocrystal Heterostructures for Optoelectronic Device Applications

B.S., Chemistry, Tufts University, 2003
Concentrations: ACS Chemistry (major), Mathematics (minor)
Research: Reaction Kinetics of Vibrationally Excited CH_4 with a Ni Surface (Utz lab)

Teaching and Experience

Teaching Assistant, 2003 - 2004
Massachusetts Institute of Technology (MIT)
Courses: Physical Chemistry Lab, General Chemistry (non-major) Lab

Teaching Assistant, 2002 - 2003
Tufts University
Courses: General Chemistry I and II

Student Researcher, 2002
Cornell University
Research: Functionalization of Self-Assembling Monolayers (SAMs) on a Silicon Substrate

Lab Technician/Marketing Engineer, 1999-2001
Thornton Inc., Waltham MA USA.
Duties: Designing, testing total organic carbon/pH/conductivity sensor/meter systems, supervised product team meetings, scheduling, budget for OEM additions to product line

Presentations

Jonathan E. Halpert, Jonathan Tischler, Gautham Nair, Brian Walker, Wenhao Liu, Vladimir Bulovic, Moungi G. Bawendi **"Synthesis and Characterization of Quantum Dots Coupled to J-aggregate Cyanine Dyes in Water"** Paper presented at the American Chemical Society 234th National Meeting & Exposition, Boston, MA USA, August 19-23, 2007.

Jean-Michel Caruge, Jonathan E. Halpert, Vanessa Wood, Vladimir Bulovic, Moungi Bawendi "**Colloidal Quantum Dot Light Emitting Devices (QD-LEDs) Using Inorganic Charge Transport Layers"** Paper presented at the American Chemical Society 233rd National Meeting & Exposition, Chicago, IL USA, March 25-29, 2007.

Vladimir Bulović, Moungi Bawendi, Jonathan Halpert, Polina Anikeeva, Seth Coe-Sullivan, Wing Woo, Jonathan Steckel, LeeAnn Kim, Jean-Michel Caruge, Vanessa Wood **"Quantum Dot LEDs"** Paper presented at SPIE Photonics West Convention, San Jose, CA USA, January 20 – 25, 2007. (Vladimir Bulovic originally scheduled to speak)

Jonathan E. Halpert, Polina Anikeeva, Vladimir Bulovic, Moungi Bawendi **"High Quantum Yield Nanocrystals for Efficient Quantum Dot Light Emitting Diodes (QD-LEDs)"** Paper presented at the Material Research Society (MRS) Fall Meeting, Boston, MA USA, November 27 - December 1, 2006

Publications

Halpert JE, Porter VJ, Zimmer JP, Bawendi MG. Synthesis of CdSe/CdTe Nanobarbells. *Journal of the American Chemical Society* 2006, **128**: 12590-12591.

Anikeeva PO*, Halpert JE*, Bawendi MG, Bulovic V . Electroluminescence from a mixed red-green-blue colloidal quantum dot monolayer. *Nano Letters* 2007, **7** *(8)*: 2196-2200. (*these authors contributed equally to this work)

J.M. Caruge*, J.E. Halpert*, V. Wood*, V. Bulović, M.G. Bawendi Colloidal Quantum Dot Light Emitting Devices with Metal-Oxide Charge Transport Layers *Nature Photonics* 2008, **2**: 247-250.

Caruge J-M, Halpert JE, Bulovic V, Bawendi MG. NiO as an Inorganic Hole-Transporting Layer in Quantum-Dot Light-Emitting Devices. *Nano Letters* 2006, **6**: 2991-2994.

Porter VJ, Geyer S, Halpert JE, Kastner MA, Bawendi MG. Photoconduction in Annealed and Chemically Treated CdSe/ZnS Inorganic Nanocrystal Films. *Journal of Physical Chemistry C* 2008, **0**: ASAP.

Steckel JS, Snee PT, Coe-Sullivan SA, Zimmer JP, Halpert JE, Anikeeva PO, Kim L-A, Bulovic V, Bawendi MG. Color-Saturated Green-Emitting QD-LEDs. *Angewandte Chemie International Edition* 2006, **45**: 5796-5799.

Fisher BR, Caruge J-M, Chan YT, Halpert JE, Bawendi MG. Multiexciton fluorescence from semiconductor nanocrystals . *Chemical Physics* 2005, **318**: 71-81.

In Press:

Venda J. Porter, Scott Geyer, Jonathan E. Halpert, Tamar S. Mentzel, Marc A. Kastner, Moungi G. Bawendi Charge Transport in Mixed CdSe and CdTe Colloidal Nanocrystal Films *(submitted to PRB)*

Jonathan Halpert, Jonathan Tischler, Gautham Nair, Brian Walker, Wenhao Liu,Vladimir Bulovic, Moungi Bawendi Synthesis and Characterization of Aqueous Quantum Dot/J-aggregate Conjugates *(submitted to JACS)*

Patents:

"Water Soluble, Ionically Coupled J-aggregate/Quantum Dot Conjugates" MG Bawendi, V Bulovic, JE Halpert, J Tischler, Provisional Filing, 18 August 2007 (filed).

"Nanocrystal Coded Beads for Biological Molecule/Protein Detection" PO Anikeeva, MG Bawendi, V Bulovic, JE Halpert, H-D Kim, B Walker, Provisional Filing, _____ (filed).

"Inorganic Transport Layer for Quantum Dot Light Emitters" A Arango, MG Bawendi, V Bulovic, J-M Caruge, S Coe-Sullivan, JE Halpert, JS Steckel, **Patent Pending**, 15 February 2006 (filed).

"Blue Emitting Quantum Dot LED using ZnCdS/ZnS Nanocrystals as Active Layer" PO Anikeeva, MG Bawendi, V Bulovic, JE Halpert, **Patent Pending**, 11 August 2007 (filed).

"White and Multcolor QD-LED" PO Anikeeva, MG Bawendi, V Bulovic, S Coe-Sullivan, JE Halpert, JS Steckel, **Patent Pending**, 14 February 2007 (filed).

"CdSe/CdTe Nanobarbells," MG Bawendi, JE Halpert, VJ Porter, **Patent Pending**, 28 December 2006 (filed).

Fellowships:

- REU Fellow (Cornell University, 2002)

Acknowledgements

Graduate school for me has been a terrific experience. Although at times exhausting, frustrating and stressful (and usually all at once), I have enjoyed working with extremely talented inviduals, whose interests and love of science and technology I keenly share. I don't think there is assembled anywhere a more collegial, motivated and productive group of scientists (and engineers) than at MIT in general, and in the Bawendi lab in particular.

I would first like to thank Moungi, whose constant support has enabled me to take risks and innovate in unexpected ways. He has allotted me the freedom to pursue my ideas while also helping to guide me towards successful results. In academia there are not many good managers, but Moungi stands out as a notable exception. I never felt I was being watched, yet I know he knew how I was doing. He was always available to meet, yet I never felt micro-managed. These are excellent traits in an adviser. His lab is productive and students are motivated without being overworked or cut-throat. In fact it is this atmosphere of collegiality, and even friendship, that has made working here so rewarding. Furthermore, Moungi's constant dedication to precision in wording and accuracy in results, has not only turned some of my worst drafts into excellent papers, it has helped me to become a better scientist as well.

I also want to thank Vladimir Bulovic who has in many ways been like a second advisor to me. His energy and enthusiasm are infectious and it has been a pleasure working in his lab. Most of my collaborators are Bulovic people.

Of course I have to thank my labmates as well. As this is the only part of my thesis they are likely to read, I have eulogized them all in a good natured way. They are all hard-working, dedicated, intelligent people whom I have felt thankful to get to know and work beside. Except for Scott. Whoa, just kidding of course...you see the kind of wacky fun we have here...ah the camaraderie, the gentle ribbing...working in lab has been made much easier by the company I've kept while working here. I don't think I could have survived without coffee time, although fewer trips to the "Beast" might have been warranted.

Of my labmates I'd first like to thank Preston (aka, Dr Chicken) for mentoring me in the ways of II-VI chemistry. Many of my brightest QDs were inspired by his teachings. Furthermore his guidance in lab helped shape me into a better scientist and helped get me through my oral. Preston is also a genuinely fun guy, he is not only the life of the party, hes the guy who makes his own t-shirt about the party then wears it to the party. He is also excellent at Halo; his game transcends the mere meaning of FPS, turning combat action into a choreographed setpiece of performance art. It is to be seen.

Also in the mentor category is Jean-Michel Caruge who taught me all about solid state and thin films processing. His guidance on our early projects together helped expand my thinking about how to design future devices. Also, he is an extremely fun guy to work with. Many were the late nights we spent in building 26 trying for the "love of Jesus" to get the inorganic device to emit. Sometimes we were rewarded. Sometimes we just went to the Beast. He is also a better dancer than Preston.

Yinthai is another of my mentors, his cool demeanor and steady hand in the lab served as the inspiration for my own meager skills. He never failed to tell a good joke or

wax eloquent about the trials and tribulations of being Yinthai. His stories about his time in the army are so good I find myself retelling them to those who would otherwise never get the honor.

Venda was one of my best friends in the lab. We also collaborated on the Chapter 4 stuff and basically spent the time between 4-4:30 kicking around ideas and getting our daily dose of espresso. We tried to think up ways to improve the mentoring program, and spent some effort to keep Dr Chicken sane. Of all the leaders our lab has had, she was the best organized and most dedicated; earning rather than demanding the respect of the younger folks. Yinthai, Presto and Venda made up my lunch crew (often with August) for three years. When she left I realized it was time for me to leave as well.

August of course deserves good mention. He is extremely bright and well mannered. There is no topic he can't discuss, and has been a good friend even though I dropped a bunch of his possessions that time I helped him move. We worked together for a while trying to get current to go through an Au-tipped CdSe NR but it just never came together. I give him much respect for never failing to take on difficult projects. He will make an excellent professor.

Of the many synthetic people, I have often shared QD tips with Greytak and Becky, who took over Preston's project. Greytak is a fun guy with a good sense of humor who knows as much as anyone should about the Simpsons (or Monty Python). He always picks up a reference when the younger kids miss it. Becky is very smart and competent; she would be intimidating if she weren't also so nice. Binil is another one of my favorite synthetic chemists, he always has interesting things to say on any topic and is very wise for a 30-something. Although he doesn't like beer he still tries to have fun at my parties which I appreciate. Jongnam also deserves some mention, mostly as the craziest volleyball player we're ever deployed. His serve is something to fear; on both sides of the net.

Of the rest of the Elder People, Jonny Steckel deserves a good mention here as a mentor. He is a precise and exacting chemist, and first took me under his wing when I joined. The collaboration he began with the Bulovic group has served me well and we have been heir to his and Seth's legend in much of our work (Chapter 2 especially), and our extracurriculars. He air humps the machinery and John Zimmer whenever possible but this is forgivable. I should include a thank you to Seth Coe Sullivan at the same time, it was he who first taught me how to make the QD-OLED for my nanorod stuff. He's a patient guy and an impressive entrepreneur. Of the rest of the elder people, Brent is always well dressed and showed me some spectroscopy. He returns every now and again to remind us of the real world. I went to Joe's wedding which has served of something of a template for my own upcoming nuptials (namely BBQ). I never understood Joe's work until his defense...and then I got it. John Zimmer never failed to debate any philosophical point and I enjoyed our discussions immensely. He also served as the finest example of a dutiful chemist.... Standards went downhill for awhile after he left. Brian Yen was good guy, he generally joined us for evening beastings and shared his dour brand of dark humor. He was a devoted minimalist and sold me a surprising amount of his furniture which was good of him. He is probably the smartest guy we've had (sorry Gautham) but I'm not sure if that helped. Dave Oertel is another solid citizen of the Bawendi lab. He was always up for an argument and liked working with his hands. Whenever he machined parts for the evaporator Venda and I would have to look up what

"knurling" meant or what a "grommet" was. Mirna yelled at me my first day and owned a little dog. I didn't know her well so I don't know what to do with that information. Nathan was also an interesting character, we had many useful discussions and sharing a hood with him was generally survivable. French Fred (Dumestre) and Xavier both gave me tips on chemistry and physics, respectively. Xavier even tried to speak French to me until he realized the kind of things I'd learned to say (ta mere…).

Hao Huang has been my good friend almost since we started here together. I say almost because for the first few months we were rivals see who would not have to be a spectroscopist. Fortunately for myself, and for science, I won at first…although in the end we both did devices. We collaborated on the NR polarization study early on, in the Appendix A.2. Ours has been a cultural exchange; he once came to my parents house for thanksgiving. For his part he puts up with my mangling of the Chinese language. Wo bu shuo hen hao de hanyu. Hao will do well no matter what he does, he has been a good friend and has taught me much about the world.

My collaboration with Polly has been fairly fruitful…we've made a LOT of devices and poured more QDs than I care to think of onto the spin coater. We've gone winter camping with her for two years now and Kira and I are always left in the dust, but she's very polite about it. She frog marched us up Mt. Algonquin with no mercy and we made it and then we made it back (I have the pictures). On my own, I might have turned around early. This is a metaphor for our collaboration. I have no doubt she will make an excellent professor as long as she steers clear of the diethyl zinc.

Similarly Yaakov and I have collaborated for some time on the QD-J's from Chapter 5. His knowledge of physics is impressive and he fears no equation. He is also a really fun guy, lots of ideas and always enthusiastic. We did a number of two day experiments that never took off, but we also did a few that turned out great. He is a good example of how a collaborator can bring a whole new angle to your work.

I should also thank Gerry Chen and Vanessa Wood, my other two collaborators in Bulovic group, as well as Conor and Alexi both of whom helped me out at some point. Conor has a particularly good sense of theory and I've found his derivation of FRET to be of enormous use.

Of the younger Bawendis, Gautham has been my good friend since he started. We don't always agree on philosophy…in fact we always disagree…but he makes up for it by whaling on me in Street Fighter 2. He is an excellent collaborator, the spectroscopist to my synthetic chemist, and has a deep knowledge of Achewood. All crucial skills.

Scott Geyer joined as Venda's apprentice and has been able to adequately fill her shoes after she left. He is a capable physicist with a lot of ideas and a good natured sense of humor. He is also one of the last of the II-VI chemists, hopefully he and Brian Walker can pass on that dark art. I once fed him nearly raw steak tips and he keeps coming back…so that says something, for better or worse. I have enjoyed our conversations.

Lisa Marshall, along with Scott and sometimes Hao or Brian, has been a constant member of the second coffee crew. She is very smart and funny. It is her job to keep me honest and have my sources ready. Her critical nature has led to more than one Wiki search as I sometimes forget why I think a thing is so (90% of the time there is a good reason). Also her skill at grilling meats is excellent both at home and away.

Wen is another funny kid, he's always up for a good time be it volleyball, the Royal Beast, or just hanging around the office. While his knowledge of stocks is up or down, depending on the day, I have great confidence that he will be successful in business one day. He has an entrepreneurial mind and a lot of potential. Oh yeah, he also bangs out bio papers two at a time. Not an easy task.

Brian Walker is my protégé, as I like to remind him constantly, much to his chagrin. I have attempted to teach him all the tricks I learned from my mentors in the hope that some of our knowledge may be passed down through the group. He is a very capable synthetic chemist and while at first I'm sure he appreciated all my "mentoring" (ie boring lectures), he can now stand on his own two feet as a researcher. He's a smart guy, I think he'll do well.

Peter is another one of the younger guys who makes the lab a fun place to work. I taught him all that know about brewing beer because, quite frankly, he probably knows more about synthesis than I do. You have to watch these kids, pretty soon they are running the place...as we did too, I suppose.

Juwell is extremely bubbly and a very precise and thorough chemist. She has seen a lot as a grad student and survived. Also she taught me two days worth of cell bio which is worth more than a semester in college. Hee-san is another person who improves my day no matter what has happened. I don't know who forgot to tell her that grad school is long and depressing because she seems pretty happy all the time. Must have missed the memo...I am sorry for her sake, but I rarely cleaned my hood. Cliff is a very introspective and philosophical person. I knew him less well than the others, I think, but I enjoyed our conversations together. I think he has some of the more creative ideas in our lab... the ones that succeed will be something really new.

I also want to sincerely thank Li Miao, our administrator. She has helped me out on several occasions and also taught Kira and I Chinese (or some of it). Please disregard my note to Hao, wo shuo y dianr hanyu. Also I want to thank the department administrator Susan Brighton who has helped me survive many pounds of paperwork. She knows how to cut through the red tape with a pair of golden scissors. If she were president this country would work right. Seriously.

Finally I did not get a chance to really get to know the newest members of the group, Liang Yi and the UROPs. So for them I have advice. Work hard and don't give up. If you can't go through a problem, find a way around it. Never feel sorry for yourself when something doesn't work because failure is part of the process, you need to fail a few preps before you succeed. If you suffer first, it just makes your triumphs all the more sweet. And lastly, never, ever, ever walk away from good data...if your experiment is working, you sit there and milk it all night if need be. Because it might not work again tomorrow.

There were many other people who aided me in my strange journey but most of them will never read this. They are the friends I had in Boston, from Tufts and from my childhood. I need to thank my parents who taught me to learn, to thirst for knowledge, and who gave me the drive to be successful. More than anyone else, I owe them for what I've become. I want to thank my brother and sister, who have supported me in my quest to be Dr. Jon, and then went about beating me to it (Kim succeeded, Rich will get there). I want to remember also my grandmother Jeanne, who passed away as I was writing this thesis, and also my uncle Dave and my college buddy Jon Snyder, both of whom died in

my fourth year. I want to thank my other supporters, friends, old teachers, aunts and uncles and cousins, future parents-in-law, former co-workers and prospective business partners.

And mostly, by a large factor, I want to thank Kira, my fiancée. I love her deeply and she has been a great source of inspiration for me; I have to work very hard just to keep up with her. Without her, none of this would be possible or even probable. It is also worth noting that she has provided the lab, over the years, with pizza and beer for movie nights, food for our BBQs and every now and again, going away on business so we can play poker. All around, this couldn't have been the same experience without her.

So looking back, as I am losing the lab and the good times I've had here, I am thinking of the new life I will have with Kira, and probably a job, maybe a house, and possibly kids…and so forth…and I'm looking forward to that. So will it be one day for all of you. Enjoy this while it lasts.